FACULTY OF SCIENCE
UNIVERSITY OF COPENHAGEN

Master's Thesis

Henrik Jacobsen

Magnetic properties of nano-scale hematite: theory, experiments and simulations

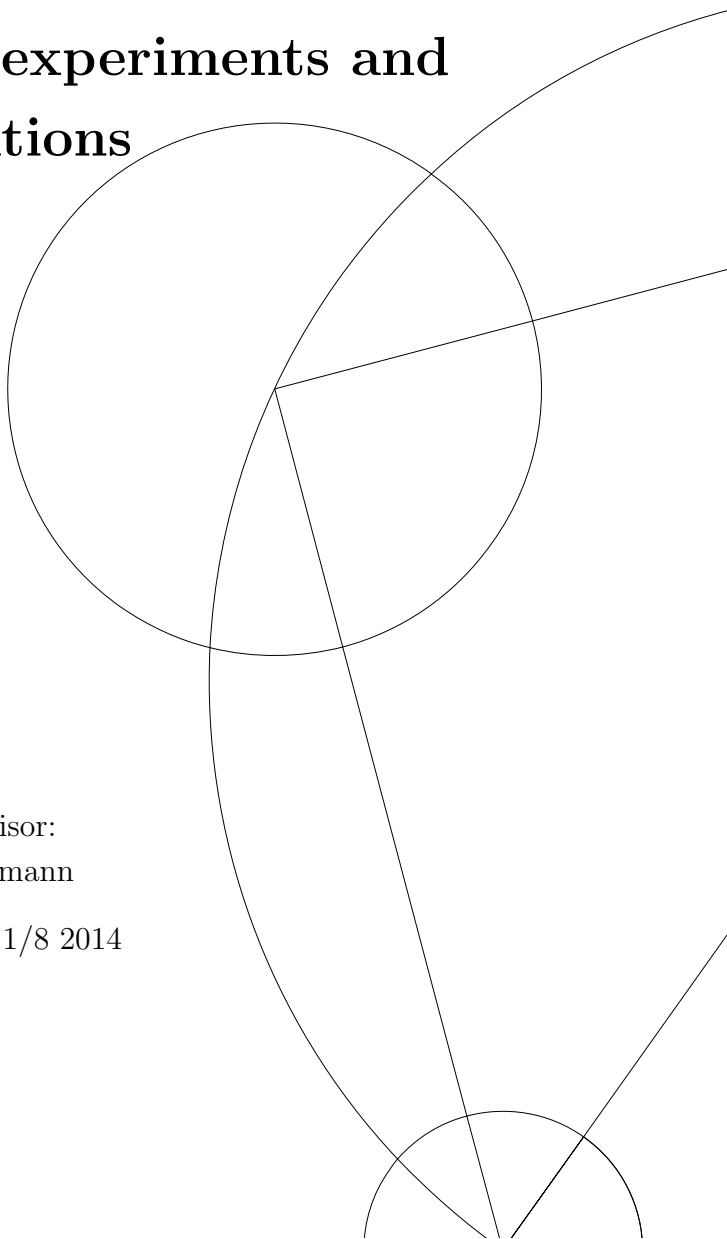

Supervisor:
Kim Lefmann

Submitted: 1/8 2014

Contents

Resumé

Hæmatit er et almindeligt mineral med en relativt simpel, lidt skrå antiferromagnetisk struktur. Hæmatits magnetisky dynamik er blevet studeret både teoretisk og eksperimentelt de sidste 40 år. Spinbølgerne er blevet målt i både bulk og nanopartikler af hæmatit, og kvantiseringen i nanopartikler er blevet eftervist.

Det er for nyligt lykkedes at syntesere mesoporøs hæmatit. Dette materiale har en makroskopisk struktur af ordnede vægge med en diameter på nano-skala. Mesoporøs hæmatit har således egenskaber til fælles med både nano-verdenen, såsom stort overfladeareal og tynde vægge, men er samtidig makroskopisk. Studier af mesoporøs hæmatit kan således hjælpe med at bygge bro over gabet mellem nano og bulk verdenen.

I denne opgave studeres hæmatit på nano-skala gennem udregninger, neutronspredningseksperimenter og numeriske simuleringer. Adskillige eksperimenter på 16 nm og 8 nm hæmatit nanopartikler og mesoporøs hæmatit analyseres. I de mesoporøse partikler vises det at easy-plane anisotropy konstanten forbliver negativ ned til de laveste temperaturer, hvilket giver en forklaring på udeblevelsen af Morin overgangen, som er til stede i bulk hæmatit.

Det primære fokus i denne opgave er studiet af nanopartikler. For første gang er lav- og højfrekvens $q = 0$ excitationerne målt samtidig i et eksperiment. Amplituderne og frekvenserne af disse excitationer bruges til at bestemme anisotropi-konstanterne i hæmatit med god nøjagtighed.

Det påpeges at ved negligering af easy-plane anisotropi konstanten har adskillige publicerede artikler overestimeret hæmatits easy axis anisotropi konstant med en faktor 2. Med denne korrektion opnås glimrende overensstemmelse mellem Mössbauer data og neutron data.

Langevin simulationer af nanopartiklernes magnetiske dynamik giver yderligere indsigt i deres opførsel. Simulationerne bekræfter validiteten af Néel-Brown-loven for både 8 nm og 16 nm partikler. Den simulerede temperaturafhængighed af begge $q = 0$ excitationer er mindre afhængig af den gennemsnitlige undergittermagnetisering in hvad teorien forudsage. Dette medfører korrektioner til de eksperimentelt bestemte værdier af anisotropi konstanterne.

Med hjælp fra simuleringerne vises det at 8 nm partiklerne sandsynligvis har et ukompenseret moment på ca. 1.5%. En ny excitation, døbt "rotor mode" observeres. Denne excitation forklarer den målte forøgelse af frekvensen af den lavfrekvente excitation, og det forudsiges at den er til stede i alle antiferromagnetiske nanopartikler med stærk in-plane anisotropy.

For både 8 nm og 16 nm partikler var det muligt at opnå god overensstemmelse mellem simuleringer og adskillige eksperimenter. Simuleringerne er således et velegnet værktøj til at analysere eksperimenter, hvilket giver en nøjagtig bestemmelse af parametrene der styrer nanopartikler af hæmatits magnetiske dynamik.

Abstract

Hematite is common mineral with a relatively simple, slightly canted antiferromagnetic structure. The magnetic dynamics of hematite has been the subject of intense theoretical and experimental studies in the last 40 years. The spin waves have been measured in both bulk and nanoparticulate hematite and have been shown to be quantized in the nanoparticles.

Recently, mesoporous hematite has been synthesized. This material has a long range ordered structure of walls with diameter on the nano-scale. Mesoporous hematite shares properties with both the nano-world, such as large surface area and thin walls, while still being macroscopic in nature. The study of mesoporous hematite thus helps bridge the gap between the nano- and the bulk world.

In this thesis, nano-scale hematite is studied by theoretical calculations, neutron scattering experiments and numerical simulations. Various experiments on 16 nm and 8 nm hematite nanoparticles and mesoporous hematite are analyzed.In the mesoporous particles, the easy-plane anisotropy constant is shown to remain negative down to the lowest temperature, providing an explanation of the absence of the Morin transition which is present in bulk hematite.

The main focus of this work is the study of the nanoparticles. For the first time, the low and high frequency $q = 0$ magnetic excitation modes have been observed simultaneously in experiments. The amplitudes and frequencies of these modes are used to determine the anisotropy constants of hematite to good precision.

It is pointed out that by neglecting the easy-plane anisotropy constant, several published papers overestimate the easy axis anisotropy constant of hematite by a factor of 2. With this correction, excellent agreement between Mössbauer data and neutron scattering data is obtained.

Langevin simulations of the magnetic dynamics of the nanoparticles provide further insight into their behavior. The simulations confirm the validity of the Néel–Brown law in both 8 nm and 16 nm particles. The simulated temperature dependence of both $q = 0$ modes is less dependent on the average sublattice magnetization than what is expected from theory. Corrections to the extracted anisotropy constants from experiments are made.

With the aid of the simulations, it is shown that the 8 nm particles contain an uncompensated moment of approximately 1.5%. A new mode, named the “rotor” mode is observed. This mode explains the observed increase in frequency of the low frequency mode, and is predicted to be a general feature of antiferromagnetic nanoparticles with a strong in-plane anisotropy.

For both 8 nm and 16 nm particles it was possible to obtain good agreement between simulations and several different experiments. The simulations are thus a useful tool to analyze experiments, providing an accurate determination of the parameters governing the magnetic dynamics of hematite nanoparticles.

Acknowledgements

This thesis could not have been made without the help from many people. First of all I would like to thank my supervisor Kim Lefmann for making the project possible. His enthusiasm and knowledge of neutron scattering and magnetism are an inspiration to me. I also wish to thank my second supervisor, Pascale Deen, for giving me the time I needed to write this thesis.

I would like to thank Mads Bertelsen for proofreading early drafts of the thesis and providing many useful suggestions for improvements. I also thank Morten Holm Christensen for proofreading parts of the thesis. I thank Feng Jiao for providing us with a new sample of mesoporous hematite when the old sample somehow got lost.

All of the experiments analyzed in this thesis were performed with the help of others. I would like to thank, in no particular order, Adrian H. Hill, Ross Stewart, Hannu Mutka, Kim Lefmann, Sonja Lindahl Holm, Tilo Seydel, Bernhard Frick, Pascale Deen, Erik Brok, Cathrine Frandsen, Goran Nilsen, Christian Bahl, Luise Theil Kuhn, Hjalte Sylvest Jacobsen and Andreas Wischnewski for their efforts. I would in particular like to thank Christian Bahl and Luise Theil Kuhn for digging up old data and letting me re-analyze it. I thank DANSCATT for financially supporting all the experiments.

The first version of the simulations were written and tested by Jakob Garde. I would like to thank Jakob for writing the code and for letting me use it. I thank Per Hedegård for his aid in the theoretical calculations needed to develop the simulations and the rotor mode (and for his red hair).

Writing a Master's thesis can sometimes be tough work, and I thank Marcella Berg for keeping my spirits up through many great conversations about the process of writing a thesis (and countless other topics). I thank the people in the reciprocal space in D311 for being great office mates.

I finally wish to thank rushold Boogie for making the past 6 years at the university a thoroughly enjoyable experience. May our battle cry be shouted for many years to come.

Chapter 1

Introduction

Hematite, α-Fe_2O_3 is a common mineral that is found all over Earth. At temperatures below 948 K, bulk hematite is an antiferromagnet with slightly canted spins, giving a net total moment [1]. This state is called the weakly ferromagnetic (WF) state. Upon further cooling below 260 K, the spins flip 90 degrees, and in this state, hematite is a pure antiferromagnet.

The magnetic properties of hematite have been studied extensively. It has been studied with neutrons for more than 40 years [2, 3, 4]. One of the first inelastic studies of bulk hematite was done by Shirane in 1970 [2], determining amongst other things the exchange constants of hematite.

The chemical and physical properties of materials on a nanoscale is a key area of scientific interest, covering disciplines from theoretical physics through to clean energy sources. The ability to tune desirable properties allows fundamental studies of the underlying physics of the material. Magnetic dynamics provided by magnetic interactions in materials is an area of interest to theoreticians and experimental physicists alike. Tuning these dynamics can provide novel magnetic materials. One way of altering the material's properties is by reducing the size of individual particles or structures (e.g. thin-films, nanoparticles, nano-structures). Once in the nano-scale region it is widely known that magnetic properties can differ greatly from the material's "bulk" counterpart [5].

Nanoscale hematite (α-Fe_2O_3) has shown potential in a variety of fields, in particular its photoelectrical properties[6, 7, 8]. Understanding the underlying dynamics and magnetism may lead to an improved understanding of the material itself, enabling chemists to direct their efforts at materials with specific features. Nano-particulate hematite has been widely studied with a variety of magnetic probes. In particular, inelastic neutron scattering has been used to study high-frequency collective magnetic excitations, enabling calculations of magnetic anisotropy constants in the system, and providing a reason for the suppression of the Morin transition in nanoparticles [9, 10, 11, 12].

Another interesting topic in dynamics of nanoparticle magnetism is superparamagnetism (SPM), where the magnetization direction spontaneously reverses direction,

assisted by temperature in an Arrhenius fashion. This effect is present also for antiferromagnetic hematite, as was shown directly using Mössbauer spectroscopy [13] and by quasi-elastic neutron scattering [9]. The relatively recent synthesis of mesoporous (pore sizes between 2 nm and 50 nm) metal oxides [14, 15] with long range crystallographic order provides an entirely new class of material with equally interesting magnetic properties. Because mesoporous materials combine high surface area, nano-sized walls and three dimensional coherent structure at a micron meter scale, they may exhibit unique properties, which cannot be observed in nano or bulk counterparts [16, 17, 18].

In this thesis we will investigate the magnetic properties of nano-scale hematite. The main focus is on nanoparticles, but mesoporous hematite particles will also be discussed. Usually, such investigations will be an interplay between analytical calculations and experiments. We here also use numerical simulations to reach into theoretical areas that are unreachable by analytical methods. Parts of the results of this work on 16 nm particles has been published in Ref. [19]. Other parts are in progress of being published in Refs. [20, 21]

This thesis is structured as follows. In Chapter 2 hematite is introduced. Some of its important properties are discussed and a short introduction to the field of magnetism is given. We also briefly review the existing literature on hematite. We continue in Chapter 3 to derive some of the magnetic excitations that can occur in hematite bulk and nanoparticles. In Chapter 4, Mössbauer spectroscopy is explained, and a short review of literature on Mössbauer spectroscopy on nanoscale hematite is given. Chapter 5 is devoted to explain the concept of neutron scattering, which comprises the bulk of the experimental part of this thesis, ending with a short review of previous neutron scattering results on hematite. This is followed by the presentation and analysis of data from several neutron scattering experiments in Chapter 6. Next, the simulations are introduced and described in Chapter 7. A discussion of the results is presented in Chapter 8, before the conclusion and outlook in Chapter 9.

Chapter 2

Magnetism and hematite

In this chapter, the theoretical foundation for the rest of the thesis is laid. We start by describing magnetism in general. First we discuss the magnetic properties of a single electron, before moving on to interaction effects: exchange interactions and anisotropies. We next describe hematite: the basic properties, crystal structure, magnetic properties, as well as characteristics of nanoparticulate, mesoporous and bulk hematite.

2.1 Magnetism

The electron is a charged particle with spin 1/2. As such, it has a magnetic moment given by

$$m = \mu_B = \frac{e\hbar}{2m_e} = 9.274 \times 10^{-24} \text{ J/T}, \tag{2.1}$$

where e is the elementary charge, $\hbar$ is Planck's constant and m_e is the mass of the electron. μ_B is named the Bohr magneton, after Niels Bohr, and we approximate $g \approx 2$. The magnetic moment is antiparallel to the spin.

It is well known that electrons interact with an applied magnetic field. The Hamiltonian for this interaction is

$$\mathcal{H}_B = -g\mu_\text{B}\mathbf{B} \cdot \sum_i \mathbf{s}_i. \tag{2.2}$$

It can be readily shown that a magnetic moment $\mathbf{m}$ in a magnetic field will perform so-called Larmor precessions around the magnetic field, obeying the equation

$$\frac{\mathrm{d}\mathbf{m}}{\mathrm{d}t} = \gamma_L \mathbf{m} \times \mathbf{B}, \tag{2.3}$$

where $\gamma_L = -e/2m_e$ is a constant called the gyromagnetic ratio. This equation of motion for a magnetic moment subjected to a magnetic field will occur frequently in this thesis.

Apart from its intrinsic spin, an electron also has an orbital angular momentum related to which shell it is in. Most atoms have more than one electron, but only

the electrons in the nonfilled shells contribute to the magnetism of the material. The magnetic moment of an atom is thus associated with is total angular momentum, **J**,

$$\mathbf{J} = \mathbf{L} + \mathbf{s}. \tag{2.4}$$

Many different values of **J** are in general possible, from $|\mathbf{L}+\mathbf{s}|$ to $|\mathbf{L}-\mathbf{s}|$. To determine the actual value of **J** in a substance, Hund's rules [22] can be used. In short, there are three rules: 1) Maximize the total spin on the atom. 2) Maximize the angular momentum, **L**. 3) If the shell is less than half filled, minimize **J**. Otherwise maximize **J**.

The magnetization of a collection of atoms is

$$M = ng_J\mu_B J, \tag{2.5}$$

where g_J is the g-factor which is typically around 2, and n is the number of magnetic moments per volume.

For a paramagnet, it can be shown that the magnetization follows the Brillouin function [22],

$$\frac{M}{M_0} = B_J(y) = \frac{2J+1}{2J}\coth\left(\frac{2J+1}{2J}J\right) - \frac{1}{2J}\coth\left(\frac{y}{2J}\right), \tag{2.6}$$

with $y = g_J\mu_B JB/(k_BT)$.

The effect of an applied magnetic field is often quantified by defining the susceptibility,

$$\chi = \frac{M}{H} \approx \mu_0\frac{M}{B}, \tag{2.7}$$

where $\mathbf{B} = \mu_0(\mathbf{H} + \mathbf{M})$. The susceptibility thus tells how an applied magnetic field changes the magnetization. For a paramagnet [22],

$$\chi = \frac{n\mu_0 g_J^2\mu_B^2 J(J+1)}{3k_BT}, \tag{2.8}$$

which is commonly known as the Curie law.

2.2 Interactions

The most common interaction between magnetic spins is the exchange interaction, which is a consequence of overlap of electronic orbitals. We will illustrate the calculations for a two-spin system, before generalizing to crystals containing a macroscopic number of spins. The calculations here are inspired by Blundell [22].

For a pair of electrons, their total wavefunction must be antisymmetric. It is well known that electrons are Fermions and thus their wavefunction must be antisymmetric.

An electron pair can either be in the singlet or triplet state, described by

$$|\Psi_S\rangle = \frac{1}{\sqrt{2}}(\psi_a(\mathbf{r}_1)\psi_b(\mathbf{r}_2) + \psi_a(\mathbf{r}_2)\psi_b(\mathbf{r}_1))\chi_s \tag{2.9}$$

$$\equiv \frac{1}{\sqrt{2}}(|\mathbf{r}_1, \mathbf{r}_2\rangle + |\mathbf{r}_2, \mathbf{r}_1\rangle). \tag{2.10}$$

We omit the spin part for readability. The triplet state is

$$|\Psi_T\rangle \equiv \frac{1}{\sqrt{2}}(|\mathbf{r}_1, \mathbf{r}_2\rangle - |\mathbf{r}_2, \mathbf{r}_1\rangle). \tag{2.11}$$

It can be shown [22] that

$$\mathcal{H} = \frac{1}{4}(E_S + 3E_T) - (E_S - E_T)\mathbf{s}_1 \cdot \mathbf{s}_2. \tag{2.12}$$

The constant term is unimportant, and by defining the exchange constant J

$$2J \equiv E_S - E_T, \tag{2.13}$$

we can rewrite the Hamiltonian to

$$\mathcal{H} = -2J\mathbf{s}_1 \cdot \mathbf{s}_2. \tag{2.14}$$

It can be readily shown that J comes from the overlap of the wavefunctions, we will outline the derivation here [22]. Assuming that the states are normalized, we can calculate the energies of the singlet and triplet states

$$E_S = \langle\Psi_S|\mathcal{H}|\Psi_S\rangle = \langle\mathbf{r}_1, \mathbf{r}_2|\mathcal{H}|\mathbf{r}_1, \mathbf{r}_2\rangle + \langle\mathbf{r}_1, \mathbf{r}_2|\mathcal{H}|\mathbf{r}_2, \mathbf{r}_1\rangle, \tag{2.15}$$

$$E_T = \langle\Psi_T|\mathcal{H}|\Psi_T\rangle = \langle\mathbf{r}_1, \mathbf{r}_2|\mathcal{H}|\mathbf{r}_1, \mathbf{r}_2\rangle - \langle\mathbf{r}_1, \mathbf{r}_2|\mathcal{H}|\mathbf{r}_2, \mathbf{r}_1\rangle, \tag{2.16}$$

and we find

$$J = \frac{E_S - E_T}{2} = \langle\mathbf{r}_1, \mathbf{r}_2|\mathcal{H}|\mathbf{r}_2, \mathbf{r}_1\rangle. \tag{2.17}$$

Repeating the calculations for more than two electrons is quite impractical. Nevertheless, this example motivates the Heisenberg Hamiltonian written as a sum of pairwise interactions

$$\mathcal{H}_J = -\sum_{ij} J_{ij}\mathbf{s}_i \cdot \mathbf{s}_j. \tag{2.18}$$

Often, only nearest neighbor interactions are assumed. J is usually quite large; in hematite the effective coupling is around 200 K, as elaborated below. This exchange interaction is often mediated by oxygen atoms in between the magnetic atoms. This effect is named superexchange.

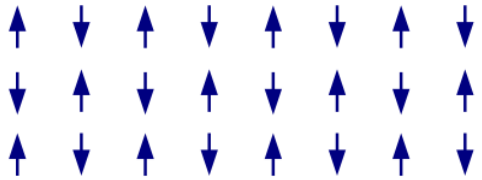

FIGURE 2.1: Illustration of antiferromagnetic order.

When $J > 0$, the energy is minimized when the spins are parallel. Thus, below a certain temperature named the Curie temperature, the spins align along an axis, and the system becomes ferromagnetic. The ordering parameter for a ferromagnet is usually taken as the magnetization, which is proportional to the sum of the spins,

$$\mathbf{s}^{\mathrm{FM}} = \sum \mathbf{s}_i. \tag{2.19}$$

The susceptibility of a ferromagnet above the ordering temperature is

$$\chi \propto \frac{1}{T - T_C}, \tag{2.20}$$

which is known as the Curie-Weiss law.

Not all spins in a bulk ferromagnet will be aligned. Instead, they will form small domains of aligned spins, but the domains will usually be arranged such that the total magnetization of the sample is far less than if all domains were aligned [22].

Conversely, when $J < 0$, the energy is (classically) minimized when the spins are antiparallel to their neighbors. It is usual to divide the lattice into two sublattices, A and B, where all the spins in each lattice are aligned, and the two sublattices are anti-aligned, see Fig. 2.1. The order parameter can thus be described as the normalized antisum of the individual spins in the sublattices [10]

$$\mathbf{s}^{\mathrm{AFM}} = \frac{1}{Ns}\left(\sum_{i\in A}\mathbf{s}_i - \sum_{j\in B}\mathbf{s}_j\right). \tag{2.21}$$

We can divide $\mathbf{s}^{\mathrm{AFM}}$ into two parts: a longitudinal ($\mathbf{s}^{\parallel}_{\mathrm{AFM}}$) and transverse ($\mathbf{s}^{\perp}_{\mathrm{AFM}}$) part, satisfying $(\mathbf{s}^{\mathrm{AFM}})^2 = (\mathbf{s}^{\mathrm{AFM}}_{\parallel})^2 + (\mathbf{s}^{\perp}_{\mathrm{AFM}})^2$. If the two sublattices are equal,

$$s^{\parallel}_{\mathrm{AFM}} = s^z_A = s^z_B \equiv s^z. \tag{2.22}$$

This classical state with two anti-aligned sublattices is called the Néel ground state. It should be noted that this state is not the quantum mechanical ground state, as is easily seen by applying the Hamiltonian to this state. The quantum mechanical ground state is a complex singlet-type state, as shown by Bethe for a 1d antiferromagnet [23]. Fortunately, Anderson showed that the Néel state is a good approximation to the ground

state for larger s [24]. For antiferromagnets, the ordering temperature is called the Néel temperature T_N. Antiferromagnets follow a similar law as ferromagnets above the ordering temperature:

$$\chi \propto \frac{1}{T + \theta_N}, \tag{2.23}$$

where $\theta_n \approx T_N$.

Dzyaloshinsky proposed in 1958 an explanation of the weak ferromagnetism observed in hematite, expanded upon below [25]. Moriya extended the discussion [26], and in their honor the interaction is named the Dzyaloshinsky-Moriya (DM) interaction. It is also sometimes named the asymmetric exchange interaction. Essentially, Dzyaloshinsky and Moriya showed that the crystal structure of hematite supports an interaction between spins of the form

$$\mathcal{H}_D = \mathbf{D} \cdot (\mathbf{s}_1 \times \mathbf{s}_2). \tag{2.24}$$

In general, $\mathbf{D}$ is a vector that can either connect the spins or be perpendicular to the vector connecting them. In hematite, $\mathbf{D}$ is parallel to spins along the (0 0 1) axis, and zero otherwise, see Fig. 2.2.

The energy of this Hamiltonian is minimized when $\mathbf{s}_1$ and $\mathbf{s}_2$ are perpendicular to each other. Usually, $D \ll J$, and the effect of the DM-interaction is thus small, and mainly introduces a slight canting of the spins, as will be shown later.

2.3 Anisotropies

Anisotropies define preferred directions of spins in particles. These anisotropies origin from the surroundings of the spins. In nanoparticles, surface anisotropies are quite common. Usually, they define a certain axis along which the spins prefer to align. This axis is usually named the easy axis. Taking the easy axis as the z axis, we can write this Hamiltonian as

$$\mathcal{H}_{\text{anis}} = -\sum_i \kappa_i (s_i^z)^2, \tag{2.25}$$

where κ_{2i} are the anisotropy constants. Two types of anisotropies can occur. If $\kappa_i > 0$, the energy is minimized when the spins are along $\pm z$. On the other hand, if $\kappa_i < 0$, the energy is minimized when the spins are in the xy plane, and this plane is referred to as the easy plane.

2.4 Hematite

Hematite, $\alpha-Fe_2O_3$ is a common mineral that is the main subject of study in this work. Hematite is an electrical insulator; hence the electrons are highly localized at the nuclei

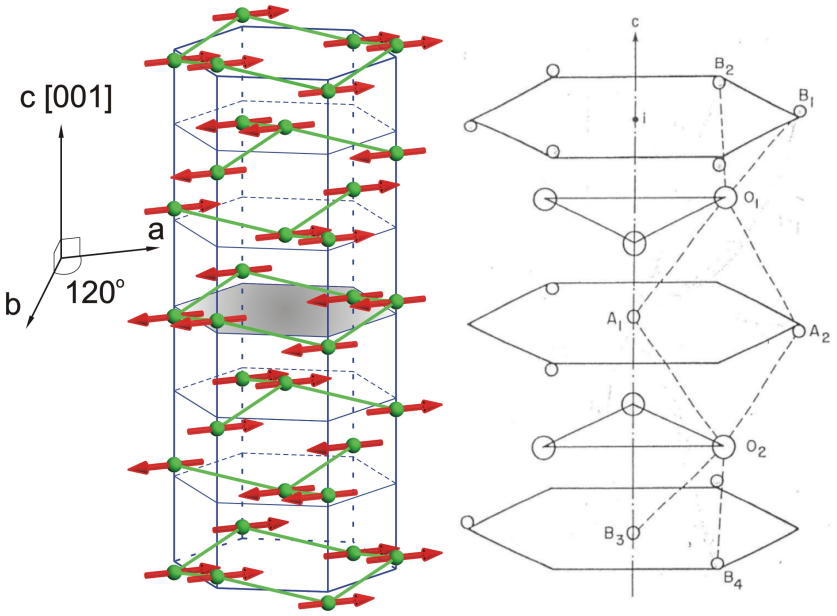

FIGURE 2.2: Left: The magnetic structure of hematite in the WF phase, by Bente Lebech. Right: Zoom in on the structure, revealing the most important paths for superexchange: J_1: A_1-O_2-B_3, J_2: A_1-O_1-A_2 and A_1-O_2-A_2, J_3: A_1-O_1-B_2, J_4: A_1-O_1-B_1 and A_1-O_2-B_4. From Morrish [1].

on the various lattice sites. The $3d^5$ valence electrons of each Fe(III) have $L = 0$ and spin 5/2, and this gives rise to the magnetic properties of hematite.

The crystal structure of hematite is described by the hexagonal-trigonal lattice, see Fig. 2.2. The Fe ions are located in layers, separated by intermediate layers of oxygen. These layers define the basal plane. The lattice parameters are $a = b = 5.034$ Å and $c = 13.74$ Å. The angle between a and b is 120°.

We define the reciprocal lattice parameters as

$$\mathbf{a}^* = \frac{\mathbf{b} \times \mathbf{c}}{\mathbf{a} \cdot \mathbf{b} \times \mathbf{c}}, \quad \mathbf{b}^* = \frac{\mathbf{c} \times \mathbf{a}}{\mathbf{a} \cdot \mathbf{b} \times \mathbf{c}}, \quad \mathbf{c}^* = \frac{\mathbf{a} \times \mathbf{b}}{\mathbf{a} \cdot \mathbf{b} \times \mathbf{c}}, \tag{2.26}$$

and a reciprocal lattice vector can in general be written as $\mathbf{G} = h\mathbf{a}* + k\mathbf{b}* + l\mathbf{c}*$, where h, k, l are integers. According to Bragg's law, scattering occurs when the scattering vector, $\mathbf{q}$ is equal to a reciprocal lattivce vector, $\mathbf{q} = \mathbf{G}$, see Chapter. 5. It is usual to denote scattering peaks by the set of (h, k, l) values. With this notation, the two most important magnetic peaks are the (003) reflection at $q = 1.37$ Å^{-1} and the (101) reflection at $q = 1.51$ Å^{-1}. Also, the nuclear $(10\bar{2})$ peak occurs at $q = 1.71$ Å^{-1}.

The nearest neighbors in hematite are shown in Fig. 2.2. The nearest neighbor exchange constants are $J_1 = 6 \pm 1.6$ K, $J_2 = 1.6 \pm 0.6$ K, $J_3 = -29.7 \pm 2$ K and $J_4 = -23.2 \pm 1$ K, as determined by neutron scattering [2]. Exchange constants to further neighbors are 1 K or less, and can therefore be ignored. As shown in the next chapter, it is convenient to work with the Fourier transform of the exchange interaction.

Leaving a full treatment for the next chapter, we simply write this as

$$J^{\mathrm{AFM}}(\mathbf{q}) = \sum_{j \in B} e^{i\mathbf{q}\cdot(\mathbf{r}_m - \mathbf{r}_j)} J(\mathbf{r}_m - \mathbf{r}_j) \quad (m \in A), \tag{2.27}$$

where the Fourier transform has been defined such that only the coupling between spins on different sublattices is used. For q along the c direction, we have

$$J(q) = (J_1 + 3J_3 + 6J_4)\cos(cq), \tag{2.28}$$

giving $J(0) = -222.3$ K.

2.4.1 Bulk hematite

Bulk hematite has a Néel temperature at ≈ 955 K, and can be adequately described as two ferromagnetic sublattices $\mathbf{s}_A$ and $\mathbf{s}_B$ coupled antiferromagnetically to each other.

At high temperatures, the moments align perpendicular to the hexagonal c axis, and lying inside the hexagonal ab basal plane, with a slight canting of the magnetic sublattices towards each other, caused by the DM-interaction. This leads to weak ferromagnetism (WF-phase). The coordinate system is chosen such that x points along the crystallographic c axis and z along a preferred direction within the basal plane. In general, z does not coincide with the crystal axes.

Upon cooling down through $T_{\mathrm{M}} \approx 263$ K, a first order magnetic transition occurs, reorientating the magnetic moments to lie almost parallel to the rhombohedral axis. This is known as the Morin transition. In the low temperature phase the magnetic moments lie anti-parallel to each other giving a pure antiferromagnetic material (AFM-phase).

The ground state spin directions are governed by the overall anisotropy of the system made up of κ_1 and κ_2 [1, 27, 28], where κ_1 is the anisotropy constant of the (001) direction and κ_2 is the uniaxial anisotropy constant in the basal plane and is positive:

$$\mathcal{H}_{\mathrm{anis}} = -\sum_i \kappa_1 (s_i^x)^2 - \sum_i \kappa_2 (s_i^z)^2. \tag{2.29}$$

In the WF-phase, κ_1 is negative, and thus the energy is minimized when the spins lie in the yz-plane. Cooling to the AFM-phase, κ_1 changes from negative to positive, and the spins flip to point along the x axis. The change of sign of κ_1 is what causes the Morin transition. In bulk hematite, the easy axis anisotropy is very small.

The spin waves in bulk hematite are continuous dispersions with a small gap due to the anisotropy. They are quite steep, peaking around 200 meV [2].

2.4.2 Nanoparticulate hematite

Nanoparticles differ fundamentally from their bulk counterparts. One major difference is that in bulk, surface effects can be neglected, whereas they are extremely important in nanoparticles. This is because the relative number of atoms near the surface is

immensely larger for nanoparticles than for bulk partikles. One surface effect in hematite nanoparticles is the presence of a uniaxial anisotropy, which will be discussed further below.

The total number of Fe(III) sites in a spherical 8 nm hematite nanoparticle is

$$N = \frac{V\rho}{m_{\mathrm{Fe}} + \frac{3}{2}m_{\mathrm{O}}} = 1.06 \times 10^4 \tag{2.30}$$

where $V = 4/3\pi r^3$ is the particle volume and $m_{\mathrm{Fe}} + 2/3m_{\mathrm{O}}$ is the mass of each Fe(III) site. $\rho = 5.26$ g/cm^3 is the density of hematite. For a 16 nm particle, the value is $N = 8.51 \times 10^4$. In [9] it is given as $N \approx 10^5$.

Dor a 8 nm spherical particle, the number of spins along the diameter is approximately

$$d = \left(\frac{6}{\pi}N\right)^{1/3} \approx 27, \tag{2.31}$$

and the ratio of surface spins to bulk spins is

$$\frac{\pi d^2}{\pi/6d^3} = \frac{6}{d} \approx 0.22. \tag{2.32}$$

In other words, more than a fifth of the spins are on the surface of the particle. For a 16 nm particle, the number of spins along the diameter is ≈ 55, and the ratio of surface spins to bulk spins is ≈ 0.11. If we assume that the surface spins have only 2/3 of the exchange interactions as the bulk spins, we would expect the value of B_X to decrease by 4% for 16 nm particles and 7% for 8 nm particles.

Another effect to be considered is that the number of spins on the two sublattices can differ; i.e. there will be a total uncompensated moment, $\xi = N_B/N_A$. In a simple model one can assume that the interior of the nanoparticle is essentially free of defects, but that the surface sites are randomly occupied such that the number of uncompensated spins is of the order of the square root of the number of surface spins [12]. For 8 nm particles, this would give

$$\xi \approx \frac{N/2 + \sqrt{\pi}d}{N/2 - \sqrt{\pi}d} \approx 1.018. \tag{2.33}$$

The 16 nm sample used in this thesis is the same as the one studied in [9, 29, 10, 11]. In the earliest of these papers, the average particle size is given as 15 nm, in the others as 16 nm. We will here assume that it is 16 nm, and neglect the distribution of particle sizes.

The preparation of the sample is described in detail in [9, 29, 10, 11]. In short, it is prepared by heating $Fe(NO_3)_3 \cdot 9H_2O$ in an oven at temperatures slowly increasing from 60 to 90°C over a period of 20 days. This method yields $\approx 10\%$ impurities, in the form of ferrihydrites. These impurities contribute slightly to the background, but can

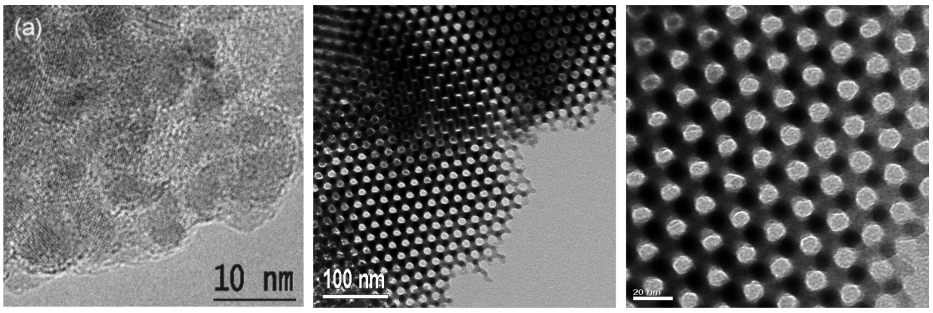

FIGURE 2.3: Left: TEM image of the coated 8 nm hematite sample, from [12]. Center and right: TEM image of the structure of mesoporous hematite, from [32].

otherwise be ignored. The 8 nm sample has been previously studied with neutrons in [12].

Frandsen et al. have shown that uncoated hematite nanoparticles have a tendency to aggregate and form clusters, effectively increasing the size of the nanoparticles [30]. We will not go into details with this effect, except noting that the effect can be minimized by coating the particles with phosphor. For larger particles, the effect is smaller. Most of the samples discussed in this thesis were coated. A TEM image of the coated 8 nm particles is shown in Fig. 2.3.

One point where hematite nanoparticles differ significantly from bulk hematite, is in the absence of the Morin transition. Hematite nanoparticles with diameter less than 20 nm are in the high temperature phase down to at least 1.5 K. Secondly, nanoparticles are small enough to be magnetically single domain. Thirdly, the spin excitations in nanoparticles are not continuous as for bulk; only certain discrete values of $\mathbf{q}$ are allowed. In a cubic nanoparticle, the allowed values of the wave vector is $q = n\pi/d$, where d is the side length and $n = 0, 1, 2, ...$ Usually, only the $q = 0$ mode is excited. For a 8 nm particle, the lowest non-zero q that is allowed is at $q = 0.039$ Å^{-1}, which from Eq. (3.43) is at roughly $\hbar\omega \approx 4$ meV.

2.4.3 Mesoporous hematite

Mesoporous hematite was first synthesized in 2006 by F. Jiao et al., [31]. A TEM image can be seen in Fig. 2.3. It consists of ordered connected walls of hematite with a thickness around 7 nm It is a porous structure, meaning that these walls are separated by pores with a diameter of 3.85 nm. The pore size was found from nitrogen adsorption-desorption measurements to peak at 3.4 nm. The pore size distribution is shown in Fig. 2.4. It thus has long range crystalline order like bulk, as has been verified by x-ray and neutron diffraction [32, 33], but it also has a very high surface area that is characteristic of nanoparticles, the typical length scales are comparable to nanoparticles and it does not undergo the Morin transition down to at least 2 K. The magnetic dynamics of mesoporous hematite seem to show a mixture of bulk and nano effects [19].

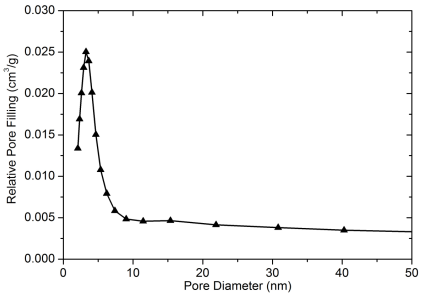

FIGURE 2.4: The pore size distribution of the mesoporous hematite sample used in this thesis as found by nitrogen adsorption measurements.

2.5 Effective fields

It can be convenient to convert the microscopic parameters like J_{ij} to the effective magnetic fields felt by a spin due to the exchange interaction, DM interaction and the anisotropies. There is some ambiguity in the literature on this point with different factors of 2, as will be discussed in the next chapter. The issue is whether the exchange Hamiltonian is written as $\mathcal{H} = \sum_{ij} J_{ij}\mathbf{s}_i \cdot \mathbf{s}_j$, $\mathcal{H} = \sum_{i\in A, j\in B} J_{ij}\mathbf{s}_i \cdot \mathbf{s}_j$ or $\mathcal{H} = 2\sum_{i\in A, j\in B} J_{ij}\mathbf{s}_i \cdot \mathbf{s}_j$.

2.5.1 Exchange field

The exchange field is defined by

$$B_X = \frac{2sJ^{\mathrm{AFM}}(0)}{g\mu_{\mathrm{B}}}. \tag{2.34}$$

In [27] and [34] this factor 2 is not included, which is due to the double counting issues that will be elaborated in the next chapter. Using the previously mentioned value of $J(0) = -222.3$ K, we find $B_X = -826$ T. In several references, this value is quoted as 900 T, e.g. [35, 36]. An overview of experimentally determined values of B_X is given in Ref. [1]. We will use 900 T as the starting point for the simulations, as this is the most common value used in the literature.

2.5.2 Anisotropy fields

The Zeeman energy of one spin (assuming that the magnetic field is along the z axis) is

$$H_Z = -g\mu_{\mathrm{B}} B s^z, \tag{2.35}$$

and the energy difference between the states $|s, s\rangle$ and $|s, s-1\rangle$ is

$$\Delta E = -g\mu_{\mathrm{B}} B. \tag{2.36}$$

The easy axis anisotropy energy difference between the two lowest levels is

$$\Delta E = -\kappa_2 s^2 + \kappa_2 (s-1)^2 = -2\kappa_2 (s - 1/2) = -g\mu_{\mathrm{B}} \frac{2\kappa_2 s'}{g\mu_{\mathrm{B}}}, \tag{2.37}$$

with $s' = s - 1/2$. It therefore makes sense to define the effective anisotropy field as

$$B_2 = \frac{2\kappa_2 s'}{g\mu_{\mathrm{B}}}. \tag{2.38}$$

In analogy with this we also define

$$B_1 = \frac{2\kappa_1 s'}{g\mu_{\mathrm{B}}}. \tag{2.39}$$

Using the values $\kappa_2 \approx 1.5$ mK and $\kappa_1 \approx -10\kappa_2$, we find $B_2 = 4.46$ mT and $B_1 = -44.6$ mT.

2.5.3 The DM-interaction

In analogy with the exchange interaction we define

$$B_D = \frac{2sD(0)}{g\mu_{\mathrm{B}}}. \tag{2.40}$$

As mentioned previously, the effect of the DM-interaction is to slightly cant the spins. We can utilize this to estimate the value of B_D as follows. Consider the equation of motion for the x component of the spin in terms of the macroscopic parameters just defined, Eq. (3.65), neglecting the magnetic field and assuming an equal number of spins on the two sublattices:

$$\frac{\mathrm{d}}{\mathrm{d}t} s_A^x = g\mu_{\mathrm{B}} B_X (s_A^y s_B^z - s_A^z s_B^y) + g\mu_{\mathrm{B}} B_2 s_A^z s_A^y - g\mu_{\mathrm{B}} B_D (s_A^z s_B^z + s_A^y s_B^y). \tag{2.41}$$

We now assume that the spins are static and cant in the basal plane,

$$\mathbf{s}_A = (0, \sin(\theta), \cos(\theta)), \quad \mathbf{s}_B = (0, \sin(\theta), -\cos(\theta)). \tag{2.42}$$

Inserting this, we find

$$0 = -2g\mu_{\mathrm{B}} B_X \sin(\theta)\cos(\theta) + g\mu_{\mathrm{B}} B_2 \sin(\theta)\cos(\theta) - g\mu_{\mathrm{B}} B_D (\sin^2(\theta) - \cos^2(\theta)), \tag{2.43}$$

which can be reduced to

$$\tan(2\theta) = -\frac{2B_D}{-2B_X + B_2}. \tag{2.44}$$

The canting angle in hematite is typically $\theta \approx 0.1°$, this yields $B_D \approx -0.0035 \times B_X = 3.1$ T. In [11, 1], the value $B_D = 2.1$ T is quoted for bulk hematite; this is the value we will use.

Chapter 3

Magnetic excitations

We here derive some of the excitations seen in magnetic nanoparticles with different anisotropies. First, we consider the Hamiltonian of the system including uniaxial anisotropy, planar anisotropy, the Dzyaloshinskii-Moriya-interaction and an external magnetic field. Next, we derive the equations of motion for this Hamiltonian and show how they give rise to spin waves. We calculate the spin wave dispersion including the uncompensated moment, and consider various relevant limiting cases. We next move on to describe superparamagnetism and the newly discovered "rotor" mode [20].

3.1 Order and Hamiltonian

In older papers, hematite is described as a four-sublattice antiferromagnet [4]. However, more recent publications, in particular the book by Morrish [1] deem this complication unnecessary, and we shall stick to a two-sublattice model. We thus describe the lattice as two ferromagnetic sublattices, A and B, that are anti-aligned.

We shall further neglect some of the weakest interactions like the crystal field. The effect of these interactions is negligible in the present context. To include the effect of these interactions, the equations of motion should be derived by analyzing the free energy as outlined by Morrish [1]. Here, the equations will be derived by the use of Ehrenfest's theorem.

With the above mentioned reservations, the accepted microscopic magnetic Hamiltonian for hematite includes the exchange interaction J_{ij}, a strong in-plane anisotropy κ_1, a weaker easy-axis anisotropy κ_2, the Dzyaloshinskii-Moriya (DM) interaction $\mathbf{D}$ and

Size	$J^{\mathrm{AFM}}(0)$ [K]	$D^{\mathrm{AFM}}(0)$ [K]	κ_1 [mK]	κ_2 [mK]	N	ξ
16 nm	242	0.57	-16	0.91	8.5×10^4	1
8 nm	242	0.57	Unknown	3.2	1.06×10^4	1-1.01
	B_X [T]	B_D [T]	B_1 [mT]	B_2 [mT]		
16 nm	900	2.1	-47.6	2.7		
8 nm	900	2.1	Unknown	9.4		

TABLE 3.1: Table of approximate parameters from the literature. J^{AFM} and D^{AFM} are calculated from the bulk values of B_X and B_D found in Ref. [1]. κ_1 is from Ref. [11] and κ_2 is from Ref. [9], both values are for 16 nm particles.

possibly an applied magnetic field $\mathbf{B}$:

$$\begin{aligned}\mathcal{H} = &-2\sum_{i\in A,j\in B} J_{ij}\mathbf{s}_i\cdot\mathbf{s}_j - \sum_{i,k\in A} J_{ik}\mathbf{s}_i\cdot\mathbf{s}_k - \sum_{j,l\in B} J_{jl}\mathbf{s}_j\cdot\mathbf{s}_l \\ &- \sum_{i\in A}\kappa_{1i}(s_i^x)^2 - \sum_{j\in B}\kappa_{1j}(s_j^x)^2 - \sum_{i\in A}\kappa_{2i}(s_i^z)^2 - \sum_{j\in B}\kappa_{2j}(s_j^z)^2 \\ &- g\mu_{\mathrm{B}}\mathbf{B}\cdot\sum_{i\in A}\mathbf{s}_i - g\mu_{\mathrm{B}}\mathbf{B}\cdot\sum_{j\in B}\mathbf{s}_j \\ &- 2\mathbf{e}_x\cdot\sum_{i\in A,j\in B} D_{ij}\mathbf{s}_i\times\mathbf{s}_j - \mathbf{e}_x\cdot\sum_{i,k\in A} D_{ik}\mathbf{s}_i\times\mathbf{s}_k - \mathbf{e}_x\cdot\sum_{j,l\in B} D_{jl}\mathbf{s}_j\times\mathbf{s}_l. \end{aligned} \tag{3.1}$$

In the following, as well as the above equation, spin indices i, k are in the A lattice and j, l are in the B lattice. The spins are operators, but for notational simplicity we write them as $\mathbf{s}_j$ instead of $\hat{\mathbf{s}}_j$. J_{ij} are the exchange coupling constants described in the previous chapter. $\kappa_1 < 0$ is the large planar anisotropy, $\kappa_2 > 0$ is the smaller axial anisotropy, D_{ij} are the DM coupling constants and $g = 2$. In hematite $|J| \gg |D| \gg |\kappa_1| > |\kappa_2|$. Approximate values of the parameters are given in Table 3.1. A full overview of the literature is given in Table 7.2.

In this notation, y and z are in the basal hematite (a, b) plane, while x is along the c-axis, see Fig. 2.2. $\mathbf{e}_x$ is a unit vector along the x axis. The direction of the DM-interaction is determined by symmetry arguments as detailed in e.g. [25, 26].

The definition of J_{ij} is ambiguous in the literature because of the double sum. In the notation used here, i and j explicitly are on separate sublattices, and to count all interactions, we therefore have both a $\mathbf{s}_i\cdot\mathbf{s}_j$ term and a $\mathbf{s}_j\cdot\mathbf{s}_i$ term. In e.g. Ref [27], only one such term is present. The exchange constant given by C. Bahl et al. therefore differs by a factor of 2 compared to our Hamiltonian. The DM-interaction is often neglected in the literature.

The total number of spins is $N = N_A + N_B$, where N_A (N_B) is the number of spins on the A (B) lattice. In bulk, it can be assumed $N_A = N_B$. In nanoparticles, on the other hand, the difference between the number of spins on each sublattice is not necessarily zero, as was theoretically proposed by Néel [5], and measured in e.g. NiO nanoparticles [37]. This uncompensated moment can have a large effect on the dynamics we are about

to investigate. It is convenient to define

$$\xi = \frac{N_B}{N_A}. \tag{3.2}$$

3.2 The equations of motion

To investigate the spin dynamics of hematite we now derive the equations of motion for a single spin on sublattice A. These are the starting point of simulations and calculations of spin waves in bulk hematite as well as all the dynamics to be found in antiferromagnetic nanoparticles. We find the equations of motion using

$$-i\frac{\mathrm{d}}{\mathrm{d}t}\mathbf{s} = [\mathcal{H}, \mathbf{s}], \tag{3.3}$$

where, for simplicity, we have set $\hbar = 1$. The commutators of the spin operators are

$$[s_i^x, s_j^y] = is_i^z\delta_{ij}, \quad [s_i^y, s_j^z] = is_i^x\delta_{ij}, \quad [s_i^z, s_j^x] = is_i^y\delta_{ij}. \tag{3.4}$$

Using these equations and Eq. (3.1), the equations of motion for a spin m in the A lattice is

$$\begin{aligned}\frac{\mathrm{d}}{\mathrm{d}t}s_m^x &= 2\sum_{j\in A,B} J_{mj}(s_m^y s_j^z - s_m^z s_j^y) + \kappa_{2m}\left(s_m^z s_m^y + s_m^y s_m^z\right) - g\mu_{\mathrm{B}}\left(B^y s_m^z - B^z s_m^y\right) \\ &\quad - 2\sum_{j\in A,B} D_{mj}(s_m^z s_j^z + s_m^y s_j^y), \end{aligned} \tag{3.5}$$

$$\begin{aligned}\frac{\mathrm{d}}{\mathrm{d}t}s_m^y &= 2\sum_{j\in A,B} J_{mj}(s_m^z s_j^x - s_m^x s_j^z) - \kappa_{2m}\left(s_m^z s_m^x + s_m^x s_m^z\right) + \kappa_{1m}\left(s_m^x s_m^z + s_m^z s_m^x\right) \\ &\quad - g\mu_{\mathrm{B}}\left(B^z s_m^x - B^x s_m^z\right) + 2\sum_{j\in A,B} D_{mj} s_m^x s_j^y, \end{aligned} \tag{3.6}$$

$$\begin{aligned}\frac{\mathrm{d}}{\mathrm{d}t}s_m^z &= 2\sum_{j\in A,B} J_{mj}(s_m^x s_j^y - s_m^y s_j^x) - \kappa_{1m}\left(s_m^x s_m^y + s_m^y s_m^x\right) - g\mu_{\mathrm{B}}\left(B^x s_m^y - B^y s_m^x\right) \\ &\quad + 2\sum_{j\in A,B} D_{mj} s_m^x s_j^z. \end{aligned} \tag{3.7}$$

We refer to Appendix A for the derivation of this result.

3.3 Spin waves

We will here derive the equations for the frequencies of the different excitations that can occur in nanoparticles. It is convenient to define the raising and lowering operators:

$$s_i^{\pm} = s_i^x \pm is_i^y, \tag{3.8}$$

which obey the following commutation relations

$$[s_i^z, s_j^\pm] = \pm\delta_{ij}s^\pm, \quad [s_i^+, s_j^-] = 2\delta_{ij}s^z. \tag{3.9}$$

We will assume that the ground state is the classical Néel state, i.e. with all the spins on sublattice A pointing along z and all the spins on sublattice B along $-z$, as done by e.g. Anderson [24]. If we neglect the DM-interaction and the magnetic field, we have the following equations

$$\begin{aligned}\frac{\mathrm{d}}{\mathrm{d}t}s_m^+ &= -2i\sum_{j\in A,B} J_{mj}(s_m^+ s_j^z - s_m^z s_j^+) + i\kappa_{1m}\left[\left(s_m^z - \frac{1}{2}\right)s_m^+ + s_m^-\left(s_m^z - \frac{1}{2}\right)\right] \\ &\quad - i\kappa_{2m}\left(2s_m^z - 1\right)s_m^+, \qquad (3.10)\\ \frac{\mathrm{d}}{\mathrm{d}t}s_m^- &= 2i\sum_{j\in A,B} J_{mj}(s_m^- s_j^z - s_m^z s_j^-) - i\kappa_{1m}\left[\left(s_m^z - \frac{1}{2}\right)s_m^+ + s_m^-\left(s_m^z - \frac{1}{2}\right)\right] \\ &\quad + i\kappa_{2m}s_m^-\left(2s_m^z - 1\right). \qquad (3.11)\end{aligned}$$

Let us work with just the raising operator. Defining $s'^z_m = s_m^z - 1/2$ we get

$$\frac{\mathrm{d}}{\mathrm{d}t}s_m^+ = -2i\sum_{j\in A,B} J_{mj}(s_m^+ s_j^z - s_m^z s_j^+) + i\kappa_{1m}\left(s'^z_m s_m^+ + s_m^- s'^z_m\right) - 2i\kappa_{2m}s'^z_m s_m^+. \tag{3.12}$$

We multiply by $\exp(\mathrm{i}\mathbf{q}\cdot\mathbf{r}_m)$, where $\mathbf{r}_m$ is the position of the m'th spin in sublattice A and sum over all m:

$$\begin{aligned}\sum_m i\frac{\mathrm{d}}{\mathrm{d}t}\exp(\mathrm{i}\mathbf{q}\cdot\mathbf{r}_m)s_m^+ &= 2\sum_{m\in A, j\in A,B}\exp(\mathrm{i}\mathbf{q}\cdot\mathbf{r}_m)J_{mj}(s_m^+ s_j^z - s_m^z s_j^+) \\ &\quad - \sum_m \exp(\mathrm{i}\mathbf{q}\cdot\mathbf{r}_m)\kappa_{1m}\left(s'^z_m s_m^+ + s_m^- s'^z_m\right) \\ &\quad + \sum_m \exp(\mathrm{i}\mathbf{q}\cdot\mathbf{r}_m)2\kappa_{2m}s'^z_m s_m^+. \qquad (3.13)\end{aligned}$$

We take each term in turn. In the last two terms we approximate $s_m^z \approx s$ and assume κ_i to be the same for all spins. We find

$$\begin{aligned}&- s'\kappa_1\sum_m \exp(\mathrm{i}\mathbf{q}\cdot\mathbf{r}_m)\left(s_m^+ + s_m^-\right) + 2s'\kappa_2\sum_m \exp(\mathrm{i}\mathbf{q}\cdot\mathbf{r}_m)s_m^+ \qquad (3.14)\\ &= -s'\kappa_1(S_A^+(\mathbf{q}) + S_A^-(\mathbf{q})) + 2s'\kappa_2 S_A^+(\mathbf{q}), \qquad (3.15)\end{aligned}$$

where we have defined the Fourier transform of the raising and lowering operators to be

$$S_A^\pm(\mathbf{q}) = \sum_m \exp(\mathrm{i}\mathbf{q}\cdot\mathbf{r}_m)s_m^\pm, \tag{3.16}$$

and similarly for sublattice B. Now we look at the first term of Eq. (3.13):

$$2 \sum_{m\in A, j\in A,B} \exp(\mathrm{i}\mathbf{q}\cdot\mathbf{r}_m) J_{mj}(s_m^+ s_j^z - s_m^z s_j^+). \tag{3.17}$$

Let us look at $j = i \in A$, where $s_j^z \approx s$:

$$2 \sum_{m\in A, j\in A} \exp(\mathrm{i}\mathbf{q}\cdot\mathbf{r}_m) J_{mj}(s_m^+ s_j^z - s_m^z s_j^+) \tag{3.18}$$

$$= 2 \sum_{m,i\in A} \exp(\mathrm{i}\mathbf{q}\cdot\mathbf{r}_m) J_{mi}(s_m^+ s_i^z) + 2 \sum_{m,i\in A} \exp(\mathrm{i}\mathbf{q}\cdot\mathbf{r}_m) J_{mi}(-s_m^z s_i^+) \tag{3.19}$$

$$= 2s \sum_{m,i\in A} \exp(\mathrm{i}\mathbf{q}\cdot\mathbf{r}_m) J(\mathbf{r}_m - \mathbf{r}_i) s_m^+ - 2s \sum_{m,i\in A} \exp(\mathrm{i}\mathbf{q}\cdot\mathbf{r}_m) J(\mathbf{r}_m - \mathbf{r}_i) s_i^+ \tag{3.20}$$

$$= 2s \sum_{m,i\in A} e^{\mathrm{i}\mathbf{0}\cdot(\mathbf{r}_m - \mathbf{r}_i)} J(\mathbf{r}_m - \mathbf{r}_i) e^{\mathrm{i}\mathbf{q}\cdot\mathbf{r}_m} s_m^+ - 2s \sum_{i,m\in A} e^{\mathrm{i}\mathbf{q}\cdot(\mathbf{r}_m - \mathbf{r}_i)} J(\mathbf{r}_m - \mathbf{r}_i) e^{\mathrm{i}\mathbf{q}\cdot\mathbf{r}_i} s_i^+ \tag{3.21}$$

$$= 2s J_A^{\mathrm{FM}}(\mathbf{0}) S_A^+(\mathbf{q}) - 2s J_A^{\mathrm{FM}}(\mathbf{q}) S_A^+(\mathbf{q}) \tag{3.22}$$

Here we have defined $J^{\mathrm{FM}}(\mathbf{r}_m - \mathbf{r}_i)$ as the interaction between spins in the same sublattice. Similarly, $J^{\mathrm{AFM}}(\mathbf{r}_m - \mathbf{r}_j)$ is the interaction between spins on different sublattices. Their Fourier transforms are

$$J_A^{\mathrm{FM}}(\mathbf{q}) = \sum_{i\in A} e^{\mathrm{i}\mathbf{q}\cdot(\mathbf{r}_m - \mathbf{r}_i)} J(\mathbf{r}_m - \mathbf{r}_i) \quad (m \in A), \tag{3.23}$$

$$J_B^{\mathrm{FM}}(\mathbf{q}) = \sum_{i\in B} e^{\mathrm{i}\mathbf{q}\cdot(\mathbf{r}_m - \mathbf{r}_i)} J(\mathbf{r}_m - \mathbf{r}_i) \quad (m \in B), \tag{3.24}$$

$$J_A^{\mathrm{AFM}}(\mathbf{q}) = \sum_{j\in B} e^{\mathrm{i}\mathbf{q}\cdot(\mathbf{r}_m - \mathbf{r}_j)} J(\mathbf{r}_m - \mathbf{r}_j) \quad (m \in A), \tag{3.25}$$

$$J_B^{\mathrm{AFM}}(\mathbf{q}) = \sum_{j\in A} e^{\mathrm{i}\mathbf{q}\cdot(\mathbf{r}_m - \mathbf{r}_j)} J(\mathbf{r}_m - \mathbf{r}_j) \quad (m \in B), \tag{3.26}$$

where $\mathbf{q}$ is a wave vector. Notice that, since the sum is infinite, the left hand side does not depend on m, except on which lattice m resides. That is, J_A and J_B may in general

be different. Let us look at $j \in B$, where $s_j^z \approx -s$.

$$2 \sum_{m\in A, j\in B} \exp(\mathrm{i}\mathbf{q}\cdot\mathbf{r}_m) J_{mj}(s_m^+ s_j^z) + 2 \sum_{m\in A, j\in B} \exp(\mathrm{i}\mathbf{q}\cdot\mathbf{r}_m) J_{mj}(-s_m^z s_j^+) \tag{3.27}$$

$$= -2s \sum_{m\in A, j\in B} \exp(\mathrm{i}\mathbf{q}\cdot\mathbf{r}_m) J^{\mathrm{AFM}}(\mathbf{r}_m - \mathbf{r}_j) s_m^+ - 2s \sum_{m\in A, j\in B} \exp(\mathrm{i}\mathbf{q}\cdot\mathbf{r}_m) J^{\mathrm{AFM}}(\mathbf{r}_m - \mathbf{r}_j) s_j^+ \tag{3.28}$$

$$= -2s \sum_{m\in A, j\in B} \exp(\mathrm{i}0\cdot(\mathbf{r}_m - \mathbf{r}_j)) J^{\mathrm{AFM}}(\mathbf{r}_m - \mathbf{r}_j) \exp(\mathrm{i}\mathbf{q}\cdot\mathbf{r}_m) s_m^+$$

$$- 2s \sum_{m\in A, j\in B} \exp(\mathrm{i}\mathbf{q}\cdot(\mathbf{r}_m - \mathbf{r}_j)) J^{\mathrm{AFM}}(\mathbf{r}_m - \mathbf{r}_j) \exp(\mathrm{i}\mathbf{q}\cdot\mathbf{r}_j) s_j^+ \tag{3.29}$$

$$= -2s \sum_{j\in B} \exp(\mathrm{i}0\cdot(\mathbf{r}_m - \mathbf{r}_j)) J^{\mathrm{AFM}}(\mathbf{r}_m - \mathbf{r}_j) S_A^+ \quad (m \in A)$$

$$- 2s \sum_{m\in A} \exp(\mathrm{i}\mathbf{q}\cdot(\mathbf{r}_m - \mathbf{r}_j)) J^{\mathrm{AFM}}(\mathbf{r}_m - \mathbf{r}_j) S_B^+ + \quad (j \in B) \tag{3.30}$$

$$= -2s J_A^{\mathrm{AFM}}(\mathbf{0}) S_A^+(\mathbf{q}) - 2s J_B^{\mathrm{AFM}}(\mathbf{q}) S_B^+(\mathbf{q}). \tag{3.31}$$

Collecting everything from before, we have

$$\begin{aligned} i\frac{\mathrm{d}}{\mathrm{d}t} S_A^+ &= \{2s[-J_A^{\mathrm{AFM}}(\mathbf{0}) + J_A^{\mathrm{FM}}(\mathbf{0}) - J_A^{\mathrm{FM}}(\mathbf{q})] - s'\kappa_1 + 2s'\kappa_2\} S_A^+(\mathbf{q}) \\ &\quad - 2s J_B^{\mathrm{AFM}}(\mathbf{q}) S_B^+(\mathbf{q}) \\ &\quad - s'\kappa_1 S_A^-(\mathbf{q}) \end{aligned} \tag{3.32}$$

$$\begin{aligned} i\frac{\mathrm{d}}{\mathrm{d}t} S_A^- &= \{2s[J_A^{\mathrm{AFM}}(\mathbf{0}) - J_A^{\mathrm{FM}}(\mathbf{0}) + J_A^{\mathrm{FM}}(\mathbf{q})] + s'\kappa_1 - 2s'\kappa_2\} S_A^-(\mathbf{q}) \\ &\quad + 2s J_B^{\mathrm{AFM}}(\mathbf{q}) S_B^-(\mathbf{q}) \\ &\quad + s'\kappa_1 S_A^+(\mathbf{q}) \end{aligned} \tag{3.33}$$

For sublattice B we get similar equations by interchanging A with B and the sign of the equations. Following Bahl *et al.* [27] we write

$$J_A^{\mathrm{FM}} = \xi J_B^{\mathrm{FM}} = \xi J^{\mathrm{FM}}, \tag{3.34}$$

$$J_A^{\mathrm{AFM}} = \xi J_B^{\mathrm{AFM}} = \xi J^{\mathrm{AFM}}. \tag{3.35}$$

We thus have

$$i\frac{\mathrm{d}}{\mathrm{d}t}\mathbf{S}(\mathbf{q}) = \mathbf{U}(\mathbf{q})\mathbf{S}(\mathbf{q}), \tag{3.36}$$

where

$$\mathbf{S}(\mathbf{q}) = (S_A^+(\mathbf{q}), S_A^-(\mathbf{q}), S_B^+(\mathbf{q}), S_B^-(\mathbf{q}))^T, \tag{3.37}$$

and

$$\mathbf{U}(\mathbf{q}) = \begin{pmatrix} \xi e + a & -b & -f & 0 \\ b & -\xi e - a & 0 & f \\ \xi f & 0 & -e - a & b \\ 0 & -\xi f & -b & e + a \end{pmatrix}, \tag{3.38}$$

where

$$a = (2\kappa_2 - \kappa_1)s' \tag{3.39}$$

$$b = \kappa_1 s' \tag{3.40}$$

$$e = 2s[-J^{\mathrm{AFM}}(0) + J^{\mathrm{FM}}(0) - J^{\mathrm{FM}}(\mathbf{q})] \tag{3.41}$$

$$f = 2sJ^{\mathrm{AFM}}(\mathbf{q}). \tag{3.42}$$

This looks slightly different than Eq. 17 in Ref. [27]. This is due to our definition of $\mathcal{H}$, the factor 2 in J_{ij} mentioned earlier and the fact that we do the calculation for all $\mathbf{q}$ instead of restricting it to $\mathbf{q} = 0$.

The eigenvalues of Eq. (3.38) are

$$\pm\omega = \frac{1}{2}\sqrt{2[(a + \xi e + b)(a + \xi e - b) + (a + e + b)(a + e - b) - 2\xi f^2] \pm 2\sqrt{g}} \tag{3.43}$$

where

$$g = e^4(\xi^2 - 1)^2 + 4ae^3(\xi - 1)(\xi^2 - 1) - 4e^2 f^2 \xi(\xi - 1)^2 + 4a^2 e^2(\xi - 1)^2 + 16b^2 f^2 \xi. \tag{3.44}$$

This is the general dispersion for a two-sublattice ferrimagnet with easy axis and in-plane anisotropies. The dispersion along the (001) direction is shown for typical values of hematite in Fig. 3.1, where it is seen to be almost sinusoidal, as expected for antiferromagnets, and with a small energy gap. The energy gap is caused by the anisotropies. The effect of the uncompensated moment is rather small, except at low q; here, the effect can more than double the excitation energies.

The expression in Eq. (3.43) is rather complicated and the role of each term is not very transparent. We will therefore now look at some special cases.

When the two sublattices are equal, which is the case for bulk hematite, $\xi = 1$, $g = 16b^2 f^2$ and Eq. (3.43) reduces to

$$\pm\omega = \sqrt{(a + e + b)(a + e - b) - f^2 \pm 2bf} \tag{3.45}$$

$$= \sqrt{(a + e + b \mp f)(a + e - b \pm f)}. \tag{3.46}$$

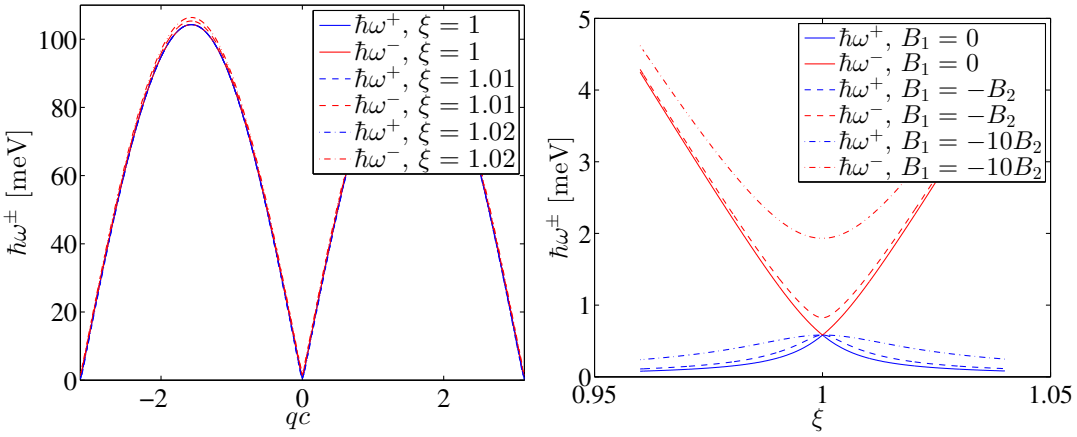

FIGURE 3.1: Left: The dispersion of hematite along the c axis, as calculated from Eq. (3.43), using typical parameters for hematite. Also shown is the effect of the uncompensated moment. This effect is quite small, except at low q. Right: The dependence of the excitation energies on ξ at $q = 0$.

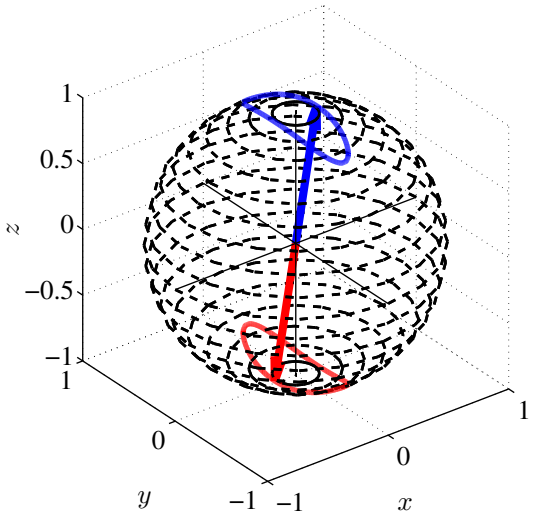

FIGURE 3.2: Illustration of one of the $q = 0$ modes rotor mode described by Eqs. (3.47) and (3.48). The ellipses shows the trajectory of the spins.

This is equivalent to Eq. (4) in Ref. [11]. When $\mathbf{q} = 0$, which is the case for nanoparticles, $f = -e$, and Eq. (3.46) becomes

$$\pm\omega_- = \sqrt{(a + 2e + b)(a - b)} = 2\sqrt{(\kappa_2 s' + s[-2J^{\mathrm{AFM}}(0)])(\kappa_2 - \kappa_1)s'} \tag{3.47}$$

$$\pm\omega_+ = \sqrt{(a + b)(a + 2e - b)} = 2\sqrt{\kappa_2 s'((\kappa_2 - \kappa_1)s' + s[-2J^{\mathrm{AFM}}(0)])}. \tag{3.48}$$

This is, apart from factors of ± 2 in the definition of J^{AFM} the same as found in e.g. [11, 27]. We see that the frequencies of both modes scale with the square root of the exchange interaction. The high frequency mode also increases with the square root of $\kappa_2 - \kappa_1$, where the low frequency mode increases with the square root of κ_2. The modes are highly elliptic, $\hbar\omega_-$ being mainly along x and $\hbar\omega_+$ being mainly along y. An illustration is given in Fig. 3.2

In Ref. [11], it is further found how the DM-interaction affects these equations. This cannot be calculated using the present method, since the approximation $s^z \approx \pm 1$ is no longer valid due to the canting of the spins. The result is that the low frequency mode, ω_+ is unaffected, while the high frequency mode has the energy

$$\pm\omega_- = \sqrt{(\omega_-(D=0))^2 + (2sD^{\mathrm{AFM}}(0))^2}. \tag{3.49}$$

If we again forget the DM-interaction and assume uniaxial symmetry, i.e., $\kappa_1 = 0$, we have $b = 0$ and Eqs. (3.47) and (3.48) reduce to a single frequency:

$$\pm\omega = \sqrt{a(a+2e)} = 2\sqrt{\kappa_2 s'(\kappa_2 s' + s[-2J^{\mathrm{AFM}}(0)])}, \tag{3.50}$$

which is the expression found in e.g. [10, 9, 35, 12].

3.4 Equations of motion with macroscopic parameters

We will now rewrite the equations of motion in terms of the effective fields introduced in Chapter 2. This is done to investigate other types of excitations than the spin waves. We will assume coherent motion of the sublattices, i.e. we set $\mathbf{q} = 0$. This makes all the ferromagnetic exchange terms cancel out because they couple spins at the same sublattice.

The starting point is Eqs. (3.5), (3.6) and (3.7) which we sum over the sublattice:

$$\begin{aligned}\sum_{m\in A}\frac{\mathrm{d}}{\mathrm{d}t}s_m^x = &\sum_{m\in A} 2\sum_{j\in A,B} J_{mj}(s_m^y s_j^z - s_m^z s_j^y) + \kappa_{2m}\left(s_m^z s_m^y + s_m^y s_m^z\right) - g\mu_{\mathrm{B}}\left(B^y s_m^z - B^z s_m^y\right)\\ &- 2\sum_{m\in A, j\in A,B} D_{mj}(s_m^z s_j^z + s_m^y s_j^y),\end{aligned} \tag{3.51}$$

$$\begin{aligned}\sum_{m\in A}\frac{\mathrm{d}}{\mathrm{d}t}s_m^y = &\sum_{m\in A} 2\sum_{,j\in A,B} J_{mj}(s_m^z s_j^x - s_m^x s_j^z) - \kappa_{2m}\left(s_m^z s_m^x + s_m^x s_m^z\right) + \kappa_{1m}\left(s_m^x s_m^z + s_m^z s_m^x\right)\\ &- g\mu_{\mathrm{B}}\left(B^z s_m^x - B^x s_m^z\right) + 2\sum_{j\in A,B} D_{mj} s_m^x s_j^y,\end{aligned} \tag{3.52}$$

$$\begin{aligned}\sum_{m\in A}\frac{\mathrm{d}}{\mathrm{d}t}s_m^z = &\sum_{m\in A} 2\sum_{j\in A,B} J_{mj}(s_m^x s_j^y - s_m^y s_j^x) - \kappa_{1m}\left(s_m^x s_m^y + s_m^y s_m^x\right) - g\mu_{\mathrm{B}}\left(B^x s_m^y - B^y s_m^x\right)\\ &+ 2\sum_{j\in A,B} D_{mj} s_m^z s_j^z.\end{aligned} \tag{3.53}$$

We define the two superspins $\mathbf{S}_A$ and $\mathbf{S}_B$ by

$$\sum_{m\in A}\mathbf{s}_m = \mathbf{S}_A, \quad \sum_{j\in B}\mathbf{s}_j = \mathbf{S}_B. \tag{3.54}$$

They have magntiude $S_A = N_A s$ and $S_B = N_B s$. It is convenient to work with normalised spins

$$\mathbf{s}_A = \frac{\mathbf{S}_A}{S_A}, \quad \mathbf{s}_B = \frac{\mathbf{S}_B}{S_B}. \tag{3.55}$$

Inserting this we find

$$\begin{aligned} N_A s \frac{\mathrm{d}}{\mathrm{d}t} s_A^x &= 2 \sum_{m\in A, j\in A,B} J_{mj}(s_m^y s_j^z - s_m^z s_j^y) + N_A s^2 \kappa_2 \left(s_A^z s_A^y + s_A^y s_A^z\right) - g\mu_\mathrm{B} N_A s \left(B^y s_A^z - B^z s_A^y\right) \\ &\quad - 2 \sum_{m\in A, j\in A,B} D_{mj}(s_m^z s_j^z + s_m^y s_j^y), \end{aligned} \tag{3.56}$$

$$\begin{aligned} N_A s \frac{\mathrm{d}}{\mathrm{d}t} s_A^y &= 2 \sum_{m\in A, j\in A,B} J_{mj}(s_m^z s_j^x - s_m^x s_j^z) - N_A s^2 \kappa_2 \left(s_A^z s_A^x + s_A^x s_A^z\right) + N_A s^2 \kappa_1 \left(s_A^x s_A^z + s_A^z s_A^x\right) \\ &\quad - N_A s g\mu_\mathrm{B} \left(B^z s_A^x - B^x s_A^z\right) + 2 \sum_{m\in A, j\in A,B} D_{mj} s_m^x s_j^y, \end{aligned} \tag{3.57}$$

$$\begin{aligned} N_A s \frac{\mathrm{d}}{\mathrm{d}t} s_A^z &= 2 \sum_{m\in A, j\in A,B} J_{mj}(s_m^x s_j^y - s_m^y s_j^x) - N_A s^2 \kappa_1 \left(s_A^x s_A^y + s_A^y s_A^x\right) - g\mu_\mathrm{B} N_A s \left(B^x s_A^y - B^y s_A^x\right) \\ &\quad + 2 \sum_{m\in A, j\in A,B} D_{mj} s_m^z s_j^z. \end{aligned} \tag{3.58}$$

It should be noted that at this point we have subtly ignored any quantum mechanical effects - the ordering of the spins no longer matters, as they are not quantized. We will get the same equations for the spin waves, but a different expression for the anisotropy fields. We will deal with this after the equations of motion have been derived (Eqs. (3.68) and (3.69)). Let us now evaluate the sum

$$\sum_{m\in A, j\in A,B} J_{mj}(s_m^y s_j^z - s_m^z s_j^y). \tag{3.59}$$

The sum over $j \in A$ cancels out. To perform the sum, we use the coherent potential approximation (CPA) [34, 38, 27], to find

$$\sum_{m\in A, j\in A,B} J_{mj}(s_m^y s_j^z - s_m^z s_j^y) = N_A s^2 J_A^{\mathrm{AFM}}(0) \left(s_A^y s_B^z - s_A^z s_B^y\right) \tag{3.60}$$

$$= N_A s^2 \xi J^{\mathrm{AFM}}(0) \left(s_A^y s_B^z - s_A^z s_B^y\right). \tag{3.61}$$

The DM terms can be handled in a similar way, and we thus reach

$$\begin{aligned}\frac{\mathrm{d}}{\mathrm{d}t}s_A^x &= 2s\xi J^{\mathrm{AFM}}(0)(s_A^y s_B^z - s_A^z s_B^y) + 2\kappa_2 s s_A^z s_A^y - g\mu_{\mathrm{B}}\left(B^y s_A^z - B^z s_A^y\right) \\ &\quad - 2s\xi D^{\mathrm{AFM}}(0)(s_A^z s_B^z + s_A^y s_B^y), \qquad (3.62)\\ \frac{\mathrm{d}}{\mathrm{d}t}s_A^y &= 2s\xi J^{\mathrm{AFM}}(0)(s_A^z s_B^x - s_A^x s_B^z) - 2\kappa_2 s s_A^z s_A^x + 2\kappa_1 s s_A^x s_A^z \\ &\quad - g\mu_{\mathrm{B}}\left(B^z s_A^x - B^x s_A^z\right) + 2s\xi D^{\mathrm{AFM}}(0) s_A^x s_B^y, \qquad (3.63)\\ \frac{\mathrm{d}}{\mathrm{d}t}s_A^z &= 2s\xi J^{\mathrm{AFM}}(0)(s_A^x s_B^y - s_A^y s_B^x) - 2\kappa_1 s s_A^x s_A^y - g\mu_{\mathrm{B}}\left(B^x s_A^y - B^y s_A^x\right) \\ &\quad + 2s\xi D^{\mathrm{AFM}}(0) s_A^z s_B^z. \qquad (3.64)\end{aligned}$$

In terms of the effective fields introduced in Section 2.5, these equations become

$$\begin{aligned}\frac{\mathrm{d}}{\mathrm{d}t}s_A^x &= g\mu_{\mathrm{B}}\xi B_X(s_A^y s_B^z - s_A^z s_B^y) + g\mu_{\mathrm{B}} B_2 s_A^z s_A^y - g\mu_{\mathrm{B}}\left(B^y s_A^z - B^z s_A^y\right) \\ &\quad - g\mu_{\mathrm{B}}\xi B_D(s_A^z s_B^z + s_A^y s_B^y), \qquad (3.65)\\ \frac{\mathrm{d}}{\mathrm{d}t}s_A^y &= g\mu_{\mathrm{B}}\xi B_X(s_A^z s_B^x - s_A^x s_B^z) - g\mu_{\mathrm{B}} B_2 s_A^z s_A^x + g\mu_{\mathrm{B}} B_1 s_A^x s_A^z \\ &\quad - g\mu_{\mathrm{B}}\left(B^z s_A^x - B^x s_A^z\right) + g\mu_{\mathrm{B}}\xi B_D s_A^x s_B^y, \qquad (3.66)\\ \frac{\mathrm{d}}{\mathrm{d}t}s_A^z &= g\mu_{\mathrm{B}}\xi B_X(s_A^x s_B^y - s_A^y s_B^x) - g\mu_{\mathrm{B}} B_1 s_A^x s_A^y - g\mu_{\mathrm{B}}\left(B^x s_A^y - B^y s_A^x\right) \\ &\quad + g\mu_{\mathrm{B}}\xi B_D s_A^z s_B^z. \qquad (3.67)\end{aligned}$$

The equations for sublattice B are found by interchanging A and B, removing ξ and changing the sign of the terms with B_D.

These equations can be compactly written as

$$\frac{\mathrm{d}\mathbf{s}_A}{\mathrm{d}t} = g\mu_B \mathbf{s}_A \times \mathbf{B}_{\mathrm{eff}}^A, \qquad (3.68)$$

$$\frac{\mathrm{d}\mathbf{s}_B}{\mathrm{d}t} = g\mu_B \mathbf{s}_B \times \mathbf{B}_{\mathrm{eff}}^B, \qquad (3.69)$$

where

$$\mathbf{B}_{\mathrm{eff}}^A = \xi B_X \mathbf{s}_B - \mathbf{B} - \begin{pmatrix} B_1 s_A^x \\ 0 \\ B_2 s_A^z \end{pmatrix} + \xi B_D \begin{pmatrix} 0 \\ s_B^z \\ -s_B^y \end{pmatrix}, \qquad (3.70)$$

$$\mathbf{B}_{\mathrm{eff}}^B = B_X \mathbf{s}_A - \mathbf{B} - \begin{pmatrix} B_1 s_B^x \\ 0 \\ B_2 s_B^z \end{pmatrix} - B_D \begin{pmatrix} 0 \\ s_A^z \\ -s_A^y \end{pmatrix}. \qquad (3.71)$$

When inserting the fields we quietly changed s to s' in the anisotropy term. The s' disappeared when we made the assumption that the spins can be treated like vectors, so we need to put it back. To see that we can recover the equations for the spin waves, let us look at the uniaxial case in zero field with $\xi = 1$, and assume only small deviations

from the energy minimum. We thus set $s_A^z \approx -s_B^z \approx 1$:

$$\frac{\mathrm{d}}{\mathrm{d}t}s_A^x = -g\mu_\mathrm{B}B_X(s_A^y + s_B^y) + g\mu_\mathrm{B}B_2 s_A^y, \tag{3.72}$$

$$\frac{\mathrm{d}}{\mathrm{d}t}s_A^y = g\mu_\mathrm{B}B_X(s_B^x + s_A^x) - g\mu_\mathrm{B}B_2 s_A^x, \tag{3.73}$$

$$\frac{\mathrm{d}}{\mathrm{d}t}s_B^x = g\mu_\mathrm{B}B_X(s_B^y + s_A^y) - g\mu_\mathrm{B}B_2 s_B^y, \tag{3.74}$$

$$\frac{\mathrm{d}}{\mathrm{d}t}s_B^y = -g\mu_\mathrm{B}B_X(s_A^x + s_B^x) + g\mu_\mathrm{B}B_2 s_B^x. \tag{3.75}$$

We now let $\mathbf{s}_A$ have an angle θ_A with the z axis, and let $\mathbf{s}_B$ have an angle θ_B with the z axis, and assume precession around the z-axis - the standard picture for AFM resonance:

$$\mathbf{s}_A = (\sin(\theta_A)\cos(\omega t), \sin(\theta_A)\sin(\omega t), \cos(\theta_A)), \tag{3.76}$$

$$\mathbf{s}_B = (-\sin(\theta_B)\cos(\omega t), -\sin(\theta_B)\sin(\omega t), -\cos(\theta_B)). \tag{3.77}$$

Inserting the expressions for $\mathbf{s}_A$ and $\mathbf{s}_B$ we find two equations:

$$-\omega\sin(\theta_A) = -g\mu_\mathrm{B}B_X(\sin(\theta_A) - \sin(\theta_B)) + g\mu_\mathrm{B}B_2\sin(\theta_A), \tag{3.78}$$

$$\omega\sin(\theta_B) = -g\mu_\mathrm{B}B_X(\sin(\theta_B) - \sin(\theta_A)) + g\mu_\mathrm{B}B_2\sin(\theta_B), \tag{3.79}$$

which we solve for ω to find

$$\omega = \pm g\mu_\mathrm{B}\sqrt{B_2(-2B_x + B_2)} = \pm 2\sqrt{\kappa_2 s'(\kappa_2 s' + s[-2J^\mathrm{AFM}(0)])}, \tag{3.80}$$

which is the same as found in Eq. (3.50). We thus see that we recover the correct expression with the redefinition of the anisotropy fields. For the angle between the sublattice spins we find

$$\frac{\sin(\theta_A)}{\sin(\theta_B)} = 1 + \frac{B_2}{-B_X} \pm \sqrt{2\frac{B_2}{-B_X} + \left(\frac{B_2}{B_X}\right)^2}, \tag{3.81}$$

meaning that a slight canting of the spins will appear. The effect of this canting has been presented in [39].

3.5 Superparamagnetism

When the spins in a ferromagnetic nanoparticle move coherently, they behave as one superspin, and the behaviour is therefore called superparamagnetism (SPM). Similarly, for an antiferromagnetic particle, the spins will behave as two superspins. Here, the term SPM will also be loosely used for superparamagnetic spin flips, to be described below. At low temperatures, the two sublattice spins will be precisely antiparallel and be in the energy minimum, $\mathbf{s}_A = (0, 0, 1)$ and $\mathbf{s}_B = (0, 0, -1)$. In many references, the height of this energy minium (the energy barrier) is given simply as $K_i V = -\kappa_i N s^2$ [19, 11, 9],

where V is the volume of the particle and K_i is a highly size-dependent constant. This is approximately correct, but neglects quantum mechanical effects.

3.5.1 Quantum mechanical corrections

To get the correct result, one must calculate the energy difference between the state with all spins parallel to z, and the same state with the lowering operator applied until the total spin of the state is at its minimum. To the best of my knowledge, no analytical results for N spins exist. However, Lefmann performed the calculations by hand for small systems with $s = 1/2, 1, 3/2$; the calculations are given in Appendix B. These results show that the correct form of the anisotropy barrier is

$$K_i V = \kappa_i N s s' = 1/2 g \mu_{\mathrm{B}} B_i N s. \tag{3.82}$$

Intuitively, this result makes sense: for a spin-1/2 system, there is no difference between the anisotropy energy of spin up and spin down, and thus no anisotropy barrier to cross.

3.5.2 Superparamagnetic spin flips

The energy barrier can be crossed due to random thermal fluctuations. This is called superparamagnetic relaxation, and was predicted by Néel in 1949 [40], and further refined by Brown [41]. For ferromagnetic nanoparticles, the Néel-Brown law predicts that the temperature dependence of the mean flip time, τ is

$$\tau = \tau_0 \exp\left(\frac{KV}{k_B T}\right). \tag{3.83}$$

In the derivation it is assumed $KV < k_B T$. In the next section, we will look at the case $KV > k_B T$. Assuming that the spins are confined to the easy plane, we have $K = K_2 = K_{\mathrm{Bu}}$. The value of τ_0 depends slightly on particles size and temperature [35], but this complication will not be discussed here. τ_0 is a measure of the average time between attempts at crossing the energy barrier. Typical values are $KV \approx 500$ K and $\tau_0 \approx 1 \times 10^{-11}$ s.

These fluctuations are dubbed longitudinal, because they are along the z direction. For antiferromagnetic nanoparticles, this relation is theoretically valid only as a first approximation [42].

3.6 Temperature dependence of excitations

As the temperature is increased, the excitation energies change. It can be shown [43, 10] that the excitation energy should be proportional to the average sublattice moment along the z-axis, i.e.

$$\omega_{\pm}(T) = \frac{\langle s^{\parallel}_{\mathrm{AFM}}(T)\rangle}{S}\omega_{\pm}(T=0). \tag{3.84}$$

The Hamiltonian for the anisotropies can be rewritten

$$\mathcal{H}_{\text{anis}} = K_2 V \sin^2(\theta) - K_1 V \cos^2(\phi), \tag{3.85}$$

where θ is the angle the spins make with the z axis and ϕ the angle with the x axis. We set $\hat{\mathbf{s}}^{\text{AFM}} = (\sin(\theta)\cos(\phi), \sin(\theta)\sin(\phi), \cos(\theta))$, and it can then be shown that [10]

$$\langle (\mathbf{s}^{\parallel}_{\text{AFM}})^2 \rangle = \frac{I_0(\alpha_2/2) + I_1(\alpha_2/2)}{2I_0(\alpha_2/2)} \frac{\alpha_1^{-1/2} \mathrm{e}^{-\alpha_1} + 1/2\sqrt{\pi}(2 - \alpha_1^{-1})\mathrm{erf}(\sqrt{\alpha_1})}{\sqrt{\pi}\mathrm{erf}(\sqrt{\alpha_1})} \tag{3.86}$$

$$\approx 1 - k_{\text{B}}T \left(\frac{1}{2|K_1 V|} + \frac{1}{2|K_2 V|} \right), \tag{3.87}$$

where $\alpha_i = K_i V / k_{\text{B}}T$, $I_n(x)$ is the modified Bessel function of order n and $\mathrm{erf}(x) = 2/\sqrt{\pi} \int_0^x \mathrm{e}^{-u^2} \mathrm{d}u$ is the error function. Similarly, $\langle \mathbf{s}^{\parallel}_{\text{AFM}} \rangle$ becomes:

$$\langle \mathbf{s}^{\parallel}_{\text{AFM}} \rangle = \frac{I_0(\alpha_1/2) + I_1(\alpha_1/2)}{2I_0(\alpha_2/2)} e^{(\alpha_2 - \alpha_1)/2} \sqrt{\frac{\alpha_1}{\alpha_2}} \frac{\mathrm{erf}(\sqrt{\alpha_2})}{\mathrm{erf}(\sqrt{\alpha_1})} \tag{3.88}$$

$$\approx 1 - k_{\text{B}}T \left(\frac{1}{4|K_1 V|} + \frac{1}{4|K_2 V|} \right). \tag{3.89}$$

The approximations are valid for low temperature $k_B T \ll K_i V$, $i = 1, 2$.

It is common in the literature to assume only uniaxial anisotropy, e.g. [9, 12]. However, one should be very careful when doing this. If we assume that the spins are confined to the easy plane [35], i.e. a 2d model with $K_1 V = \infty$, we find

$$\langle \mathbf{s}^{\parallel}_{\text{AFM}} \rangle = \frac{\int_0^{\pi/2} e^{-\alpha_2 \sin^2(\theta)} \cos(\theta) \mathrm{d}\theta}{\int_0^{\pi/2} e^{-\alpha_2 \sin^2(\theta)} \mathrm{d}\theta} \tag{3.90}$$

$$= \frac{\mathrm{erf}(\sqrt{\alpha_2})}{\sqrt{\pi}\sqrt{\alpha_2} e^{-\alpha_2/2} I_0(\alpha_2/2)} \approx \frac{1}{1 + \frac{1}{4\alpha_2} + \frac{9}{32\alpha^2}} \approx 1 - \frac{k_{\text{B}}T}{4K_2 V}, \tag{3.91}$$

in agreement with Eq. 3.88 for $K_1 V = \infty$. However, if we assume only uniaxial anisotropy and that the spins are not confined to the easy plane, $K_1 V = 0$, the approximations leading to Eq. 3.88 break down and we find

$$\langle \mathbf{s}^{\parallel}_{\text{AFM}} \rangle = \frac{\int_0^{\pi/2} e^{-\alpha_2 \sin^2(\theta)} \cos(\theta)\sin(\theta) \mathrm{d}\theta}{\int_0^{\pi/2} e^{-\alpha_2 \sin^2(\theta)} \sin(\theta) \mathrm{d}\theta} \tag{3.92}$$

$$= \frac{e^{\alpha_2} - 1}{\sqrt{\pi}\sqrt{\alpha_2}\,\mathrm{erfi}(\sqrt{\alpha})} \approx \frac{1 - e^{-\alpha_2}}{1 + \frac{1}{2\alpha} + \frac{3}{4\alpha^2}} \approx 1 - \frac{k_{\text{B}}T}{2K_2 V}. \tag{3.93}$$

We thus see a factor two difference between the 2d and the 3d model calculations of $K_2 V / k_B T$ at low temperatures.

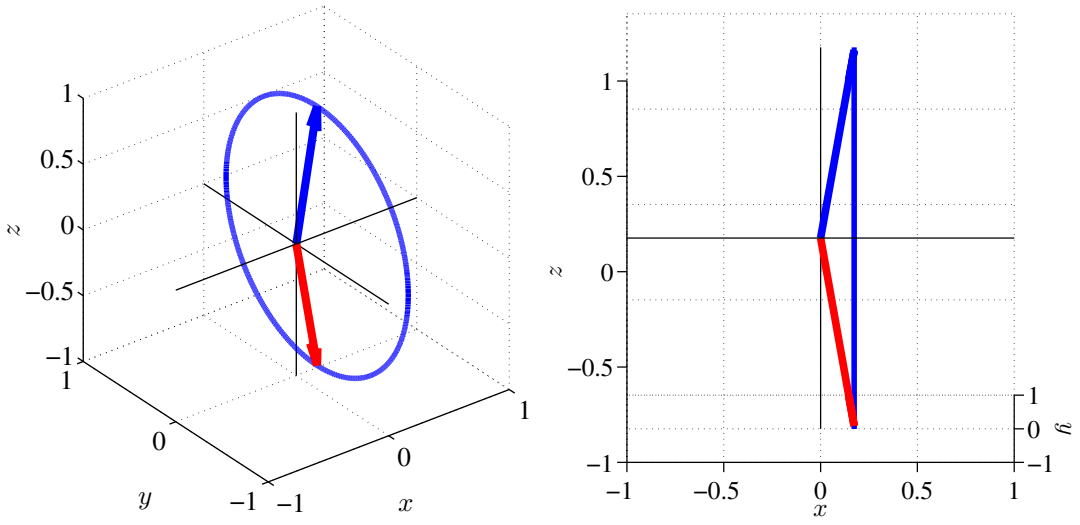

FIGURE 3.3: Illustration of the rotor mode described by Eq. (3.108). The spins are canted slightly out of the yz-plane. The circle shows the trajectory of one of the spins.

3.7 Rotor mode

It was recently discovered by K. Lefmann *et al* that a mode, different from the spin waves and superparamagnetism discussed before, exists in antiferromagnetic particles. This discovery will be published in the near future, and the derivations presented here are from the draft of the paper [20]. This mode is driven by the exchange interactions, and occurs when the temperature is larger than the uniaxial anisotropy, but smaller than the in-plane anisotropy.

The starting point for this calculation is Eqs. (3.65), (3.66) and (3.67), where we will ignore the DM-interaction, the uncompensated moment and the magnetic field:

$$\frac{\mathrm{d}}{\mathrm{d}t}s_A^x = g\mu_\mathrm{B}B_X(s_A^y s_B^z - s_A^z s_B^y) + g\mu_\mathrm{B}B_2 s_A^z s_A^y, \tag{3.94}$$

$$\frac{\mathrm{d}}{\mathrm{d}t}s_A^y = g\mu_\mathrm{B}B_X(s_A^z s_B^x - s_A^x s_B^z) - g\mu_\mathrm{B}B_2 s_A^z s_A^x + g\mu_\mathrm{B}B_1 s_A^x s_A^z, \tag{3.95}$$

$$\frac{\mathrm{d}}{\mathrm{d}t}s_A^z = g\mu_\mathrm{B}B_X(s_A^x s_B^y - s_A^y s_B^x) - g\mu_\mathrm{B}B_1 s_A^x s_A^y. \tag{3.96}$$

Let us now assume that the spin cant slightly out of the basal plane, i.e., we will assume that the spins will have a small component along the x direction. In a small angle approximation, we can write

$$\mathbf{s}_A = (\theta_A, s^y, s^z), \quad \mathbf{s}_B = (\theta_B, -s^y, -s^z). \tag{3.97}$$

This canting can come from thermal fluctuations and is illustrated in Fig. 3.3. This

leads to

$$\frac{\mathrm{d}}{\mathrm{d}t}\theta_A^x = g\mu_\mathrm{B}B_2 s^z s^y, \tag{3.98}$$

$$\frac{\mathrm{d}}{\mathrm{d}t}s^y = g\mu_\mathrm{B}B_X\left(\theta_A\left(1+\frac{B_1-B_2}{B_X}\right)+\theta_B\right)s^z, \tag{3.99}$$

$$\frac{\mathrm{d}}{\mathrm{d}t}s^z = -g\mu_\mathrm{B}B_X\left(\theta_A\left(1+\frac{B_1}{B_X}\right)+\theta_B\right)s^z. \tag{3.100}$$

If we assume that $|B_X| \gg |B_1|, |B_2|$, which is the case for hematite, and we also assume that the angles θ_A and θ_B are constant in time, the spins will perform full 2π rotations around the x-axis with a frequency given by

$$\omega_\mathrm{rot} = g\mu_\mathrm{B}B_X(\theta_A+\theta_B). \tag{3.101}$$

We define the total canting angle as

$$\theta = \theta_A + \theta_B. \tag{3.102}$$

To calculate θ we use statistical mechanics:

$$\langle\theta^2\rangle = \frac{\int_0^\pi \theta^2\exp(-\beta\mathcal{H})2\pi\sin(\theta)\mathrm{d}\theta}{\int_0^\pi \exp(-\beta\mathcal{H})2\pi\sin(\theta)\mathrm{d}\theta} \tag{3.103}$$

The leading term in the Hamiltonian is the exchange term, which can be written

$$\mathcal{H}_X = -2\sum_{i\in A, j\in B} J_{ij}\mathbf{s}_i\cdot\mathbf{s}_j = 2J^\mathrm{AFM}(0)N_A s^2\cos(\theta) = g\mu_\mathrm{B}B_X N_A s\cos(\theta). \tag{3.104}$$

We now substitute $\cos(\theta) = x$ and $\beta g\mu_\mathrm{B}B_X N s = y$ to get

$$\langle\theta^2\rangle = \frac{\int_{-1}^1 \theta^2\exp(-xy)\mathrm{d}x}{\int_{-1}^1\exp(-xy)\mathrm{d}x}. \tag{3.105}$$

Since θ is small, we can approximate $\theta^2 = 2(1-\cos(\theta))$, and then the integrals can be performed to get

$$\langle\theta^2\rangle = -\frac{2}{y} + 2(1+\coth(y)) \approx \frac{2}{-y}, \tag{3.106}$$

where the last approximation is valid when $y > 1$, i.e. $-g\mu_\mathrm{B}B_X N_A s > k_B T$, which is the case here. The rotor frequency is therefore

$$\omega_\mathrm{rot} = -g\mu_\mathrm{B}B_X\sqrt{\frac{2k_B T}{-g\mu_\mathrm{B}B_X N_A s}} \tag{3.107}$$

$$= \sqrt{\frac{-2k_B T g\mu_\mathrm{B}B_X}{N_A s}}. \tag{3.108}$$

As for the spin waves, the rotor frequency increases with the square root of the exchange field. It also increases with the square root of the temperature. The derivation rests on the assumption that $|\mathrm{d}/\mathrm{d}t\theta_A|$ is negligible. We have

$$\frac{\mathrm{d}}{\mathrm{d}t}\theta_A^x = g\mu_\mathrm{B}B_2 s^z s^y = g\mu_\mathrm{B}B_2 \sin(\omega_\mathrm{rot})\cos(\omega_\mathrm{rot}) \tag{3.109}$$

$$= \frac{g\mu_\mathrm{B}B_2}{2}\sin(2\omega_\mathrm{rot}), \tag{3.110}$$

which means $|\mathrm{d}/\mathrm{d}t\theta_A| < g\mu_\mathrm{B}B_2/2$. Comparing this to the rotor frequency we find

$$\frac{\frac{\mathrm{d}\theta_a}{\mathrm{d}t}}{\omega_\mathrm{rot}} = \sqrt{-\frac{B_2}{B_X}\frac{g\mu_\mathrm{B}B_2}{8k_BT}N_A s}. \tag{3.111}$$

When this is smaller than 1, the angles stay approximately fixed long enough for the rotations to occur.

Inserting the realistic values for a 8 nm particle, $B_X = 900$ T, $B_2 = 5$ mT, $N_A = 5000$, $s = 5/2$, $T = 150$ K, we find

$$\frac{\frac{\mathrm{d}\theta_a}{\mathrm{d}t}}{\omega_\mathrm{rot}} = 6 \times 10^{-4}, \tag{3.112}$$

indicating the the model is indeed valid. We will return to this in Chapter 7.

Chapter 4

Mössbauer spectroscopy

Mössbauer spectroscopy is a technique that has been widely used ever since it was discovered by Rudolf Mössbauer in 1957. We will first briefly describe the basics of Mössbauer spectroscopy, based on notes by C. Frandsen [44], then move on to a literature review. Mössbauer spectroscopy gives information about the environment of the nuclei in the sample. This can be used to measure the energy barriers, KV and the jump time, τ_0.

4.1 Basics of Mössbauer spectroscopy

The technique is based on γ-radiation. Consider a nucleus of mass M which has a low lying excited state, E_2 that is an energy distance E_0 from the ground state, E_1. ^{57}Fe has $E_0 = 14.41$ keV. The nucleus can decay from the excited state by emission of a photon with energy $\hbar\omega = E_0$. Due to the finite lifetime of the excited state, τ_m, the energy is not sharply defined, but is a Lorentzian with full width at half max (FWHM) Γ_m, where $\Gamma_m \tau_m = \hbar$. For ^{57}Fe, $\Gamma_m = 2.4$ neV. In a similar fashion, the nucleus can also absorb a photon and be excited from the ground state to the excited state.

Due to conservation of momentum, the atom emitting or absorbing the radiation will recoil. This recoil shifts the energy at which photons can be absorbed/emitted such that there is no overlap between the two. However, if the nucleus is in a crystal lattice, the recoil momentum can be distributed over the entire lattice, and will be negligible. There will thus be significant overlap between the emission and absorption energies. The linewidths are so sharp that only transmission between states of the same type of atom can be done, i.e. only a photon from a ^{57}Fe source can be absorbed by a ^{57}Fe atom.

The energy of the emitted photons can be changed by moving the source relative to the sample, utilizing the Doppler effect. If the source is moved with velocity v, the energy of the emitted radiation is

$$E = E_0 \left(1 + \frac{v}{c}\right). \tag{4.1}$$

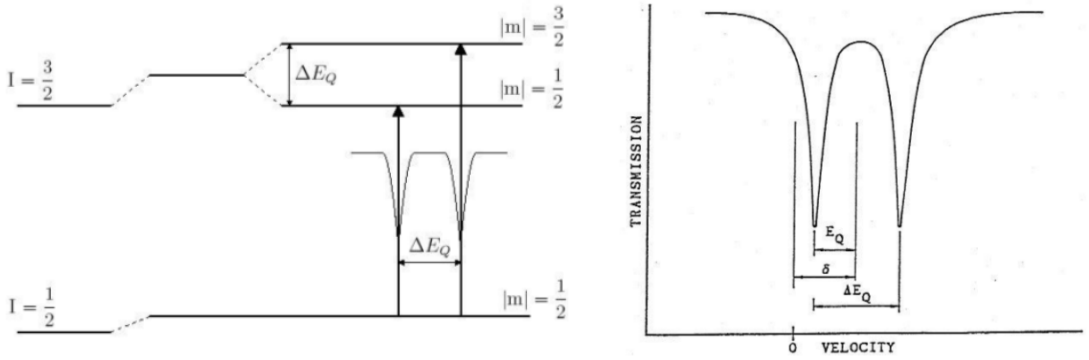

FIGURE 4.1: Illustration of isomer shift and quadropole splitting in Mössbauer spectroscopy. Left: illustration of the energy levels. Right: illustration of the resulting Mössbauer spectrum. Figures from [44].

Typical velocities are in the mm/s range, giving energy shifts of the order of $\Delta E/E \approx 10^{-11}$. The linewidth of ^{57}Fe is around 0.05 mm/s. A Mössbauer experiment is thus performed in the following way: A source of radiation is set to oscillate, thus scanning the energy of the incoming radiation. The source radiates on the sample, behind which a detector is placed, measuring the transmission of the radiation. If the source and sample atoms are exactly identical, a dip in transmission will be seen at $v = 0$ where the sample absorbs radiation.

The use of Mössbauer spectroscopy comes from the fact that the source and sample atoms can be in different environments. Typically, three different effects can change the observed spectrum: The isomer shift, quadropole splitting and hyperfine interaction.

The isomer shift, δ results from the electrostatic interaction between the charge distribution of the nucleus and those electrons which have a finite probability of being found in the region of the nucleus. This slightly shifts the energies of the excited and ground states, such that absorption will no longer take place at $v = 0$, but at a non-zero velocity.

Nuclear states with spin quantum number $I > 1/2$ possess non-zero quadropole moments that can interact with the electric field gradient at the nucleus. If e.g. $I = 3/2$, as is the case for iron, the effect is to split the state into two: one with $m = \pm 1/2$ and one with $m = \pm 3/2$. The ground state is not split. This is illustrated in Fig. 4.1

The hyperfine interaction is the interaction with the nuclear magnetic moment and the effective magnetic field at the nucleus. The Hamiltonian describing this interaction is

$$\mathcal{H} = -g_n \mu_n \mathbf{I} \cdot \mathbf{B}, \tag{4.2}$$

where g_n is the gyromagnetic ratio and $\mu_n = 5.05 \times 10^{-27}$ J/T is the nuclear magneton. For ^{57}Fe, the gyromagnetic ratio is $g_e = -0.104$ in the excited state and $g_g = 0.181$ in the ground state. The magnetic interaction splits the nuclear energy levels into 2I+1 sublevels, as illustrated in Fig. 4.2. It can be shown that only transitions given by

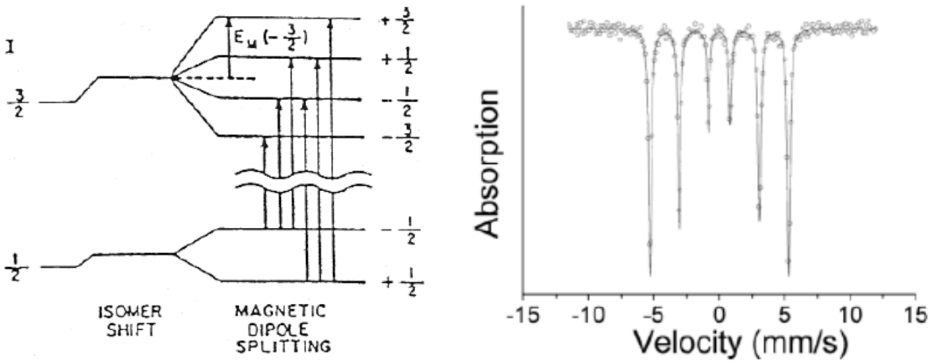

FIGURE 4.2: Illustration of the isomer shift and the hyperfine interaction in Mössbauer spectroscopy. Left: illustration of the energy levels. Right: illustration of the resulting Mössbauer spectrum. Figures from [44].

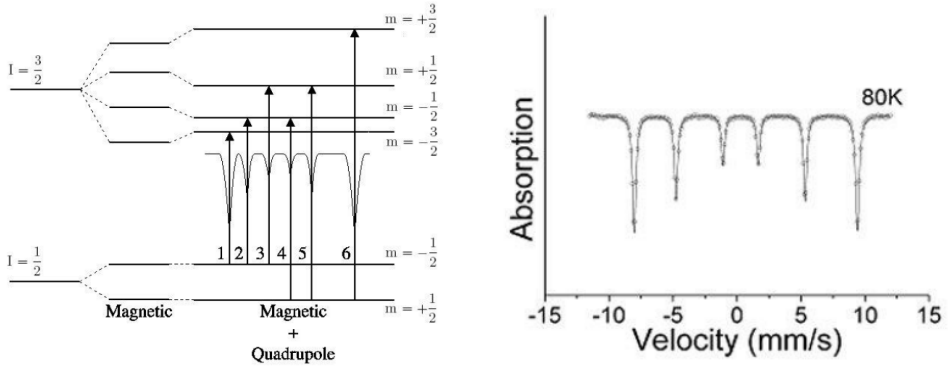

FIGURE 4.3: Illustration of the quadropole splitting and the hyperfine interaction in hematite. Left: illustration of the energy levels. Right: illustration of the resulting Mössbauer spectrum. Figures from [44].

$\Delta I = 1$ and $\Delta m = 0, \pm 1$ are possible; this gives a total of 6 transitions as seen in the figure.

In hematite, the quadropole splitting can be seen as a pertubation to the hyperfine splitting as illustrated in Fig. 4.3.

The effective magnetic field felt by the nucleus is a sum of several terms:

$$\mathbf{B} = \mathbf{B}_{\text{ext}} + \mathbf{B}_{\text{orb}} + \mathbf{B}_D + \mathbf{B}_C, \tag{4.3}$$

where $\mathbf{B}_{\text{ext}}$ is the external field, $\mathbf{B}_{\text{orb}}$ is the contribution from orbital motion of the electrons, $\mathbf{B}_D$ comes from the magnetic moment of spins outside the nucleus and $\mathbf{B}_C$ is the contribution from the electron spin density at the nucleus arising from s-electrons.

By fitting the data from Mössbauer spectroscopy, the magnetic field at the nucleus can be found. It is very important at this point to consider time-scales. As described in the previous chapter, the spins are not static. Spin waves and superparamagnetism cause the spins to fluctuate, and in Mössbauer spectroscopy, only the average value of the magnetic field at the atom will be observed. The typical time scale for a Mössbauer measurement is $\sim 10^{-9}$ s, and the average should be performed over this time. The

observed value of $\mathbf{B}$ is

$$\mathbf{B}_{\text{obs}} = B_0 \mathbf{s}^{\parallel}_{\text{AFM}} \approx B_0 \left(1 - k_B T \left(\frac{1}{4|K_1 V|} + \frac{1}{4|K_2 V|}\right)\right). \tag{4.4}$$

As the temperature is increased, superparamagnetic spin flips occur more and more frequently. When the time scale of superparamagnetic spin flips is shorter than $\sim 10^{-9}$ s, the average value of the measured magnetic field will be zero, and no sextet will be seen. The temperature at which this happens is called the blocking temperature.

4.2 Mössbauer spectroscopy on hematite

Hematite has been studied extensively with Mössbauer spectroscopy. The first measurements on hematite nanoparticles were in 1966 by Kundig [13]. Here, we will just mention some of the most recent results on 8 nm and 16 nm hematite nanoparticles, as well as measurements on mesoporous hematite.

In [36] they measured 16 nm particles. They consider a log-normal distribution of volume-weighted energy barriers, with width σ:

$$f(y)\mathrm{d}y = \frac{1}{\sqrt{2\pi}\sigma y} \exp\left(-\frac{\ln^2(y)}{2\sigma^2}\right) \mathrm{d}y, \tag{4.5}$$

where $y = E_b/E_{\text{bm}}$, where E_{bm} is the mean energy barrier. They find the following parameters for the same uncoated sample as we have used: $\tau_0 = 6.5^{+10.5}_{-4.5} \times 10^{-11}$ s, $K_2V = 590^{+150}_{-120}$ K, $\sigma = 0.6 \pm 0.1$

In [29] they measured a range of nanoparticle sizes. They found for 16 nm particles $K = 4000$ Jm^{-3}, or $KV = 620$ K, with $\tau_0 = 5.3 \times 10^{-11}$ s, which is in good agreement with the previous result. For 8 nm particles they find $K = 16000$ Jm^{-3}, or $KV = 310$ K, with $\tau_0 = 9.7 \times 10^{-12}$ s. It seems that these particles have not been coated; but it is unclear from the paper.

In [12], the same 8 nm particles as are investigated here, were measured with Mössbauer spectroscopy. For the coated particles, they find $K_2V = 335(35)$ K. However, they assume only uniaxial anisotropy. If a strong in-plane anisotropy is assumed, which I believe is the correct approach, the value found would be $K_2V = 168(18)$ K. For the uncoated particles, they find, using the uniaxial model, $4K_2V + E_{\text{int}} = 1330(180)$ K, where E_{int} is the interaction energy between the particles. An overview of these results is given in Table 7.2.

In ordered mesoporous hematite, the spectra look like bulk hematite, even though the wall thicknesses are less than 8 nm [31]. In mesoporous hematite with disordered walls the spectra look like nanoparticles, but no quantitative analysis has been performed.

Chapter 5

Neutron scattering

In this chapter the basics of neutron scattering will be covered. The focus will mainly be on magnetic neutron scattering. This chapter is not intended as a complete review of neutron scattering, but rather as a reminder to the reader of the most important equations of neutron scattering, outlining some of the derivations. The basics of data analysis will be described, as well as some typical instruments that have been used in this thesis. Finally, a short review of the literature is given. This chapter is highly inspired by the notes by K. Lefmann [45] and the book by G. L. Squires [46]. For a full treatment, the reader is referred to these texts.

5.1 Theory of neutron scattering

The neutron is a neutral particle with mass $m_{\mathrm{n}} = 1.675 \times 10^{-27}$ kg and spin 1/2. It interacts with the nucleus and with the magnetic field from unpaired electrons. Being charge neutral, neutrons penetrate matter more deeply than e.g. x-rays. They therefore serve as valuable probes of bulk materials, and are an excellent complimentary technique to x-ray scattering.

Apart from the qualities mentioned above, the main reason for using neutrons is that they can be moderated to wavelengths similar to the typical distance between atoms in materials, and with energies similar to the typical excitation energies in materials. In addition, the magnetic interaction makes neutrons sensitive to magnetic order and magnetic fluctuations.

5.1.1 General scattering theory

The flux of a neutron beam is defined as

$$\Psi = \frac{\#\text{ of neutrons impinging on a surface area per second}}{\text{surface area perpendicular to the neutron beam direction}}. \tag{5.1}$$

In neutron scattering experiments, a beam of neutrons is directed towards a sample, which in general is any kind of collection of atoms. Various types of measurements can be made on the neutrons after they have interacted with the sample, and the results

of these measurements are given as cross sections. We define the partial differential scattering cross section as

$$\frac{\mathrm{d}^2\sigma}{\mathrm{d}\Omega \mathrm{d}E_f} = \tag{5.2}$$
$$\frac{1}{\Psi}\frac{\#\text{ of neutrons scattered per second into the solid angle d}\Omega\text{ with energy between } E_f \text{ and } E_f + dE}{\mathrm{d}\Omega \mathrm{d}E_f}.$$

If we do not measure the energy of the neutrons, we integrate over E_f to obtain the differential cross section

$$\frac{\mathrm{d}\sigma}{\mathrm{d}\Omega} = \frac{1}{\Psi}\frac{\#\text{ of neutrons scattered per second into the solid angle d}\Omega}{\mathrm{d}\Omega}. \tag{5.3}$$

Finally, if we sum up all the neutrons from a scattering event we find the total scattering cross section

$$\sigma = \frac{\#\text{ of neutrons scattered per second}}{\Psi}. \tag{5.4}$$

In general, experimentalists measure these cross sections, and theoreticians calculate the cross sections. Neutrons can also be absorbed by the sample, and an absorption cross section can also be defined. We will here only consider the scattering cross section.

To get started, let us now consider scattering of a neutron by a single nucleus, fixed in space, labeled j. We wish to calculate the differential scattering cross section, $\mathrm{d}\sigma/\mathrm{d}\Omega$. The wavefunction of the incoming neutron can be written as

$$\psi_i = \exp(\mathrm{i}\mathbf{k}_i \cdot \mathbf{r}), \tag{5.5}$$

The scattered wave is spherically symmetric, and the wave vector has the same magnitude as before [46]. With the origin at the center of the nucleus, the wavefunction of the scattered wave at a point $\mathbf{r}$ is therefore

$$\psi_f(\mathbf{r}) = \psi_i(\mathbf{r}_j)\frac{-b_j}{|\mathbf{r} - \mathbf{r}_j|}\exp(\mathrm{i}\mathbf{k}_f \cdot (\mathbf{r} - \mathbf{r}_j)), \tag{5.6}$$

where b_j, the so-called scattering length, is a constant related to the nucleus and the total spin of the neutron-nucleus system. The scattering length varies greatly between different elements and isotopes, and even between the two possible spin states of the neutron-nucleus system. With unpolarized neutrons the scattering length is the average of the two. This variation of scattering length is a very useful property of the neutron, as e.g. hydrogen, which is practically invisible to x-rays, has a rather large incoherent scattering cross section. For the study of hematite, however, this turns out to be a burden rather than a blessing, as we shall see in the next chapter.

Now, $\mathbf{r}$ is on the order of 1 m, while $\mathbf{r}_j$ is on the order of the sample size, i.e. mm. We can thus approximate the density of outgoing neutrons, $|\psi_f|^2$ as

$$|\psi_f|^2 \approx |\psi_i|^2 \frac{b_j^2}{r^2}. \tag{5.7}$$

The number of neutrons per second intersecting a small area $\mathrm{d}A$ is $v|\psi_f|^2\mathrm{d}A$. In other words, the number of neutrons scattered into a solid angle $\mathrm{d}\Omega = \mathrm{d}A/r^2$ is $v|\psi_i|^2 b_j^2 \mathrm{d}\Omega$. The incoming flux is $\Psi = b|\psi_i|^2$, and we thus find

$$\frac{\mathrm{d}\sigma}{\mathrm{d}\Omega} = b_j^2. \tag{5.8}$$

Integrating, we find the total scattering cross section:

$$\sigma = 4\pi b_j^2. \tag{5.9}$$

Much more interesting is the case when the neutron interacts with several atoms. Now interference effects occur, as each nucleus acts as a source of a spherical wave. We will illustrate the calculations for a system of two identical nuclei, still fixed in space. Their scattering lengths are $b_j = b_l = b$. The final wave can now be written

$$\psi_f(\mathbf{r}) = \psi_i(\mathbf{r}_j)\frac{-b}{|\mathbf{r}-\mathbf{r}_j|}\exp(\mathrm{i}\mathbf{k}_f\cdot(\mathbf{r}-\mathbf{r}_j)) + \psi_i(\mathbf{r}_l)\frac{-b}{|\mathbf{r}-\mathbf{r}_l|}\exp(\mathrm{i}\mathbf{k}_f\cdot(\mathbf{r}-\mathbf{r}_l)). \tag{5.10}$$

Again, we have $\mathbf{r} \gg \mathbf{r}_j, \mathbf{r}_l$, leading to

$$\psi_f(\mathbf{r}) = \frac{-b}{r}\exp(\mathrm{i}\mathbf{k}_f\cdot\mathbf{r})\left(\exp(\mathrm{i}\mathbf{q}\cdot\mathbf{r}_j) + \exp(\mathrm{i}\mathbf{q}\cdot\mathbf{r}_l)\right), \tag{5.11}$$

where we have defined the scattering vector,

$$\mathbf{q} = \mathbf{k}_i - \mathbf{k}_f. \tag{5.12}$$

Squaring Eq. (5.11) we find

$$\frac{\mathrm{d}\sigma}{\mathrm{d}\Omega} = b^2|\exp(\mathrm{i}\mathbf{q}\cdot\mathbf{r}_j) + \exp(\mathrm{i}\mathbf{q}\cdot\mathbf{r}_l)|^2 = 2b^2(1+\cos(\mathbf{q}\cdot(\mathbf{r}_j-\mathbf{r}_l)). \tag{5.13}$$

We here see the interference in action: the scattering cross section varies with $\mathbf{q}$ and the distance between the atoms.

For an infinite system, the equation is generalized to

$$\frac{\mathrm{d}\sigma}{\mathrm{d}\Omega} = b^2\sum_j |\exp(\mathrm{i}\mathbf{q}\cdot\mathbf{r}_j)|^2. \tag{5.14}$$

This sum will be zero unless $\mathbf{q}\cdot\mathbf{r} = 2\pi n$, where n is an integer.

The derivation of the general results for N atoms that are not fixed in position is rather lengthy, and will be omitted here. We simply state without proof that the nuclear

scattering cross section is

$$\left(\frac{\mathrm{d}^2\sigma}{\mathrm{d}\Omega \mathrm{d}E_f}\right)_{\mathrm{nuc}} = \frac{k_f}{k_i}\frac{1}{2\pi\hbar}\sum_{ij} b_i b_j \int_{-\infty}^{\infty} \langle \exp(-\mathrm{i}\mathbf{q}\cdot\mathbf{R}_j(0))\exp(\mathrm{i}\mathbf{q}\cdot\mathbf{R}_i(t))\rangle \exp(-i\omega t)\mathrm{d}t. \tag{5.15}$$

By assuming a large system and no correlation between the b_i values, one can divide the scattering cross section into two parts; coherent and incoherent scattering:

$$\left(\frac{\mathrm{d}^2\sigma}{\mathrm{d}\Omega \mathrm{d}E_f}\right)_{\mathrm{coh}} = \frac{\sigma_{\mathrm{coh}}}{4\pi}\frac{k_f}{k_i}S(\mathbf{q},\omega), \tag{5.16}$$

$$\left(\frac{\mathrm{d}^2\sigma}{\mathrm{d}\Omega \mathrm{d}E_f}\right)_{\mathrm{inc}} = \frac{\sigma_{\mathrm{inc}}}{4\pi}\frac{k_f}{k_i}S_i(\mathbf{q},\omega), \tag{5.17}$$

where

$$S(\mathbf{q},\omega) = \frac{1}{2\pi\hbar}\sum_{ij} b_i b_j \int_{-\infty}^{\infty} \langle \exp(-\mathrm{i}\mathbf{q}\cdot\mathbf{R}_j(0))\exp(\mathrm{i}\mathbf{q}\cdot\mathbf{R}_i(t))\rangle \exp(-i\omega t)\mathrm{d}t, \tag{5.18}$$

$$S_i(\mathbf{q},\omega) = \frac{1}{2\pi\hbar}\sum_{i} b_i^2 \int_{-\infty}^{\infty} \langle \exp(-\mathrm{i}\mathbf{q}\cdot\mathbf{R}_j(0))\exp(\mathrm{i}\mathbf{q}\cdot\mathbf{R}_j(t))\rangle \exp(-i\omega t)\mathrm{d}t, \tag{5.19}$$

and

$$\sigma_{\mathrm{coh}} = 4\pi(\bar{b})^2, \quad \sigma_{\mathrm{inc}} = 4\pi((\bar{b^2}) - (\bar{b})^2). \tag{5.20}$$

$S(\mathbf{q},\omega)$ is known as the scattering function of the system. We note here that the scattering cross sections are basically the time and space Fourier Transform of the atom positions. The coherent scattering comes from correlations between different atoms at different times, and thus gives rise to interference effects. The incoherent scattering, on the other hand, comes from correlations between the same atom at different times, and thus does not give interference effects.

In general, both the coherent and incoherent scattering give information about the sample. However, for our measurements, the information content of the incoherent scattering is of no use, and the incoherent signal is thus considered as background.

We continue developing the nuclear coherent cross section for now. We assume that the sample is crystalline. Due to thermal motion, the center of the nuclei will be displaced from their equilibrium:

$$\mathbf{r}_j = \langle \mathbf{r}_j \rangle + \mathbf{u}_j. \tag{5.21}$$

Assuming that the interactions between atoms in the sample are harmonic, the coherent scattering cross section can be rewritten to

$$\left(\frac{\mathrm{d}^2\sigma}{\mathrm{d}\Omega\mathrm{d}E_f}\right)_{\mathrm{coh}} = \frac{\sigma_{\mathrm{coh}}}{4\pi}\frac{k_f}{k_i}\frac{N}{2\pi\hbar}\exp\langle U^2\rangle\sum_j \exp(\mathrm{i}\mathbf{q}\cdot\mathbf{r}_j)\int_{-\infty}^{\infty}\exp\langle UV\rangle\exp(-i\omega t)\mathrm{d}t, \tag{5.22}$$

where

$$U = -\mathrm{i}\mathbf{q}\cdot\mathbf{u}_0(0), \quad V = \mathrm{i}\mathbf{q}\cdot\mathbf{u}_j(t). \tag{5.23}$$

The term $\langle U^2\rangle$ in Eq. (5.22) is called the Debye-Waller factor, and is usually written as

$$-\langle U^2\rangle = 2W = \frac{1}{3}\mathbf{q}^2\langle u^2\rangle, \tag{5.24}$$

where $\langle u^2\rangle$ is the mean of u^2, and the last equality holds only for cubic crystals. For other crystals, the equation is still approximately true, although the factor 1/3 will vary. The Debye-Waller factor is thus a measure of the average displacement of the nuclei in the sample. It is close to 1 at small $\mathbf{q}$ and gradually decreases to zero as $\mathbf{q}$ is increased.

The term $\exp\langle UV\rangle$ is rather complicated to calculate. One practical way to approach it is through the so-called phonon expansion, where we expand [46]

$$\exp\langle UV\rangle = 1 + \langle UV\rangle + \frac{1}{2!}\langle UV\rangle^2 + ... \tag{5.25}$$

The first term gives the elastic scattering, the second scattering concerning one phonon, the third term involving 2 phonons etc. We will here only be concerned with the elastic scattering. In general, coherent 1-phonon scattering makes measurements of phonon dispersion relations possible, whereas higher order phonon processes usually only contribute to the background. Incoherent 1-phonon scattering can be used to measure the phonon density of states [46].

5.1.2 Elastic scattering

If we substitute $\exp\langle UV\rangle = 1$ in Eq. (5.22), both the sum and the integral can be immediately evaluated. The integral gives a delta function in energy, and the sum gives a sum of delta functions in $\mathbf{q} - \boldsymbol{\tau}$, where $\boldsymbol{\tau}$ is a reciprocal lattice vector. The equation thus becomes

$$\left(\frac{\mathrm{d}^2\sigma}{\mathrm{d}\Omega\mathrm{d}E_f}\right)_{\mathrm{el}} = \frac{\sigma_{\mathrm{coh}}}{4\pi}N\frac{(2\pi)^3}{v_0}\sum_{\boldsymbol{\tau}}\delta(\mathbf{q}-\boldsymbol{\tau})\delta(\hbar\omega), \tag{5.26}$$

where v_0 is the volume of the unit cell. This leads directly to Bragg's law: scattering only occurs when $\mathbf{q} = \boldsymbol{\tau}$, which can be readily transformed to the more familiar form

$$\tau = 2k\sin(\theta), \tag{5.27}$$

where θ is the scattering angle.

It should be noted that Eq. 5.26 only holds for simple cubic systems. In systems with more advanced unit cells, the equation is modified to

$$\left(\frac{\mathrm{d}^2\sigma}{\mathrm{d}\Omega \mathrm{d}E_f}\right)_{\mathrm{el}} = N\frac{(2\pi)^3}{v_0}\sum_{\boldsymbol{\tau}}\delta(\mathbf{q}-\boldsymbol{\tau})|F_N(\mathbf{q})^2|\delta(\hbar\omega), \tag{5.28}$$

where the nuclear structure factor, $F_N(\mathbf{q})$ is

$$F_N(\mathbf{q}) = \sum_j \bar{b}_j \exp(i\mathbf{q}\cdot\mathbf{r}_j)\exp(-W_j), \tag{5.29}$$

with W_j being the Debye-Waller factor. The j sum runs over one unit cell. This modification has the practical effect that some peaks are "forbidden", meaning that even though they fulfill Bragg's law, the cross section is zero due to the nuclear structure factor.

5.1.3 Magnetic scattering

We now turn to magnetic scattering. The subject is rather large and in some ways more complicated than nuclear neutron scattering. The general equation for the magnetic scattering cross section is

$$\frac{\mathrm{d}^2\sigma}{\mathrm{d}\Omega \mathrm{d}E_f} = \frac{(\gamma r_0)^2}{2\pi\hbar}\frac{k_f}{k_i}\left(\frac{g}{2}F(\mathbf{q})\right)^2\sum_{\alpha\beta}(\delta_{\alpha\beta}-\hat{q}_\alpha\hat{q}_\beta)\,S_{\alpha\beta}(\mathbf{q},\omega), \tag{5.30}$$

where

$$S^{\alpha\beta}(\mathbf{q},\omega) = N\frac{1}{2\pi\hbar}\sum_{j,l}\int_{-\infty}^{\infty}\mathrm{d}t\, e^{-\mathrm{i}\omega t}\left\langle e^{\mathrm{i}\mathbf{q}\cdot\mathbf{r}_j(0)}s_j^\alpha(0)e^{\mathrm{i}\mathbf{q}\cdot\mathbf{r}_l}s_l^\beta(t)\right\rangle, \tag{5.31}$$

and

$$F(\mathbf{q}) = \int \exp(\mathrm{i}\mathbf{q}\cdot\mathbf{r})s(\mathbf{r})\mathrm{d}^3\mathbf{r} \tag{5.32}$$

is the magnetic form factor, with $s(\mathbf{r})$ the normalized spin density. $F(0) = 1$ and F decreases smoothly to zero with increasing q. The δ-function in α and β reflects the fact that neutrons only see the spin component perpendicular to $\mathbf{q}$. The scattering function is essentially the time and space Fourier Transform of the spins of the atoms.

Four different types of magnetic scattering can occur: Purely magnetic elastic scattering, similar to elastic nuclear scattering, purely magnetic inelastic scattering, similar to inelastic nuclear scattering, and two cross terms where the neutron excites phonons via the magnetic interactions and terms which give inelastic scattering in both the spin and phonons.

The elastic magnetic scattering cross section for a crystal is quite similar to the nuclear expression, Eq. (5.28)

$$\left(\frac{\mathrm{d}\sigma}{\mathrm{d}\Omega}\right)_{\mathrm{magn,el}} = \frac{(\gamma r_0)^2}{2\pi\hbar}\left(\frac{g}{2}F(q)\right)^2 \exp(-2W)\frac{N(2\pi)^2}{v_0}|F_M(\mathbf{q})|^2 \sum_{\boldsymbol{\tau}} \delta(\mathbf{q}-\boldsymbol{\tau}-\mathbf{Q}), \quad (5.33)$$

where $\mathbf{Q}$ is the ordering vector of the magnetic structure and the magnetic structure factor is

$$F_M(\mathbf{q}) = \sum_j \exp(-\mathrm{i}\mathbf{q}\cdot\mathbf{r}_j)\langle \mathbf{s}_{j\perp}\rangle, \quad (5.34)$$

where $\mathbf{s}_{j,\perp}$ means the component of $\mathbf{s}_j$ that is perpendicular to $\mathbf{q}$. In unpolarized neutron scattering experiments, there is no way to distinguish between coherent nuclear, incoherent nuclear and magnetic scattering. They can be separated by various tricks like varying the temperature or applying a magnetic field, but we will not consider this here. We thus observe a sum of the three types of scattering described above. This may complicate the analysis.

With polarized neutrons, the three types of scattering can be distinguished. Polarized neutron scattering plays only a minor role in this thesis, and therefore the mathematical details of the analysis will not be presented here. The principle is rather simple: By analyzing the spin of the neutrons before and after interacting with the sample, additional information can be gained. This information can be used to determine exactly what kind of scattering process occurred. The downside to using polarized neutrons is that the flux is lower than for unpolarized neutrons, and several additional measurements need to be performed to obtain a full data set.

5.2 Analysis of neutron scattering data from nanoparticles

The results described in the previous section are quite general, and apply to almost any type of scattering. We will here describe the type of signal to be expected from the magnetic excitations described in Chap. 3. We first describe superparamagnetism, then spin waves from nanoparticles.

5.2.1 Superparamagnetism

For superparamagnetism, the spin-spin correlation function has the form

$$\langle s_i^\alpha(0)s_j^\beta(t)\rangle = s^2\exp(-t/\tau)\delta^{\alpha\beta}\delta^{\alpha z}\sigma_{ij}, \quad (5.35)$$

where $\sigma_{j,l} = 1$ (-1) for spins in the same (different) sublattice. Inserting this in Eq. 5.30 and assuming that the nuclear part of the scattering is elastic (i.e. no phonons) we find

$$\frac{\mathrm{d}^2\sigma}{\mathrm{d}\Omega \mathrm{d}E_f} = s^2 \exp(-2W)(\gamma r_0)^2 \frac{k_f}{k_i} \left(\frac{g}{2} F(q)\right)^2 (1 - \hat{q}^z \hat{q}^z)\, N \frac{1}{2\pi\hbar} \sum_{j,l} e^{\mathrm{i}\mathbf{q}\cdot(\mathbf{r}_j - \mathbf{r}_l)} \sigma_{j,l} \int_{-\infty}^{\infty} \mathrm{d}t\, e^{-\mathrm{i}\omega t} \exp(-t/\tau), \tag{5.36}$$

The time Fourier transform gives a Lorentzian in energy. For an infinite system, the space Fourier transform gives a delta function in reciprocal lattice vectors, and we find

$$\frac{\mathrm{d}^2\sigma}{\mathrm{d}\Omega \mathrm{d}E_f} = s^2 \exp(-2W)(\gamma r_0)^2 \frac{k_f}{k_i} \left(\frac{g}{2} F(q)\right)^2 F_m(\mathbf{q})\, (1 - \hat{q}^z \hat{q}^z)\, N \times \frac{1}{\pi} \frac{\Gamma}{\Gamma^2 + (\hbar\omega)^2} \sum_{\boldsymbol{\tau}} \delta(\mathbf{q} - \boldsymbol{\tau} - \mathbf{Q}), \tag{5.37}$$

where $\Gamma = \hbar/\tau$. Typically, Γ is of the order of μeV or meV. Superparamagnetic scattering thus appears at the magnetic Bragg peak positions and gives rise to a quasielastic broadening of the signal in energy. In our case we are interested in the scattering near the (101) and (003) Bragg peaks. The spins are located in the ab-plane, but the exact orientation is to the best of my knowledge not known. However, it can be estimated from experiments as described in Section 6.2. We find, remembering that $(1-(\hat{q}^z)^2) = 1$ for the (003) peak

$$\left(\frac{\mathrm{d}^2\sigma}{\mathrm{d}\Omega \mathrm{d}E_f}\right)^{(003)}_{\mathrm{SPM}} = C(\mathbf{q} = (003)) \frac{A_{\mathrm{spm}}}{\pi} \frac{\Gamma}{\Gamma^2 + (\hbar\omega)^2}, \tag{5.38}$$

$$\left(\frac{\mathrm{d}^2\sigma}{\mathrm{d}\Omega \mathrm{d}E_f}\right)^{(101)}_{\mathrm{SPM}} = C(\mathbf{q} = (101))(1 - (\hat{q}^z)^2) \frac{A_{\mathrm{spm}}}{\pi} \frac{\Gamma}{\Gamma^2 + (\hbar\omega)^2}. \tag{5.39}$$

The constant includes all the numerical prefactors and the structure and form factors. We thus see superparamagnetism as a Lorentzian broadening in energy of the magnetic Bragg peaks. By extracting the width of these peaks, Γ, we can experimentally test the Néel-Brown law mention in Chap. 3, Eq. (3.83).

We note that for nanoparticles, the lattice sum does not give a delta function, but rather a function which is peaked at the same points as the delta function, but with a finite width. For a cubic particle, with $\mathbf{q}$ along the x axis, we have

$$\left| \sum_{j=0}^{m-1} e^{\mathrm{i}\mathbf{q}\cdot\mathbf{r}_j} \right|^2 = \left| \frac{\sin(mq_x a/2)}{\sin(q_x a/2)} \right|^2, \tag{5.40}$$

which peaks at $q_x = 2\pi/a$. The width is $\Delta q_x \approx 2\pi/(ma) = 2\pi/L$, where L is the length of the particle.

The superparamagnetic fluctuations are dubbed longitudinal, because they are along the z direction.

5.2.2 Spin waves

We will now briefly discuss the neutron scattering signal from spin waves. We will restrict the discussion to nanoparticles, as these form the bulk of the thesis. The dispersion relations were derived in Chap. 3, and as mentioned, in nanoparticles, only the $q = 0$ mode has ever been observed. The spin waves are called called transverse, because the fluctuations are along the x and y axes. The low frequency mode $(+)$ is primarily along y, while the high frequency mode $(-)$ is primarily along the hard x-axis.

The $q = 0$ mode is modeled as a damped harmonic oscillator (DHO). The derivation of the exact expression is more complicated than for SPM, and is omitted here. It can be found in e.g. [47]. The result is (again, $(1 - (\hat{q}^y)^2) = 1$ for $\mathbf{q} = (003)$)

$$I_+^{(003)} = C(\mathbf{q} = (003))\frac{A_+}{\pi}\frac{2\gamma(\hbar\omega_0)^2}{\left((\hbar\omega)^2 - (\hbar\omega_0)^2\right)^2 + 4\gamma_\pm^2(\hbar\omega)^2}, \tag{5.41}$$

$$I_+^{(101)} = C(\mathbf{q} = (101))(1 - (\hat{q}^y)^2)\frac{A_+}{\pi}\frac{2\gamma(\hbar\omega_0)^2}{\left((\hbar\omega)^2 - (\hbar\omega_0)^2\right)^2 + 4\gamma_\pm^2(\hbar\omega)^2}, \tag{5.42}$$

$$I_-^{(003)} = 0 \tag{5.43}$$

$$I_-^{(101)} = C(\mathbf{q} = (101))(1 - (\hat{q}^x)^2)\frac{A_-}{\pi}\frac{2\gamma(\hbar\omega_0)^2}{\left((\hbar\omega)^2 - (\hbar\omega_0)^2\right)^2 + 4\gamma_\pm^2(\hbar\omega)^2}. \tag{5.44}$$

The total area of the high frequency mode and the low frequency mode is

$$A_{\mathrm{DHO}} = A_+ + A_-. \tag{5.45}$$

The integrated intensity of the longitudinal scattering, i.e. A_{SPM}, is proportional to the square of the longitudinal part of $\mathbf{s}^{\mathrm{AFM}}$,

$$A_{\mathrm{SPM}} \propto \langle(\mathbf{s}_{\mathrm{AFM}}^{\parallel})^2\rangle, \tag{5.46}$$

and similarly

$$A_{\mathrm{DHO}} \propto \langle(\mathbf{s}_{\mathrm{AFM}}^{\perp})^2\rangle. \tag{5.47}$$

Combining these relations we find

$$\frac{A_{\mathrm{SPM}}}{A_{\mathrm{SPM}} + A_{\mathrm{DHO}}} = \langle(\mathbf{s}_{\mathrm{AFM}}^{\parallel})^2\rangle. \tag{5.48}$$

The temperature dependence of $s_{\mathrm{AFM}}^{\parallel}(T)$ can be calculated using Eq. (3.88). One downside to doing this calculation is that it requires knowledge of the energy barrier $KV = N\kappa_2 ss'$, which is unknown in the mesoporous particles. The second method is to utilize the fact that at the magnetic reflections, $\mathbf{Q} = \boldsymbol{\tau}$, where $\boldsymbol{\tau}$ refers to (003) and (101)

reflections, the elastic scattering is proportional to the square of the ordered moment:

$$I(\hbar\omega = 0, |\mathbf{q}| = |\boldsymbol{\tau}|) \propto \langle (s^{\parallel}_{\mathrm{AFM}})^2 \rangle \approx \langle s^{\parallel}_{\mathrm{AFM}} \rangle^2. \tag{5.49}$$

The last approximation is readily verified using Eqs. (3.87) and (3.88).

An important concept when describing inelastic neutron scattering is detailed balance. In equilibrium, the excitations have a certain population, P, satisfying

$$P(q, \omega) = P(q, -\omega) \exp(\hbar\omega / k_b T) \tag{5.50}$$

To account for this in the fitting procedure, all signals that are related to motion are multiplied by the detailed balance factor, $D(\hbar\omega)$ as used in e.g. [9]

$$D(\hbar\omega) = \frac{\hbar\omega}{k_B T} \left(\frac{1}{\exp(\hbar\omega / k_B T) - 1} + 1 \right). \tag{5.51}$$

5.2.3 Resolution function

Everything we measure has an uncertainty, and this leads to the very important concept of the resolution function. Ideally, if we measure elastic scattering from a crystal and plot the intensity of neutrons as a function of θ or q, we should according to Bragg's law Eq. (5.27) see delta functions at the values fulfilling this equation.

However, in real experiments, this is not observed. Instead, the peaks are usually shaped like either a Gaussian (G), a Lorentzian (L) or a Voigt (V) which is the convolution ($*$) of the two former:

$$V(x) = (G * V)(x) = \int_{-\infty}^{\infty} G(t) L(x - t) dt \tag{5.52}$$

$$= \int_{-\infty}^{\infty} \left(\frac{A_G}{\sqrt{2\pi\sigma}} \exp\left(\frac{x^2}{2\sigma} \right) \right) \left(\frac{A_L}{\pi} \frac{\gamma}{(x-t)^2 + \gamma^2} \right) dt, \tag{5.53}$$

A_G is the area of the Gaussian, σ is the standard deviation of the Gaussian, A_L is the area of the Lorentzian and γ is the half width at half max (HWHM). The area of the Voigt function is $A_V = A_G \times A_L$.

The observed shape of the Bragg peaks is what we usually define as the resolution function. In general, when we observe a distribution (e.g. intensity as function of $\hbar\omega$), the observed distribution is the convolution of the true distribution with the resolution function [48]. It is easy to check that the convolution of a delta function with the resolution function precisely is the resolution function.

The resolution function is both q and $\hbar\omega$ dependent. The effect of the dependence of energy transfer is small and very hard to measure because inelastic scattering is needed. Therefore, it is neglected in this work.

There are several ways to determine resolution functions. One common method is to measure vanadium, which has a large incoherent scattering cross section and a small coherent scattering cross section. Another way is to use a measurement of the sample

itself at low temperatures as the resolution function, since almost no inelastic scattering is expected at low temperatures. This is the method that will be used in this thesis. As mentioned, the resolution function is usually Gaussian, but it can also have more complicated shapes.

Advanced tools to estimate resolution functions exist. For so-called triple axis spectrometers, described Section 5.3.1, software such as Reslib [49] can be used to calculate the resolution function in every point in reciprocal space. Monte Carlo ray-tracing programs such as McStas [50] or VITESS [51] can also be used to simulate full experiments, thus providing quite accurate estimates of the resolution function. However, such advanced methods are very time consuming and unnecessary for this project.

When we are fitting the data from experiments, the fitting function is the convolution of the experimentally determined resolution function with the theoretical true distribution. In practice, this is calculated using the convolution theorem,

$$f * g = \mathcal{F}^{-1}(\mathcal{F}(f) \cdot \mathcal{F}(g)), \tag{5.54}$$

where $\mathcal{F}$ denotes a Fourier transform. This speeds up calculations immensely, since efficient algorithms exist for calculating Fourier transforms numerically.

5.2.4 Uncertainties in fitting parameters

In the measurements presented in the next chapter, we will in general observe the high frequency mode, the low frequency mode and superparamagnetism. This gives a total of 8 free parameters: the area of the DHOs, $A_{\pm}$, their widths, $\gamma_{\pm}$, their positions, $\hbar\omega_{\pm}$, the area of the superparamagnetic scattering, A_{SPM} and the width, Γ. We also fit an offset in the energy, giving a total of 9 free parameters, which is a lot

When fitting experimental data there will be some uncertainty in the extracted parameters. For simple fits, e.g. when fitting a Gaussian amplitude and width to a peak, the parameters can be assumed to be uncorrelated. In this case, it is fairly straightforward to calculate the uncertainties of the fitted parameters. In the program we use, spec1d, [52], the uncertainties are given as the square root of the diagonal elements of the covariance matrix of the variables. When the parameters are correlated, however, this method fails and can some times give wildly inaccurate results. The ideal solution would be to transform to some variables that are completely uncorrelated, but this is impractical and possibly not doable in practice.

In our case, some parameters are independent, like the parameters describing the fit to the low frequency mode and the high frequency mode: the two sets of peaks are so far apart in energy that they do not influence each other. However, if e.g. the position of the low frequency mode, $\hbar\omega_{+}$ is increased, a better fit is obtained if also the width, γ_{+} is increased.

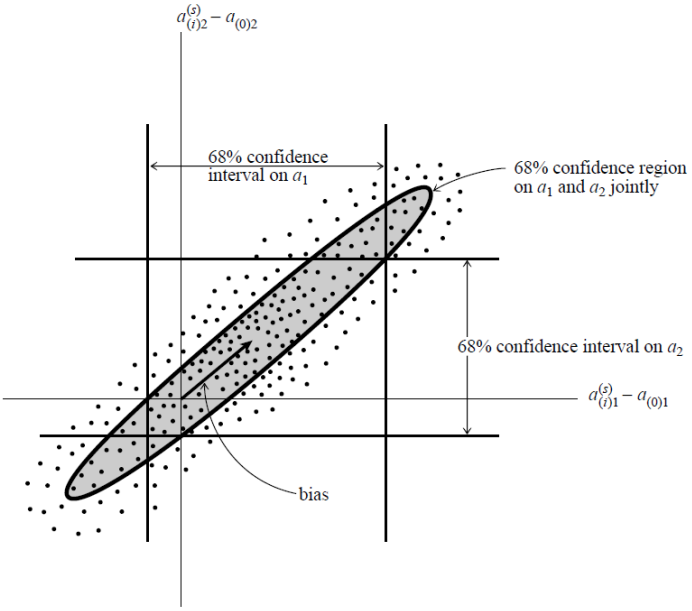

FIGURE 5.1: Illustration of the concept of confidence intervals. Figure taken from Ref. [53].

The goodness of fit is measured by χ^2, given by

$$\chi^2 = \sum_{\text{data}} \left(\frac{y_{\text{data}} - y_{\text{fit}}}{\sigma_{\text{data}}} \right)^2 , \tag{5.55}$$

where σ_{data} is the uncertainty in each data point, and the sum runs over all measured data points. Sometimes, the reduced χ^2 is used; this is χ^2 divided by (the number of data points minus the number of free parameters). The fitting routine aims to minimize the value of χ^2 by varying the parameters. In the experiments described in the next chapter, any number between 3 and 9 parameters are fitted simultaneously.

We will use the 68% confidence interval of our variables as the error bars. When varying only one parameter, this confidence interval is given by points where χ^2 has increased by 1 from its minimum. When varying two parameters, the confidence interval is the contour where χ^2 has increased by 2.3 from its minimum [53]. The interval can usually be well approximated by an ellipsoid in the n dimensional variable space. For correlated parameters, the ellipsoid will be skewed. Calculating this ellipsoid for 9 variables, however, would require calculating χ^2 several billion times for each data set. This is quite impractical. We therefore calculate only the width of this ellipsoid along each variable dimension. We do this by varying one parameter manually, while optimizing the other parameters. An illustration of these concepts is given in Fig. 5.1.

It was mentioned above that $\hbar\omega_+$ and γ_+ are correlated. This is illustrated in Fig. 5.2, where these two parameters have been varied individually, while optimizing all the other parameters. The color scale shows χ^2. The data behind this figure will be presented in the next chapter. It is apparent that the parameters are indeed correlated. The extracted confidence intervals are shown.

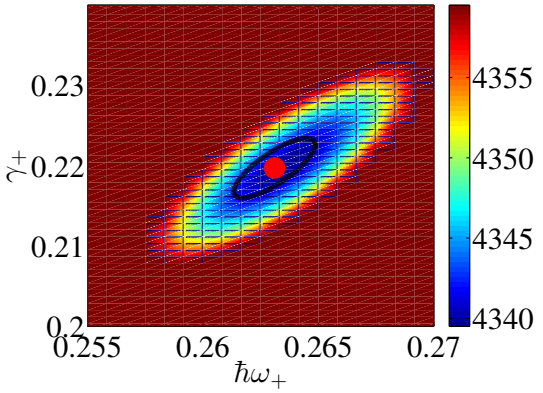

FIGURE 5.2: The value of χ^2 of the fit of a typical data set from IN5 as function of the position of the DHO, $\hbar\omega_+$ and the width γ_+. The black ellipse shows the 68% confidence interval. The skewness of the ellipse shows that the two parameters are correlated.

To summarize, we find the uncertainties of a parameter by varying it and fitting all the other relevant parameters. The boundary values where χ^2 has increased by 1 compared to the optimal value is taken as the uncertainty intervals. This method has been used to estimate the uncertainties in all fits of the magnetic signal presented in the next chapter. When fitting background, the number of parameters is smaller, and they are independent to a good approximation, so the standard routines of the fitting program are sufficient to accurately determine the uncertainties.

5.3 Instruments

In this section, the different types of neutron scattering instruments that have been used in this thesis will be briefly described. The basic concept of a neutron scattering instrument is the same for all spectrometers: we need to determine $\mathbf{k}_i$ and $\mathbf{k}_f$ in order to calculate the momentum transfer, $\mathbf{q}$ and the energy transfer, $\hbar\omega$. Since detection of a neutron is by absorption, this determination must be done with a single measurement. There are in general two techniques to do this: The first is to utilize Bragg's law using a so-called monochromator, which is a crystal with a well defined lattice constant. By choosing a certain scattering angle, only neutrons with the wavelength fulfilling Braggs law will be reflected at this angle, and a monochromatic beam will be obtained.

The second technique is time-of-flight, where $\mathbf{k}_i$, $\mathbf{k}_f$ or both are determined through their time of flight. Usually, one or more choppers are used. A chopper is a rotating blade of neutron absorbing material with a wedge in it. This provides a way to time stamp neutrons such that by registering the time of detection of a neutron, its velocity and thus its wave vector is known.

Getting absolute cross sections from an experiment is quite difficult. Fortunately, we are often only interested in relative intensities. To normalise the intensity, one places a

so-called monitor before the sample, which measures a small, but well defined, fraction of the incoming neutrons. In this way, we have a measure of the incoming flux.

The choice of instrument for an experiment is very important. A variety of instruments exist, optimized for different tasks. In general, one should match the resolution of the instrument to the desired range of energy and momentum transfer to be studied. Usually, one must balance a trade-off between high resolution, and high flux - both are not obtainable with neutrons. If motion on the scale of μeV is to be observed, an energy resolution on the scale of meV is far too large, and will yield no results. Conversely, using a very narrow resolution will make the counting times increase to beyond what is feasible. Furthermore, high resolution instruments usually have a quite narrow dynamical range, meaning that it is difficult to measure excitations on several different time scales in the same experiment.

5.3.1 Two axis and triple axis spectrometers

Triple axis spectrometers are some of the most widely used instruments in neutron scattering, being available at almost every neutron scattering facility in the world. They are called so because the detected neutrons change direction three time in a normal experiment. A sketch of the RITA-II triple axis spectrometer at PSI in Switzerland [54] is shown in Fig. 5.3. The incoming wavelength is selected with the monochromator, utilizing Bragg's law, Eq. (5.27). Next, the neutron scatters from the sample, and a crystal similar to the monochromator is used to determine the outgoing wavevector. Finally, a detector measures the neutron. In this way, $S(\mathbf{q}, \omega)$ can be mapped point by point. This is very useful for measuring e.g. dispersion relations.

Cold triple axis spectrometers usually have a Gaussian resolution of approximately 0.1 meV (FWHM), depending on the exact configuration. The dynamical range is usually around 10 meV on the upscattering side (neutron gaining energy) and 3 meV on the down scattering side (neutron losing energy) for a constant final energy of $E_f = 5$ meV.

A similar instrument is the two-axis spectrometer. Here, there is no analyzer, and the detector thus integrates over ω, measuring $S(\mathbf{q})$. Bragg peaks are usually orders of magnitude stronger than excitations, and in most cases, it is a good approximation to assume that the measured $S(\mathbf{q}) = S(\mathbf{q}, \omega = 0)$, perhaps with an added slightly q-dependent background.

This is useful for determining the atomic structure of a material in powder form using e.g. Rietveld refinement [55].

5.3.2 Time of flight spectrometers

As mentioned above, this type of instrument uses the time of flight of the neutrons to determine their wavevectors. A typical instrument, IN5 (located at ILL) is illustrated in Fig. 5.4

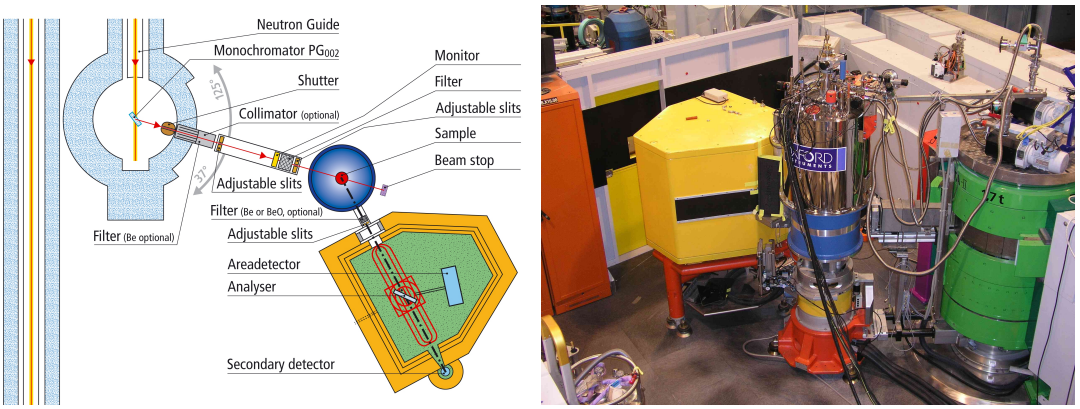

FIGURE 5.3: Left: A sketch of the RITA-II triple axis spectrometer located at PSI. Right: A picture of RITA-II. The monochromator is inside the green shielding, the sample in the blue cylinder and the analyzer and detector are in the yellow container. The pictures are from the PSI webpage [54].

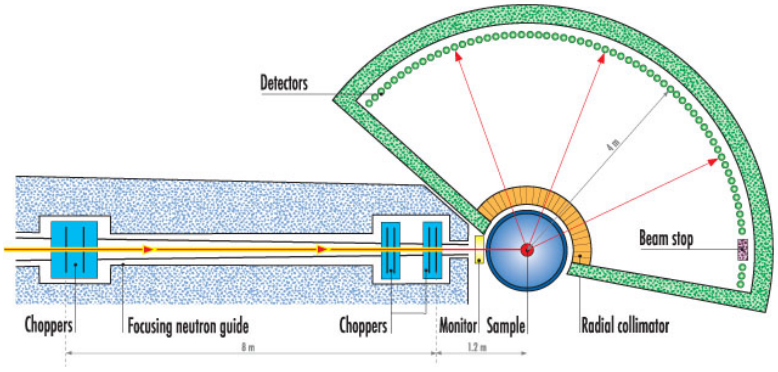

FIGURE 5.4: A sketch of the IN5 spectrometer. The picture is from the ILL webpage [56].

A set of choppers can be set to rotate in such a way that only neutrons with a specific wavelength come through. In this way, $\mathbf{k}_i$ and the timing of the neutrons are determined. When the neutrons reach the detector, their $\mathbf{k}_f$-vector can be determined through timing.

Time of flight spectrometers map entire sections of reciprocal space in one measurement, and are extremely powerful. The information content is much greater than what can be obtained from triple axis spectrometers, with a similar resolution.

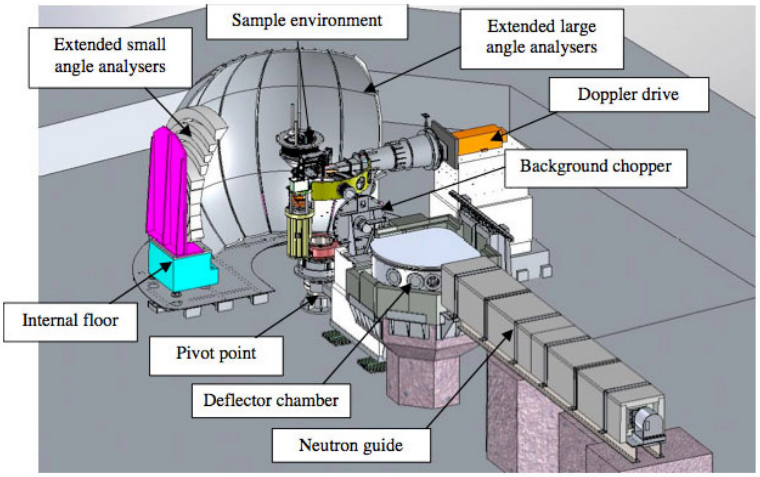

FIGURE 5.5: A sketch of the newly commissioned IN16b backscattering spectrometer at ILL. The picture is from the ILL webpage [58].

5.3.3 Backscattering

Backscattering spectrometers have extremely high energy resolution, but correspondingly poor q resolution. They are widely used in the field of biophysics to measure dynamics of molecular water, as we e.g. show in [57]. A backscattering instrument is illustrated in Fig. 5.5

As the name implies, backscattering, i.e. scattering with $2\theta \approx 180°$ is used. The error in the energy becomes very small, and the resolution is typically 1 μeV. To see this, we differentiate Bragg's law:

$$n\mathrm{d}\lambda = 2d\cos(\theta)\mathrm{d}\theta + 2, \tag{5.56}$$

leading to

$$\frac{\mathrm{d}\lambda}{\lambda} = \cot(\theta)\mathrm{d}\theta, \tag{5.57}$$

which goes to zero as θ goes to 180°. The price for the high resolution is a low flux and a poor q resolution.

To change the energy of the incoming neutrons, a so-called Doppler drive is used. The monochromator scattering the incoming neutrons towards the sample is set to oscillate, and by the Doppler effect the energy of the neutrons is slightly shifted. The dynamical range thus obtained is typically ± 15 μeV, and thus backscattering is usually for quasi-elastic scattering.

5.4 Previous neutron scattering experiments on nanoscale hematite

Several papers describing neutron scattering experiments on nanoscale hematite have been published. We will here go through most of them chronologically, starting with the first paper on inelastic neutron scattering measurements on 16 nm nanoparticles of hematite [9], where both superparamagnetism and the low frequency mode are observed. Using only a uniaxial model for the dynamics they find through Eq. (3.90) $K_2V = 1000(400)$ K. Assuming strong in-plane anisotropy, they would have found $K_2V = 500(200)$ K. This is indeed what they find from SPM through the Néel-Brown law, Eq. 3.83, with $\tau_0 = 7 \times 10^{-12}$, with an uncertainty of an order of magnitude. From the frequency of the low frequency mode, $\hbar\omega_+$, using $B_X = 927$ T, they find $\kappa_2 = 0.91(5)$ mK. The width of the peaks are found to increase slightly with temperature. In a later discussion [35], they refine the data analysis on the data from [9], and indeed find $K_2V = 500(200)$ K.

In [10] they measure the same 16 nm particles. They estimate $|K_1V = 2600|$ K, and with this they find from Eq. 3.88 $K_2V = 150^{+600}_{-50}$ K; using $K_1V = \infty$, i.e. the 2d model Eq. 3.92, they find $K_2V = 110^{+490}_{-40}$. From the Néel-Brown law, they find $K_2V = 490(30)$ K, and $\tau_0 = 1.9(4) \times 10^{-11}$ s. From the temperature evolution of the low frequency mode, they find $K_2V = 330^{+590}_{-230}$ K if $K_1V = 2600$ K and $K_2V = 350^{+690}_{-250}$ K for $K_1V = \infty$. The width of the peaks are found to increase slightly with temperature.

In [11], the high frequency mode was observed for the first time for 8 nm particles. the frequency was found to increase with temperature, which they explained by an increase of $|\kappa_1|$ with temperature. They found $\kappa_1 = -16(1)$ mK at low temperature. They assumed $s^z/s \approx 1$ throughout the temperatures measured, which is not a good approximation at elevated temperatures, so their estimates of the temperature evolution of κ_1 is not correct. The width of the peaks are found to increase slightly with temperature.

In [12], 8 nm particles were investigated. Using the 2d model they found $K_2V = 250(30)$ K for the coated particles. Using the 3d-model with $K_1V = \infty$ would yield $K_2V = 125(15)$ K.

An overview of these results is given in Table. 7.2.

Chapter 6

Experiments

I will here present and analyze several neutron scattering experiments that have been performed on hematite. First, an overview of the experiments is given. Next, the experiments are analyzed one at a time, and finally some conclusions are drawn.

6.1 Overview of experiments

A number of neutron scattering experiments have been performed as part of this thesis. They will here be mentioned in their order of appearance below: Inelastic scattering on bulk, mesoporous and 16 nm nanoparticulate hematite were done at IN5, ILL [59] by Adrian H. Hill, Ross Stewart, Hannu Mutka, and Kim Lefmann in June 2010. Backscattering on mesoporous and 16 nm nanoparticulate hematite were done at IN10, ILL [60] by Adrian H. Hill, Sonja L. Holm, Tilo Seydel and myself in November 2010. The results of these two experiments were described in my bachelor thesis [61] and in a recent publication [19]. Furthermore, backscattering on the 16 nm particles were done at IN16b, ILL [62] by Tilo Seydel in July 2013; these results were also published in Ref. [19].

The mesoporous sample was investigated with polarized neutrons on D7, ILL in March 2012 by Erik Brok, Pascale Deen, Cathrine Frandsen, Goran Nilsen and myself. These measurements have not been described before.

Finally, the 8 nm particles have been measured on DMC at PSI in 2001. An overview of the experiments is given in Table 6.1.

In this chapter, each experiment will be described in turn. The first section, about the IN5 experiment, also briefly explains the model used for fitting the data.

All fitting was done using MATLAB R2013b with the spec1d package [52]. To calculate the convolution of the resolution function with the model, the `fastconvn` from iFit was used [63]. iFit was also used to import some of the data.

6.2 Measurements 16 nm and mesoporous particles (IN5)

IN5 is a time of flight spectrometer as described in the previous chapter. It is one of the most powerful of its kind in the world, and as we shall see, the amount of data

Sample	Facility	Instrument	Year	Henrik?	Section
Bulk Mesoporous 16 nm	ILL	IN5	2010	No	6.2
16 nm Mesoporous	ILL	IN10	2010	Yes	6.3
Mesoporous	ILL	D7	2013	Yes	6.4
16 nm	ILL	IN16b	2013	Yes	6.3
8 nm coated	PSI	DMC	2001	No	6.5
8 nm coated	PSI	RITA-II	2001	No	6.5
8 nm coated 8 nm uncoated	Jülich	BSS	2005	No	6.6

TABLE 6.1: Overview of the experiments that were analyzed in this thesis.

Bulk	$\lambda = 4.8$ Å	1.5	—	—	150	200	—	300
	$\lambda = 6.5$ Å	1.5	—	—	150	200	—	300
Mesoporous	$\lambda = 4.8$ Å	1.5	50	100	150	200	250	300
	$\lambda = 6.5$ Å	1.5	50	100	150	200	250	300
16 nm nanoparticles	$\lambda = 4.8$ Å	1.5	50	100	150	—	—	300
	$\lambda = 6.5$ Å	1.5	50	100	150	—	—	—

TABLE 6.2: Overview of the temperatures (in K) that have been measured at the IN5 experiment.

produced is huge. Powders of 16 nm particles, mesoporous particles and bulk particles were measured. The sample environment used was a standard orange cryostat, with the sample held in a cylindrical aluminium can. Incident neutron energies of $E_i = 3.55$ meV ($\lambda_i = 4.8$ Å) and $E_i = 1.94$ meV ($\lambda_i = 6.5$ Å) were selected to provide both large energy transfer and high energy resolution respectively. The FWHM of the resolution functions were determined (from low temperature data, see below) to be ~ 0.13 meV and ~ 0.04 meV for $\lambda_i = 4.8$ Å and $\lambda_i = 6.5$ Å respectively, with a slight q and sample dependence.

The momentum transfer (q) range studied covers the first three Bragg reflections, (003), (101), and $(10\bar{2})$, which occur at 1.37 Å^{-1}, 1.51 Å^{-1}, and 1.70 Å^{-1} respectively. An overview of the measured temperatures is given in Table 6.2

The neutron data were converted from time-of-flight to energy using standard treatments (using the Large Array Manipulation Program, LAMP [64]) and corrected for the empty aluminum can signal, solid angle and detector efficiency using standard techniques. An example IN5 spectra of the bulk, α-Fe_2O_3 taken at 150 K with $\lambda_i = 4.8$ Å is shown in Fig. 6.1. The steep, continuous spin wave dispersion is clearly visible. For the nanoparticles, the $\hbar\omega_-$ mode is clearly seen at $\hbar\omega = \pm 1.1$ meV at $q = 1.51$ Å^{-1}.

The elastic line is plotted in Fig. 6.2. The bulk sample shows clear, resolution limited Bragg peaks at the expected positions. The Morin transition is observed as the drop

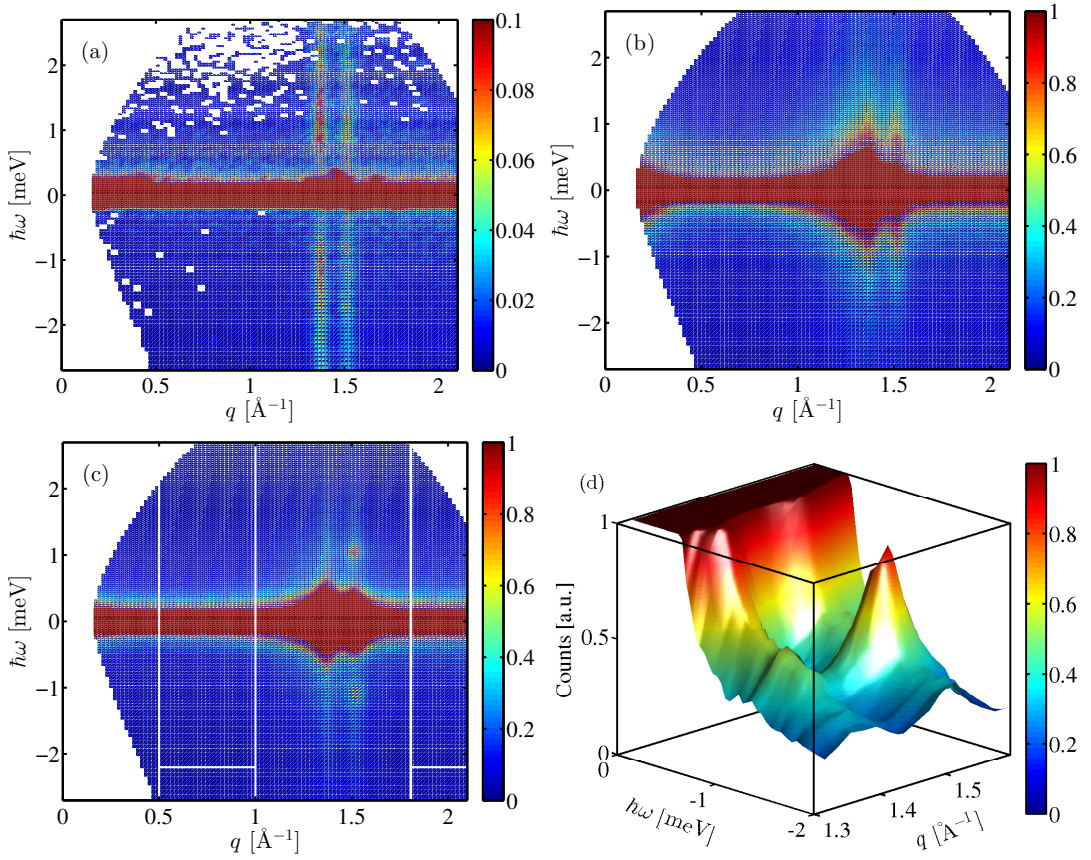

FIGURE 6.1: (Color online) Spectra of (a) bulk, (b) mesoporous, and (c) nanoparticulate α-Fe_2O_3 taken at 150 K with $\lambda_i = 4.8$ Å. Quasi-elastic magnetic peaks and the associated spin-waves at $q = 1.37$ Å^{-1} and $q = 1.51$ Å^{-1} are clearly visible. These are continuous in the bulk spectrum and quantized in the nanoparticulate spectrum, as seen near $\hbar\omega \approx 1.1$ meV at $q = 1.51$ Å^{-1}. The mesoporous spectrum shows behavior between these two states. In (c) the lines indicate the limits within which the incoherent background has been found as described in the text. Panel (d) is a 3d visualization of a part of the data for nanoparticulate α-Fe_2O_3 at 300 K, where the high frequency mode is visible at both $q = 1.37$ Å^{-1} and $q = 1.51$ Å^{-1}

of intensity in the (0 0 3) peak with decreasing temperature. In the mesoporous and nanoparticle samples, the peaks are broader due to the finite size of the particles, and no hints of the Morin transition is seen. We also see a large incoherent background in all three samples. This background is caused by water adsorbed to the surface of the particles, and is a major complication in data analysis. At small angles, incoherent small angle scattering from the particles dominates the signal. This background goes as q^{-4}.

The integrated intensities of the three first Bragg peaks are shown in Fig. 6.3. Here, the Morin transition is again clearly observed in the bulk sample. However, it is not seen at the expected temperature of ∼260 K, but instead somewhere between 150 K and 250 K. This could indicate that the bulk sample is not of high quality. In the two other samples, no signs of the Morin transition are seen. This is to be expected based on previous results [32, 31].

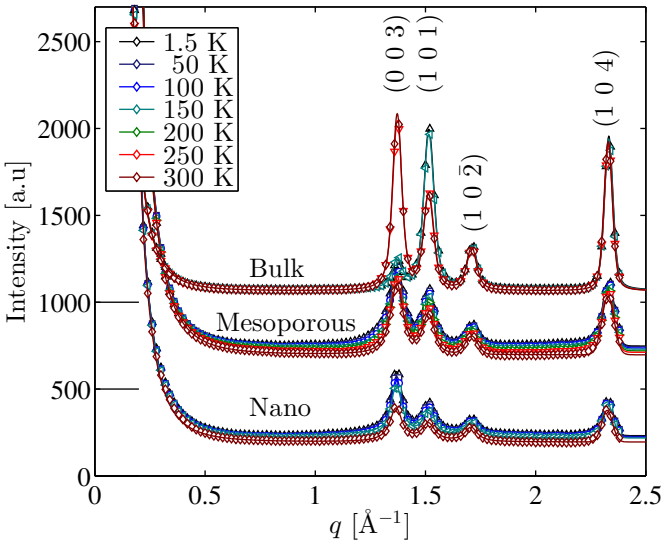

FIGURE 6.2: The elastic part of the signal at IN5 for nano, mesoporous and bulk hematite for $\lambda = 4.8$ Å. The data for different particle types have been offset for clarity; the black lines indicate the offset.

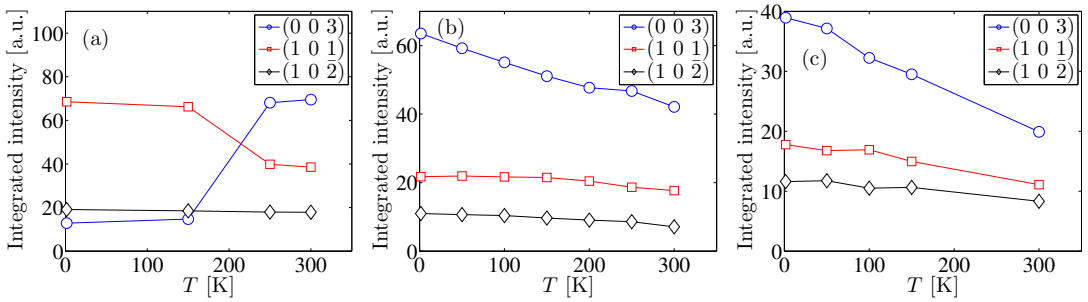

FIGURE 6.3: The integrated intensity of the magnetic (003) and (101) peaks and the nuclear (1 0 $\bar{2}$) peak as function of temperature for $\lambda = 4.8$ Å for (a) bulk, (b) mesoporous and (c) 16 nm nanoparticles. The Morin transition is obvious in the bulk sample. The $\lambda = 6.5$ Å data gives similar plots

6.2.1 Modeling 16 nm particle data from IN5

We will now describe how to model the magnetic signal for the nanoparticle sample. The general procedure is the following. First, the resolution is determined. Next, the background from the incoherent signal is estimated at the magnetic peaks. Then the signal at the magnetic peaks is fitted, and finally the extracted parameters are analyzed.

6.2.1.1 Determining the resolution function

First, the resolution function must be determined. In some experiments, it can be found using an incoherent scatterer like vanadium, but here the resolution is very sensitive to tiny changes in experimental conditions, like thickness of the sample holder. Therefore, the sample itself was used at the lowest possible temperature.

A Gaussian was found insufficient to accurately model the data. The peak shape is broader at the top and falls off quicker than a Gaussian away from the top. This was

modelled as two narrower Gaussians with the center slightly displaced. In addition to this, a small tail in the upscattering side was modeled as a Lorentzian when fitting the incoherent signal. At the magnetic peak positions, this detail could not be accurately modeled due to the presence of inelastic magnetic scattering.

6.2.1.2 Estimating the background

To model the magnetic signal, we first need to determine the background at the magnetic peaks. It is clear in Fig. 6.1 that the background is q-dependent, becoming broader at larger q. The signal also broadens with increasing temperature. This is typical of water dynamics, which is usually modeled as an elastic signal for the static hydrogen atoms plus a number of Lorentzians to account for the different types of motion the water can perform: vibration, rotation etc. [65]. The temperature and q dependence of the amplitude and width of these Lorentzians can yield information about the water dynamics. However, this is not of interest here, and the simplest possible model with just a single Lorentzian has been found sufficient to accurately model the background. Thus,

$$I_{\text{incoh}} = A_{\text{el}}\delta(\hbar\omega) + D(\hbar\omega)\left(\frac{A_{\text{qel}}}{\pi}\frac{\Gamma_{\text{qel}}}{\Gamma_{\text{qel}}^2 + \hbar\omega^2}\right) + C, \tag{6.1}$$

where $D(\hbar\omega) = \hbar\omega(n(\hbar\omega) + 1)$ is the detailed balance factor Eq. (5.51) [9]. Cuts in the data of constant energy for every value of q (referred to as q cuts) of width $\delta q = 0.02$ Å^{-1} were made and Eq. (6.1) was fitted to the data. The energy bin size was 0.03 meV and 0.01 meV for incident neutron wavelengths of $\lambda_i = 4.8$ Å and $\lambda_i = 6.5$ Å, respectively. Data within ~ 0.3 Å of $q = 1.37$ Å^{-1} and $q = 1.51$ Å^{-1} were ignored due to the presence of magnetic scattering, and data at $q < 0.5$ Å^{-1} were ignored due to the presence of small angle scattering. The limits are shown with vertical lines in Fig. 6.1(c).

Examples of the fit at various temperatures and q-values are shown in Fig. 6.4. Everywhere, the background is accurately modeled by Eq. (6.1).

The extracted parameters for the Lorentzian and background as function of q for all measured temperatures for the nanoparticles are shown in Fig. 6.5 along with fits to polynomials of first or second order, depending on what is appropriate. There are several points to notice here: Firstly, the magnetic intensity is quite broad in q, as is expected for nanoparticles, and thus a large part of the data cannot be used to determine the background. Secondly, small angle scattering becomes important already at $q \sim 0.5$ Å. As a consequence of this, only data within the vertical lines have been used for the fit.

Using the fits to the background well away from the magnetic scattering, we can estimate the background at the magnetic peaks.

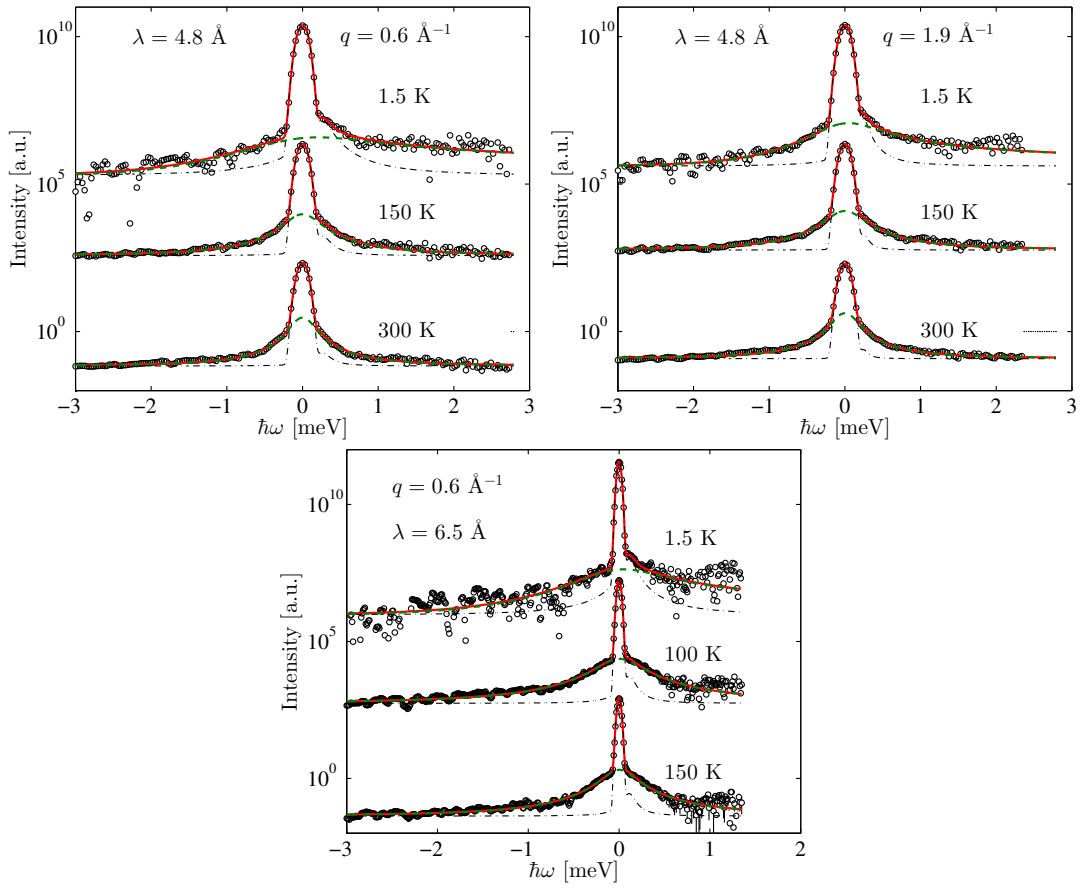

FIGURE 6.4: Examples of the incoherent signal from 16 nm particles at various temperatures. Everywhere, the signal is accurately described by Eq. (6.1).

6.2.1.3 The magnetic signal

As discussed previously, the full magnetic signal consists of; a superparamagnetic Lorentzian, area A_{SPM}; and the two excitation modes (modeled with two damped harmonic oscillators, DHOs), area $A_{\pm}$, width $\gamma_{\pm}$ and position $\hbar\omega_{\pm}$, providing a model for the total scattering present, Eq. (6.2), with the incoherent scattering fixed from Eq. (6.1) [10, 11, 12, 19]

$$I_{\mathrm{model}} = I_{\mathrm{incoh}} + D(\hbar\omega)\left\{\frac{A_{\mathrm{SPM}}}{\pi}\frac{\Gamma}{\Gamma^2+(\hbar\omega_0)^2} + \sum_{\pm}\frac{A_{\pm}}{\pi}\frac{2\gamma_{\pm}(\hbar\omega_{\pm})^2}{\left((\hbar\omega)^2-(\hbar\omega_{\pm})^2\right)^2+4\gamma_{\pm}^2(\hbar\omega)^2}\right\}. \tag{6.2}$$

In this experiment, the SPM broadening is so small compared to the resolution, that it cannot be distuingished. The term $(A_{\mathrm{SPM}}/\pi)\Gamma/(\Gamma^2+(\hbar\omega)^2))$ is thus replaced with $A_{\mathrm{SPM}}\delta(\hbar\omega)$. In the fitting procedure, an offset in energy has been allowed. Also, it was found that the detailed balancing was not fulfilled at 1.5 K. Fitting the temperature returned a value of 10 K, which has been used. An explanation of this elevated temperature in the sample could be slow thermalization.

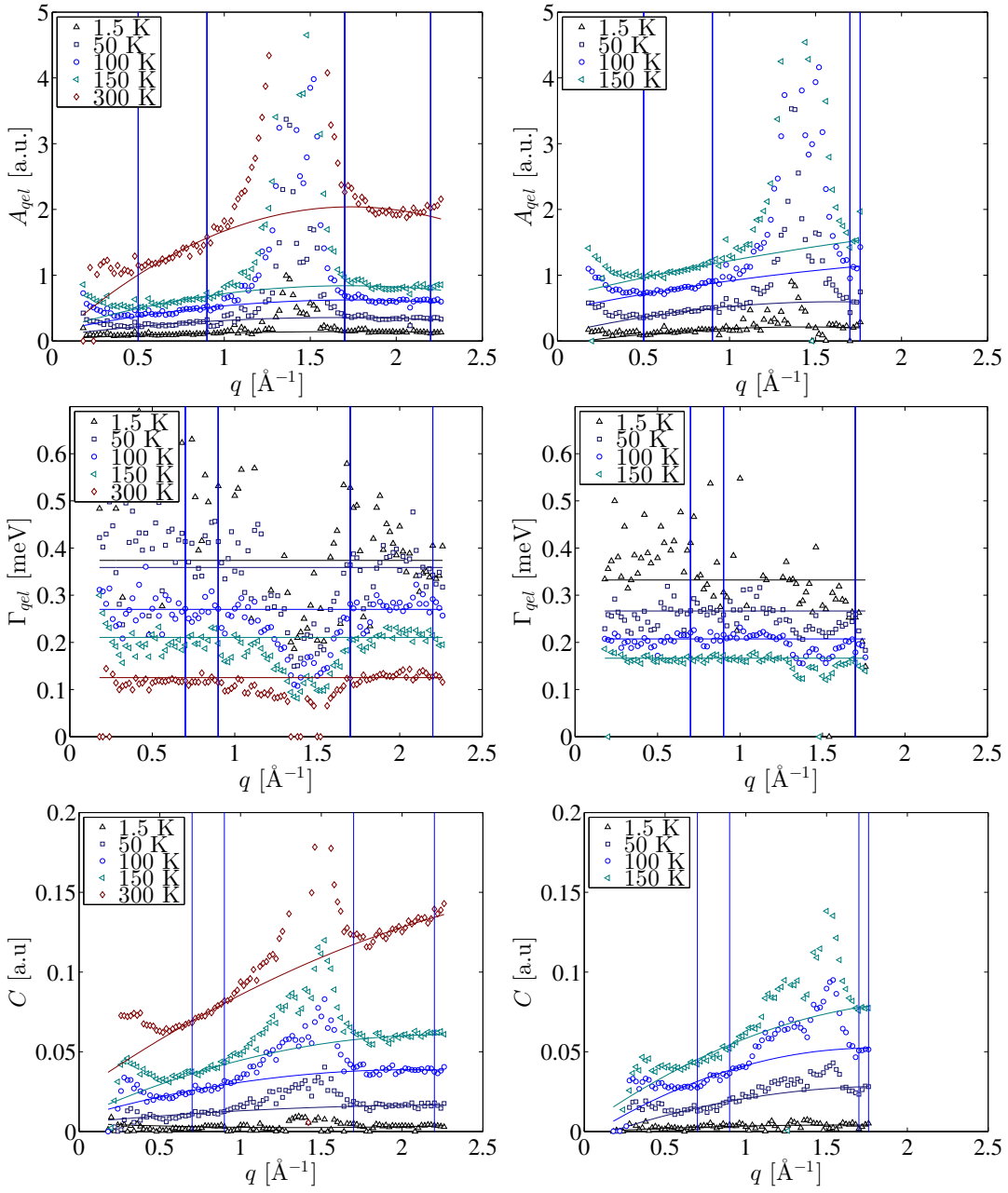

FIGURE 6.5: Some of the parameters describing the incoherent signal for the nanoparticles. Every point is the result of a fit as described in the text. The left column shows the parameters for $\lambda_i = 4.8$ Å, right for $\lambda_i = 6.5$ Å. Disregarding the lowest q-values and the q-range near the magnetic peaks, the area of the Lorentzian, A_{qel}, is seen to increase with q and temperature, the width Γ_{qel} is approximately constant in q and the background increases with q. The solid lines show fits to polynomials of first or second order to the data within the vertical lines.

Some example fits are shown in Fig. 6.6. In Figs. (a), (b), (d) and (e), the data at the (1 0 1) peak are shown. Here, both the $\hbar\omega_\pm$ modes are see, the ω_- as a peak near $\hbar\omega = 1.1$ meV, the ω_+ as a broad shoulder to the elastic signal. In Figs. (c) and (f), at the (003) peak, only the low frequency mode is clearly visible, although hints of the high frequency mode can be seen. At low temperature, Fig. 6.6(a), the intensity of magnetic scattering is quite low.

Several things are immediately apparent from these fits. The fits at the (101) peak are excellent at energies below around ± 1.5 meV. At higher energies, there is a magnetic signal which is not accounted for by the model. This signal is likely caused by either larger particles with a bulk-like dispersion or from aggregated particles. At the (003) peak, Figs 6.6(c) and (f), it is difficult to distinguish the high frequency mode above this signal, and attempts to fit the data with a second DHO have not been successful. As a result, the fit is only reliable up to ± 0.9 meV. Even so, the fits have a tendency to increase the position and width of the low frequency mode to reduce the χ^2 of the fit. To counter this behaviour, we have fixed the values of $\hbar\omega_+$ and γ_+ at the (003) peak from the (101) values; this still produces excellent results as seen in Fig. 6.6.

One of the reasons for choosing to measure at different resolutions was to use the high resolution data to fix the position of the low frequency mode. However, this turned out to not be necessary.

From these fits, eight parameters of interest can be extracted: The frequencies, widths and areas of the high- and low frequency mode, and the area of the (quasi-)static signal. The parameters will be analyzed using the equations described in the previous chapters. In the next section, we re-analyze the parameters using numerical simulations.

6.2.1.4 Analysis of parameters from magnetic fits

Let us first look at the intensity of the (quasi-)static signal, I_{SPM}, Fig. 6.7. It is seen to decrease with temperature. This means that the fraction of static spins (as seen by IN5) decreases with increasing temperature. We also see a difference between the different peak positions, and the different wavelengths used. This is consistent with Eqs. (5.38) and (5.39): the observed intensity is not directly comparable to A_{SPM}. By normalizing to the low temperature data, we see to a good approximation that the temperature dependence of A_{SPM} is independent of q and λ_i, as it should be.

We now turn to the area of the low frequency mode, I_+. To extract $A_\pm$, we first remove the λ dependence by normalizing by the measured value of A_{SPM} at low temperature. The result is shown in Fig. 6.8 We now find

$$\frac{I_+^{(003)}}{I_{\text{SPM}}^{(003)}} = \frac{A_+}{A_{\text{SPM}}} \tag{6.3}$$

$$\frac{I_+^{(101)}}{I_{\text{SPM}}^{(101)}} = \frac{1-(\hat{q}^y)^2}{1-(\hat{q}^z)^2}\frac{A_+}{A_{\text{SPM}}}, \tag{6.4}$$

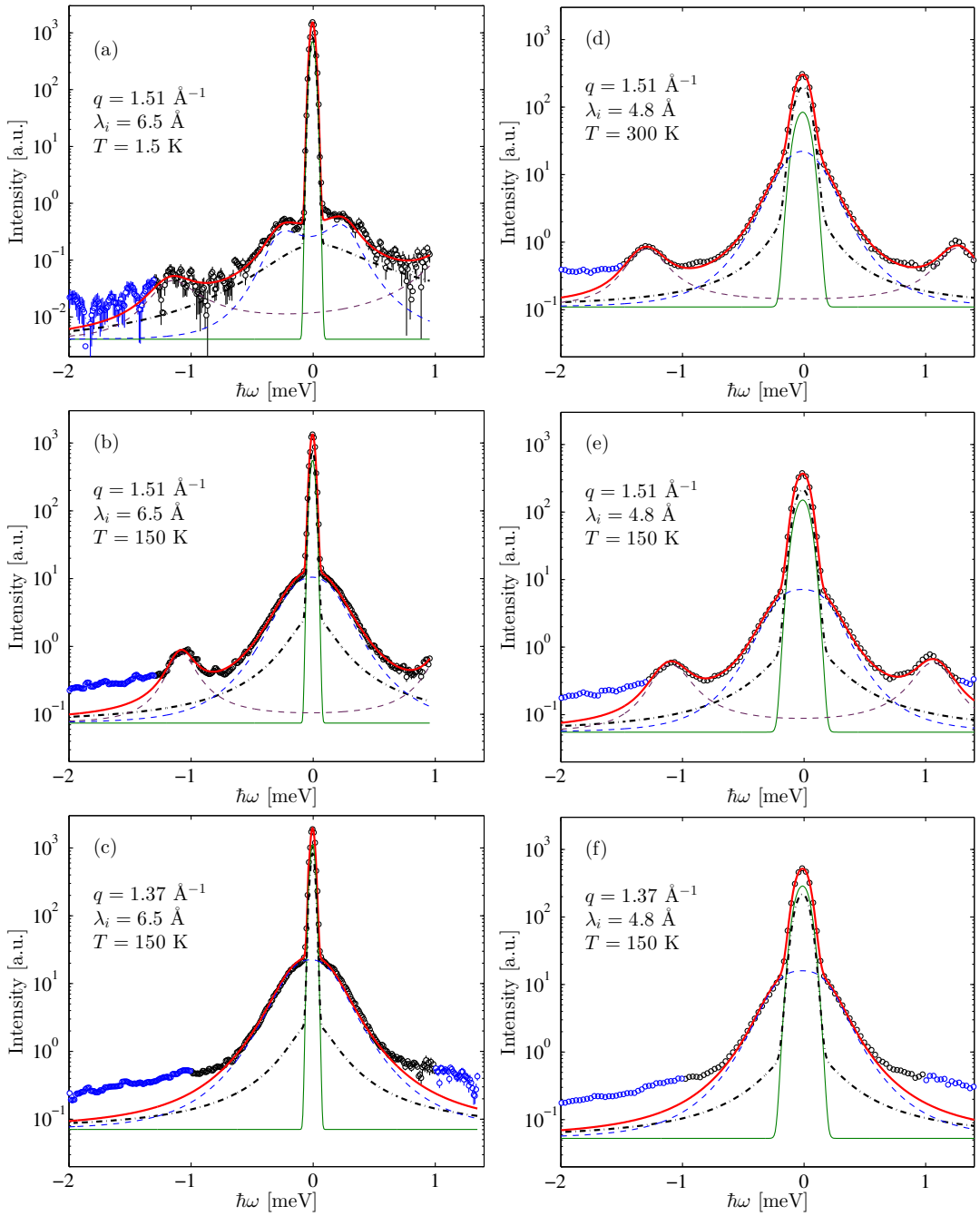

FIGURE 6.6: IN5 data at various temperatures for the 16 nm nanoparticles. The data used for the fit are shown with black circles, blue circles show data excluded from the fit. The incoherent signal is shown by black dashed lines, the magnetic signal with solid green, and the low- and high-frequency mode with dashed blue and purple, respectively. The left column row is for $\lambda_i = 6.5$ Å, the right for $\lambda_i = 4.8$ Å. Note that the bottom part of the scale at 1.5 K is much smaller than at the other temperatures. (a) shows the low temperatur data. (b) and (c) show data at 150 K at the two magnetic peak positions. The signals are similar, except for the presence of the high frequency mode at $q = 1.51$ Å^{-1}. (b) and (e), and (c) and (f) show the difference between the high- and low-resolution data at the two magnetic peaks. Finally, (d) shows the signal at 300 K, where a much larger fraction of the total scattering is inelastic.

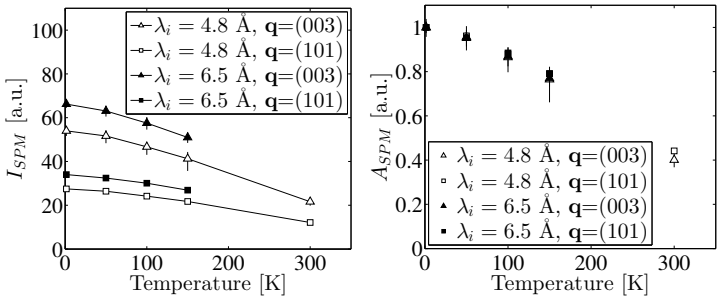

FIGURE 6.7: Left: the observed intensity, I_{SPM} and right: the extracted values of A_{SPM} as function of temperature for the different wavelengths and q-values that were measured at IN5. Left: The raw data. Right: The data normalized to the low temperature data. A_{SPM} is seen to be independent of λ and $\mathbf{q}$, as expected.

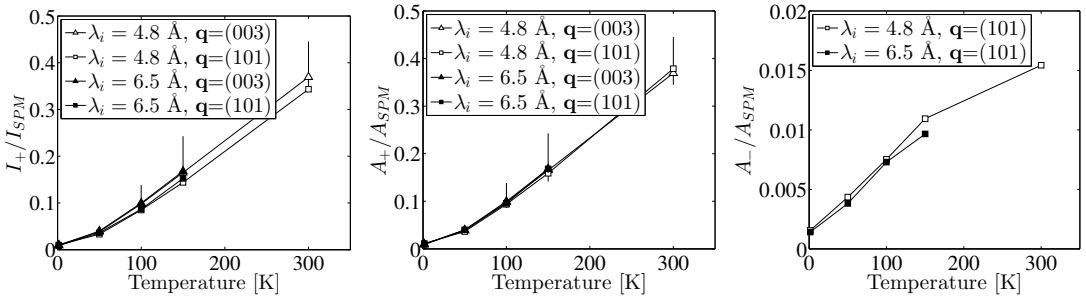

FIGURE 6.8: The areas of the two modes. $A_{\pm}$. Left figure shows the results of incorrect normalization of the + mode, $I_+/I_{\mathrm{SPM}}(1.5\ \mathrm{K})$, center shows the correct value and right figure shows the high frequency mode.

where $\hat{q}^y$ ($\hat{q}^z$) is the component of the (101) vector along the y (z) direction in the basal plane. Unfortunately, the spin direction within the basal plane in hematite is, to the best of my knowledge, unknown. We have assumed that the spins are exactly in the basal plane, and that the low frequency mode is purely along y. We know x is aligned along the crystallographic c axis, but not how y and z are oriented compared to the crystallographic axes. However, the orientations can be estimated using the present data. We can calculate $1-(q^x)^2 = 0.9085$. We can rewrite the above equations to

$$\frac{I_+^{(101)}}{I_+^{(003)}}\frac{I_{\mathrm{SPM}}^{(003)}}{I_{\mathrm{SPM}}^{(101)}} = \frac{2-(1-(\hat{q}^x)^2)-(1-(\hat{q}^z)^2)}{1-(\hat{q}^z)^2}, \tag{6.5}$$

or

$$1-(\hat{q}^z)^2 = \frac{2-(1-(\hat{q}^x)^2)}{1+\frac{I_+^{(101)}}{I_+^{(003)}}\frac{I_{\mathrm{SPM}}^{(003)}}{I_{\mathrm{SPM}}^{(101)}}} = 0.573(17), \tag{6.6}$$

where the measured intensities have been inserted. The uncertainty given is the standard deviation of the calculation for all the different temperatures and wavelengths that have been measured. We further find

$$1-(\hat{q}^y)^2 = 0.519(17). \tag{6.7}$$

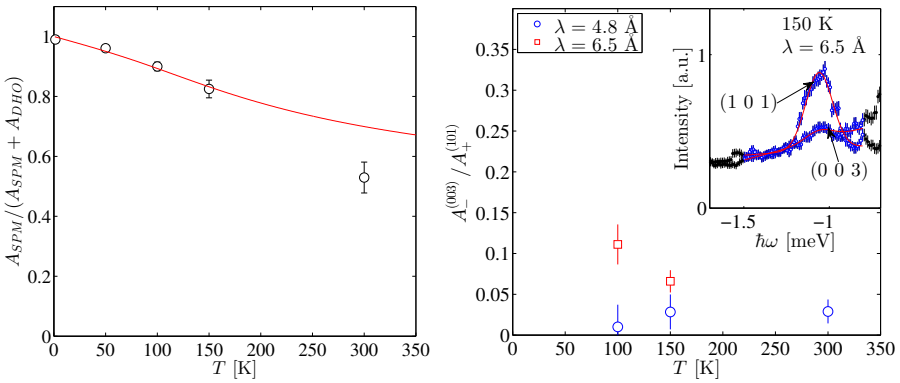

FIGURE 6.9: Left: The average value of $A_{\mathrm{SPM}}/(A_{\mathrm{SPM}}+A_{\mathrm{DHO}})$ as function of temperature. The line through the data points is the best fit to Eq. (3.87), where the values of K_1V found from $\hbar\omega_\pm$ is used. With this assumption, the fit gives $K_2V = 624(65)$ K. Right: $I_-^{(003)}/I_+^{(101)}$. The data have been normalized by I_{SPM}. The peak is barely visible above the background at 100 K at the (003) peak, and not at all at lower temperatures. The inset shows an example of the fit.)

The normalization of the data we shall use is thus

$$\frac{A_+}{A_{\mathrm{SPM}}(1.5\ \mathrm{K})} = \frac{I_+^{(003)}}{I_{\mathrm{SPM}}^{(003)}(1.5\ \mathrm{K})} = 1.10\frac{I_+^{(101)}}{I_{\mathrm{SPM}}^{(101)}(1.5\ \mathrm{K})} \tag{6.8}$$

$$\frac{A_-}{A_{\mathrm{SPM}}(1.5\ \mathrm{K})} = 0.630\frac{I_+^{(101)}}{I_{\mathrm{SPM}}^{(101)}(1.5\ \mathrm{K})}. \tag{6.9}$$

The result of this normalization is shown in Fig. 6.8.

In Fig. 6.9, $A_{\mathrm{SPM}}/(A_{\mathrm{SPM}}+A_{\mathrm{DHO}})$ is plotted, along with a fit to Eq. (3.87),with K_1V fixed to the value given below. The fit gives $K_2V = 624(65)$ K.

We now investigate the ellipticity of the high frequency mode. As is apparent from Fig. 6.1, the high frequency mode is just visible at the (003) peak. We find $I_-^{(003)}/I_+^{(101)} \approx 0.04(1)$. This is smaller than the value of 0.11 observed in [11], and shows that the modes indeed are highly elliptic.

We now move on to the frequencies of the two modes, see Fig. 6.10. The frequency of the low frequency mode decreases with temperature, which is a known effect, see Eq. (3.84). The high frequency mode initially slightly decreases in frequency, and then increases. This increase can only be explained by an increase in the absolute value of the in-plane anisotropy, κ_1. This increase is observed for both the nanoparticles and the mesoporous particles.

The frequencies have been fitted simultaneously to Eqs. (3.48) and (3.49), with the temperature dependence given by Eq. (3.84) and $B_X = 900\ T$ and $B_D = 2.1$ T. The temperature dependence of κ_1 has been chosen as an even fourth order polynomial, as used in [19], and κ_2 is assumed to be constant.

We find $\kappa_2 = 1.34(1)$ mK, corresponding to $B_2 = 3.99(3)$ mT. Assuming $N = 8.51 \times 10^4$, this translates into $K_2V = 570$ K. The uncertainty on this value is by far determined by the uncertainty in N.

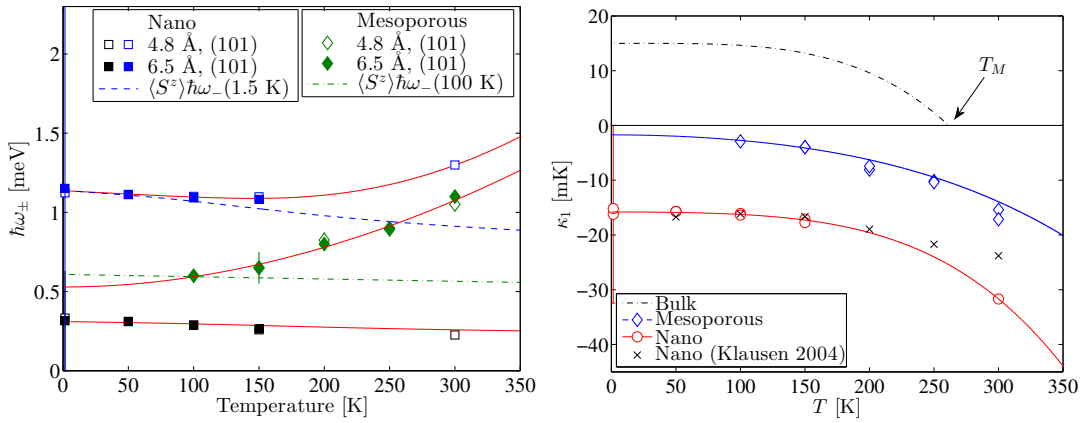

FIGURE 6.10: Left: The frequencies of the low and high frequency mode in nanoparticles and mesoporous particles. Also shown is the temperature dependence of $\langle s^z \rangle$ and fits to Eqs. (3.47) and (3.48), with the temperature dependence given by Eq. (3.84). Right: The temperature dependence of κ_1. The tendency is the same for nano, mesoporous and bulk particles. It is seen that κ_1 does not change sign for the mesoporous and the nanoparticles.

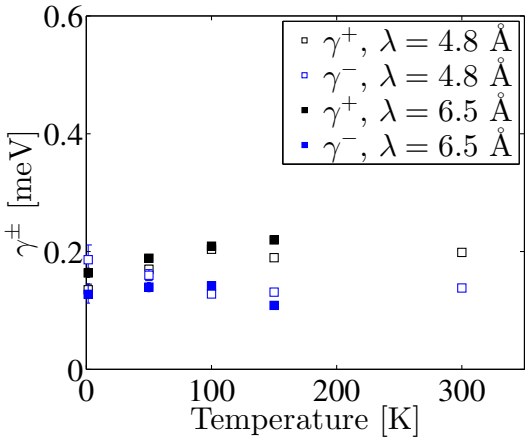

FIGURE 6.11: The width $\gamma_\pm$ of the two modes measured on 16 nm particles.

The extracted values of κ_1 are shown as function of temperature in Fig. 6.10. At 0 K, the value $\kappa_1 = -15.8(1)$ mK is found, corresponding to $B_1 = -47.0(4)$ mT. As before, this yields $K_1 V = 6.72 \times 10^3$ K. The results are in agreement with those obtained in Ref. [11] at lower temperatures. At elevated temperatures, they assume $s^z \approx 1$, which

The final parameters to investigate are the widths of the two modes, $\gamma_\pm$. They are shown in Fig. 6.11. The low frequency mode in general is wider than the high frequency mode. Also, the width seems to increase with temperature, whereas it remains roughly constant for the high frequency mode. The widths are fairly consistent between the measured wavelengths. In [9], the width was found to decrease with temperature.

6.2.2 Modeling mesoporous particles data from IN5

We now turn to the mesoporous sample. The same fitting procedure as for the nanoparticles has been applied, but with no success. We will here briefly show the attempt. The

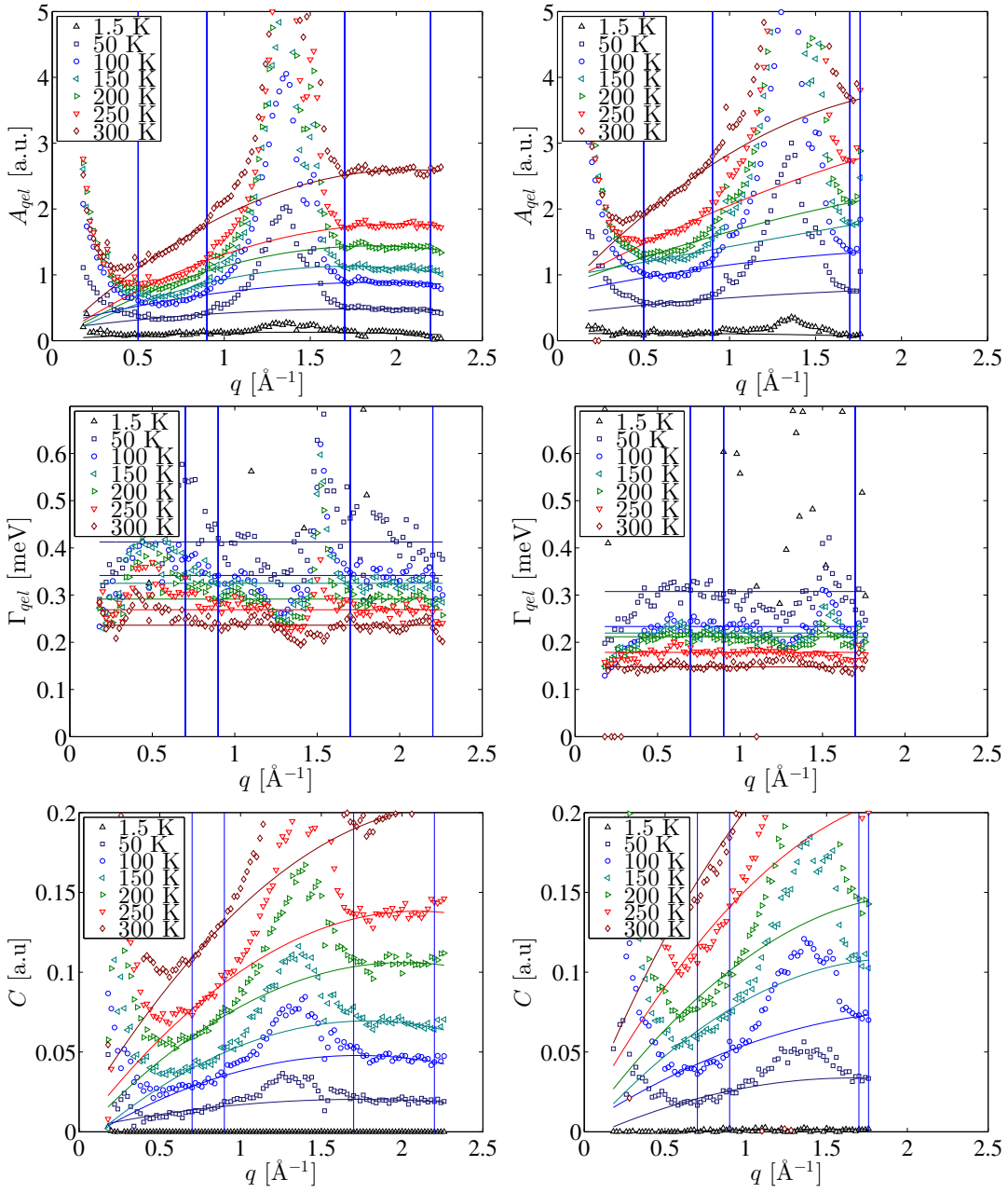

FIGURE 6.12: Some of the parameters describing the incoherent signal for the mesoporous particles. Every point is the result of a fit as described in the text. The left column shows the parameters for $\lambda_i = 4.8$ Å, right for $\lambda_i = 6.5$ Å. Disregarding the lowest q-values and the q-range near the magnetic peaks, the area of the Lorentzian is seen to increase with q and temperature, the width is approximately constant in q and the background increases with q. The solid lines show fits to polynomials of first or second order to the data within the vertical lines.

incoherent signal is quite easy to fix, and follows the same trend as the nanoparticles, as seen in Fig. 6.12.

The magnetic signal at $\mathbf{q} = (101)$ and $\mathbf{q} = (003)$ from the IN5 data is shown in Fig. 6.13. We see a broadening of the elastic line, and clear peaks at $\hbar\omega \approx 1$ meV.

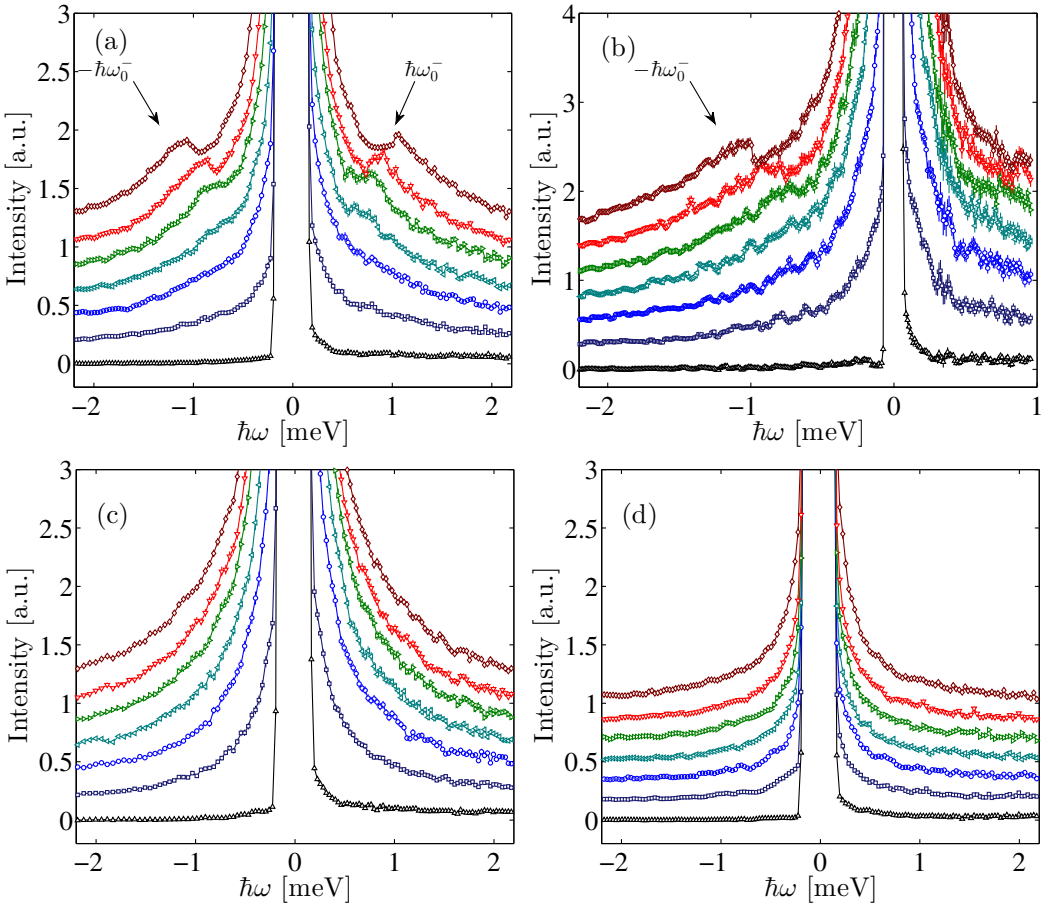

FIGURE 6.13: Temperature dependence of the mesoporous α-Fe_2O_3 spectra at (a) $q = 1.51$ Å^{-1}, with $\lambda_i = 4.8$, (b) $q = 1.51$ Å^{-1}, with $\lambda_i = 6.5$, showing the evolution of the high frequency mode at ≈ 1 meV (300 K). Spectra are arranged from 300 K (top) in steps of 50 K to 10 K (bottom) offset from each other for clarity. (c) shows the signal at $q = 1.37$ Å^{-1}, with $\lambda_i = 4.8$ and (d) shows the signal at $q = 0.9$ Å^{-1}, with $\lambda_i = 4.8$. In (a)-(c) a magnetic signal is clearly seen above the background in (d).

The broadening of the elastic line is of magnetic origin and is not due to superparamagnetism, as was shown by Mössbauer spectroscopy [31]. This is also confirmed by the backscattering data presented in the next section.

However, the magnetic signal cannot be modeled by the same procedure as the nanoparticles can. This is probably due to the hybrid nature of the mesoporous material: it is more bulk-like than the nano-particles, but the high frequency mode still shows distinct peaks indicating quantized spin waves.

The attempts at fitting the data are shown in Fig. 6.14. Although the fits look fairly good, the parameters are senseless. The "width" and "position" of the innermost DHO have values greater than 20 meV, which is completely unphysical, and signifies a breakdown of the model. Additionally, the outer lying DHO significantly overestimates the value of $\hbar\omega_-$, as seen in Fig. 6.14(d).

The frequency of the high frequency mode has therefore been extracted by eye from the data in Fig. 6.13. The same analysis as applied to the nanoparticles still yields good

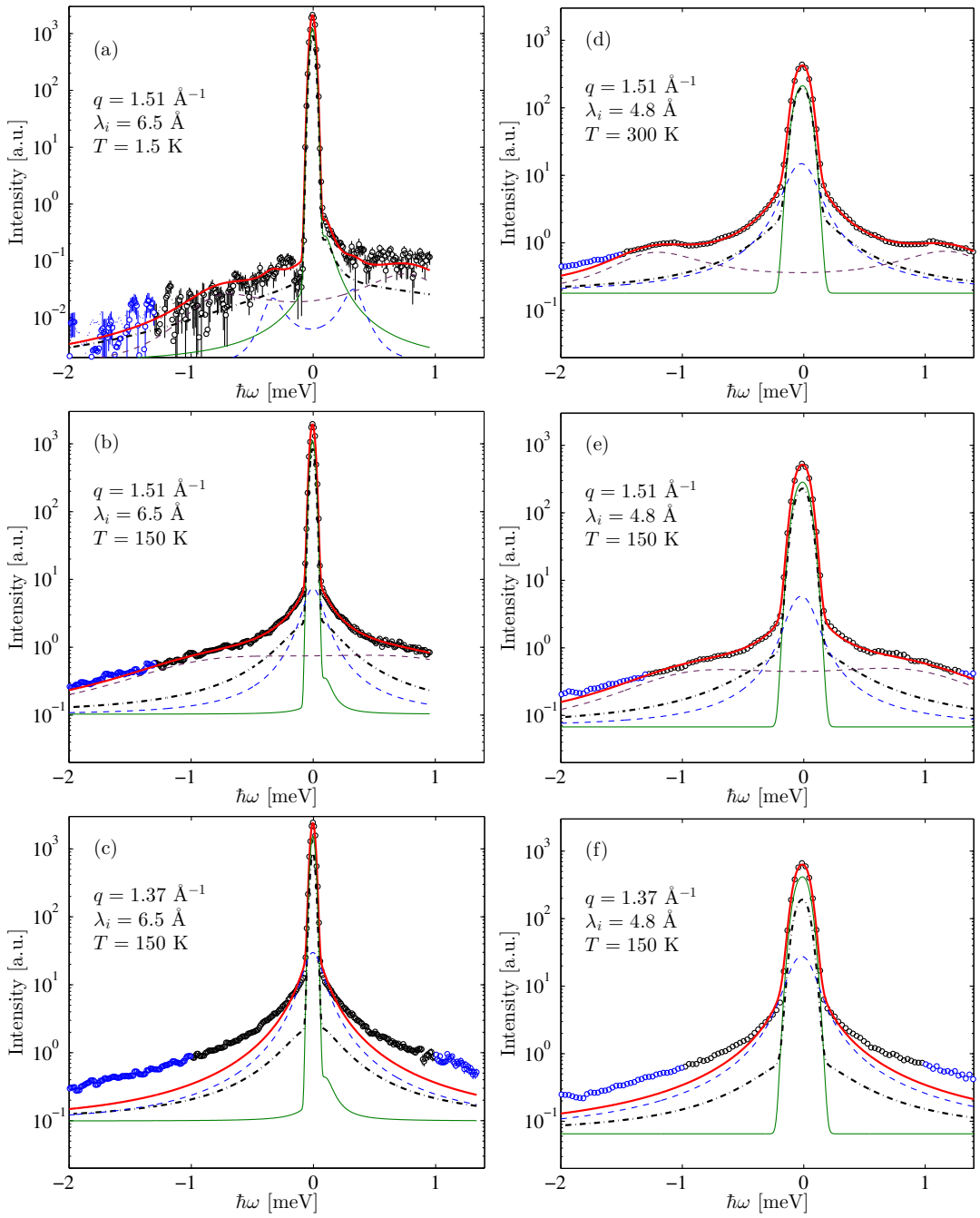

FIGURE 6.14: IN5 data at various temperatures for the mesoporous particles. The data used for the fit are shown with black circles, blue circles show data excluded from the fit. The incoherent signal is shown by black dashed lines, the magnetic signal with solid green, and the low- and high-frequency mode with dashed blue and purple, respectively. The left column row is for $\lambda_i = 6.5$ Å, the right for $\lambda_i = 4.8$ Å. Note that the scale at 1.5 K is much smaller than at the other temperatures. (a) shows the low temperatur data. (b) and (c) show data at 150 K at the two magnetic peak positions. The signals are similar, except for the presence of the high frequency mode at $q = 1.51$ Å^{-1}. (b) and (e), and (c) and (f) show the difference between the high- and low-resolution data at the two magnetic peaks. Finally, (d) shows the signal at 300 K, where a much larger fraction is inelastic.

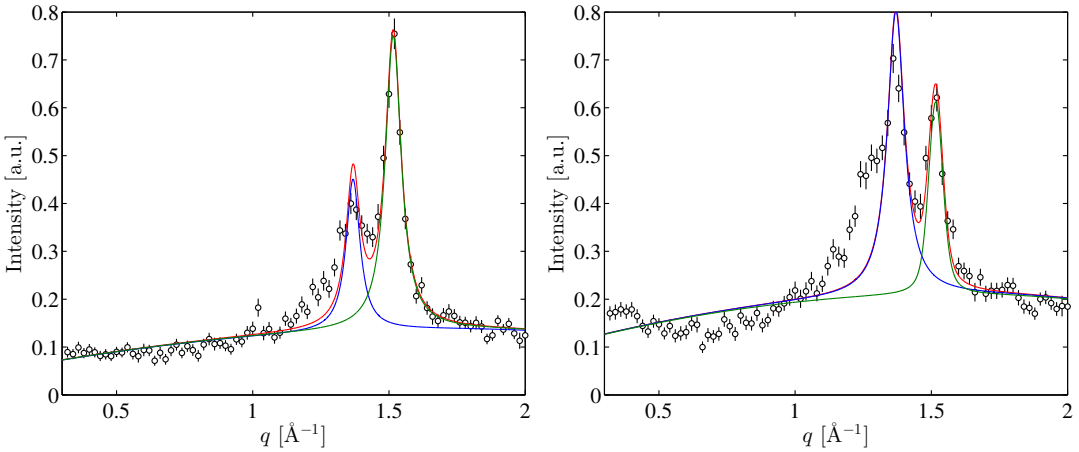

FIGURE 6.15: Examples of the IN5 data at constant $\hbar\omega = 1.1$ meV for the nanoparticles (left) and the mesoporous particles (right) at 150 K for $\lambda_i = 4.8$ Å. Extra intensity is seen at low q; the (003) peak is asymmetric.

estimates of the temperature dependence of κ_1, as shown in Fig. 6.10.

6.2.3 Alternative analysis method of IN5 data

In the analysis presented above, we have chosen to fit the background by making cuts at constant $\hbar\omega$. We could also have made cuts in the other direction, and fitted the data as function of q for fixed values of $\hbar\omega$. The area of the peaks as function of $\hbar\omega$ would ideally correspond to the purely magnetic signal. The data would then be fitted with a background function and a peak function for the magnetic signal. In most cases, this procedure yields results that are identical to the procedure described above. However, there are several difficulties, which make this model impractical. Several thousand fits must be made, and thus inspection and correction of each fit is not feasible. The fitting procedure must thus be quite robust. But the signal varies drastically as function of $\hbar\omega$: Near $\hbar\omega = 0$ the signal is very different from the inelastic signal. The q dependence of the inelastic background is quite complicated and difficult to model. Thirdly, the peaks are quite close in q which further complicates the analysis. Finally, the peaks are not as simple as expected. An example of such a fit is shown in Fig. 6.15.

In both the nanoparticles and the mesoporous particles, an extra signal is seen at q slightly smaller than the (003) peak position at $q = 1.37$ Å^{-1}. The origin of this peak is unknown. The asymmetric shape of the peak could be a signature of short ranged magnetic correlations, as seen in e.g. frustrated magnetic materials. [66]. However, it is apparent that this simple fit neither gives a good estimate of the background nor of the peak amplitude. Time did not allow to pursue this further.

Another advantage to sticking to fitting the background by making cuts at constant $\hbar\omega$ is consistency. The the method is applicable to all the other data sets to be presented in this thesis, whereas fitting along q requires a data set of the size of IN5 data.

IN10	Mesoporous	1.5	50	—	150	200	250	300	350	400
	16 nm	1.5	50	100	150	200	250	300	350	—
IN16b	16 nm	2	—	—	150	—	250	—	—	—

TABLE 6.3: Overview of the temperatures (in K) that have been measured at the IN10 and IN16b experiments.

6.3 High resolution data on 16 nm and mesoporous particles measured at IN10 and IN16b

The quasi-elastic features of the mesoporous and nanoparticulate samples were studied using the backscattering instrument IN10 at the ILL [60], with incident energy $E_i = 2.08$ meV ($\lambda_i = 6.27$ Å). The instrument uses Si (111) analyzers and has 7 detectors, located at $q/\text{Å}^{-1}$=(0.38, 0.75, 1.08 1.37, 1.68, 1.85, 1.96), with $\hbar\omega$ range of ± 12 μeV. The energy resolution was found from low temperature measurements of the sample. It could be accurately modeled by a Gaussian with Lorentzian tails and a second, smaller Gaussian which was slightly displaced in energy. The FWHM was approximately 1.0 μeV.

Data were collected for the nanoparticle sample at 1.5 K, 50 K, 100 K, 150 K, 200 K, 250 K, 300 K and 350 K, while the mesoporous were measured at 1.5 K, 50 K, 150 K, 200 K, 250 K, 300 K, 350 K and 400 K. An overview of the temperatures is given in Table 6.3

The excitations $\hbar\omega_\pm$ could not be observed within the energy window of IN10, and below around 150 K, almost no broadening of the peaks are seen in either detector, i.e. $A_{\text{qel}} \approx 0$. At 150 K motion of water sets in and gives rise to a quasi-elastic broadening in all detectors. Around this temperature, the magnetic signal at $q = 1.37$ Å^{-1} also starts to broaden.

The quasi-elastic features of the nanoparticulate sample were further studied using the newly commissioned backscattering instrument IN16b at the ILL [62, 67], with incident energy $E_i = 2.08$ meV ($\lambda_i = 6.27$ Å). The instrument uses Si (111) analyzers and has 16 detectors, with an energy range of ± 30 μeV. The energy resolution was found from low temperature measurements of the sample to be mostly Gaussian with a FWHM of 0.8 μeV, but with small Lorentzian tails. Data were collected at 2 K, 150 K and 250 K.

The IN10 and IN16b background data are quite similar. An example of the background measured at IN16b at two different values of q is shown in Fig. 6.16. The background was fitted to Eq. (6.1). For the IN10 data, the quasi-elastic signal was only included at temperatures above 150 K, and the constant signal was only included at temperatures below 150 K.

The temperature dependence of some of the incoherent parameters in the IN16b experiment is shown in Fig. 6.17. These parameters were fixed in the same way as for the IN5 experiments, with the change that only first order polynomials were used, due

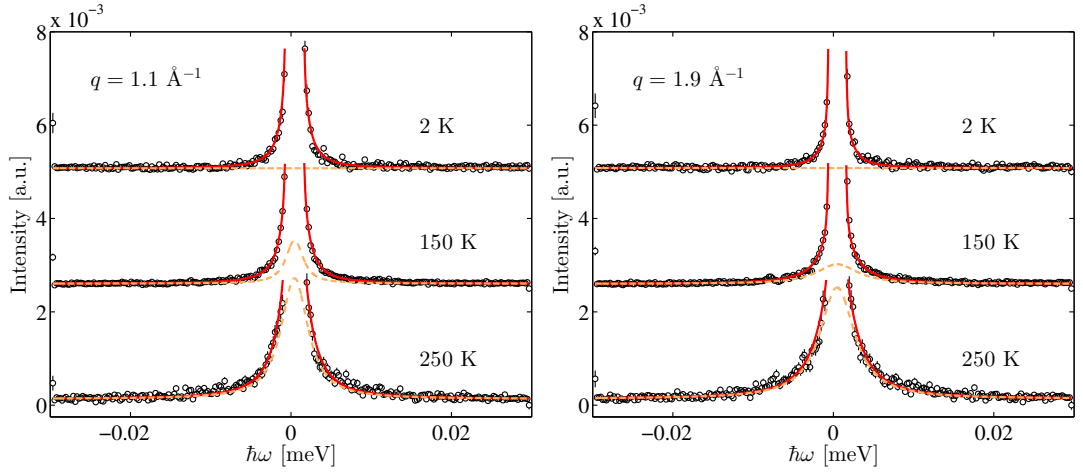

FIGURE 6.16: The incoherent signal at IN16b for the 16 nm particles. The dashed line shows the Lorentzian part of the signal.

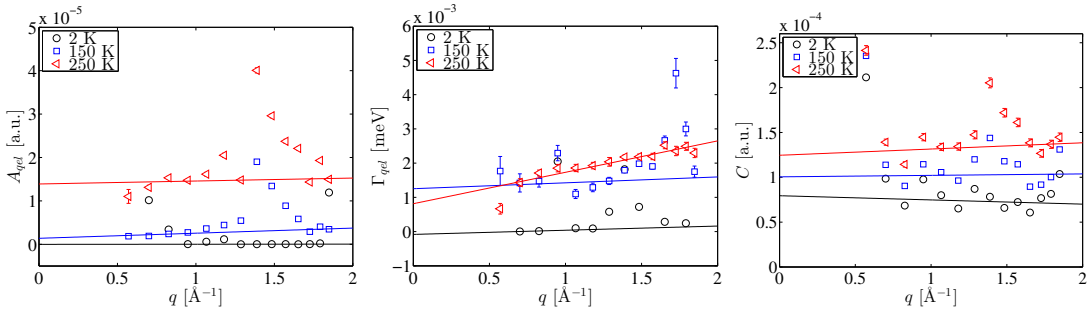

FIGURE 6.17: The area, width and and background of the incoherent signal in the IN16b experiment. The error bars at 1.5 K are rather large and obscure the plot, so they are not shown.

to the small amount of detectors. It should be noted that the final fit of the magnetic signal is not very sensitive to the exact values of the parameters.

The magnetic signal has been fitted with Eq. (6.2) without the DHOs. Example fits for the IN10 and IN16b data are shown in Fig. 6.18

The extracted values of Γ are shown in Fig. 6.19. The line through the data is a fit to the Néel-Brown law, with the parameters $K_2V = 726(200)$ K and $\tau_0 = 5.4(5) \times 10^{-12}$ s.

6.4 Polarized experiment on mesoporous particles at D7

As shown in section 6.2.3 about the IN5 data, the inelastic mesoporous data show an odd symmetry as function of q. We got a single day of beamtime to investigate this with polarized neutrons at D7, ILL. It was unfortunately necessary to use a different sample than the one used in the IN5 experiment. However, initial characterization, as described in section 2.4.3 showed that the new sample was similar to the previous sample.

Polarized neutrons provide a unique opportunity to investigate the sample without the huge background from water adsorbed on the surface of the particles. As we have

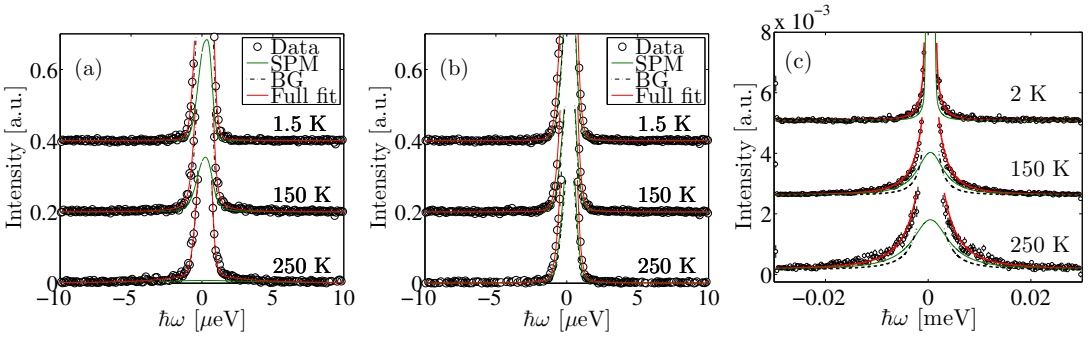

FIGURE 6.18: Example of data from IN10 and IN6b at several temperatures at $q = 1.37$ Å^{-1}. (a) shows the nanoparticle sample, where the broadening of the magnetic signal with temperature is visible. At 250 K, the signal is so broad that it is hard to distinguish from the background. (b) shows the mesoporous sample, where no such broadening is seen. (c) Shows the data from IN16b for the nanoparticle sample.

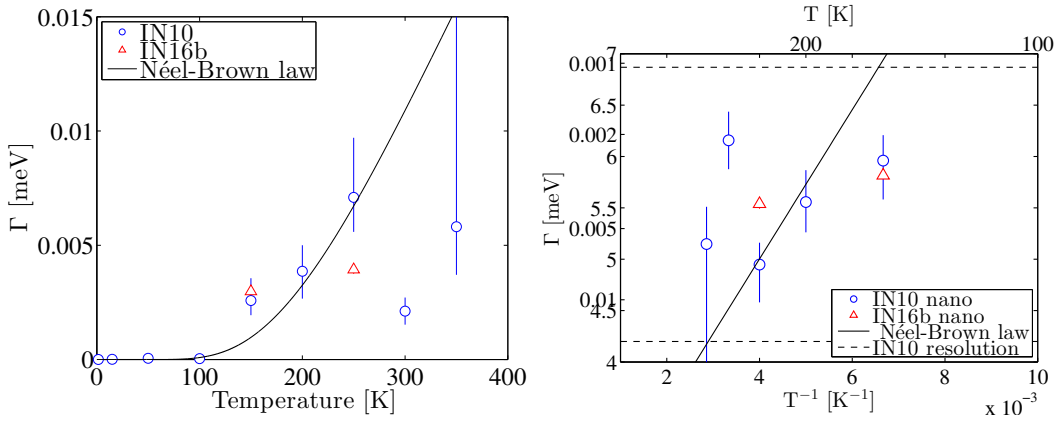

FIGURE 6.19: The width Γ of the magnetic signal measured in the IN10 and IN16b experiments along with a fit to Eq. (3.83).

seen, the incoherent scattering from hydrogen provides a large background and complicates the analysis. For this experiment, the instrument had been calibrated for elastic measurements, and it was therefore not possible to investigate inelastic scattering in this experiment.

The wavelength chosen was $\lambda = 3.12$ Å. This allowed the probing of q within $0.14 - 3.91$ Å^{-1}. The resolution was determined using a standard scatterer (YIG) and was found to be Gaussian with a q-dependent FWHM of ≈ 0.07 Å^{-1}.

The sample was loaded in a 1 mm thick hollow cylinder, to minimize multiple scattering. The transmission was found to be 86%. Measurements were performed at 1.5 K, 100 K, 200 K, 250 K and 300 K.

The different contributions to the scattering at 1.5 K are shown in Fig. 6.20. Also shown is the magnetic signal at all temperatures, as well as the total fit to this signal. The magnetic contribution has been fitted with Voigt functions, with the Gaussian width set equal to that of the resolution function. The Lorentzian broadening is due to the finite size of the structure.

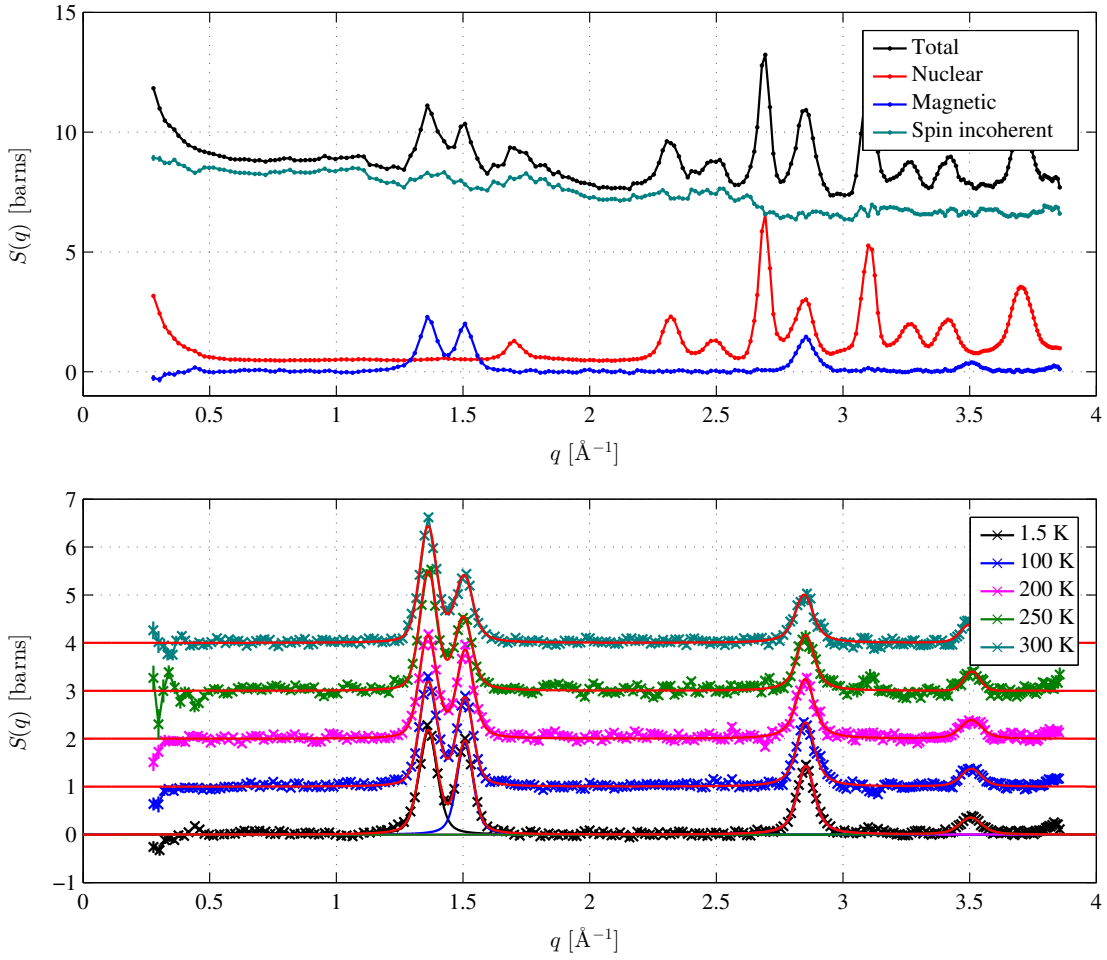

FIGURE 6.20: (a) The components of the measured signal at 1.5 K. (b) The magnetic signal for every temperature. The magnetic contribution has been fitted with Voigt functions, with the Gaussian width set equal to that of the resolution function. The Lorentzian broadening is due to the finite size of the structure. The data have been displaced for clarity.

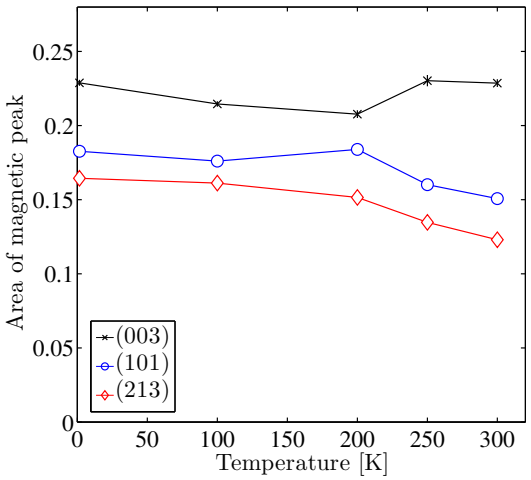

FIGURE 6.21: The integrated area of the magnetic peaks as function of temperature. A change in behavior is seen near 200 K.

In Fig. 6.21 we show the integrated area under the magnetic peaks as function of temperature. Here we see a transition happening near 250 K, with an effect similar to the Morin transition. The effect is, however, quite small.

We have found no sign of elastic diffuse magnetic scattering in the mesoporous hematite sample. The question about the nature of the asymmetry of the inelastic scattering is still unresolved, and requires additional measurements to be answered.

The sample showed hints of a Morin transition, which has been shown previously to be suppressed in mesoporous hematite. One possible explanation of this could be bulk impurities in the sample.

Another conclusion to be drawn from this experiment is that the incoherent background is indeed quite complicated to model. Also, the small angle scattering is nuclear, and is thus not related to the water adsorbed to the surface of the particles.

We now turn to experiments on the 8 nm particles.

6.5 8 nm particles measured at DMC and RITA-II

As described earlier, two sets of 8 nm nanoparticles have been investigated. In the experiments on DMC and RITA-II, the coated nanoparticles were used, As described in the previous chapter, DMC is a two axis spectrometer, which therefore measures the energy integrated signal. The result of measurements here are plotted in Fig. 6.22, where the background has been subtracted. The first three peaks are seen at the expected positions, and the intensities drop slightly with temperature because of the Debye-waller factor.

The diffraction signal from the same sample was subsequently measured at RITA-II, as also shown in the figure. In an initial scan,, only the elastic signal is measured, and we see a remarkable difference between the two temperatures. The nuclear $(10\bar{2})$ peak is nearly unchanged, from 10 K to 300 K, but the magnetic signals disappear. This means that within the resolution of RITA-II, most of the magnetic signal has become inelastic at 300 K.

The inelastic features were also measured at RITA-II with $E_f = 3.7$ meV and a BeO filter after the sample. The data were taken before the upgrade to multiple blades, i.e. with a single detector. Data were taken at 10 K, 50 K, 100 K, 150 K, 190 K, 240 K, 276 K and 300 K. Background measurements were performed at $q = 0.93$ Å^{-1} and $q = 1.83$ Å^{-1}. The same fitting procedure as described previously has been used, except that background interpolation was simpler, as described below. The resolution was found to be Gaussian with an asymmetric half-Lorentzian tail with a FWHM of approximately 0.12 meV. The resolution can be difficult to determine at the magnetic peaks because of the magnetic excitations. We have assumed that the excitations are so small that they have negligible influence on the apparent resolution. Examples of fits to the incoherent signal are shown in Fig. 6.23

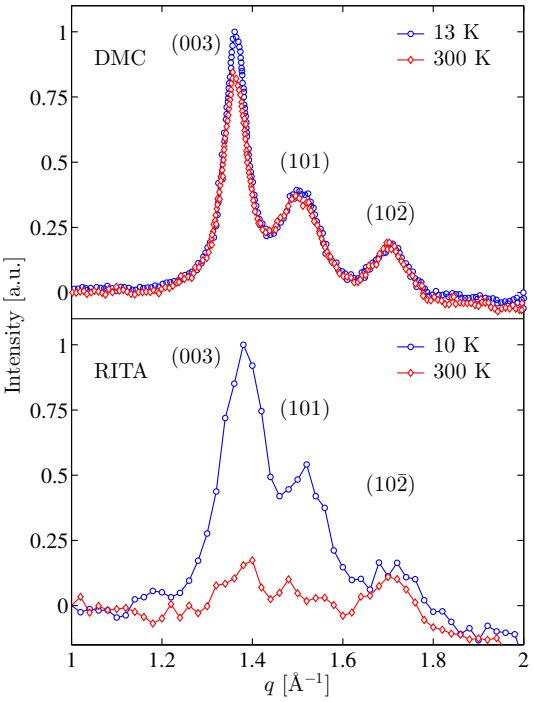

FIGURE 6.22: Neutron diffraction data around the (003) AFM Bragg peak in coated 8 nm hematite nanoparticles from DMC and RITA-II.

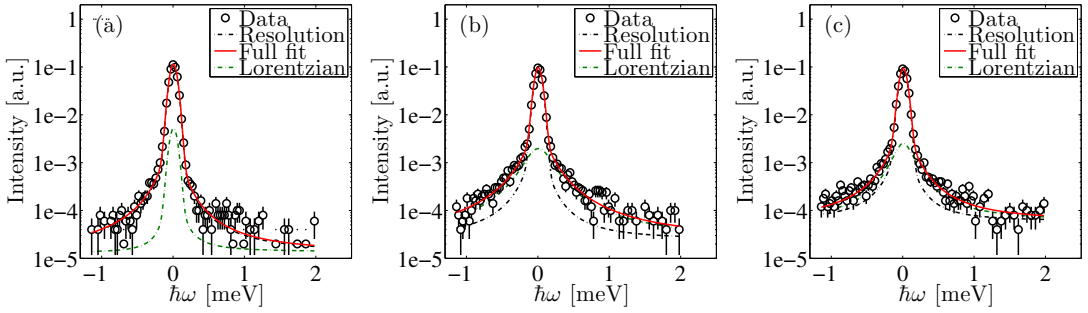

FIGURE 6.23: Fits to the incoherent signal from RITA experiment on coated 8 nm particles at (a) $q = 0.93$ Å^{-1}, $T = 10$ K, (b) $q = 0.93$ Å^{-1}, $T = 190$ K and (c) $q = 1.83$ Å^{-1}, $T = 190$ K.

The background parameter C is also very q-dependent, especially at higher temperatures, and can therefore not be determined accurately from just two q values. It was thus kept free in the fits.

Examples of fits of the magnetic signal can be seen in Fig. 6.25.

The values of A_{SPM} and A_+ are shown in Fig. 6.26. The solid lines are fits to Eq. (3.87), assuming $|K_1 V| \gg K_2 V$. The fit to $A_{\mathrm{SPM}}/(A_{\mathrm{SPM}} + A_+)$ gives $K_2 V = 157(11)$ K. Assuming $N = 1.06 \times 10^4$, this gives $\kappa_2 = 2.9(2)$ mK or $B_2 = 8.81(3)$ mT.

The excitation energy of the low frequency mode is shown in Fig. 6.27. It increases with temperature, in contrast with the 16 nm particles. This result was unexplained until recently, but can be understood in terms of the rotor mode, Sec. 3.7: at elevated temperatures, the motion gradually shifts from the two $q = 0$ modes towards the rotor

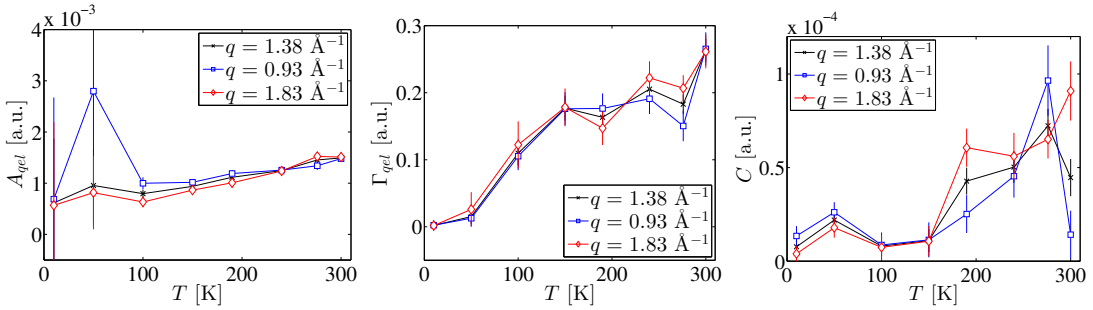

FIGURE 6.24: Incoherent parameters from RITA experiment on 8 nm particles. The parameters at $q = 1.38$ Å^{-1} are found by a weighted average of the two background measurements.

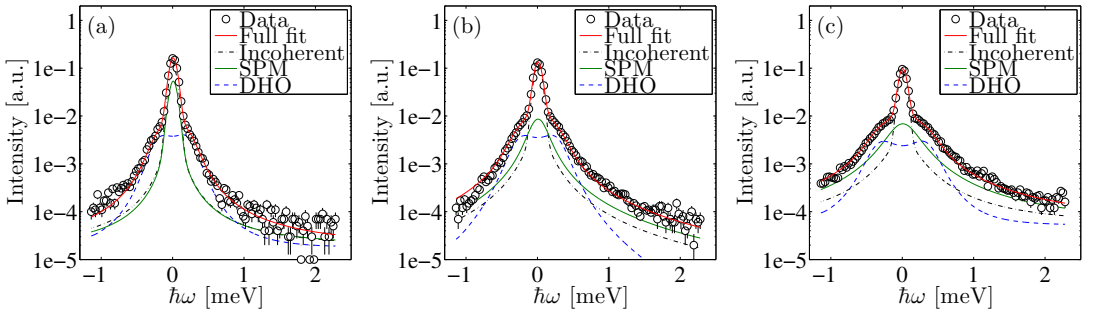

FIGURE 6.25: Fits of the magnetic signal from the RITA-II experiment on 8 nm particles at (a) 50 K, (b) 150 K and (c) 300 K.

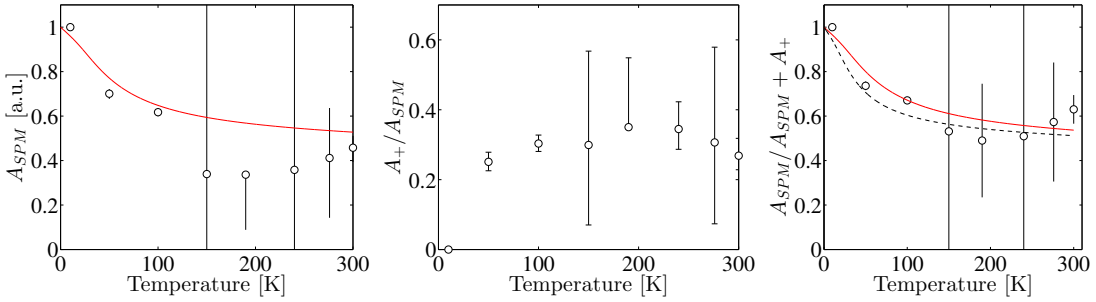

FIGURE 6.26: The values of A_{SPM} and A_+ on the 8 nm particles. Left: The value of A_{SPM}. Center: The value of A_+. Right: $A_{\mathrm{SPM}}/(A_{\mathrm{SPM}} + A_+)$. The solid lines are fits to Eq. (3.87), assuming $|K_1 V| \gg K_2 V$. The

mode. The effect will be described more thoroughly in the next chapter. In the figure, we have plotted the fit to Eq. (3.84). We find $\kappa_2 = 1.47$ mK, which is very close to the value for 16 nm particles. This gives an energy barrier of $K_2 V = 78$ K. The frequency of the rotor mode, Eq. (3.108) is also plotted

The width of the SPM signal, Γ, is significantly larger than for the 16 nm particles, as shown in Fig. 6.27. At temperatures above 200 K, the peak is so broad that it is barely visible. This is reflected in the relative area of this peak compared to the total magnetic signal, which has large uncertainties at elevated temperatures. It is seen to increase with temperature, but the uncertainties are quite large. Analysis of the width is postponed to the next section describing backscattering measurements on the same

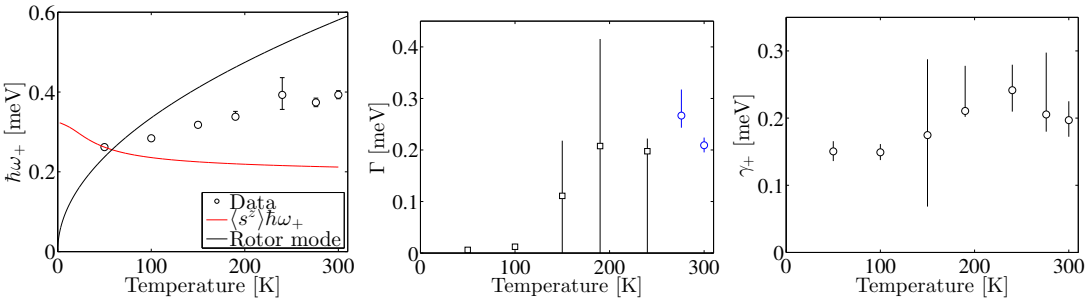

FIGURE 6.27: The temperature dependence of the magnetic parameters for coated 8 nm particles measured at RITA-II. (a) shows the excitation energy, $\hbar\omega_+$, (b) the width of the SPM signal Γ, and (c) shows the width of the DHO, γ_+. In (b), the data at highest temperature are unreliable, since almost no signal is seen.

particles.

Finally, the width of the DHO, γ_+ appears to increase slightly with temperature. The values are consistent with 16 nm particles measured at IN5.

6.6 8 nm particles measured at BSS

Backscattering measurements were performed at BSS in Julich.

6.6.1 The experimental setup

The wavelength of the neutrons used was $\lambda = 6.271$ Å. BSS has 14 detectors in total, but several of them are not useful for this work. The interesting detectors for our purpose are detector 2 to 6, that are placed at $q/$ Å^{-1}= 1.87, 1.72, 1.52, 1.28, 1.02, each covering around 0.2 Å^{-1}. It is seen that detector 3 is placed on the structural $[10\bar{2}]$ peak, detector 4 is placed on the magnetic [101] peak and detector 5 is placed on the [003] peak. There are more detectors at smaller q, but these cannot be used due to the increased background from small angle scattering. The detector at $q = 1.02$ Å^{-1}, already suffers from this problem, so much that it cannot be used to determine the background. This means only the detector at 1.9 Å^{-1} can be used to determine the background.

Experiments were performed on two different powder samples of 8 nm hematite nanoparticles. One as prepared (FD), where there is a strong interparticle (exchange) interaction, and one where the particles had been individually coated with phosphate thus reducing these interactions significantly (PO). In [30], it was shown that due to the interaction between these particles, the uncoated sample forms small clusters of 2-4 nanoparticles, thereby effectively increasing the size of the particles.

In total, measurements were performed at the following temperatures for around 12 hours each: PO: 4K, 25K, 50K, 75K, 100K, 125K, 150K, 175K, 250K, 295K. FD: 4K, 50K, 100K, 150K, 175K (twice), 225K, 275K, 295K. An overview is given in Table 6.4

Furthermore, vanadium was measured at 4 K for both experiments. Also, measurements were performed at temperatures 4 K, 14 K,...,294 K for roughly 1 hour each on

FD	april	—	—	—	—	—	—	—	175	225	295
	september	4	—	50	—	100	—	150	175	275	—
PO	april	4	—	—	75	100	125	—	175	—	295
	september	—	25	50	—	—	—	150	—	250	—

TABLE 6.4: Overview of the temperatures (in K) measured at the BSS experiment.

both samples with the Doppler drive turned off. This was to determine the temperature dependence of the intensity of the elastic signal.

The raw data were converted by Christian Bahl to intensity vs. energy for each detector using standard routines at the spectrometer. No initial normalization or background subtraction has been done.

The vanadium measurements have been used to find the resolution function for each detector. It was found to be adequately described by a Gaussian with Lorentzian tails, and a second Gaussian displaced slightly from the first. The FWHM is estimated to be 1.2 μeV, but the tails are clearly distinguishable from the background in a range of roughly 5 μeV.

The intensity of the elastic line on the measurements of vanadium is different on each detector. At 4 K, the Debye-Waller factor is approximately 1 for all q, and since vanadium scatters almost purely incoherently [45], the data have been normalized such that the area of the incoherent elastic signal for vanadium is the same for all detectors. The uncertainty in the area of the incoherent elastic peak from vanadium is approximately 1% and therefore unimportant in the following.

6.6.2 Elastic scattering

In Fig. 6.28 the intensity of elastic scattering as a function of temperature is shown. For the coated particles, the intensity at the magnetic peaks falls quickly at low temperatures, and near 80 K it is on par with the background. Near 150-200 K a change in the slope of the background is seen. For the uncoated particles, the magnetic intensity is noticeably larger than the background until around 200 K. At 200 K, the background changes character. This is the dynamics of water that sets in, with the incoherent scattering becoming quasielastic and moving out of the window of BSS.

The difference between the change of the slope at 200 K for the two samples means that for the uncoated sample, motion of water is more important than for the coated sample. This is probably related to the formation of clusters mentioned earlier.

For the coated sample, the intensity decreases sharply at the magnetic peaks already around 20 K, which means that the DHO and SPM get activated. Thus the DHO and SPM are important at all temperatures for this sample. At temperatures above 100 K, the behavior is indistuingishable from the structural and non-magnetic peaks. Therefore, it is expected that the magnetic signal is almost purely quasi-elastic or inelastic here.

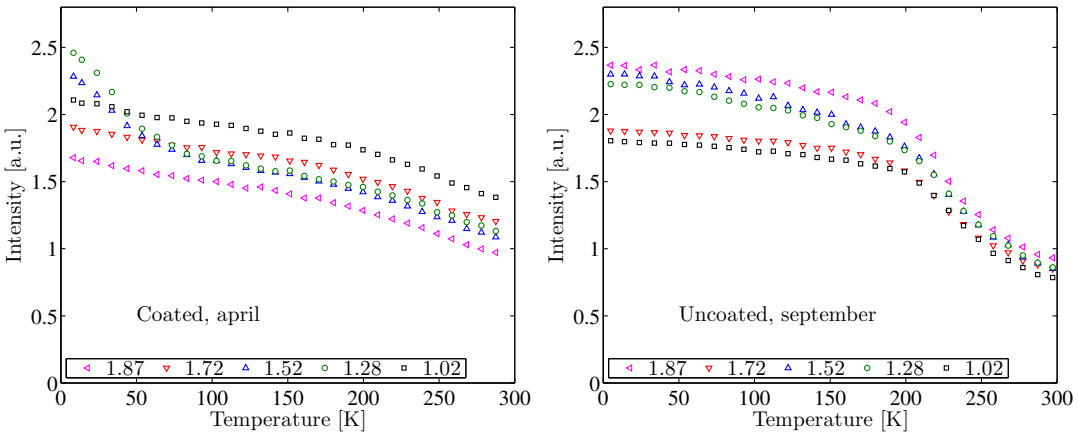

FIGURE 6.28: Measurements of the elastic line on 8 nm particles at BSS. Left: The coated particles. The intensity at the magnetic peaks falls quickly at low temperatures. Near 200 K a change in the slope of the background is seen. Right: The uncoated particles. Here, the magnetic intensity is noticeably larger than the background until around 200 K. At 200 K, the background changes character.

For the uncoated sample, the decrease of the magnetic signal is not so fast, but still present, meaning that also here, magnetic dynamics get activated.

6.6.3 Quasielastic scattering

The incoherent signal is very difficult to treat in this experiment. The nano-particles are half as large as those measured at IN5, and a rough estimate tells us that the small angle scattering is important in a q-range that is twice as large, i.e. up to around $q = 1$ Å^{-1}. [1] This is also apparent in Fig. 6.28 where it is seen that the area of the elastic incoherent peak at $q = 1.1$ Å^{-1} is much larger than at $q = 1.9$ Å^{-1}. At the IN5 experiment, Section 6.2, it was found that apart from the small angle scattering, the elastic incoherent signal is nearly constant in q. It was also shown that, although the quasielastic part and the background are q dependent, they saturate to constant values for large q. This will be assumed to be true for these particles as well, and therefore only detector 2 ($q = 1.9$ Å^{-1}) will be used to fix the incoherent signal.

At temperatures below 200 K, the incoherent signal will be modeled by an elastic line and a constant background:

$$I_{\text{incoh}}^{T<200\text{ K}} = A_{\text{el}}\delta(\epsilon) + C, \tag{6.10}$$

Where A_{el} is the area of the elastic peak and C is a constant. Above 200 K, a Lorentzian will be used instead of the constant:

$$I_{\text{incoh}}^{T\geq200\text{ K}} = A_{\text{el}}\delta(\epsilon) + D(\epsilon)\frac{A_{\text{qel}}}{\pi}\frac{\Gamma_{\text{qel}}}{\Gamma_{\text{qel}}^2 + \epsilon^2}, \tag{6.11}$$

[1] The small angle scattering approximation is $qa \ll 2\pi$, where a is a typical distance [45].

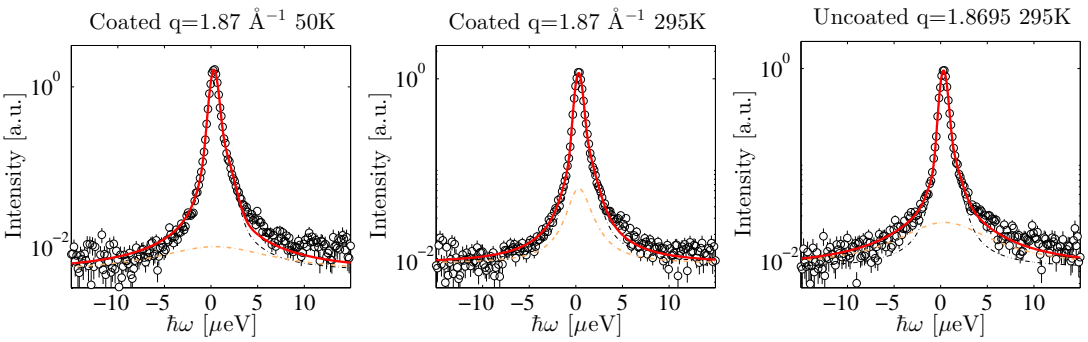

FIGURE 6.29: Examples of the fits of the incoherent signal at various temperatures.

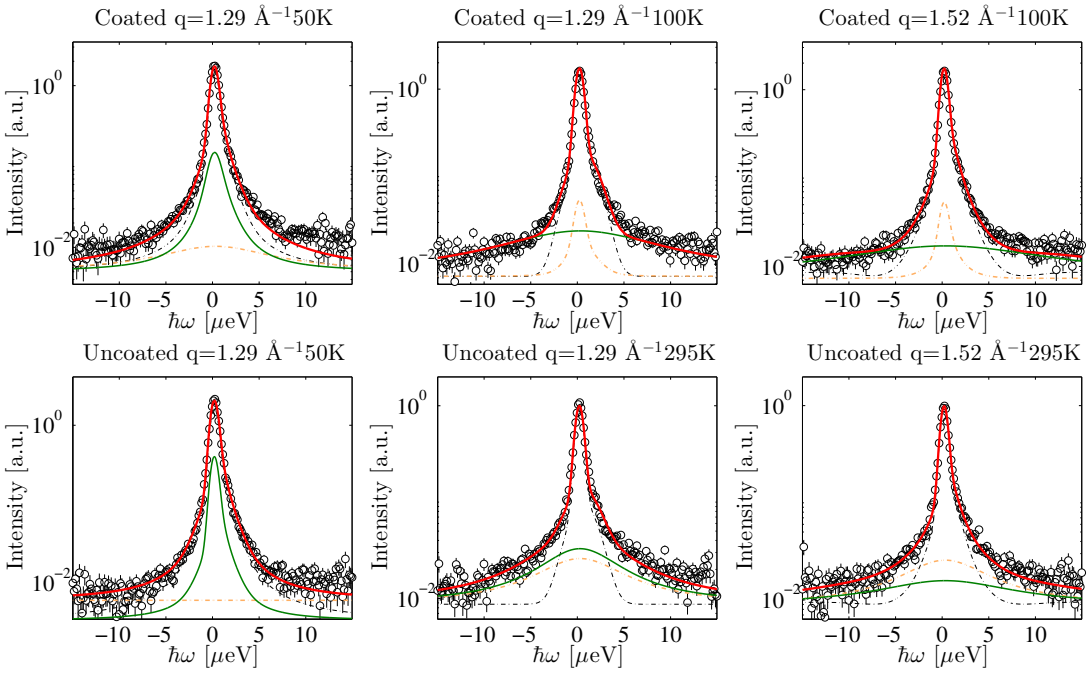

FIGURE 6.30: Examples of fits to the magnetic signal from BSS.

where A_{el} is the area of the elastic peak, $D(\epsilon)$ is the detailed balance factor and A_{qel} and Γ_{qel} are the area and HWHM of the quasi–elastic peak. The addition of a constant background was not needed. In the fitting procedure, I_{incoh} is convoluted with the resolution function. Examples of the fits to the incoherent signal are shown in Fig. 6.29.

The magnetic signal has been fitted with Eq. (6.2) without the DHOs. Example fits are shown in Fig. 6.30 The extracted values of Γ are shown in Fig. 6.31. For the coated particles, we see the width increasing with increasing temperature, and the data follows the Néel-Brown law quite clearly, with $K_2V = 98(9)$ K and $\tau_0 = 2.2(2) \times 10^{-11}$ s. This is in good agreement with the value $K_2V = 78$ K obtained from the value of $\hbar\omega_+$ from the RITA-II data.

For the uncoated particles, the results are less clear. A broadening appears at higher temperatures, but the data quality is too poor to make definite conclusions. This is due to interactions between the particles, as described in [12, 30].

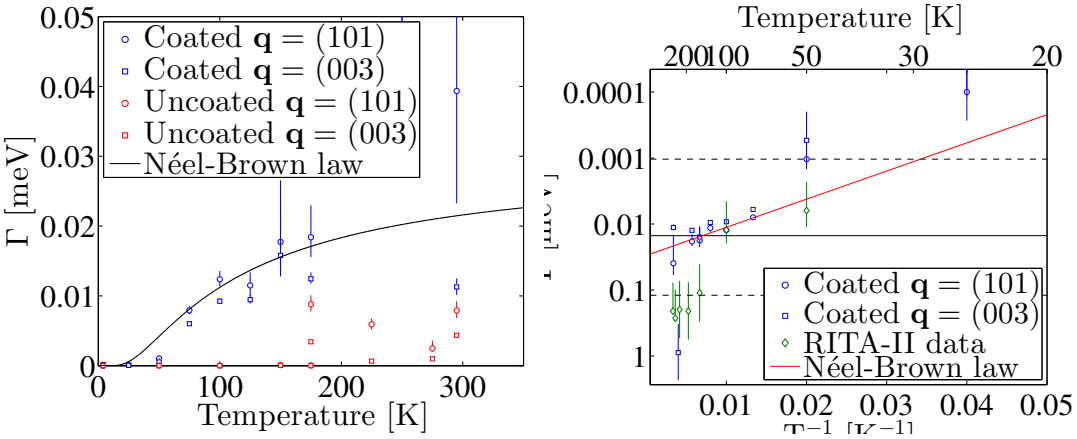

FIGURE 6.31: The width of the SPM signal in the 8 nm particles measured at BSS. The the figure to the right, the data from RITA have been included. The dashed black lines indicate the resolution of BSS and RITA, while the solid black line indicates the energy maximum of BSS.

6.7 Conclusions

Before moving on to the simulations, it is worthwhile to pause and get an overview of the results presented in this chapter.

Data from D7 on mesoporous particles confirm that the high background observed in all experiments indeed is spin incoherent scattering from hydrogen, due to water adsorbed on the surface of the particles.

In the 16 nm particles, both the high and low frequency mode have been observed simultaneously. The frequency of the high frequency mode first decreases with temperature, and subsequently increases. This can be interpreted as an increase in the absolute value of the anisotropy constant, $|\kappa_1|$. The low frequency mode decreases with temperature. The fraction of inelastic intensity compared to elastic intensity increases with temperature.

The spin direction within the basal plane in the 16 nm particles was determined. SPM broadening of the peaks is observed with backscattering measurements at IN10 and IN16b. The Néel-Brown law gave $K_2V = 726(200)$ K with $\tau_0 = 0.54(5) \times 10^{-11}$. The temperature window within which the broadening can be observed is very narrow, and there is a rather large uncertainty in the observed values, primarily due to the high background. For the 16 nm particles, the easy axis anisotropy constant was found in the IN5 experiment to be $\kappa_2 = 1.34(1)$ mK, corresponding to $B_2 = 3.99(1)$ mT. Assuming $N = 8.51 \times 10^4$, this translates into $K_2V = 570$ K. The uncertainty on this value is by far determined by the uncertainty in N. A 10% uncertainty seems reasonable. The value of κ_1 at low temperatures was found to be $\kappa_1 = -15.8(1)$ mK, corresponding to $B_1 = -47.0(1))$ mT or $K_1V = 6.72 \times 10^3$ K. Using the relative area of the excitations we found $K_2V = 624(66)$ K.

In the 8 nm particles, the low frequency mode is observed. We find that the frequency increases with temperature, contrary to the 16 nm particles. This can be explained by

the onset of the rotor mode. SPM broadening is observed with both triple axis measurements and backscattering. For the coated particles, where inter particle interactions are minimized, the broadening increases with temperature. For the uncoated particles, no clear results can be extracted from the backscattering measurements. We also find, for the coated particles, that the magnetic scattering becomes almost purely inelastic within the resolution of RITA-II. Again, this is explained by the rotor mode.

The energy barrier was found using the relative areas to be $K_2V = 157(11)$ K. This translates into $\kappa_2 = 2.96(2)$ mK, $B_2 = 8.81(3)$ mT. The Néel-Brown law gave $K_2V = 98(9)$ K and $\tau_0 = 2.2(2) \times 10^{-11}$ s. From the measurements of the low frequency mode we found, assuming $\xi = 1$ that $\kappa_2 = 1.47$ mK, which is very close to the value for 16 nm particles. This gives an energy barrier of $K_2V = 77.9$ K.

In the mesoporous particles, only the high frequency mode was observed. The frequency was found to increase with temperature, which as for the 16 nm particles can be seen as an increase in $|\kappa_1|$. Backscattering measurements confirm the absence of SPM broadening of the elastic peak.

An overview of all the parameters is given in Table. 7.2

Chapter 7

Simulations

Numerical simulation is an incredibly powerful tool which becomes more and more used in all areas of physics. Simulations complement theory and experiments very well: In theory we must, as we have seen in previous chapters, make many simplifying assumptions to reach analytically computable results. This limitation is not necessary to the same extent for simulations, allowing us to probe the effect of various interactions where our analytical tools fall short. The most important effect here is temperature, which is included as random fluctuations. This type of simulations is named Langevin simulations.

Simulations can provide unique insight into phenomena that are unreachable to us as experimentalists. Simulations give us direct control of most of the parameters that can affect our results.

The first version of this simulation tool was written in MATLAB by Jacob Garde and described in great detail in his Masters thesis [34]. The simulations were inspired by Ref. [68] who simulated ferromagnetic nanoparticles.. I have extended the work by Garde by 1) Implementing the uncompensated moment of spins 2) Implementing the DM-interaction 3) Correcting minor errors and numerical values and 4) Speeding up the code by roughly a factor 300.

In this chapter I will first outline the derivation of the equations of motion that are being numerically integrated. Next follows an explanation of how this integration is done, as well as how to relate the simulations to experiments. The simulations are validated by some simple test cases, and are then compared to the data. The input parameters are adjusted to best match the data, and the numerous results of the simulations are described.

7.1 Implementation

In the simulations we model the nanoparticles as two superspins, as already described in Chapter 3. We numerically integrate Eqs. (3.68) and (3.69), where we now reinserted

$\hbar$ for completeness:

$$\frac{\mathrm{d}\mathbf{s}_A}{\mathrm{d}t} = \gamma \mathbf{s}_A \times \mathbf{B}^A_{\text{eff}}, \tag{7.1}$$

$$\frac{\mathrm{d}\mathbf{s}_B}{\mathrm{d}t} = \gamma \mathbf{s}_B \times \mathbf{B}^B_{\text{eff}}, \tag{7.2}$$

where

$$\mathbf{B}^A_{\text{eff}} = \xi B_X \mathbf{s}_B - \mathbf{B} - \begin{pmatrix} B_1 s^x_A \\ 0 \\ B_2 s^z_A \end{pmatrix} + \xi B_D \begin{pmatrix} 0 \\ s^z_B \\ -s^y_B \end{pmatrix}, \tag{7.3}$$

$$\mathbf{B}^B_{\text{eff}} = B_X \mathbf{s}_A - \mathbf{B} - \begin{pmatrix} B_1 s^x_B \\ 0 \\ B_2 s^z_B \end{pmatrix} - B_D \begin{pmatrix} 0 \\ s^z_A \\ -s^y_A \end{pmatrix}. \tag{7.4}$$

These equations, however, are valid only at 0 K. To add temperature effects we couple the two macrospins to a heat bath. The calculations are described in detail in Ref. [34] and briefly outlined in the appendix, Chapter C. The idea is to modify Eqs. (7.1) and (7.2) to include temperature effects. This is done by adding a small, random fluctuation term and a corresponding damping term. The resulting equations are

$$\frac{\mathrm{d}\mathbf{s}_A}{\mathrm{d}t} = \gamma \mathbf{s}_A \times (\mathbf{B}^A_{\text{eff}} + \mathbf{b}_A) - \lambda \gamma \mathbf{s}_A \times (\mathbf{s}_A \times \mathbf{B}^A_{\text{eff}}), \tag{7.5}$$

$$\frac{\mathrm{d}\mathbf{s}_B}{\mathrm{d}t} = \gamma \mathbf{s}_B \times (\mathbf{B}^B_{\text{eff}} + \mathbf{b}_B) - \lambda \gamma \mathbf{s}_B \times (\mathbf{s}_B \times \mathbf{B}^B_{\text{eff}}), \tag{7.6}$$

where $\mathbf{b}$ is a random fluctuating field, and $\lambda \ll 1$ is a damping term. The fluctuations are uncorrelated in time, and the amplitude is such that the total energy of the system remains constant. This is done by utilizing the fluctuation-dissipation theorem [69].

The relationship between $\mathbf{b}$ and λ is

$$\langle b^i_A(t) b^j_A(t') \rangle = 2 \frac{\lambda}{\gamma g \mu_B s N_A} k_B T \delta^{ij} \delta(t - t'). \tag{7.7}$$

One important thing to notice here is that we have implemented temperature in absolute units. It is thus possible to directly compare the simulations to the experiments described in the previous chapter. It is also interesting to note from this equation that e.g. doubling the particle size exactly corresponds to halving the temperature.

As mentioned above, we numerically integrate Eqs. (7.5) and (7.6). This gives a real space trajectory for each spin, which can be related to experiments by Fourier Transforming, as will be described later. The integration method used is the second order Runge-Kutta method [53], in which we have $\mathbf{s}_{i+1} = \mathbf{s}_i + \Delta\mathbf{s}_i$, with

$$\Delta\mathbf{s}_i = \left(\frac{1}{2} \frac{\partial \mathbf{s}_i}{\partial t} + \frac{1}{2} \frac{\partial \mathbf{s}'_{i+1}}{\partial t} \right) \Delta t + \gamma \mathbf{s} \times \Delta \mathbf{b} \tag{7.8}$$

where

$$\mathbf{s}'_{i+1} = \mathbf{s}_i + \Delta t \frac{\partial \mathbf{s}_i}{\partial t} \tag{7.9}$$

and $\Delta\mathbf{b}$ are random numbers following a Gaussian distribution with variance

$$\langle \Delta(b_A)^2 \rangle = 2\frac{\lambda}{\gamma g \mu_B s N_A} k_B T \Delta t. \tag{7.10}$$

After each step, the spins are renormalized to length 1, to avoid buildup of errors during the simulations. Typical simulations in this thesis are 100 ns with a timestep of 1 fs.

7.2 Relating simulations to experiments

A power spectrum is defined as

$$P^\alpha(\omega) = \left| \frac{1}{T} \int_0^T \mathrm{d}t \, e^{\mathrm{i}\omega t} s^\alpha(t) \right|^2, \tag{7.11}$$

where $s^\alpha(t)$ is the α'th component of the spin at time t. The power spectrum is thus the absolute square of the Fourier Transform of the spins.

The Wiener-Kinchin theorem states that [48]

$$\langle P^\alpha(\omega) \rangle = \frac{1}{T} \int_0^T \mathrm{d}t \, e^{\mathrm{i}\omega t} \langle s^\alpha(0) s^\alpha(t) \rangle, \tag{7.12}$$

where T is the total simulation time. It is useful to note that the power spectrum of e.g. one 10 ns simulation to a good approximation is equal to the sum of 10 simulations of each 1 ns. This is useful since the RAM usage of calculating these Fourier Transforms numerically can exceed what is readily available on a home computer.

We recall from Eq. (5.30) that

$$\frac{\mathrm{d}^2\sigma}{\mathrm{d}\Omega \mathrm{d}E_f} \propto C(\mathbf{q}) \sum_{\alpha\beta} \left(\delta^{\alpha\beta} - \hat{q}^\alpha \hat{q}^\beta \right) \int_{-\infty}^{\infty} \mathrm{d}t \, e^{-\mathrm{i}\omega t} \left\langle s^\alpha(0) s^\beta(t) \right\rangle, \tag{7.13}$$

where $C(\mathbf{q})$ includes the magnetic form factor and structure factor, and we ignored the atomic positions, since they are irrelevant for the simulations.

From this, it is evident that the power spectra, which are calculated from the simulated trajectories of the spins, can be compared with experiments. To be concrete, we have the two relations

$$\left(\frac{\mathrm{d}^2\sigma}{\mathrm{d}\Omega \mathrm{d}E_f} \right)_{(003)} \propto C((003))(P^y + P^z), \tag{7.14}$$

$$\left(\frac{\mathrm{d}^2\sigma}{\mathrm{d}\Omega \mathrm{d}E_f} \right)_{(101)} \propto C((101))(0.9085P^x + 0.519P^y + 0.573P^z), \tag{7.15}$$

where the numerical values are from Section 6.2. These relations make it possible to directly compare experiments and simulations.

The simulated data will be modeled in the same way as the real data. We thus use the following model:

$$I_{\text{sim}} = \frac{A_{\text{SPM}}}{\pi}\frac{\Gamma}{\Gamma^2 + (\hbar\omega)^2} + \sum_{\pm}\frac{A_{\pm}}{\pi}\frac{2\gamma_{\pm}(\hbar\omega_{\pm})^2}{\left((\hbar\omega)^2 - (\hbar\omega_{\pm})^2\right)^2 + 4\gamma_{\pm}^2(\hbar\omega)^2}. \tag{7.16}$$

The normalization is done in the exact same way as for the experiment.

Another very useful tool for analyzing the simulations is to directly look at the time evolution of the spins. This provides insight into the actual motion of the spins, and will be used from time to time in the following.

7.3 Validation

A number of parameters can be adjusted in the simulations. Some are physical constants that must be found by comparing the simulations to experiments: the total number of spins, $N_A + N_B$, the uncompensated moment, $\xi = N_B/N_A$, the strength of the applied magnetic field, $\mathbf{B}$ and of the effective fields B_X, B_1, B_2, and B_D, and the damping parameter, λ. Others are more artificial, but equally important. These include the time step Δt in the simulations, the total simulation time T and the time of each simulation part, ΔT. Finally, as we shall see, the simulated data must be convolved with a resolution function with a certain width, σ, and this must also be chosen carefully. It is of course vital that all these parameters have the correct values.

We will first validate the implementation of the code by comparing with analytic results. This also serves as a demonstration of the effect of some of the parameters in the model.

7.3.1 Exchange driven precessions

Let us consider the effect of the exchange term only, with no damping at zero temperature. The motion described here is similar to the rotor mode described in Sec. 3.7, except that a small angle approximation is made in that derivation. This restriction is easily lifted in the simulations.

Considering only the exchange term at zero temperature, we have

$$\frac{\mathrm{d}\mathbf{s}_A}{\mathrm{d}t} = \gamma B_X \mathbf{s}_A \times \mathbf{s}_B, \tag{7.17}$$

$$\frac{\mathrm{d}\mathbf{s}_B}{\mathrm{d}t} = \gamma B_X \mathbf{s}_B \times \mathbf{s}_A. \tag{7.18}$$

We thus see that if the spins are not antiparallel, they will precess in the plane perpendicular to $\mathbf{s}_A \times \mathbf{s}_B$, which we here take as the x-axis. Without loss of generality, we can

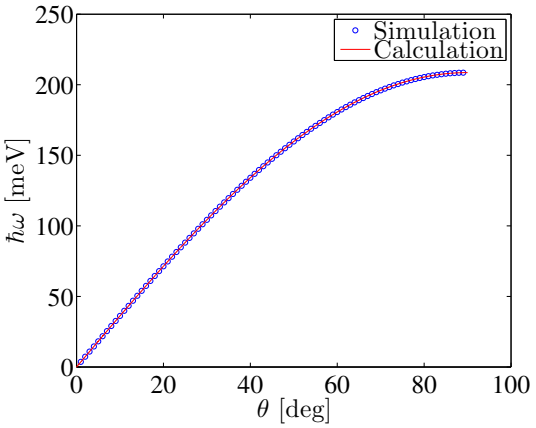

FIGURE 7.1: The precession frequency as function of deviation angle, θ for two spins coupled only by the exchange field, $B_X = 900$ T.

assume that the spins cant by the same angle, θ:

$$\mathbf{s}_A = (\sin(\theta), \cos(\theta)\sin(\omega t), \cos(\theta)\cos(\omega t)), \tag{7.19}$$

$$\mathbf{s}_B = (\sin(\theta), -\cos(\theta)\sin(\omega t), -\cos(\theta)\cos(\omega t)), \tag{7.20}$$

which leads to

$$\frac{\mathrm{d}\mathbf{s}_A}{\mathrm{d}t} = \begin{pmatrix} 0 \\ \omega\cos(\theta)\cos(\omega t) \\ -\omega\cos(\theta)\sin(\omega t) \end{pmatrix} = \gamma B_X^A \begin{pmatrix} 0 \\ 2\sin(\theta)\cos(\theta)\cos(\omega t) \\ -2\sin(\theta)\cos(\theta)\sin(\omega t) \end{pmatrix} \tag{7.21}$$

or

$$\omega = 2\gamma B_X \sin(\theta). \tag{7.22}$$

We note in passing that

$$\omega \approx \gamma B_X(\theta_A + \theta_B) \tag{7.23}$$

for small values of θ; this is in accordance with the derivations in Sec. 3.7. The simulated value of ω is plotted as function of θ in Fig. 7.1. The time step used here was $\mathrm{d}t = 10^{-18}$ s, to ensure sufficiently small time steps at the larger frequencies. A total of 10^7 time steps were simulated for each angle. The agreement is excellent.

7.3.2 $q = 0$ spin waves

Let us now simulate the $q = 0$ spin waves described by Eqs. (3.47) and (3.48). We also add the DM-interaction, which is described by Eq. (3.49). In terms of the effective

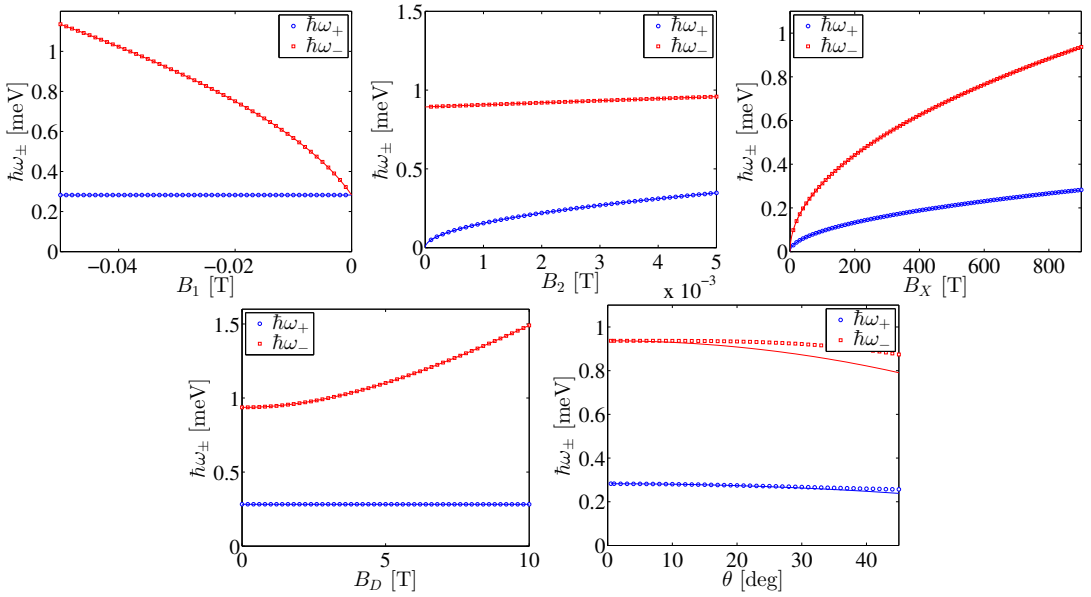

FIGURE 7.2: Varying B_1, B_2, B_X, B_D and the canting angle, θ. The solid lines are Eqs. (7.24) and (7.25). The solid lines in the plot of the canting angle is Eq. (3.84).

.

fields, these equations become

$$\pm\omega_- = g\mu_B\sqrt{(B_2+2B_X)(B_2-B_1)+B_D^2}, \tag{7.24}$$

$$\pm\omega_+ = g\mu_B\sqrt{B_2(B_2-B_1+2B_X)}. \tag{7.25}$$

In the simulations we tilt the spins a small angle away from the minimum, still keeping the temperature and damping at zero. The spins then perform oscillations with the frequencies given by these equations. $\hbar\omega^\pm$ as function of B_1, B_2, B_X and B_D are shown in Fig. 7.2. The solid lines in these figures are Eqs. (7.24) and (7.25). Again, we see excellent agreement.

We also investigated the effect of the size of the canting angle. Theoretically, the frequency should decrease according to Eq. (3.84). However, we see the frequencies do not decrease as quickly as expected. Time did not allow for a careful investigation of this effect.

7.3.3 Damping

Let us now introduce damping into the equations, while keeping the temperature at 0. An example of the time evolution of the spins is given Fig. 7.3. We see that the spins indeed precess in the x and y directions, with the amplitude gradually decreasing.

The power spectra were fitted using a DHO. Examples of the fits for various values of λ are shown in Fig. 7.4. We see clear peaks in both the x and y direction; the position of these peaks is the frequency of the oscillations. At very small and very large damping, the fits are not very good. The y mode becomes overdamped for $\lambda \approx 1\times10^{-3}$, the x mode for $\lambda \approx 6\times10^{-3}$. It is clear that the width increases with λ.

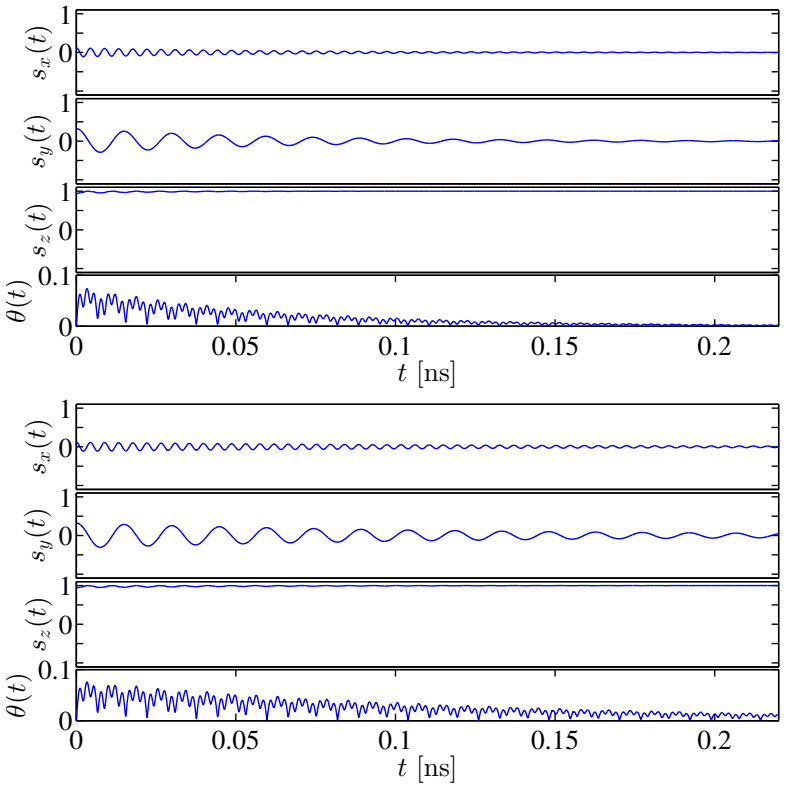

FIGURE 7.3: The time evolution of the spins at different dampings. Top: $\lambda = 1 \times 10^{-4}$. Bottom: $\lambda = 5 \times 10^{-5}$.

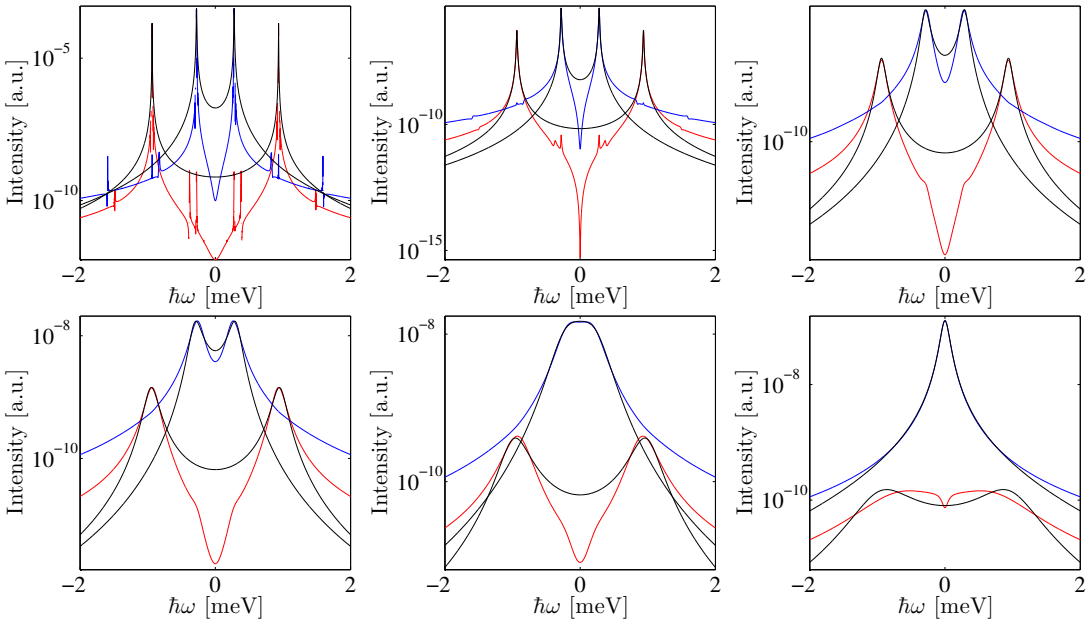

FIGURE 7.4: P^x (red) and P^y (blue), fitted to a damped harmonic oscillator (black), for different values of λ. From left to right, the values are: top row: $\lambda = 1 \times 10^{-6}$, $\lambda = 5 \times 10^{-5}$, $\lambda = 6 \times 10^{-4}$, bottom row: $\lambda = 1 \times 10^{-3}$, $\lambda = 2 \times 10^{-3}$, $\lambda = 6 \times 10^{-3}$

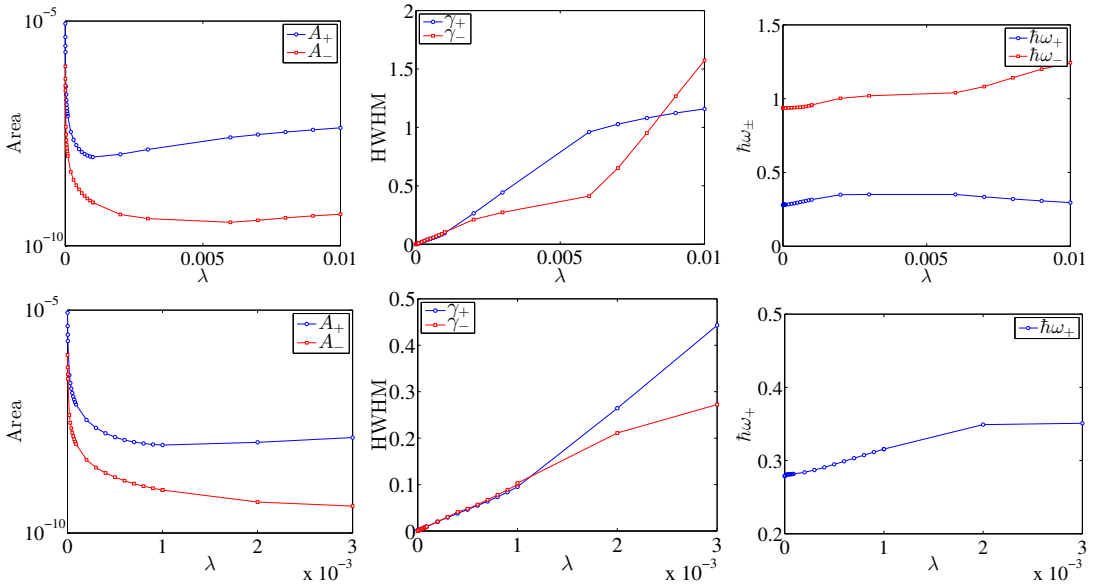

FIGURE 7.5: The area, width and position of the peaks as function of the damping parameter, λ. The bottom row is a zoom in on small values of λ. The width and position of the peaks is seen to increase with λ. For the low frequency mode, the position of the peaks is roughly constant for $\lambda > 2 \times 10^{-3}$.

The extracted parameters from the fitting are shown in Fig. 7.5. The width of the peaks increases with λ. We also see a slight increase in the positions of the peaks at low values of λ. At $\lambda \gtrsim 2 \times 10^{-3}$, the fits are unreliable. The origin of this increase is unknown to me. For a damped harmonic oscillator, the frequency is expected to decrease with increasing damping.

7.3.4 Temperature effect on a paramagnetic moment in a field

To test the implementation of the temperature, a single paramagnetic moment of $s = 5/2$ is simulated as function of temperature and magnetic field. Theoretically, the magnetization should follow the Langevin function:

$$\frac{\langle s^z \rangle}{s} = L(s, B, T) = \coth\left(\frac{g\mu_B sB}{k_B T}\right) - \frac{k_B T}{g\mu_B sB}. \tag{7.26}$$

The simulations as well as Eq. (7.26) are shown in Fig. 7.6 for various temperatures and magnetic fields. The agreement is excellent, except for some uncertainties in the simulated data.

7.3.5 Total simulation time

Convergence of the power spectra depends on the damping parameter λ. For a rather low damping, $\lambda = 6 \times 10^{-4}$, the convergence of power spectra happens after around 100 ns. The convergence is faster for higher damping, but no systematic study has been performed. The evolution of the three components are shown at typical values for 16 nm particles in Fig. 7.7.

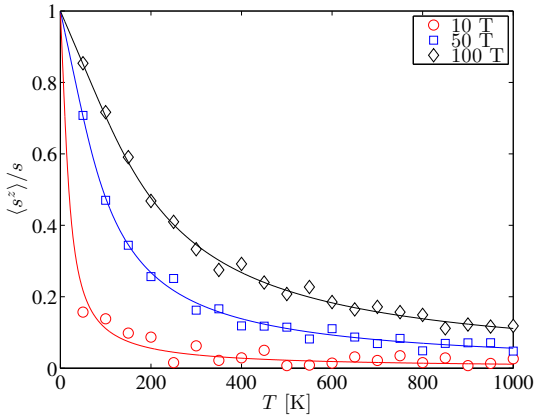

FIGURE 7.6: Simulations of the ordered moment for a single paramagnetic $s = 5/2$ spin in a magnetic field. Symbols are simulations and the solid lines show the theoretical prediction, Eq. (7.26).

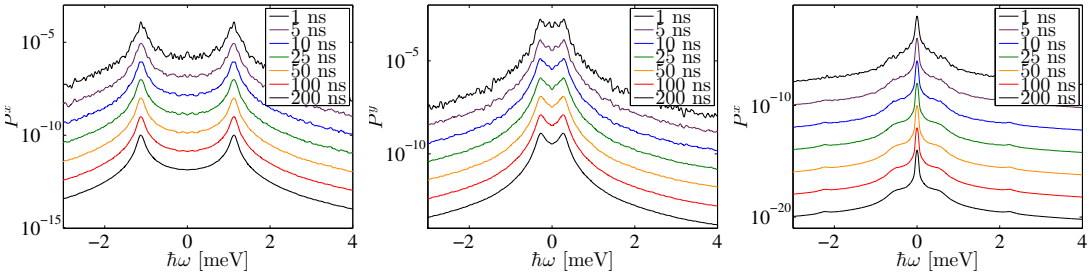

FIGURE 7.7: The x (left), y (center) and z (right) components of the power spectra at various times for a 16 nm particle. Convergence is seen after around 100 ns.

7.3.6 Different simulation times

In the work by J. Garde [34], the system was simulated for 60 times of 1 ns each. This was mainly done due to the long simulation times of several minutes per simulated ns. With the improvement described in the introduction, this limitation is no longer necessary. It is therefore worthwhile to investigate the difference of the two approaches. I have thus simulated the same system for 100 ns in one run, and in 100 runs of 1 ns. The results are shown in Fig. 7.8. The outermost double peaks are P^x, the inner double peaks are P^y, and the peak at the center is P^z. We see almost no difference between the two runs. This confirms that the sum of individual power spectra indeed is equal to the power spectrum of the total simulation.

7.3.7 Time step

The size of the time step in the numerical integration is very important. If the step is too large, the results will not be correct. However, the shorter the step, the longer the computation time must be for convergence of the power spectra.

The lowest value of the time step is given partly by the increase in computing time, and partly in the increase in size of the produced files. For instance, the five plots in

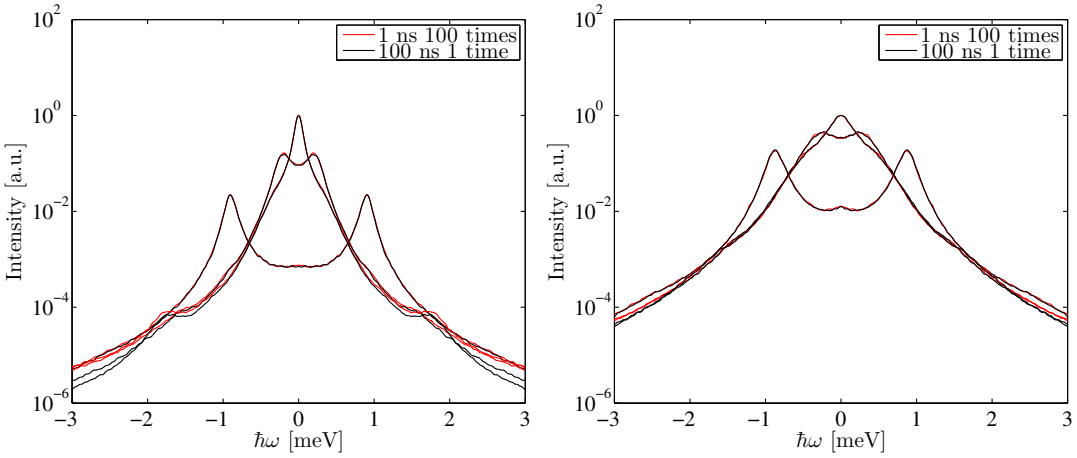

FIGURE 7.8: Comparison of simulations for 8 nm particles. Left: 50 K. Right: 150 K. The plots have been normalized so the z component peaks at 1.

Fig. 7.2 required almost 1 Gb of simulated data; they were run with a time step of $\mathrm{d}t = 10^{-16}$ s for a total of 1 ns.

The highest excitation energies we encountered in the measurements were approximately 1.3 meV, corresponding to frequencies of 2×10^{12} s^{-1}, or time steps of $\mathrm{d}t = 5 \times 10^{-13}$ s. A time step of $\mathrm{d}t = 10^{-15}$ s thus gives at least 500 points within each oscillation, which should be more than sufficient. In [34] a time step of $\mathrm{d}t = 10^{-14}$ s was used.

To ensure that a time step of $\mathrm{d}t = 10^{-15}$ s is an optimal choice, a range of time steps were simulated at two temperatures, 50 K and 150 K for 8 nm particles. A representative choice of the simulations are shown in Fig. 7.9. The three components are plotted individually for several different time steps. From this figure, it is seen that a time step of $\mathrm{d}t = 10$ fs is on the verge of being too large, as already a time step of twice this size gives quite different results. No large difference is seen between a time step of 1 fs and 0.1 fs, proving that 1 fs is sufficiently small.

All these simulations were done for 200 ns to ensure beyond doubt that convergence had been achieved.

7.4 Comparing with data

It is now time to relate the simulations to the data described in the previous chapter. We will first analyze the 15 nm particles, comparing the simulations with the IN5 experiment and the two backscattering experiments at IN10 and IN16b. We will vary B_X, B_1, B_2 and λ, to find the values that overall fits best with the data. We will set the DM-field equal to the bulk value, $B_D = 2.1$ T [1]. From the simulations, the following parameters can be extracted, as function of temperature: A_{SPM}, Γ, $A_\pm$, $\gamma_\pm$ and $\hbar\omega^\pm$, all of which can be compared to the data.

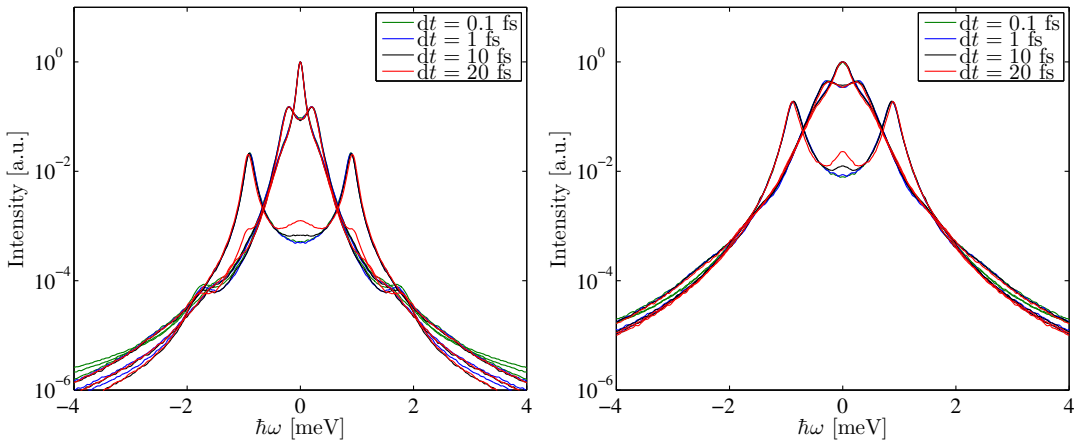

FIGURE 7.9: Comparing the time step dt at 50 K (left) and 150 K (right). It is seen that a time step smaller than 10 fs is required to get consistent results.

The general strategy to be employed is the following: The simulated data will be convolved with the resolution function of the relevant instrument, in order for the comparison to be as realistic as possible. The data will be fitted to Eq. (7.16) convoluted with the resolution function in the same energy window as the real data, and the resulting parameters will be plotted as function of temperature, comparing to the data.

Ideally, adjustment of the parameters to match the simulations to the experiments would be done by some sort of χ^2 minimization. However, there are several problems with this method. First of all, the simulated data will need to be fitted automatically. The fits are very sensitive to the starting guess, convergence only happens if the starting guess is already quite close to minimizing χ^2. This means that a robust method to estimate the parameters would have to be developed. In addition to this, the simulated data is inherently noisy. The default optimizer, based on the Lewenberg-Marquadt algorithm [70, 71], is not suitable for noisy data. For noisy problems, the particle swarm algorithm [72] has shown promising results in other areas [73], but convergence is not guaranteed and usually requires more than $\sim$ 1000 iterations of each $\sim$ 20 minutes. These problems makes a χ^2 optimization impractical.

Instead, the parameters will be adjusted by visually comparing the results of the simulations to the data and adjusting the parameters one at a time.

7.4.1 16 nm particles: IN5, IN10 and IN16b

In this section we will compare the simulations with data on the 16 nm particles. We first compare with the experimental parameters found in the previous chapter, then move on to adjust the parameters.

7.4.1.1 Direct comparison

We first compare the simulations directly with the experimental parameters that were found in the previous chapter.

We perform the simulations for several values of λ: $\lambda = 1 \times 10^{-4}$, $\lambda = 3 \times 10^{-4}$, $\lambda = 6 \times 10^{-4}$, $\lambda = 12 \times 10^{-4}$ and $\lambda = 18 \times 10^{-4}$.

Examples of the simulated data and the fits at $\mathbf{q} = (101)$ are shown in Fig. 7.10. The simulated data were convolved with a Gaussian with the same width as the resolution function of IN5 at the high resolution experiment, $\lambda_i = 6.5$ Å. The model is seen to give a good fit over approximately 5 orders of magnitude in intensity, which is quite impressive.

The extracted parameters from the fits are shown in Fig. 7.11. The simulated values are quite close to the measured values, but with some important differences. First of all, the temperature dependence of the high frequency mode, $\hbar\omega_-$ is much more pronounced in the simulations than in the experiment. This means that the temperature dependence of the extracted values of κ_1 is wrong. To get a better fit with the simulations, the temperature dependence should be smaller. The explanation of this is that the high frequency mode, for constant κ_1 does not change as significantly with temperature as expected. A second observation is that A_{SPM} is overestimated, while $A_\pm$ are underestimated in the simulations at high temperature. Finally, we see from Fig. 7.11 that λ primarily influenced three parameters: Γ and $\gamma_\pm$. Increasing λ will in all three cases increase the width.

7.4.1.2 Adjustment of parameters

It is clear that some of the parameters need to be adjusted, as the simulations and the experimental data do not match. The parameters have been adjusted one at a time, by simulating a few values and comparing with the data as in Fig. 7.11. More examples of these adjustments are shown in Appendix D. Here, an overview of the effect of the different parameters is given.

Increasing λ mainly increases $\gamma_\pm$. Γ also increases slightly, but not uniformly. At higher temperatures, higher λ also slightly increases A_{SPM} and decreases $A_\pm$.

Increasing the number of spins, $N = N_A + N_B$ primarily has an effect on the areas and Γ: increasing N increases A_{SPM} and decreases $A_\pm$ and Γ. Smaller N also means a more pronounced temperature dependence of $\hbar\omega_+$.

Increasing B_2 decreases Γ and increases $\hbar\omega_+$ and A_{SPM} increases with increasing B_2, while A_+ decreases. Increasing B_1 increases $\hbar\omega_-$, while A_- decreases. Increasing B_X increases $\hbar\omega_\pm$ and $\gamma_\pm$ and leaves the areas unchanged. Finally, increasing ξ shifts the energies, as expected: $\hbar\omega_-$ is increased and $\hbar\omega_+$ is decreased. Also, increasing ξ slightly reduces A_- and $\gamma_\pm$. A summary of this is given in Table 7.1. The final result is shown in Fig. 7.12.

We see that quite good agreement between simulations and experiments are obtained by using the same values of N, B_X, B_2 and ξ as used in the experiments. The only major difference is in the widths of the DHO's, $\gamma_\pm$. They are significantly narrower in the simulations. To match the widths to the experiments, the damping was set to

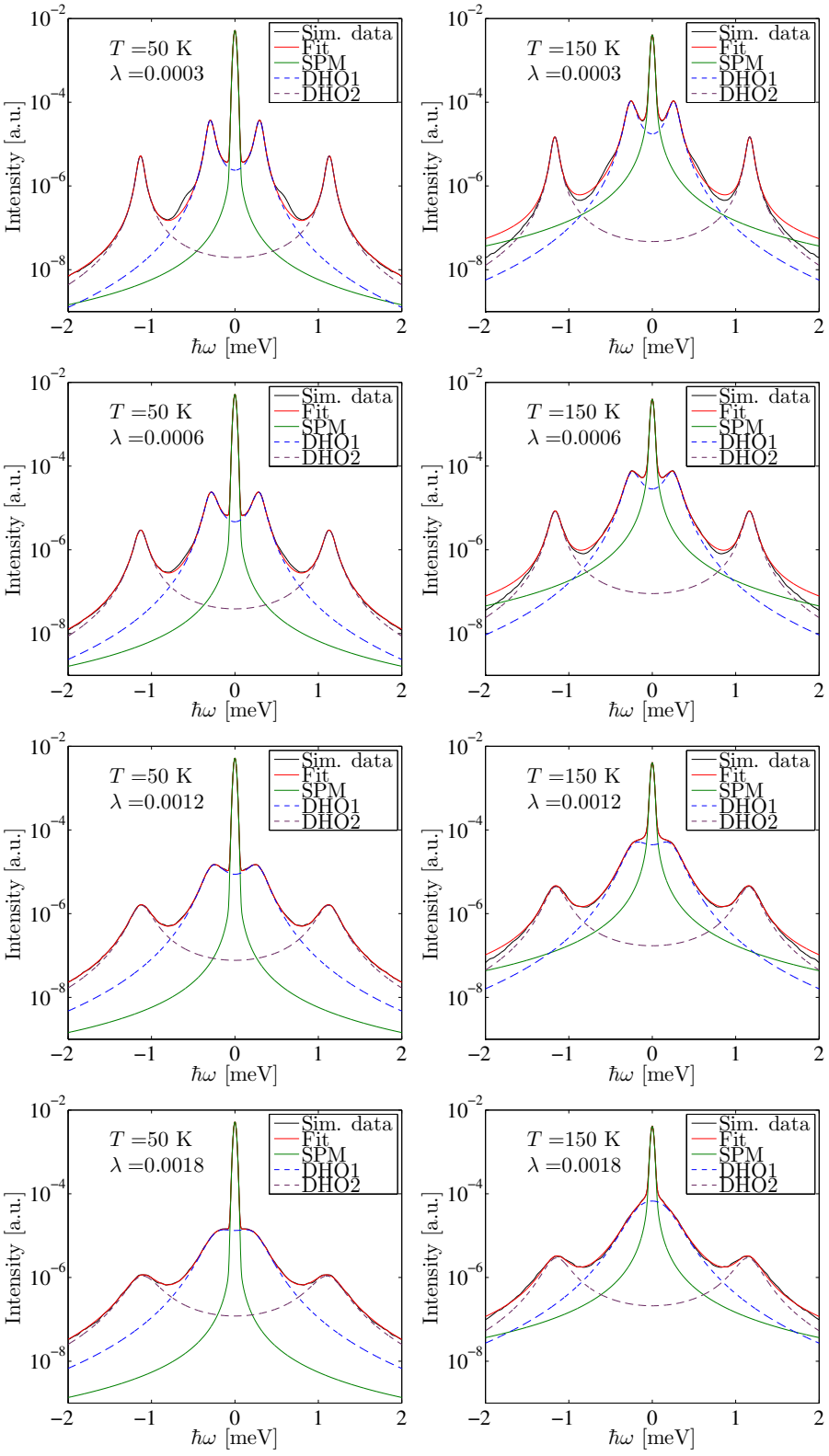

FIGURE 7.10: Examples of simulated data for the 16 nm particles. Left column at 50 K, right column at 150 K. Going from top to bottom, λ takes the values 3×10^{-4}, 6×10^{-4}, 12×10^{-4} and 18×10^{-4}. The broadening with increasing λ is evident.

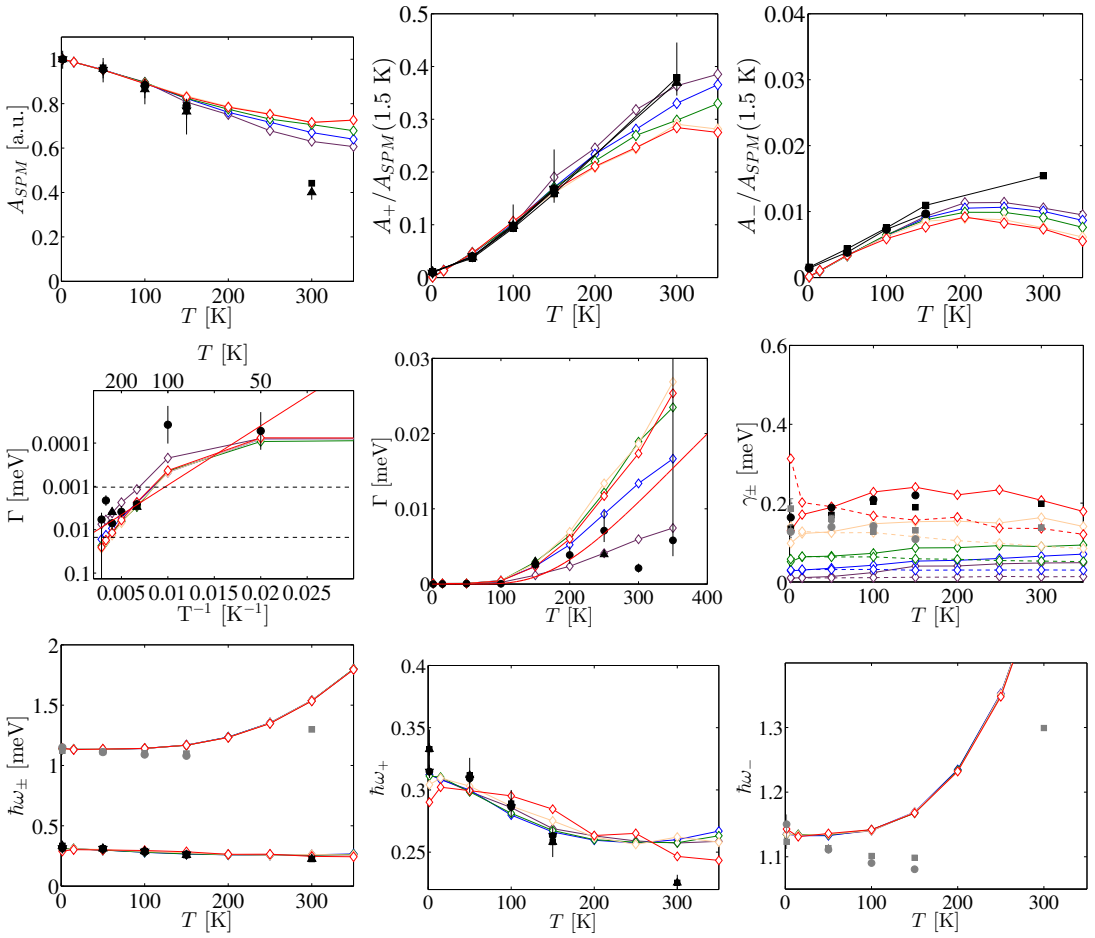

FIGURE 7.11: The extracted parameters from the fits for different λ. Filled symbols are experimental data, open are simulations. Gray symbols are for the high frequency mode. In the simulations, the high frequency mode is marked by dashed lines. First row shows the areas, from left to right: A_{SPM}, A_+ and A_-. Second row shows the widths, from left to right: Γ, Γ on a scale where the Néel-Brown law is a straight line and $\gamma_\pm$. Third row shows the $q = 0$ spin wave frequencies, $\hbar\omega_\pm$. From left to right: Both peaks, $\hbar\omega_+$ and $\hbar\omega_-$.

	λ	N	B_2	B_1	B_X	ξ
A_+	$(-)$	$-$	$-$			
$\hbar\omega_+$			$+$		$+$	$+$
γ_+	$+$					$-$
A_-		$-$		$-$		$-$
$\hbar\omega_-$				$+$	$+$	$+$
γ_-	$+$					$-$
A_{SPM}	$(-)$	$+$	$+$			
Γ		$-$	$-$			

TABLE 7.1: The correlation between the input parameters to the simulations and the parameters extracted from fitting the simulated data. $+$ indicates positive correlation, $-$ negative correlations, $(-)$ indicates slightly negative correlation.

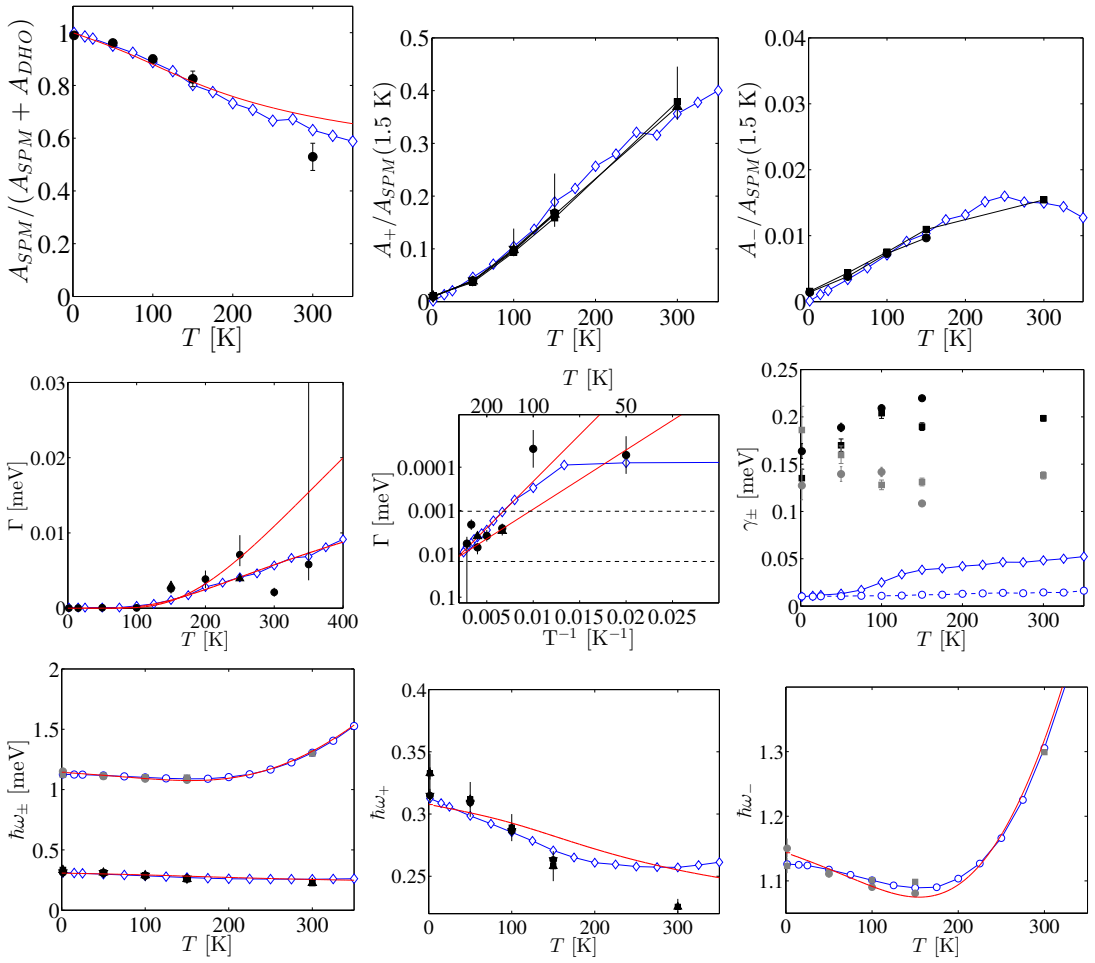

FIGURE 7.12: The final simulation results after parameter optimization for the 16 nm particles. Gray symbols are for the high frequency mode. In the simulations, the high frequency mode is marked by a circle. First row shows the areas, from left to right: $A_{\mathrm{SPM}}/(A_{\mathrm{SPM}}+A_{\mathrm{DHO}})$, A_+ and A_-. Second row shows the widths, from left to right: Γ, Γ on a scale where the Néel-Brown law is a straight line and $\gamma_\pm$. Third row shows the $q=0$ spin wave frequencies, $\hbar\omega_\pm$. From left to right: Both peaks, $\hbar\omega_+$ and $\hbar\omega_-$.

$\lambda = 1\times10^{-4}$, which is quite small. From Fig. 7.10 it is clear that the simulated data do not look like the experimental data.

The temperature dependence of κ_1 is not as pronounced as expected from the data analysis in the previous chapter. The temperature dependence of κ_1 as determined by the simulations is shown in Fig. 7.13.

Fitting the simulated data gives quite consistent results: The Néel-Brown law gives 2.12×10^{-11} s and $K_2V = 505$ K, which is close to the input $K_2V = \kappa_2 ss' N = 579$ K. Fitting the temperature dependence of $A_{\mathrm{SPM}}/(A_{\mathrm{SPM}}+A_+ + A_-)$ to Eq. (3.88) yields $K_2V = 575$ K. All the values are given in Table 7.2. Discussion of details is left for the next chapter.

1	Particle	Method	κ_2	B_2	K_2V	κ_1	B_1	K_1V	τ_0	B_X	N	B_D	ξ
Neutron			mK	mT	K	mK	mT	K	s	T		T	
[9]	16 nm	(1)	0.91(5)	2.71	600					927	10^5	0	1
		(2)	1	2.9745	500(200)	—	—	—	$0.7 \times 10^{-11(1)}$	—	10^5	—	1
		(3c)	2	5.949	1000(400)	0	0	0	—	—	10^5	—	1
[35]	16 nm	(3b)	1	2.97	500(200)	∞	∞	∞	—	—	10^5	—	1
		(1a)	0.776	2.31	330^{+590}_{-230}	-6.11	-18.2	-2600	—	900	Unknown	0	1
		(1b)	0.823	2.45	350^{+690}_{-250}	∞	∞	∞	—	900	Unknown	0	1
[10]	16 nm	(3a)	0.353	1.049	150^{+600}_{-50}	-6.11	-18.18	-2600	—	Unknown	Unknown	0	1
		(3b)	0.259	0.769	110^{+490}_{-40}	∞	∞	∞	—	Unknown	Unknown	0	1
		(2)	1.15	3.42	490(30)	—	—	—	$1.9(4) \times 10^{-11}$	—	Unknown	—	1
[11]	PO 8 nm	(1)	1.25	3.72	66.3	-16(1)	-47.6	-848	—	827	Unknown	0	1
[12]	PO 8 nm	(3c)	4.72	14.03	250(30)	0	0	0	—	900	Unknown	0	1.011
		(3b)	2.36	7.02	125(15)	∞	∞	∞	—	900	Unknown	0	1.011
Mössbauer													
[36]	16 nm	(4b)	1.39	4.12	590^{+150}_{-120}	∞	∞	∞	$6.5^{+10.5}_{-4.5} \times 10^{-11}$	—	Unknown	0	1
[29]	16 nm		1.46	4.33	620				5.3×10^{-11}	—	Unknown	0	1
[29]	8 nm	(4b)	0.759	2.26	323	∞	∞	∞	0.97×10^{-11}	—	Unknown	0	1
[12]	PO 8 nm	(4c)	6.32	18.80	335(35)	0	0	0	Unknown	—	Unknown	0	1
		(4b)	3.17	9.43	168(18)	∞	∞	∞	Unknown	—	Unknown	0	1
This work													
IN5	16 nm	(1)	1.34	3.99	570(60)	-15.8	-47.0	-6.72×10^3	—	900	8.51×10^4	2.1	1
		(3a)	1.47	4.36	624(66)	-15.8	-47.0	-6.72×10^3	—	—	8.51×10^4	—	1
	Mesoporous	(1)	—	—	—	-1.72	-5.11	—	—	900	—	2.1	1
IN10+IN16b	16 nm	(2)	1.71	5.08	726(200)	—	—	—	$0.54(5) \times 10^{-11}$	—	8.51×10^4	—	1
RITA-II	Coated 8 nm	(1)	1.47	4.37	77.91	$-10\kappa_2$	$-10B_2$	$-10K_2V$	—	900	1.06×10^4	2.1	1
		(3a)	2.96	8.81	157(11)	$-10\kappa_2$	$-10B_2$	$-10K_2V$	—	—	1.06×10^4	—	1
BSS	Coated 8 nm	(2)	1.85	5.50	98(9)	—	—	—	$2.2(2) \times 10^{-11}$	900	1.06×10^4	2.1	1
Simulations													
	16 nm	Input	1.34	3.99	570	-15.47	-46.00	-6.58×10^3	—	900	8.51×10^4	2.1	1
		(1)	1.312	3.91	560	-16.03	-47.7	-6.83×10^3	—	900	8.51×10^4	2.1	1
		(3a)	1.35	4.02	575	-15.47	-46.00	-6.58×10^3	—	900	8.51×10^4	2.1	1
		(2)	1.19	3.53	505	—	—	—	2.12×10^{-11}	900	8.51×10^4	2.1	1
$\xi = 1$	8 nm	Input	3.17	9.43	168	-31.7	-94.3	-1680	—	450	1.06×10^4	2.1	1
		(1)	3.03	9.02	161	$-10\kappa_2$	$-10B_2$	$-10K_2V$	—	450	1.06×10^4	2.1	1
		(3a)	2.83	8.88	150	$-10\kappa_2$	$-10B_2$	$-10K_2V$	—	450	1.06×10^4	2.1	1
		(2)	3.00	8.92	159	—	—	—	0.52×10^{-11}	450	1.06×10^4	2.1	1
$\xi = 1.015$	8 nm	Input	3.17	9.43	168	-31.7	-94.3	-1680	—	900	1.06×10^4	2.1	1.015
		(1)	3.06	9.12	162	$-10\kappa_2$	$-10B_2$	$-10K_2V$	—	900	1.06×10^4	2.1	1.015
		(3a)	2.99	8.88	158	$-10\kappa_2$	$-10B_2$	$-10K_2V$	—	900	1.06×10^4	2.1	1.015
		(2)	3.08	9.15	163	—	—	—	1.64×10^{-11}	900	1.06×10^4	2.1	1.015

TABLE 7.2: Overview of parameters describing nanoscale hematite. Black color is the reported measured values, blue indicates values I have calculated from the given results and green indicates values that have been assumed in the calculations. The different methods are: Method 1:($\hbar\omega$). 1a: full mode. 1b: 2d model. Method 2: (Néel-Brown). Method 3: $A_{\mathrm{SPM}}/(A_{\mathrm{SPM}} + A_{\mathrm{DHO}})$. 3a: Full model. 3b: 2d model. 3c: uniaxial model. Method 4: Mössbauer. 4a: full model. 4b: 2d model. 4c: uniaxial model. For unknown spin number, the values $N = 8.51 \times 10^4$ and $N = 1.06 \times 10^4$ have been used for 16 nm and 8 nm particles, respectively. κ_1, B_1 and K_1V are given at 0 K.

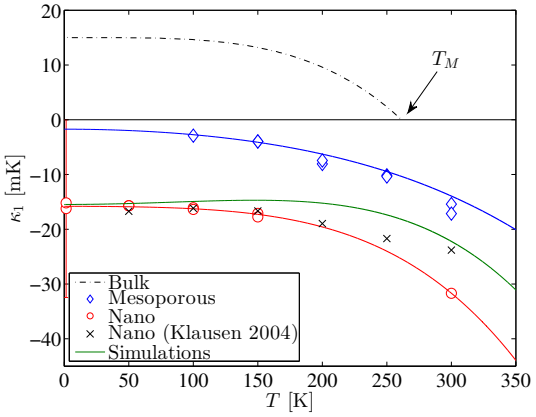

FIGURE 7.13: The extracted values of κ_1 from the experiments, as well as the values found in the simulations.

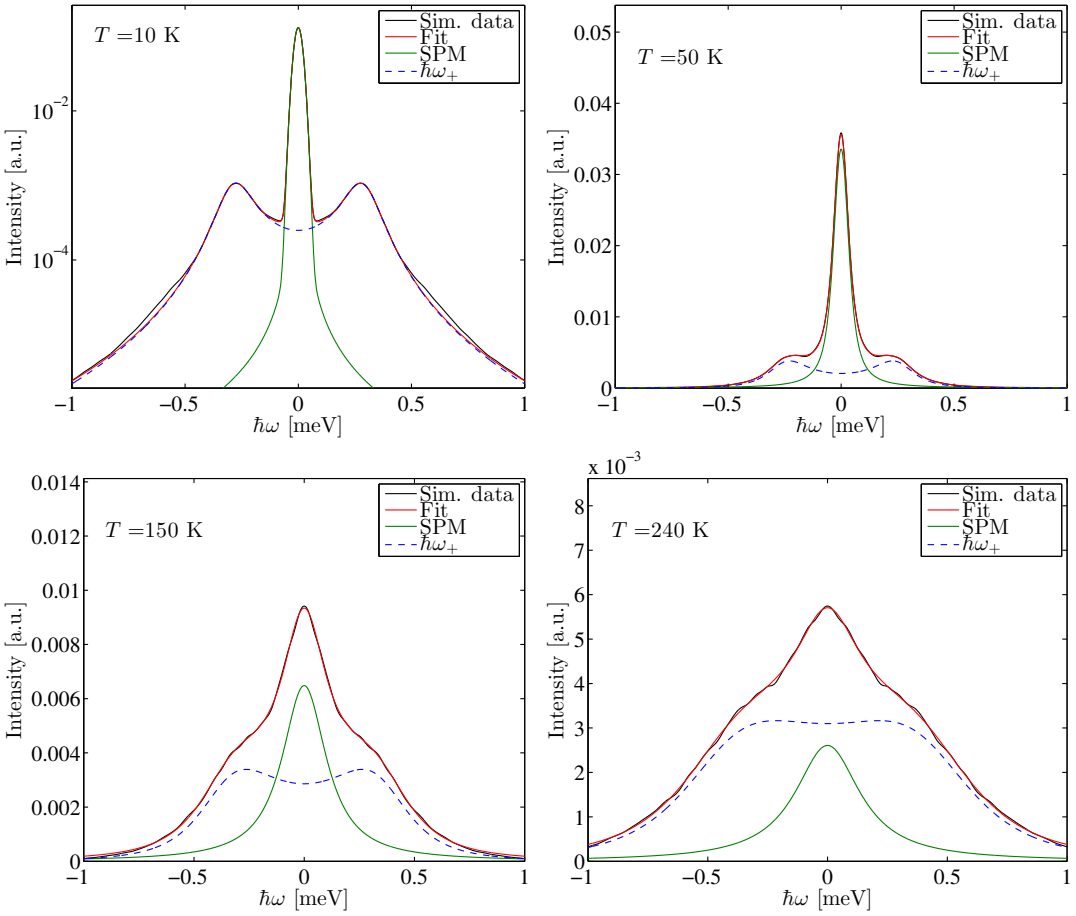

FIGURE 7.14: Examples of the simulations for 8 nm particles, with the parameters determined from the experimental chapter. The data at 10 K are on a log scale, the rest on a linear scale. Broadening of the peaks with temperature is clearly seen.

7.4.2 8 nm particles: RITA and BSS

We now compare the simulations to the data on 8 nm particles. This comparison is significantly more difficult, for several reasons. First of all, smaller particle size corresponds directly to higher temperatures. Most of the approximations described in this thesis are for low temperature, and are therefore a priori expected to fail at larger temperature. The damped harmonic oscillator model for the oscillations, for instance, does not give a very good fit at elevated temperatures. Secondly, the data quality is not as good as for the 16 nm particles. With these disclaimers in mind, let us look at the simulations. We start by simulating at $N = 1.06 \times 10^4$, $B_X = 900$ T, B_2=4.37 mT, $B_1 = -10B_2$, $\xi = 1$, $\lambda = 6 \times 10^{-4}$. These simulations are done for 150 ns to ensure convergence. Example fits at various temperatures are shown in Fig. 7.14. It is immediately apparent that the spins are much more mobile than before, as seen by the broad Lorentzian and high amplitude of the $\hbar\omega_+$ mode. The extracted parameters are shown in Fig. 7.15 for various values of λ.

As before, we vary the parameters one at a time and compare with the data. The most reliable of the data is the frequency $\hbar\omega_+$, and the primary goal will be to adjust the

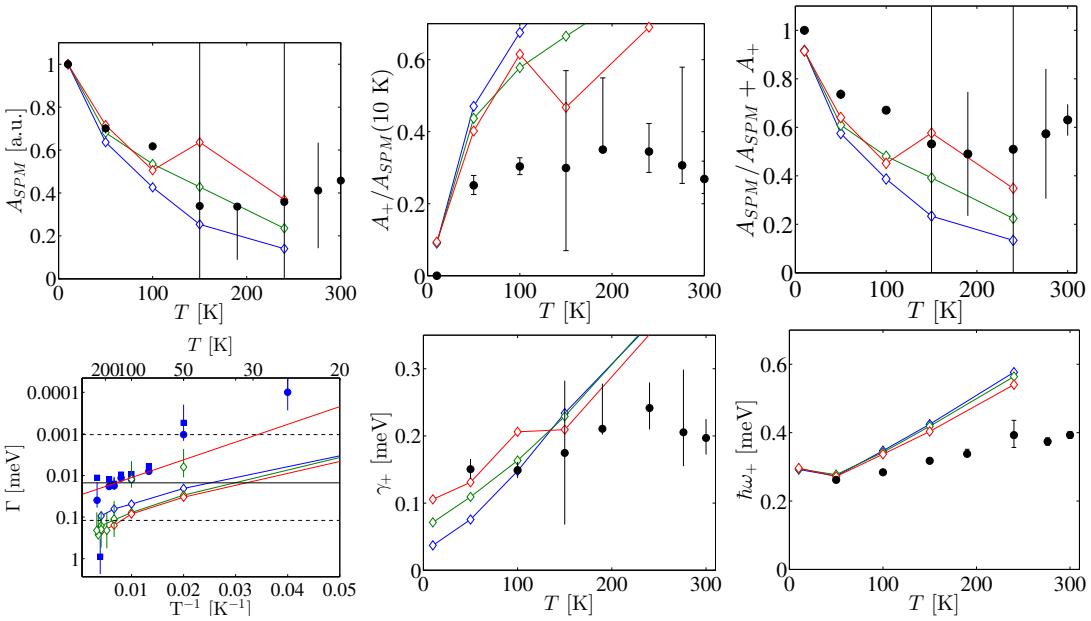

FIGURE 7.15: Scan of λ for the 8 nm particles, varying from $\lambda = 3 \times 10^{-4}$ (blue), $\lambda = 6 \times 10^{-4}$ (green), $\lambda = 9 \times 10^{-4}$ (red).

parameters such that the temperature evolution of this matches the data. The secondary goal is to get the correct temperature evolution of the areas. The widths, both Γ and γ_+ are quite difficult to match, as we also saw for the 16 nm particles.

To reduce the number of free parameters, we will assume $N = 1.06 \times 10^4$. As long as $|B_1|$ is large compared to B_2, B_1 does not influence any parameters that were measured in the experiments. We will therefore fix $B_1 = -10B_2$. This leaves λ, B_2, B_X and ξ to vary. We cannot a priori exclude the possibility of an uncompensated moment; for an 8 nm particle it is estimated to be around 1-2% as shown in Section 2.4.2. Furthermore, B_X is the average exchange field felt by the spins. This could be reduced by there being less exchange bridges for surface spins than for interior spins. For an 8 nm particle, the ratio of surface spins to interior spins is much higher than for a 16 nm particle, so this is plausible. The effect is estimated to be around a 10% reduction, see Section 2.4.2.

From Table 7.1, it is seen that λ mainly influences γ_+. We will for now fix it to $\lambda = 6 \times 10^{-4}$ used by Garde [34]. Now, $\hbar\omega_+$ is influenced by all three of the remaining parameters. We will therefore first fulfill the secondary goal of matching the areas by varying B_2. The result (show in the appendix, Chapter D) is that B_2 is significantly larger than what was obtained from the experiments, where $\xi = 1$ and $B_X = 900$ T was assumed. The optimal value is found to be close to the value found by Mössbauer spectroscopy, and thus $K_2V = 168$ K is used, leading to $B_2 = 9.43$ mT.

Now, to adjust B_X and ξ, we essentially have three possible approaches. 1) Assume no uncompensated moment, $\xi = 1$ and adjust B_X to the data. 2) Assume $B_X = 900\ T$ and adjust ξ accordingly. 3) Assume both ξ and B_X differ from the bulk values and adjust both accordingly. The third option is not feasible with this data set; we do not

have data of high enough quality to refine B_X and ξ simultaneously. The next best thing is to explore the relationship between ξ and B_X, which we will do to some extent.

We first set $\xi = 0$ and refine B_X. The optimal value is found to be near $B_X = 450\ T$; approximately half of the bulk value.

The simulations have been done for two different values of the damping, $\lambda = 9\times10^{-4}$, where the simulated data have been fitted exactly as the experimental data, and $\lambda = 2\times10^{-4}$, where the peaks are much narrower, and the rotor mode can be distinguished. Examples of the fits are shown in Fig. 7.16. For $\lambda = 2\times10^{-4}$ the SPM signal matches the experimental data, which is not the case for $\lambda = 9\times10^{-4}$.

The results of the fitting are shown in Fig. 7.17. $A_{\mathrm{SPM}}/(A_{\mathrm{SPM}} + A_+$ is fitted to Eq. (3.88), yielding $K_2V \approx 150$ K, which is not far off from the input, $K_2V = 168$ K. Γ is fitted to the Néel-Brown law, giving $K_2V = 159$ K and $\tau_0 = 1.77\times10^{-11}$ s. It is clear that the simulated data follow the Néel-Brown law, and the fitted value is very close to the input. Finally, the temperature evolution of $\hbar\omega_+$ is fitted to Eq. 3.84, and excellent agreement is seen at lower temperature.

In Fig. 7.17, the expected frequency of the rotor mode, Eq. (3.108) is plotted along with $\hbar\omega_+$.

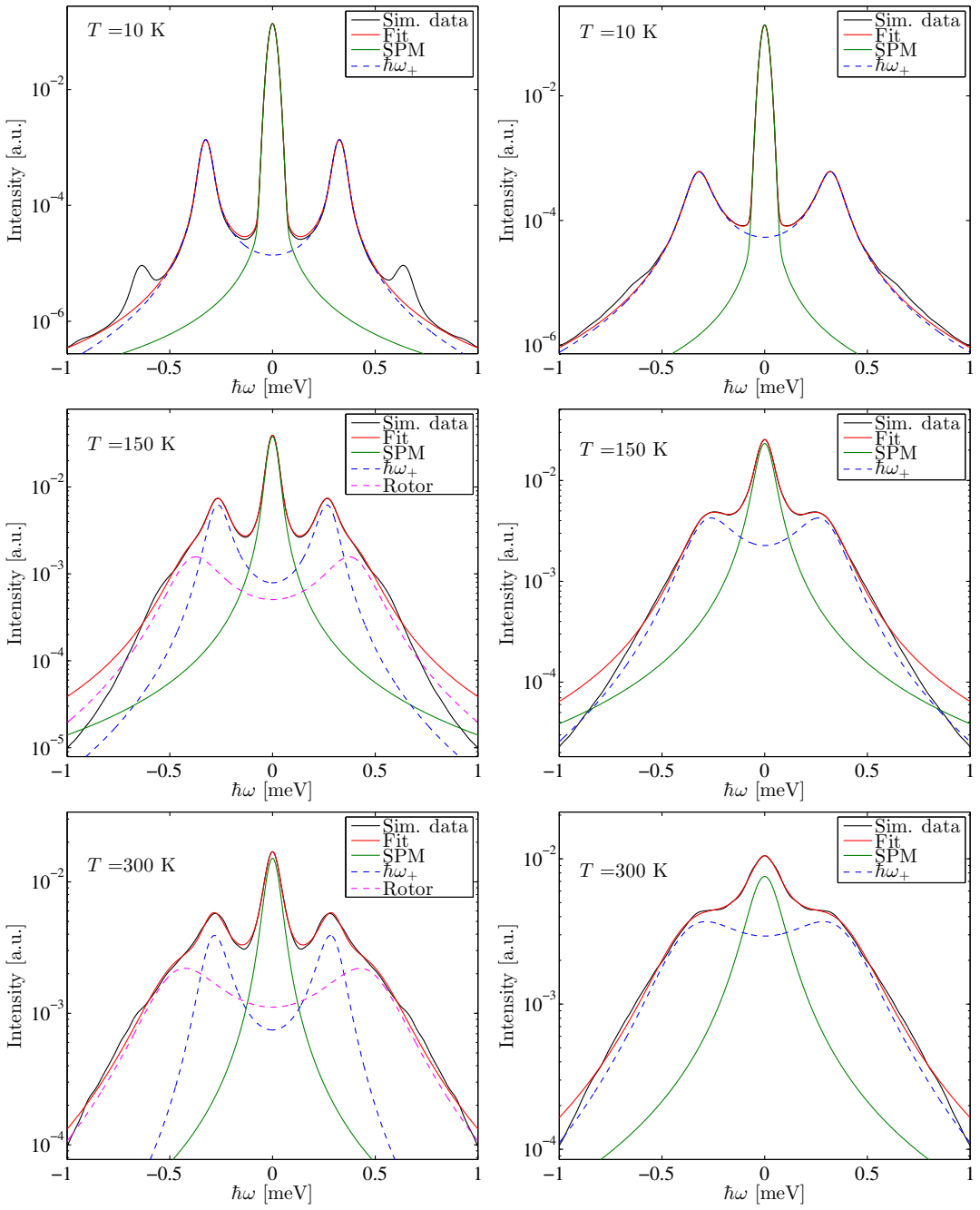

FIGURE 7.16: Examples of the final fits for 8 nm particles for $\lambda = 2 \times 10^{-4}$ (left) and $\lambda = 9 \times 10^{-4}$ (right) at several different temperatures. The data with $\lambda = 2 \times 10^{-4}$ have been fitted with an extra DHO for the rotor mode at temperatures above 100 K.

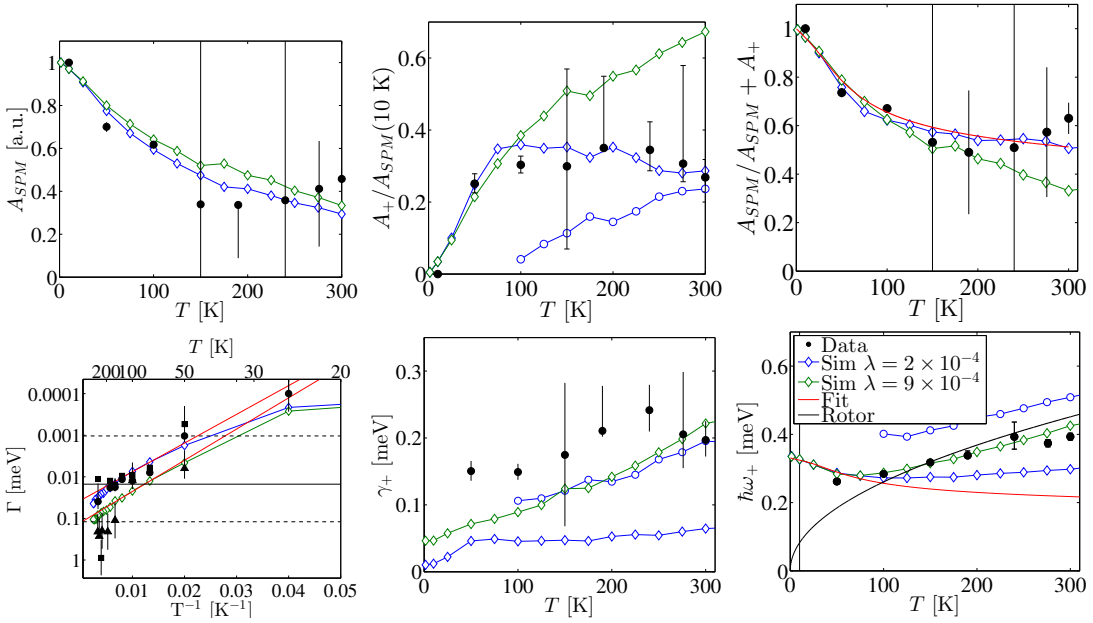

FIGURE 7.17: The final simulations assuming $\xi = 1$, leading to $B_X = 450$ T. Filled points are experimental data, open are simulations. Blue points are for $\lambda = 2 \times 10^{-4}$, green for $\lambda = 9 \times 10^{-4}$. Solid lines are fits to the simulated dataTop row shows the areas, from left to right: A_{SPM}, A_+/A_{SPM} and $A_{\mathrm{SPM}}/(A_{\mathrm{SPM}} + A_+)$. Second row shows the width of the SPM signal, Γ, the width of the low frequency mode, γ_+ and the frequency of the low frequency mode, $\hbar\omega_+$. The simulated data have been fitted as described in the text.

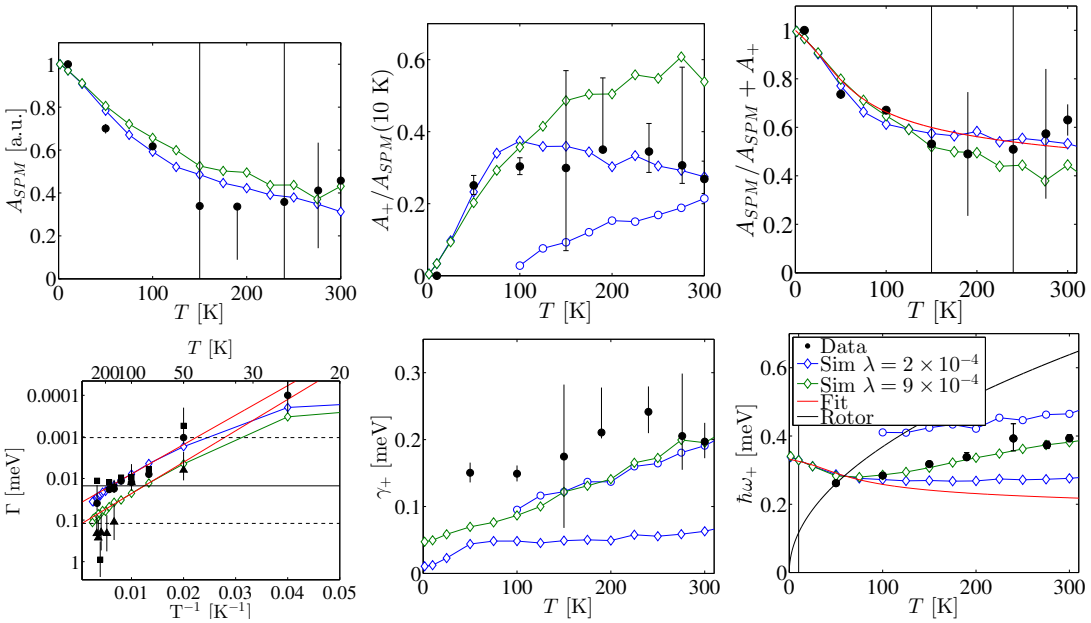

FIGURE 7.18: The final simulations assuming $B_X = 900$ T, leading to $\xi = 1.015$. Filled points are experimental data, open are simulations. Blue points are for $\lambda = 2 \times 10^{-4}$, green for $\lambda = 9 \times 10^{-4}$. Solid lines are fits to the simulated data. Top row shows the areas, from left to right: A_{SPM}, A_+/A_{SPM} and $A_{\mathrm{SPM}}/(A_{\mathrm{SPM}} + A_+)$. Second row shows the width of the SPM signal, Γ, the width of the low frequency mode, γ_+ and the frequency of the low frequency mode, $\hbar\omega_+$. The simulated data have been fitted as described in the text.

We next set $B_X = 900$ T and refine ξ, the plots are shown in the appendix (Fig. D.16). The optimal value is near $\xi = 1.015$. The results are shown in Fig. 7.18. It is apparent that the fit is exactly as good as the previous with $B_X = 450$ T and $\xi = 1$.

The expected rotor frequency for $\xi = 1$ is plotted along with $\hbar\omega_+$. It should be noted that this frequency probably depends on ξ, but no analytical calculations have yet been made.

Finally, we look at some intermediate values, setting $\xi = 1.010$ and refine B_X, finding $B_X = 600$ T. The results are shown in Fig. 7.18. Again, the fit is exactly as good as the previous two.

The simulations have been done for a few different values of ξ to see how ξ and B_X depend on each other. The results are shown in Fig. 7.20.

The results will be discussed in the next chapter. Before that, we will take a look at the spin configurations in real space.

7.4.2.1 Time evolution

Let us consider the time evolution of the spins for the two cases described in the previous section for 8 nm particles: a($\xi = 1$ and $B_X = 450$ T, b) $\xi = 1.015$ and $B_X = 900$ T. Typical 1 ns examples are shown in Figs. 7.21 and 7.22. At low temperature we see rapid, low amplitude oscillations in x, slower, higher amplitude oscillations in y and constant values of s^z, followed by near instant flips of s^z: superparamagnetism. At

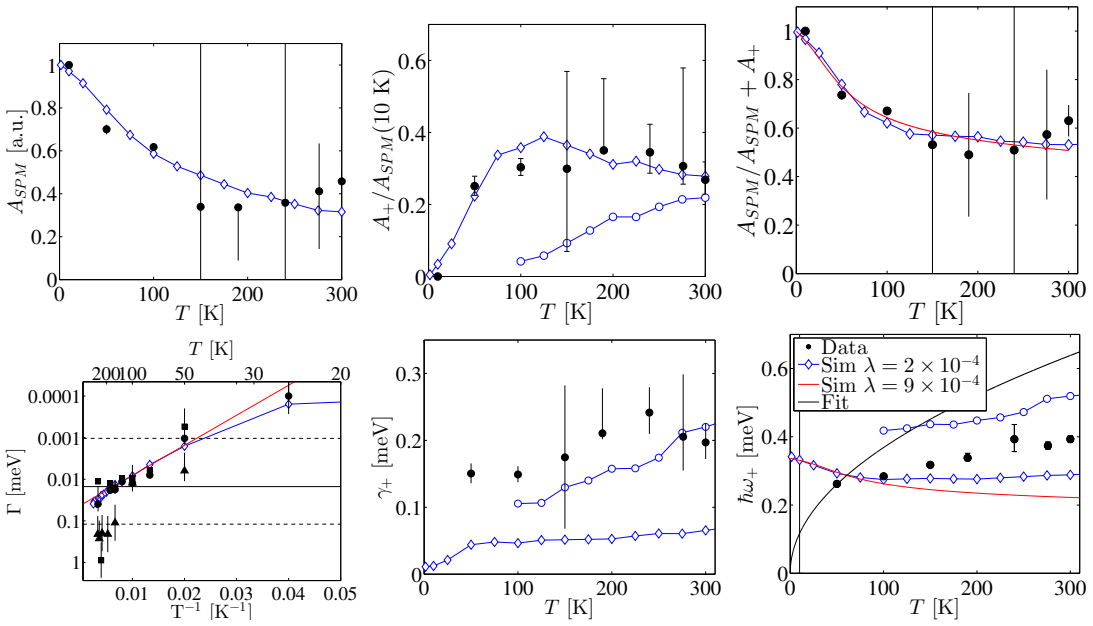

FIGURE 7.19: The final simulations assuming $\xi = 1.01$, leading to $B_X = 600$ T. Filled points are experimental data, open are simulations. Blue points are for $\lambda = 2 \times 10^{-4}$, green for $\lambda = 9 \times 10^{-4}$. Solid lines are fits to the simulated data. Top row shows the areas, from left to right: A_{SPM}, A_+/A_{SPM} and $A_{\mathrm{SPM}}/(A_{\mathrm{SPM}} + A_+)$. Second row shows the width of the SPM signal, Γ, the width of the low frequency mode, γ_+ and the frequency of the low frequency mode, $\hbar\omega_+$. The simulated data have been fitted as described in the text.

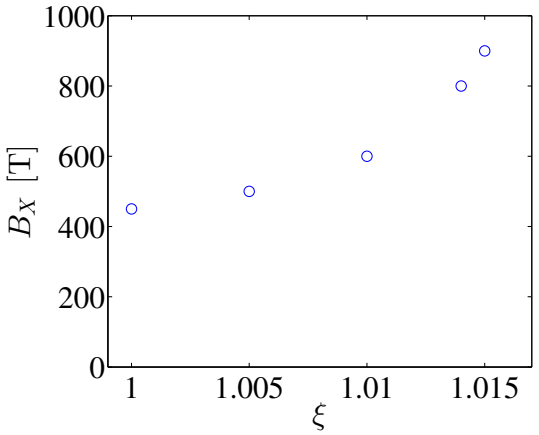

FIGURE 7.20: The optimal values of B_X for different values of ξ for 8 nm particles with B_2 fixed to the value found from Mössbauer spectroscopy.

150 K, the flips happen more frequently, and coupled motion of s^z and s^y is encircled with red. Only one or two full rotations are seen before thermal fluctuations de-excite the mode.

At 300 K, the spins oscillate almost freely in the yz plane, and the rapid coupled oscillations of s^z and s^y are encircled. This is a direct observation of the rotor mode described in Section 3.7. The dynamics are quite similar in the two cases, except that the average canting angle is larger when B_X is smaller.

To further investigate the rotor mode, the individual components of the power spectra are shown in Fig. 7.23 at different temperatures. For both values of ξ, the rotor mode is clearly seen in P^z. At low temperaturesl small peaks are seen in P^z. Their cause have not been systematically investigated, but they are likely an effect of the oscillations in the x and y directions.

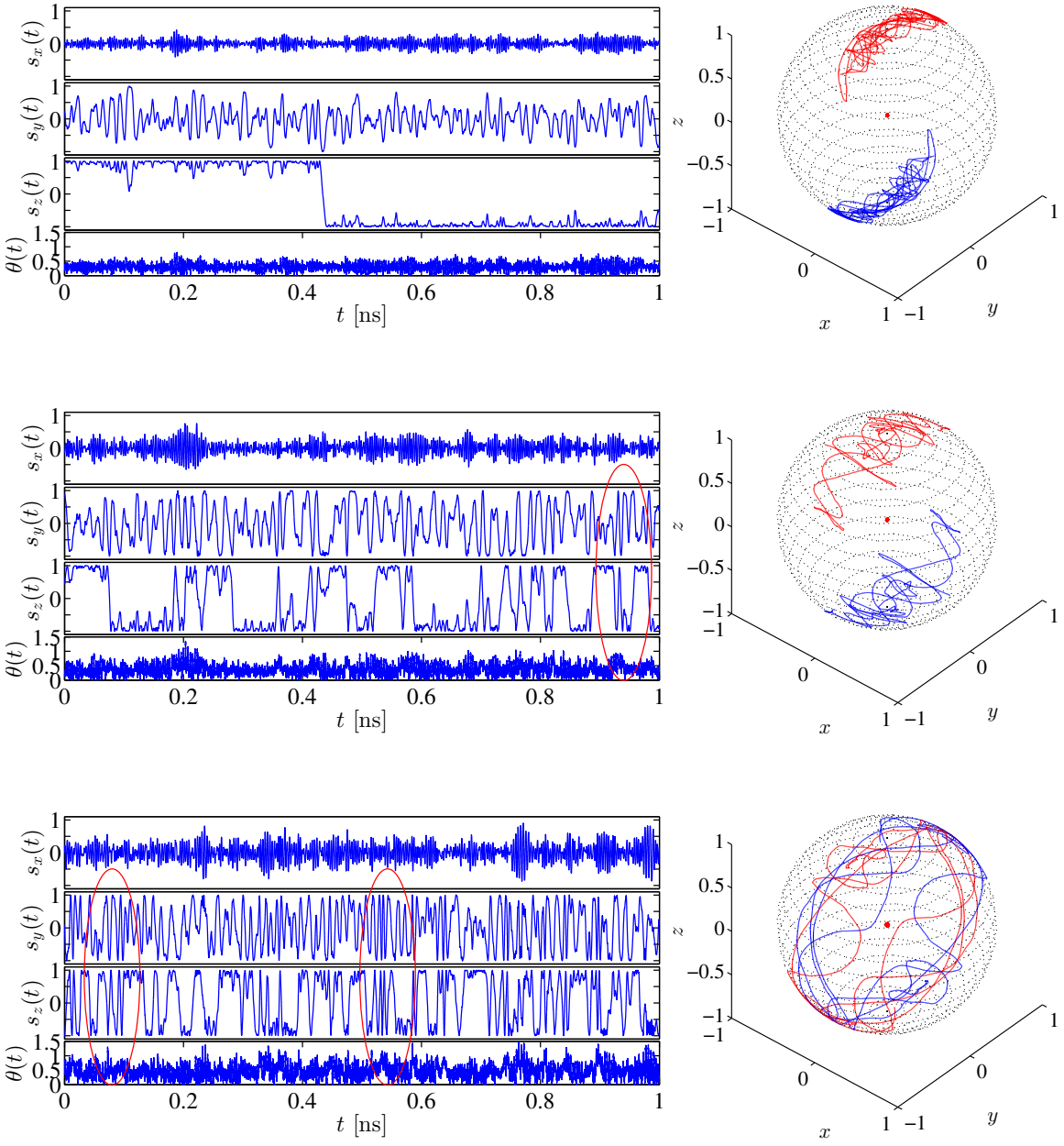

FIGURE 7.21: The time evolution of the spins for 8 nm particles at 50 K (top), 150 K (center) and 300 K (bottom) for $\xi = 1$. Rapid, low amplitude oscillations along the x axis indicate the high frequency mode, slower, higher amplitude oscillations along the y axis indicate the low frequency mode, and superparamagnetic spin flips are seen in the z axis as s^z being near constant and suddenly switching sign. The red ellipses mark rapid coupled oscillations within the yz-plane, correlated with large deviation angle from the spins being antiparallel. The right hand figures show the motion of the spins on the unit sphere.

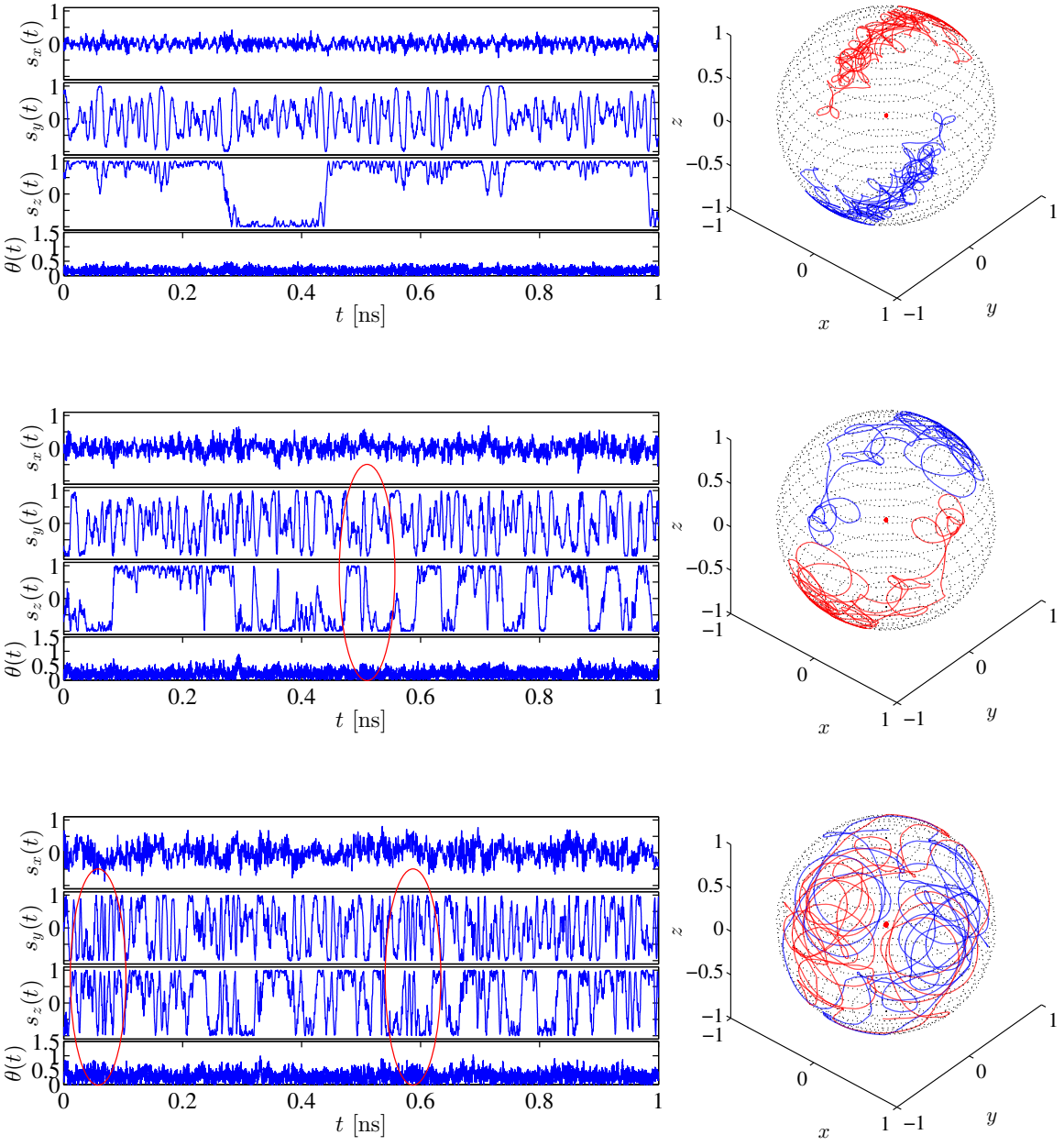

FIGURE 7.22: The time evolution of the spins for 8 nm particles at 50 K (top), 150 K (center) and 300 K (bottom) for $\xi = 1.015$ and $B_X = 900$ T. Rapid, low amplitude oscillations along the x axis indicate the high frequency mode, slower, higher amplitude oscillations along the y axis indicate the low frequency mode, and superparamagnetic spin flips are seen in the z axis as s^z being near constant and suddenly switching sign. The red ellipses mark rapid coupled oscillations within the yz-plane, correlated with large deviation angle from the spins being antiparallel. The right hand figures show the motion of the spins on the unit sphere.

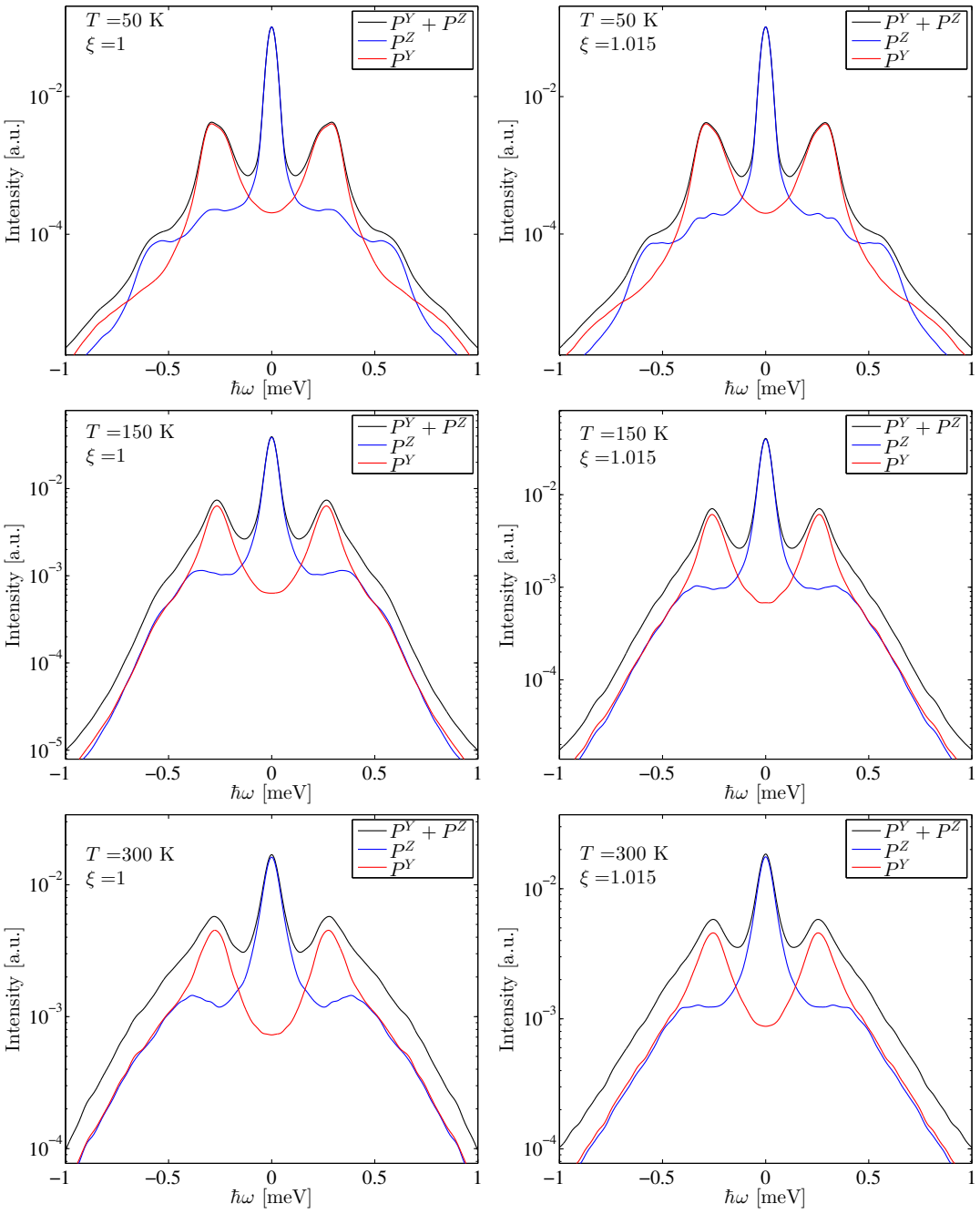

FIGURE 7.23: The power spectra for 8 nm particles at different tempeatures, clearly showing the existence of the rotor mode at elevated temperatures as a peak in P^z and a broad shoulder to the $\hbar\omega_+$ mode seen in P^y.

Chapter 8

Discussion

In this section, the results of the neutron scattering experiments presented in Chapter 6 and the simulations presented in Chapter 7 will be discussed. We will first discuss the mesoporous particles, and then the nanoparticles.

8.1 Mesoporous particles

The mesoporous particles were investigated with inelastic time of flight neutron scattering, neutron backscattering and polarized neutron diffraction. In all experiments, a huge incoherent background was seen. The polarized neutrons showed that the background indeed is non-magnetic in origin, and thus comes from water adsorbed to the surface of the particles.

The backscattering experiment showed with no doubt that superparamagnetic spin flips do not occur in mesoporous particles; verifying the results from Mössbauer spectroscopy [31]. Never the less, the magnetic dynamics are not the same as in bulk. Clear inelastic peaks were observed and identified as the high frequency mode, $\hbar\omega_-$. Signs of the low frequency mode, $\hbar\omega_+$ were also seen, although it could not be fitted with the damped harmonic oscillator model that was used for the nanoparticles. Several plausible explanations of this exist: the mesoporous particles contain a macroscopic number of spins, and the lowest mode with $q > 0$ is probably at lower energy than in the nanoparticles. The observed scattering could thus likely be caused by a combination of $q = 0$ and $q > 0$ modes, which would serve to broaden the peaks.

From the values of $\hbar\omega_-$, the temperature dependence of κ_1 was determined. it was assumed that κ_2 had the same value as in the 16 nm particles. from the presence of magnetic scattering at low energy transfers, it seems that this is a valid assumption. Furthermore, B_X and B_D were assumed to be equal to their bulk values.

The mesoporous particles showed an asymmetry in the inelastic signal along q. It seems that a broad signal is present at q slightly smaller than $q = 1.37$ Å^{-1}, where the magnetic (003) reflection is observed. The asymmetry of the peak is puzzling; if it was merely a size effect it would be symmetric in q, and would probably also be seen in the

(101) reflection. The broadness of the peak is reminiscent of diffuse magnetic signal seen in magnetically frustrated compounds.

To investigate the mesoporous particles in more detail, I will suggest inelastic polarized neutrons with better resolution than was used at IN5. This is a very demanding experiment, and it is questionable if there even exists an instrument that can do this.

8.2 Nanoparticles

The main focus of this thesis has been on 16 nm and 8 nm hematite particles. We will first discuss some results that are valid for both the 8 nm and 16 nm particles investigated here, before discussing them individually.

The incoherent background from water adsorbed to the surface of the particles has been a major problem in the data analysis. The analysis of the IN5 data provided a basis for increasing our understanding of this background compared to previous measurements. The q-dependence of the parameters is not trivial, and the width of the magnetic signals makes it necessary to go quite far away in q to measure only the background. Never the less, a quite robust method to analyze the background was developed.

The error bars on the parameters derived from fitting the experimental data were defined as the value of the parameters where χ^2 was increased by 1 compared to the optimal value. This yields a quite good estimate of the uncertainties, but still neglects a very important factor: the background determination. As already mentioned, it is quite difficult to estimate the background at the magnetic positions. The effect of the uncertainty in the background parameters was not considered in the fits.

Since the parameters found by simulations were estimated by varying one parameter at a time and by eye determining the optimal value, the uncertainties in these parameter values are rather large. Better results could perhaps be obtained by a χ^2 minimization, but as already discussed in the previous chapter, this was not a viable option for this thesis.

The implementation of the simulations was tested quite thoroughly. Agreement between simple theoretical cases and simulations was excellent, validating the implementation.

It was found that the temperature dependence for large particles/at low temperatures was quite well described by the analytical calculations, Eqs. (3.84) and (3.88). At elevated temperatures, the simulations and the calculations deviated. One reason for this could be that the calculations do not take the effect of superparamagnetic spin flips into account. Thus, at elevated temperatures, the simulations probably give a more accurate picture of the dynamics than the calculations.

The simulations show clearly that the Néel-Brown law to a very good approximation is valid for antiferromagnetic nanoparticles. The extracted values of K_2V are within uncertainties identical to the input.

8.2.1 16 nm

The results of the experiments on 16 nm particles were quite consistent, as is evident in Table 7.2. The energy barrier, K_2V was found to be 624(66) K from the temperature evolution of $A_{\mathrm{SPM}}/(A_{\mathrm{SPM}} + A_+ + A_-)$, 570 K from the temperature evolution of $\hbar\omega_\pm$ and K_2V = 726(200) K from the Néel-Brown law. These results are within the error bars of all previously reported results. One major difference between neutron scattering experiments and Mössbauer experiments is in the estimated value of the attempt frequency, τ_0, which is roughly an order of magnitude larger in Mössbauer experiments than in neutron scattering experiments. Furthermore, the temperature dependence of $A_{\mathrm{SPM}}/(A_{\mathrm{SPM}}+A_++A_-)$ is more pronounced in the IN5 experiment than theory predicts.

One explanation of this could be population of modes with $q > 0$: A_{SPM} measures the fraction of spins that are seen as static within the resolution of IN5, whereas $A_\pm$ are a measure of the fraction of spins that are moving. The simulations seem to support these conclusions. In the simulations, only $q = 0$ modes are simulated. Here, the temperature dependence of $A_{\mathrm{SPM}}/(A_{\mathrm{SPM}}+A_++A_-)$ follows the theory very closely. At 300 K, about 40% of the magnetic scattering is inelastic in the experiments.

The simulations matched the data quite well. In particular, the temperature dependence of the low frequency mode, $\hbar\omega_+$ matches the experiments well, showing that the decrease is indeed caused by thermal fluctuations. It was found from the simulations that the temperature dependence of κ_1 is not as pronounced as previously expected. This is mainly caused by $\hbar\omega_-$ not depending as much on s^z/s as expected from the theory.

In the simulations, fitting $\hbar\omega_\pm$ and $A_{\mathrm{SPM}}/(A_{\mathrm{SPM}} + A_+ + A_-)$ gave nearly identical results. The Néel-Brown law gave slightly smaller values of K_2V than what was expected. The discrepancy could perhaps be caused by the assumption that τ_0 remains constant over the entire temperature region, which is only an approximation [35].

From both simulations and experiments, it seems that B_X and ξ are very close to their bulk values.

In the simulations, it is possible to match all the experimentally determined parameters, except for the widths. The damping parameter, λ has quite a large influence on Γ and $\gamma_\pm$. We chose to decrease it to the point where the experimentally determined values of Γ and the simulated values matched. A side effect of this is that the values of $\gamma_\pm$ are severely underestimated in the simulations. One explanation for this is that in the simulations and the models we assume monodisperse particles. In the experiments we have a distribution of particle sizes. It is well known that κ_1 and κ_2 depend on particle size, and thus $\hbar\omega_\pm$ will be slightly different for different particle sizes. This will cause the observed peaks to broaden compared to the ideal situation. This could be checked by simulating a range of particle sizes and analyzing a weighted average of the power spectra. Unfortunately, time did not allow the pursuit of this idea. An illustration of the concept is shown in Fig. 8.1. Here, a single DHO with a well defined with an position is plotted alongside the sum of 1000 DHOs with the same width but position

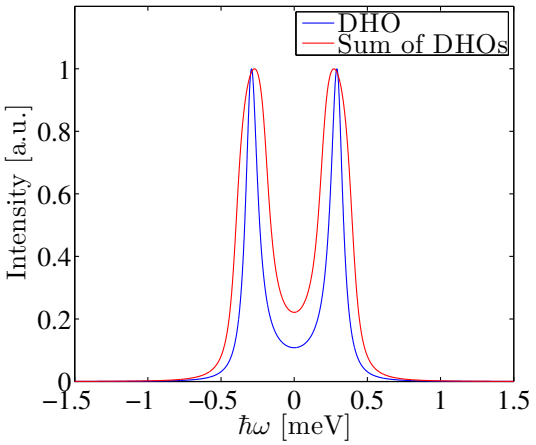

FIGURE 8.1: Illustration of broadening of signal by summing several narrow signals. The blue graph shows a single DHO, the red a sum of 1000 DHOs with the same width as the blue, but position varying between $\hbar\omega_0 = 0.2$ meV and 0.4 meV.

varying between $\hbar\omega_0 = 0.2$ meV and 0.4 meV. It is seen that the resulting peak function is significantly broader than the single DHO.

It would also be possible to increase λ to the point where the simulations and the data looked more similar. The downside of this would be an overestimation of Γ, which is harder to explain than an underestimation of $\gamma_{\pm}$.

Magnetic scattering was seen in the experiments at energies larger than $\hbar\omega_-$. This signal is quite weak, and has thus not been observed before. The origin is probably from either bulk impurities/large particles in the sample or from $q > 0$ modes.

It was shown that the modes are highly elliptic, with the $\hbar\omega_-$ mode barely visible at the (003) peak - the intensity was roughly 4% compared to the (101) peak. This makes it a reasonable assumption that all the the motion giving rise to the $\hbar\omega_+$-mode is only observed along the y-axis. With this assumption, the average orientation of the y and z axes within the basal plane of hematite were found, yielding, for the (101) peak, $1 - (\hat{q}^z)^2 = 0.573(17)$ and $1 - (\hat{q}^y)^2 = 0.519(17)$. The uncertainties are the standard deviation found between different temperatures and wavelengths. The values are close to being identical, and taking into account the errors introduced in assuming that the $\hbar\omega_+$-mode is only along the y axis, it is plausible that the orientation of the y and z axes are randomly distributed within the basal plane in the particles.

8.2.2 8 nm

Analyzing the experimental data for the 8 nm particles is more complicated than for the 16 nm particles. Most of the theory is developed as low temperature expansions, assuming the spins to move coherently and not deviate much from pointing along the easy axis. However, the experiments clearly show that most of the magnetic signal becomes inelastic at higher temperatures, invalidating this assumption. Never the less, the data could be fitted quite well with this simple model.

In the experiments, the frequency of the low frequency mode was seen to increase with temperature, a result that was most surprising the first time it was observed [12]. Furthermore, the anisotropy constants found from the Néel-Brown law and from the low temperature values of $\hbar\omega_+$, assuming B_X and ξ to be equal to the bulk values did not match. The increase of $\hbar\omega_+$ with temperature is what prompted the writing of the simulations [34]. We will first discuss the values of B_2, B_X and ξ before moving on to the rotor mode.

8.2.2.1 Parameter values

In this work it was found that several publications used a model in which the in-plane anisotropy, κ_1 was neglected. This provides values of K_2V that are up to a factor 2 larger than what would be expected if κ_1 is included.

With the aid of the simulations, it was possible to determine the optimal value of κ_2 from the relative area of the low frequency mode, A_+. It was found that κ_2 was close to the value found in Mössbauer spectroscopy and in the temperature evolution of $A_{\mathrm{SPM}}/(A_{\mathrm{SPM}} + A_+)$. As a consequence of this, the values of B_X and ξ can not both be equal to their bulk values. It was argued in Section 2.4.2 that the value of B_X can be up to $\sim 10\%$ smaller than the bulk value, and that $\xi \sim 1 - 1.02$ is realistic.

With the available data, it was not possible to determine both B_X and ξ. Any value of B_X has a corresponding value of ξ that matches the data as well as any other value of B_X, as illustrated in Fig. 7.20. It was therefore chosen to investigate the two limiting cases: a) $\xi = 1$, leading to $B_X = 450$ T and b) $B_X = 900$ T, leading to $\xi = 1.015$. A halving of the effective exchange field in 8 nm particles seems unrealistic, and the real values are probably quite close to option b. With $B_X = 800$ T, i.e. a reduction of $\sim$10% compared to the bulk value, the value $\xi = 1.014$ was found.

It would be interesting to use another technique to measure the uncompensated moment.

8.2.2.2 The rotor mode

With the aid of simulations, the mechanism responsible for the increase of $\hbar\omega_+$ with temperature in 8 nm particles was found. As the temperature is increased, the motion gradually shifts from oscillations around the energy minimum to faster rotations within the yz-plane - the rotor mode. In this model, only the $q = 0$ motion is assumed.

The rotor mode was directly observed in the real space pictures of the spin trajectories in Figs. 7.21 and 7.22. Here, it was also seen that the rotor mode is quite short lived. This means that it will be broad, as the mean precession time, τ_{rot} is inversely proportional to the width of the peak, γ_{rot}: $\tau_{\mathrm{rot}} \sim 1/\gamma_{\mathrm{rot}}$.

The broadness of the peak, and the presence of $\hbar\omega_+$ means that the peak from the rotor mode will be very hard, if not impossible, to distinguish from $\hbar\omega_+$ in a real experiment. Indeed, only a single peak was observed in the experiment on 8 nm particles. Thus, the effect of the rotor mode as observed in an experiment is to shift spectral

weight from lower energies to higher energies. Fitting the data to a single DHO provides a reasonable fit, but with an effective position somewhere between the position of the pure low frequency mode and the pure rotor mode. The width of this peak will be quite large.

This is exactly what was observed in the simulated power spectra, Fig. 7.16. At high damping, the data can be adequately fitted with a single DHO, and the value of $\hbar\omega_+$ from this DHO begins to increase as the temperature is increased. By reducing the damping in the simulations, we can reduce the width of γ_+. This made it possible to observe the rotor mode in the power spectra, as illustrated in Fig. 7.23.

In Figs. 7.17 and 7.18 the resulting parameters for low and high damping are shown. The center of the low frequency peak at low damping does not increase with temperature. The rotor peak begins to set in near 100 K and increases slightly with temperature. The temperature dependence is, however, not as pronounced as is expected from the calculations, and the calculations overestimate the frequency. This is not an artifact of the fitting procedure, as identical results are obtained by fitting the z component of the power spectra separately. The deviation between theory and simulations must therefore be explained by the assumptions made in the derivation of the rotor frequency. Time did not allow for a careful reinvestigation of the derivation.

Chapter 9

Conclusions and outlook

I will here summarize the results of this thesis, and provide an outlook for possible future work. In this thesis the magnetic dynamics of nanoscale hematite has been studied. The primary focus has been on nanoparticles, but in addition to this, several neutron scattering experiments on mesoporous hematite have been analyzed.

9.1 Conclusions

A total of 7 different neutron scattering experiments on hematite were presented and analyzed. Both of the magnetic $q = 0$ modes were simultaneously observed in 16 nm particles for the first time, and the analysis of the data lead to determination of the anisotropy constants and the average spin direction in the particles. Agreement was found between different experimental methods of obtaining the anisotropy constants. For 16 nm particles, the easy axis energy barrier was found to be $K_2V = 570(60)$ K, corresponding to $\kappa_2 = 1.34$ mK. The easy plane anisotropy barrier was significantly larger, $K_1V = -6.6(6) \times 10^3$ K at low temperatures, corresponding to $\kappa_1 = -15.5$ mK, decreasing with increasing temperature.

The mesoporus hematite showed distinct peaks corresponding to quantized excitations, but the asymmetry of the peaks was reminiscent of bulk hematite. The in-plane anisotropy constant of mesoporous hematite was also found, and shown to remain negative down to 1.5 K, explaining the absence of the Morin transition in mesoporous hematite. The values of κ_1 were in between those of nano and bulk, starting at $\kappa_1 = -1.7$ mK at low temperatures.

Langevin simulations proved to be a very useful tool in analyzing the neutron scattering data on hematite nanoparticles. In particular, effects such as the DM-interaction, uncompensated moment and temperature were incorporated in the simulations. The simulations showed that antiferromagnetic nanoparticles do indeed follow the Néel-Brown law to a good approximation. Excellent agreement between simulations and experiments was obtained for all experiments on 8 nm particles and 16 nm particles, and for all parameters but one: the widths of the excitations were significantly smaller

in the simulations than in the experiments. A likely explanation for this is the polydispersity of the particles in the experiments: The sum of similar signals with slightly different peak positions would combine to effectively broaden the peak.

Some errors in the literature have been identified and corrected. It is common to assume that hematite has only a uniaxial anisotropy, neglecting the stronger in-plane anisotropy. This leads to equations that are identical to those obtained by assuming a strong in-plane anisotropy, but with energy barriers that are a factor 2 larger than what is found in the correct model. With these corrections, agreement was found between Mössbauer data from the literature, neutron scattering data from the literature and the neutron scattering data analyzed in this thesis. Furthermore, we found that the expression for the macroscopic barrier for superparamagnetic spin flips in terms of the microscopic parameters should be corrected to $K_iV = \kappa_i ss'N$, slightly smaller than the value $K_iV = \kappa_i s^2 N$ quoted in the literature.

In the 8 nm particles, the rotor mode was observed both experimentally and in simulations, explaining the observed increase in excitation energy with temperature. At low damping the rotor mode could be distinguished from the $\hbar\omega_+$ mode in the simulations. The $\hbar\omega_+$ mode does not increase with temperature; the observed frequency increase is entirely caused by the rotor mode. The rotor frequency increases slightly with temperature as predicted, but the rotor frequency is larger in the simulations than theory predicts, by roughly 20%. The increase in observed frequency is thus caused by a shift of spectral weight towards higher energies as the amplitude of the rotor mode increases.

Assuming strong in-plane anisotropy as for the 16 nm particles, the easy axis anisotropy barrier was found from the simulations to be close the value measured by Mössbauer spectroscopy, $K_2V = 168$ K, or $\kappa_2 = 3.2$ mK, with errors estimated to 10-20%. The simulations furthermore showed that either a) the exchange field, B_X in 8 nm particles is reduced compared to the bulk value, or b) that the two sub-lattices are not equal such that the particles have a net uncompensated moment, $\xi > 1$, or c) a combination of the two. With the available data, it was not possible to determine precise values of B_X and ξ. Assuming a 10% decrease in B_X compared to bulk, $\xi = 1.014$ was found. The simulations are thus a useful tool to analyze experiments, providing an accurate determination of the parameters governing the magnetic dynamics of hematite nanoparticles.

9.2 Outlook

The incoherent background from water adsorbed to the particles is the main experimental challenge to overcome. It would be very interesting to measure the magnetic dynamics in hematite with polarized neutrons, to separate out the magnetic signal. Furthermore, investigating mesoporous hematite with a higher resolution than was used at IN5 would perhaps allow the low frequency mode to be resolved. In addition to these experiments, it would be interesting to measure even smaller nanoparticles. The high

frequency mode has still not been observed in 8 nm hematite nanoparticles. Observation of this would enable calculation of the in-plane anisotropy constant.

In the nanoparticles we have assumed that all spins can be treated equally. It would be interesting to extend the simulations to distinguish between surface spins and interior spins. Ideally, the motion of all spins would be simulated, but it is probably more realistic to divide the spins into four lattices: an interior spin up lattice, a surface spin up lattice and the similar spin down lattices.

Verifying that the rotor mode indeed occurs in other magnetic nanoparticles should be done. A good candiate could be NiO, which also has both an in-plane and easy-axis anisotropy.

Instead of comparing the analysis of the experimental data to the analysis of simulated data, it would be interesting to directly use the simulations to fit the experimental data. By varying an overall scale factor and B_X, B_1, B_2, λ (and possibly B_D), the simulations could be directly compared to the data, removing the need for approximations such as the DHO model. Unfortunately, the discrepancy between the measured and the simulated values of $\gamma_\pm$ would probably make it difficult to obtain a good fit.

Appendix A

Deriving the equations of motion

In this chapter, the derivation of the equations of motion is described in detail. We calculate each of the terms one by one, starting with exchange, then anisotropies, the magnetic field and finally the DM-term. We give the results both in terms of the x, y and z components of $\mathbf{s}$, as well as in terms of the raising and lowering operators. We find the equations of motion using

$$-i\frac{\mathrm{d}}{\mathrm{d}t}\mathbf{s} = [H, \mathbf{s}], \tag{A.1}$$

where, for simplicity, we have set $\hbar = 1$. The commutators of the spin operators are

$$[s_i^x, s_j^y] = is_i^z\delta_{ij}, \quad [s_i^y, s_j^z] = is_i^x\delta_{ij}, \quad [s_i^z, s_j^x] = is_i^y\delta_{ij}. \tag{A.2}$$

Some useful commutator identities are

$$[A, BC] = [A, B]C + B[A, C], \tag{A.3}$$
$$[AB, C] = A[B, C] + [A, C]B, \tag{A.4}$$
$$[AA, B] = A[A, B] + [A, B]A \tag{A.5}$$
$$[AB, A] = A[B, A] \tag{A.6}$$
$$[AB, B] = [A, B]B \tag{A.7}$$

A.1 The exchange part

The exchange part of the equations of motion for a spin m in the A lattice is

$$-i\frac{\mathrm{d}}{\mathrm{d}t}\mathbf{s}_m = \left[-2\sum_{i\in A, j\in B} J_{ij}\mathbf{s}_i\cdot\mathbf{s}_j - \sum_{i,k\in A} J_{ik}\mathbf{s}_i\cdot\mathbf{s}_k - \sum_{j,l\in B} J_{jl}\mathbf{s}_j\cdot\mathbf{s}_l,\ \mathbf{s}_m\right]. \tag{A.8}$$

The last term vanishes, and the other terms are only non-zero when $i = m$ or $k = m$, leading to

$$-i\frac{\mathrm{d}}{\mathrm{d}t}\mathbf{s}_m = \left[-2\sum_{j\in B} J_{ij}\mathbf{s}_m\cdot\mathbf{s}_j - \sum_{i\in A} J_{im}\mathbf{s}_i\cdot\mathbf{s}_m - \sum_{k\in A} J_{mk}\mathbf{s}_m\cdot\mathbf{s}_k,\ \mathbf{s}_m\right]. \tag{A.9}$$

We find

$$\begin{aligned}
-i\frac{\mathrm{d}}{\mathrm{d}t}\mathbf{s}_m &= \left[-2\sum_{j\in B} J_{ij}\mathbf{s}_m\cdot\mathbf{s}_j - \sum_{i\in A} J_{im}\mathbf{s}_i\cdot\mathbf{s}_m - \sum_{k\in A} J_{mk}\mathbf{s}_m\cdot\mathbf{s}_k,\ \mathbf{s}_m\right] && \text{(A.10)}\\
&= -2\sum_{j\in B} J_{mj}[s_m^x s_j^x + s_m^y s_j^y + s_m^z s_j^z, \mathbf{s}_m] && \text{(A.11)}\\
&\quad - \sum_{i\in A} J_{im}[s_i^x s_m^x + s_i^y s_m^y + s_i^z s_m^z, \mathbf{s}_m] && \text{(A.12)}\\
&\quad - \sum_{k\in A} J_{mk}[s_m^x s_k^x + s_m^y s_k^y + s_m^z s_k^z, \mathbf{s}_m], && \text{(A.13)}
\end{aligned}$$

Since $J_{ij} = J_{ji}$, and spins of different sites commute, this leads to

$$\begin{aligned}
-i\frac{\mathrm{d}}{\mathrm{d}t}\mathbf{s}_m &= -2\sum_{j\in B} J_{mj}[s_m^x s_j^x + s_m^y s_j^y + s_m^z s_j^z, \mathbf{s}_m] && \text{(A.14)}\\
&\quad - 2\sum_{i\in A} J_{im}[s_i^x s_m^x + s_i^y s_m^y + s_i^z s_m^z, \mathbf{s}_m]. && \text{(A.15)}
\end{aligned}$$

We finally reach

$$\frac{\mathrm{d}}{\mathrm{d}t}s_m^x = 2\sum_{j\in B} J_{mj}(s_m^y s_j^z - s_m^z s_j^y) + 2\sum_{i\in A} J_{mi}(s_m^y s_i^z - s_m^z s_i^y), \tag{A.16}$$

$$\frac{\mathrm{d}}{\mathrm{d}t}s_m^y = 2\sum_{j\in B} J_{mj}(s_m^z s_j^x - s_m^x s_j^z) + 2\sum_{i\in A} J_{mi}(s_m^z s_i^x - s_m^x s_i^z), \tag{A.17}$$

$$\frac{\mathrm{d}}{\mathrm{d}t}s_m^z = 2\sum_{j\in B} J_{mj}(s_m^x s_j^y - s_m^y s_j^x) + 2\sum_{i\in A} J_{mi}(s_m^x s_i^y - s_m^y s_i^x). \tag{A.18}$$

More compactly, we can write

$$\frac{\mathrm{d}}{\mathrm{d}t}s_m^x = 2\sum_{j\in A,B} J_{mj}(s_m^y s_j^z - s_m^z s_j^y), \tag{A.19}$$

$$\frac{\mathrm{d}}{\mathrm{d}t}s_m^y = 2\sum_{j\in A,B} J_{mj}(s_m^z s_j^x - s_m^x s_j^z), \tag{A.20}$$

$$\frac{\mathrm{d}}{\mathrm{d}t}s_m^z = 2\sum_{j\in A,B} J_{mj}(s_m^x s_j^y - s_m^y s_j^x). \tag{A.21}$$

In terms of the raising and lowering operators, we find

$$\frac{\mathrm{d}}{\mathrm{d}t}\left(s_m^x + is_m^y\right) = 2\sum_{j\in A,B} J_{mj}((s_m^y - is_m^x)s_j^z - s_m^z(s_j^y - is_j^x)) \tag{A.22}$$

$$\frac{\mathrm{d}}{\mathrm{d}t}\left(s_m^x - is_m^y\right) = 2\sum_{j\in A,B} J_{mj}((s_m^y + is_m^x)s_j^z - s_m^z(s_j^y + is_j^x)), \tag{A.23}$$

which can be rewritten as

$$\frac{\mathrm{d}}{\mathrm{d}t}s_m^+ = -2i\sum_{j\in A,B} J_{mj}(s_m^+ s_j^z - s_m^z s_j^+) \tag{A.24}$$

$$\frac{\mathrm{d}}{\mathrm{d}t}s_m^- = 2i\sum_{j\in A,B} J_{mj}(s_m^- s_j^z - s_m^z s_j^-). \tag{A.25}$$

A.2 The in-plane anisotropy

The in-plane anisotropy part of the equations of motion for a spin m in the A lattice is

$$-i\frac{\mathrm{d}}{\mathrm{d}t}\mathbf{s}_m = \left[-\sum_{i\in A}\kappa_{1i}(s_i^x)^2 - \sum_{j\in B}\kappa_{1j}(s_j^x)^2,\ \mathbf{s}_m\right]. \tag{A.26}$$

The second term vanishes, and the first term is only non-zero for $i = m$ so we find

$$-i\frac{\mathrm{d}}{\mathrm{d}t}\mathbf{s}_m = -\kappa_{1m}\left[(s_m^x)^2, \mathbf{s}_m\right]. \tag{A.27}$$

The x-component of the r.h.s. is zero. The y-component is

$$-i\frac{\mathrm{d}}{\mathrm{d}t}s_m^y = -\kappa_{1m}\left[(s_m^x)^2,\ s_m^y\right] \tag{A.28}$$

$$= -\kappa_{1m}\left(s_m^x[s_m^x, s_m^y] + [s_m^x, s_m^y]s_m^x\right) \tag{A.29}$$

$$= -\kappa_{1m}\left(is_m^x s_m^z + is_m^z s_m^x\right), \tag{A.30}$$

which is rewritten to

$$\frac{\mathrm{d}}{\mathrm{d}t}s_m^y = \kappa_{1m}\left(s_m^x s_m^z + s_m^z s_m^x\right). \tag{A.31}$$

Similarly, we find

$$\frac{\mathrm{d}}{\mathrm{d}t}s_m^z = -\kappa_{1m}\left(s_m^x s_m^y + s_m^y s_m^x\right). \tag{A.32}$$

In summary:

$$\frac{\mathrm{d}}{\mathrm{d}t}s_m^x = 0, \tag{A.33}$$

$$\frac{\mathrm{d}}{\mathrm{d}t}s_m^y = \kappa_{1m}\left(s_m^x s_m^z + s_m^z s_m^x\right), \tag{A.34}$$

$$\frac{\mathrm{d}}{\mathrm{d}t}s_m^z = -\kappa_{1m}\left(s_m^x s_m^y + s_m^y s_m^x\right). \tag{A.35}$$

To rewrite to raising and lowering operators, we use $s_m^x s_m^z = [s_m^x, s_m^z] + s_m^z s_m^x$. We find

$$\frac{\mathrm{d}}{\mathrm{d}t}s_m^y = \kappa_{1m}\left(2s_m^z s_m^x - i s_m^y\right). \tag{A.36}$$

Using

$$s_m^x = \frac{s_m^+ + s_m^-}{2}, \quad i s_m^y = \frac{s_m^+ - s_m^-}{2}, \tag{A.37}$$

we find

$$\frac{\mathrm{d}}{\mathrm{d}t}s_m^y = \kappa_{1m}\left(s_m^z(s_m^+ + s_m^-) - \frac{1}{2}(s_m^+ - s_m^-)\right) \tag{A.38}$$

$$= \frac{1}{2}\kappa_{1m}((2s_m^z - 1)s_m^+ + (2s_m^z + 1)s_m^-), \tag{A.39}$$

leading to

$$\frac{\mathrm{d}}{\mathrm{d}t}s_m^+ = i2\kappa_{1m}\left(\left(s_m^z - \frac{1}{2}\right)s_m^+ + s_m^-\left(s_m^z - \frac{1}{2}\right)\right), \tag{A.40}$$

$$\frac{\mathrm{d}}{\mathrm{d}t}s_m^- = -i2\kappa_{1m}\left(\left(s_m^z - \frac{1}{2}\right)s_m^+ + s_m^-\left(s_m^z - \frac{1}{2}\right)\right). \tag{A.41}$$

A.3 The easy axis anisotropy

The easy axis anisotropy part of the equations of motion for a spin m in the A lattice is

$$-i\frac{\mathrm{d}}{\mathrm{d}t}\mathbf{s}_m = \left[-\sum_{i\in A}\kappa_{2i}(s_i^z)^2 - \sum_{j\in B}\kappa_{2m}(s_j^z)^2, \mathbf{s}_m\right]. \tag{A.42}$$

The second term vanishes, and the first term is only non-zero for $i = m$ so we find

$$-i\frac{\mathrm{d}}{\mathrm{d}t}\mathbf{s}_m = -\kappa_{2m}\left[(s_m^z)^2, \mathbf{s}_m\right]. \tag{A.43}$$

The z-component of the r.h.s. is zero. The x-component is

$$-i\frac{\mathrm{d}}{\mathrm{d}t}s_m^x = -\kappa_{2m}\left[(s_m^z)^2, s_m^x\right] \tag{A.44}$$

$$= -\kappa_{2m}\left(s_m^z[s_m^z, s_m^x] + [s_m^z, s_m^x]s_m^z\right) \tag{A.45}$$

$$= -\kappa_{2m}\left(i s_m^z s_m^y + i s_m^y s_m^z\right), \tag{A.46}$$

which is rewritten to

$$\frac{\mathrm{d}}{\mathrm{d}t}s_m^x = \kappa_{2m}\left(s_m^z s_m^y + s_m^y s_m^z\right). \tag{A.47}$$

Similarly, we find

$$\frac{\mathrm{d}}{\mathrm{d}t}s_m^y = -\kappa_{2m}\left(s_m^z s_m^x + s_m^x s_m^z\right). \tag{A.48}$$

In summary:

$$\frac{\mathrm{d}}{\mathrm{d}t}s_m^x = \kappa_{2m}\left(s_m^z s_m^y + s_m^y s_m^z\right), \tag{A.49}$$
$$\frac{\mathrm{d}}{\mathrm{d}t}s_m^y = -\kappa_{2m}\left(s_m^z s_m^x + s_m^x s_m^z\right), \tag{A.50}$$
$$\frac{\mathrm{d}}{\mathrm{d}t}s_m^z = 0. \tag{A.51}$$

In terms of the raising and lowering operators, the equations become

$$\begin{aligned}
\frac{\mathrm{d}}{\mathrm{d}t}s_m^+ &= \kappa_{2m}\left(s_m^z s_m^y + s_m^y s_m^z - i s_m^z s_m^x - i s_m^x s_m^z\right) && \text{(A.52)}\\
&= \kappa_{2m}\left(s_m^z(s_m^y - i s_m^x) + (s_m^y - i s_m^x) s_m^z\right) && \text{(A.53)}\\
&= -i\kappa_{2m}\left(s_m^z s_m^+ + s_m^+ s_m^z\right) && \text{(A.54)}\\
&= -i\kappa_{2m}\left(2 s_m^z s_m^+ + [s_m^+, s_m^z]\right) && \text{(A.55)}\\
&= -i\kappa_{2m}\left(2 s_m^z - 1\right) s_m^+. && \text{(A.56)}\\
&= -i\kappa_{2m} s_m^+\left(2 s_m^z + 1\right). && \text{(A.57)}
\end{aligned}$$

Using similar calculations, or that $(s_m^+)^\dagger = s_m^-$ as well as $(AB)^\dagger = B^\dagger A^\dagger$, we find

$$\begin{aligned}
\frac{\mathrm{d}}{\mathrm{d}t}s_m^- &= \kappa_{2m}\left(s_m^z s_m^y + s_m^y s_m^z + i s_m^z s_m^x + i s_m^x s_m^z\right) && \text{(A.58)}\\
&= \kappa_{2m}\left(s_m^z(s_m^y + i s_m^x) + (s_m^y + i s_m^x) s_m^z\right) && \text{(A.59)}\\
&= i\kappa_{2m}\left(s_m^z s_m^- + s_m^- s_m^z\right) && \text{(A.60)}\\
&= i\kappa_{2m}\left(2 s_m^- s_m^z + [s_m^z, s_m^-]\right) && \text{(A.61)}\\
&= i\kappa_{2m} s_m^-\left(2 s_m^z - 1\right). && \text{(A.62)}\\
&= i\kappa_{2m}\left(2 s_m^z + 1\right) s_m^-. && \text{(A.63)}
\end{aligned}$$

Another way to write these equations is this:

$$\frac{\mathrm{d}}{\mathrm{d}t}s_m^+ = -i\kappa_{2m}\left(2 s_m^z - 1\right) s_m^+. \tag{A.64}$$
$$\frac{\mathrm{d}}{\mathrm{d}t}s_m^- = i\kappa_{2m} s_m^-\left(2 s_m^z - 1\right). \tag{A.65}$$

The difference between the $2s_m^z \pm 1$ terms is the ordering of the operators.

A.4 The magnetic field term

The magnetic field part of the equations of motion for a spin m in the A lattice is

$$-i\frac{\mathrm{d}}{\mathrm{d}t}\mathbf{s}_m = \left[-g\mu_\mathrm{B}\mathbf{B}\cdot\sum_{i\in A}\mathbf{s}_i - g\mu_\mathrm{B}\mathbf{B}\cdot\sum_{j\in B}\mathbf{s}_j, \mathbf{s}_m\right]. \tag{A.66}$$

The second term vanishes, and the first term is only non-zero for $i = m$ so we find

$$-i\frac{\mathrm{d}}{\mathrm{d}t}\mathbf{s}_m = -g\mu_\mathrm{B}\left[B^x s_m^x + B^y s_m^y + B^z s_m^z, \mathbf{s}_m\right], \tag{A.67}$$

leading to

$$\frac{\mathrm{d}}{\mathrm{d}t}s_m^x = -g\mu_\mathrm{B}\left(B^y s_m^z - B^z s_m^y\right), \tag{A.68}$$

$$\frac{\mathrm{d}}{\mathrm{d}t}s_m^y = -g\mu_\mathrm{B}\left(B^z s_m^x - B^x s_m^z\right), \tag{A.69}$$

$$\frac{\mathrm{d}}{\mathrm{d}t}s_m^z = -g\mu_\mathrm{B}\left(B^x s_m^y - B^y s_m^x\right). \tag{A.70}$$

We further find

$$\frac{\mathrm{d}}{\mathrm{d}t}s_m^+ = -ig\mu_\mathrm{B}\left(B^z s_m^+ - (B^x + iB^y)s^z\right), \tag{A.71}$$

$$\frac{\mathrm{d}}{\mathrm{d}t}s_m^- = ig\mu_\mathrm{B}\left(B^z s_m^- - (B^x - iB^y)s^z\right). \tag{A.72}$$

A.5 The DM-term

The DM part of the equations of motion for a spin m in the A lattice is

$$-i\frac{\mathrm{d}}{\mathrm{d}t}\mathbf{s}_m = \left[2\mathbf{e}_x\cdot\sum_{i\in A,j\in B}D_{ij}\mathbf{s}_i\times\mathbf{s}_j - \mathbf{e}_x\cdot\sum_{i,k\in A}D_{ik}\mathbf{s}_i\times\mathbf{s}_k - \mathbf{e}_x\cdot\sum_{j,l\in B}D_{jl}\mathbf{s}_j\times\mathbf{s}_l, \mathbf{s}_m\right]. \tag{A.73}$$

The last term vanishes, and the other terms are only non-zero when $i = m$ or $k = m$. Performing calculations similar to above, we find

$$\frac{\mathrm{d}}{\mathrm{d}t}s_m^x = -2\sum_{j\in A,B}D_{mj}(s_m^z s_j^z + s_m^y s_j^y), \tag{A.74}$$

$$\frac{\mathrm{d}}{\mathrm{d}t}s_m^y = 2\sum_{j\in A,B}D_{mj}s_m^x s_j^y, \tag{A.75}$$

$$\frac{\mathrm{d}}{\mathrm{d}t}s_m^z = 2\sum_{j\in A,B}D_{mj}s_m^x s_j^z, \tag{A.76}$$

using $D_{ij} = -D_{ji}$.

These cannot be written in terms of the raising and lowering operators.

Appendix B

Analytical calculations for small systems

This section is part of an internal document written by Kim Lefmann. It shows the results of exact calculations for small systems, extrapolating to larger systems. The main result is that the anisotropy barrier, KV is given by $KV = N\kappa_2 ss'$ and not $KV = N\kappa_2 s^2$ as has been used until now.

The equation of motion of a spin in a uniaxial anisotropy is from Eq. A.65

$$\frac{\mathrm{d}}{\mathrm{d}t} s_j^- = i\kappa_2 s_m^- \left(2s_j^z - 1\right). \tag{B.1}$$

We note that the frequency depends on the magnetization along the easy axis, s_j^z. This is due to the non-harmonicity of the anisotropy potential.

To interpret the difference between the movements of s_j^+ and s_j^-, let us look at the transition between the ground state $|m = s\rangle$ and the excited state $|m = s-1\rangle$. Here, the energy difference is $\hbar\omega = 2\kappa_2(s-1/2)$, corresponding to what is found for the frequency of s_j^- Eq. (B.1) in the positive-m ground state. Likewise, for the negative-m ground state we would use the frequency of the s_j^+ operator. When it can be assumed that the system is in its ground state, we can replace s_z with s, giving

$$\hbar\omega \approx 2\kappa_2(s - \frac{1}{2}) = 2\kappa_2 s', \tag{B.2}$$

where $s' = s - 1/2$.

Summing Eq. (B.1) over all sites, we obtain the equation of motion of the total spin lowering operator,

$$S^- = \frac{1}{\sqrt{N}} \sum_j s_j^-. \tag{B.3}$$

Assuming that all values of s_j^z are equal,

$$s_j^z = \langle s_j^z \rangle, \tag{B.4}$$

we reach

$$i\hbar\frac{d}{dt}S^- = \kappa_2 S^- \left(2\langle s^z\rangle - 1\right). \tag{B.5}$$

B.1 The easy-plane part

The easy-plane (κ_1 term) is in essence equal to the easy-axis term, just with the z-axis replaced by the x-axis. Thus, the equations of motion ends up being

$$-i\hbar\frac{d}{dt}s_j^{-x} = -\kappa_1 s_j^{-x}\left(-2s_j^x + 1\right), \tag{B.6}$$

where $s_j^{-x} = s_j^y + is_j^z$.

In the case, where both κ_1 and $k_\mathrm{B}T$ dominates κ_2, we can neglect κ_2, and the ground state is where the two sublattices are (anti)parallel. Here, s_j^x has the average eigenvalue 0, but I cannot derive the precession frequency analytically!

B.2 The easy-plane part, numerical solutions

In lack of an analytical solution, we here solve exactly the eigenvalue problem for one sublattice, for finite-sized systems of different spin values. We assume $|\kappa_1| \ll zJ_\mathrm{nn}$, and hence that we can approximate the lowest lying states of the sublattice by $|S, m\rangle$, where here m is the eigenvalue of S^x. The anisotropy energy can then be obtained through first order perturbation theory. Below, we mention the individual results for each spin value, and generalize to the infinite system.

$s = 1/2$

Here, the spin up and spin down states, $|\uparrow\rangle$ and $|\downarrow\rangle$ have equal anisotropy energy. Hence, the anisotropy energies are equal, leading to $\hbar\omega = 0$ for all states.

$s = 1$

The anisotropy energy is now different, $-\kappa_1$, for the states with $m = \pm 1$, $|\uparrow\rangle$ and $|\downarrow\rangle$, and 0 for the state with $m = 0$, $|\cdot\rangle$.

We briefly sketch the calculations for the $N = 2$, $S = 1$ system. We start by viewing the $|S = 2, m = 2\rangle$ state

$$\begin{aligned} |S = 2, m = 2\rangle &= |\uparrow\uparrow\rangle \\ \langle S = 2, m = 2|H_\mathrm{anis}|s = 2, m = 2\rangle &= -2\kappa_1. \end{aligned} \tag{B.7}$$

Using the total spin lowering operator, $S^- = N^{-1/2}\sum_i s_i^-$, we easily reach the $m = 1$ state:

$$\begin{aligned} |S=2,m=1\rangle &= cS^-|S=2,m=2\rangle \\ &= \frac{1}{\sqrt{2}}\left(|\cdot\uparrow\rangle + |\uparrow\cdot\rangle\right) \end{aligned} \tag{B.8}$$

$$\langle S=2,m=1|H_{\text{anis}}|s=2,m=1\rangle = -\kappa_1, \tag{B.9}$$

where c is a normalization constant. In the same way, we find the $m = 0$ state

$$\begin{aligned} |S=2,m=0\rangle &= S^-|S=2,m=1\rangle \\ &= \frac{1}{\sqrt{6}}\left(|\downarrow\uparrow\rangle + 2|\cdot\cdot\rangle + |\uparrow\downarrow\rangle\right) \end{aligned} \tag{B.10}$$

$$\langle S=2,m=0|H_{\text{anis}}|s=2,m=0\rangle = -\frac{2}{3}\kappa_1. \tag{B.11}$$

The precession frequencies, $\hbar\omega_m$, of S^- are given by the energy difference between the levels. For $N = 2$, these are $\hbar\omega_{m=2} = |\kappa_1|$ and $\hbar\omega_{m=1} = |\kappa_1|/3$. The $m = 0$ state is the ground state and could be assigned the negative frequency $\hbar\omega_{m=1} = -|\kappa_1|/3$, since the state with smaller m has a higher energy.

In table B.1, we show all numerical results for N values of 2, 3, and 4. The trend is very clear: The transition frequencies are always linear in normalized magnetization, m/m_{max}, and has the value $|\kappa_1|$ at the maximum magnetization as prescribed by (B.2). The offset value, $\hbar\omega_{m=0}$ extrapolates to zero as $1/N$. For a macroscopic spin number, the frequencies therefore becomes:

$$\hbar\omega_{s=1,m} = |\kappa_1|m/m_{\text{max}}. \tag{B.12}$$

$s = 3/2$

We treat this case exactly as for $s = 1$. The calculations are more tedious due to the larger number of spin states, and we have limited ourselves to 1, 2, and 3 spins. The results are shown in table B.2. Like for $s = 1$, all results are linear in the magnetization, and the large-N equation reads:

$$\hbar\omega_{s=3/2,m} = 2|\kappa_1|m/m_{\text{max}}. \tag{B.13}$$

Higher values of s

We did not calculate clusters of higher values of s. However, we know from (B.2) that the transition frequency for $m = m_{\text{max}}$ is $\hbar\omega_1 = |\kappa_1|(2s-1)$. Assuming the higher spin values to also display dispersions linear in m, with zero offset, we reach our final relation

$$\hbar\omega_{s,m} = (2s-1)|\kappa_1|\frac{m}{m_{\text{max}}}. \tag{B.14}$$

N	m	$m/m_{\max}$	$E_{\text{anis}}(m)/\lvert\kappa_1\rvert$		$\hbar\omega_m/\lvert\kappa_1\rvert$
1	1	1	1	Ns^2	1
	0	0	0	$Ns/2-1/2$	-1
2	2	1	2	Ns^2	1
	1	1/2	1		1/3
	0	0	2/3	$Ns/2-1/3$	-1/3
3	3	1	3	Ns^2	1
	2	2/3	2		3/5
	1	1/3	7/5		1/5
	0	0	6/5	$Ns/2-3/10$	-1/5
4	4	1	4	Ns^2	1
	3	3/4	3		5/7
	2	1/2	16/7		3/7
	1	1/4	13/7		1/7
	0	0	12/7	$Ns/2-2/7$	-1/7

TABLE B.1: Numerical results, showing anisotropy energies and transition frequencies for ferromagnetic (sublattice) clusters of $s = 1$ spins as a function of magnetization, measured in terms of $m_{\max} = Ns$.

N	m	$m/m_{\max}$	$E_{\text{anis}}(m)/\lvert\kappa_1\rvert$		$\hbar\omega_m/\lvert\kappa_1\rvert$
1	3/2	1	9/4	Ns^2	2
	1/2	1/3	1/4	$Ns/2-1/2$	0
2	3	1	9/2	Ns^2	2
	2	2/3	5/2		6/5
	1	1/3	13/10		2/5
	0	0	9/10	$Ns/2-3/5$	-2/5
3	9/2	1	27/4	Ns^2	2
	7/2	7/9	19/4		3/2
	5/2	5/9	13/4		1
	3/2	1/3	9/4		1/2
	1/2	1/9	7/4	$Ns/2-1/2$	0
4	6	1	9	Ns^2	2
	5	5/6	7		18/11
	4	2/3	59/11		14/11
	3	1/2	45/11		10/11
	2	1/3	35/11		6/11
	1	1/6	29/11		2/11
	0	0	27/11	$Ns/2-6/11$	-2/11

TABLE B.2: Numerical results, showing anisotropy energies and transition frequencies for ferromagnetic (sublattice) clusters of $s = 3/2$ spins as a function of magnetization, measured in terms of $m_{\max} = Ns$.

N	m	$m/m_{\max}$	$E_{\text{anis}}(m)/\lvert\kappa_1\rvert$	$\hbar\omega_m/\lvert\kappa_1\rvert$
N	Ns	1	Ns^2	$2(s-1/2)$
even	$Ns-1$	$1-1/(Ns)$	Ns^2-2	$2(s-1/2)-4/(2Ns-1)$
	$Ns-2$	$1-2/(Ns)$	$Ns^2-4+4/(2Ns-1)$	$2(s-1/2)-8/(2Ns-1)$
	...	...	...	...
	0	0	$Ns/2-1/2$	$-2/(2Ns-1)$

TABLE B.3: Extrapolation from numerical results, showing anisotropy energies and transition frequencies for ferromagnetic (sublattice) clusters of arbitrary spins s as a function of magnetization, measured in terms of $m_{\max} = Ns$.

This is exactly the same as precession around the x-axis in a field given by the strength $g\mu_{\text{B}}B_{\text{anis}} = \hbar\omega_{s,m}$ or

$$B_{\text{anis}} = 2\frac{(s-1/2)|\kappa_1|}{g\mu_{\text{B}}}\frac{\langle s^z\rangle}{s} \tag{B.15}$$

B.3 Bulk anisotropies

In nanoparticles, it is often convenient to express the anisotropy of a complete particle. In particular, the superparamagnetic relaxation is given by The Néel-Brown law

$$\tau = \tau_0 \exp(KV/k_{\text{B}}T), \tag{B.16}$$

where KV is the energy barrier of the uniaxial anisotropy.

According to our data in table B.3, the difference between the maximum and minimum anisotropy energy in the thermodynamic limit is $E_{\text{an,max}} - E_{\text{an,min}} = \kappa_2 Ns(s-1/2)$. Relating macroscopic and microscopic units, we then have

$$KV = \kappa_2 Ns(s-1/2). \tag{B.17}$$

Appendix C

Getting temperature into the equations

In this chapter we will briefly outline how to include temperature in the equations of motion. The text is highly inspired by [34]. We will sometimes use Einstein notation, in which summation of repeated indices is implied.

C.1 Langevin equation

The equation of motion for a single spin in a magnetic field is

$$\frac{\partial \mathbf{s}}{\partial t} = \gamma \mathbf{s} \times \mathbf{B}. \tag{C.1}$$

Thermal excitations are added as a random magnetic field, $\mathbf{b}$, while friction is a torque term that slows down the change of spin and thus is proportional to $\mathbf{s} \times \partial \mathbf{s}/\partial t$. We add friction and thermal excitations:

$$\frac{\partial \mathbf{s}}{\partial t} = \gamma \mathbf{s} \times (\mathbf{B} + \mathbf{b}) \pm \lambda \mathbf{s} \times \frac{\partial \mathbf{s}}{\partial t}. \tag{C.2}$$

For weak damping, λ, we can insert one iteration of $\partial \mathbf{s}/\partial t$:

$$\frac{\partial \mathbf{s}}{\partial t} = \gamma \mathbf{s} \times (\mathbf{B} + \mathbf{b}) \pm \lambda \mathbf{s} \times \left(\gamma \mathbf{s} \times (\mathbf{B} + \mathbf{b}) \pm \lambda \mathbf{s} \times \frac{\partial \mathbf{s}}{\partial t} \right). \tag{C.3}$$

Neglecting second order terms in λ we reach

$$\frac{\partial \mathbf{s}}{\partial t} = \gamma \mathbf{s} \times (\mathbf{B} + \mathbf{b}) - \lambda \gamma \mathbf{s} \times (\mathbf{s} \times \mathbf{B}). \tag{C.4}$$

The $\mathbf{b}$ field is random, and thus

$$\langle b_i \rangle = 0. \tag{C.5}$$

It can be shown that a good choice of $\mathbf{b}$ is

$$\langle b_i(t)b_j(t')\rangle = A\delta_{ij}\delta(t-t'), \tag{C.6}$$

where A will now be determined.

C.2 The total energy

The full Hamiltonian is

$$\begin{aligned}\mathcal{H} =& -2\sum_{i\in A,j\in B} J_{ij}\mathbf{s}_i\cdot\mathbf{s}_j - \sum_{i,k\in A} J_{ik}\mathbf{s}_i\cdot\mathbf{s}_k - \sum_{j,l\in B} J_{jl}\mathbf{s}_j\cdot\mathbf{s}_l \\ &- \sum_{i\in A}\kappa_{1i}(s_i^x)^2 - \sum_{j\in B}\kappa_{1j}(s_j^x)^2 - \sum_{i\in A}\kappa_{2i}(s_i^z)^2 - \sum_{j\in B}\kappa_{2j}(s_j^z)^2 \\ &- g\mu_{\mathrm{B}}\mathbf{B}\cdot\sum_{i\in A}\mathbf{s}_i - g\mu_{\mathrm{B}}\mathbf{B}\cdot\sum_{j\in B}\mathbf{s}_j \\ &- 2\mathbf{e}_x\cdot\sum_{i\in A,j\in B} D_{ij}\mathbf{s}_i\times\mathbf{s}_j - \mathbf{e}_x\cdot\sum_{i,k\in A} D_{ik}\mathbf{s}_i\times\mathbf{s}_k - \mathbf{e}_x\cdot\sum_{j,l\in B} D_{jl}\mathbf{s}_j\times\mathbf{s}_l,\end{aligned} \tag{C.7}$$

as described in Chapter. 3. Restricting to $q=0$ in nanoparticles, this becomes

$$\begin{aligned}\mathcal{H} =& 2N_A s^2\xi J^{\mathrm{AFM}}(0)\mathbf{s}_A\cdot\mathbf{s}_B \\ &- N_A s s'(\kappa_1(s_A^x)^2+\kappa_2(s_A^z)^2) - N_B s s'(\kappa_1(s_B^x)^2+\kappa_2(s_B^z)^2) \\ &- g\mu_{\mathrm{B}}s\mathbf{B}\cdot(N_A\mathbf{s}_A+N_B\mathbf{s}_B) \\ &2N_A s^2\xi D^{\mathrm{AFM}}(0)\mathbf{e}_x\cdot(\mathbf{s}_A\times\mathbf{s}_B).\end{aligned} \tag{C.8}$$

In terms of effective fields, the energy is given by

$$\begin{aligned}\frac{g\mu_B}{s}E =& N_A\xi B_X\mathbf{s}_A\cdot\mathbf{s}_B \\ &- \frac{N_A}{2}(B_1(s_A^x)^2+B_2(s_A^z)^2) - \frac{N_B}{s}(B_1(s_B^x)^2+B_2(s_B^z)^2) \\ &- g\mu_{\mathrm{B}}\mathbf{B}\cdot(N_A\mathbf{s}_A+N_B\mathbf{s}_B) \\ &N_A\xi B_D\mathbf{e}_x\cdot(\mathbf{s}_A\times\mathbf{s}_B).\end{aligned} \tag{C.9}$$

We now differentiate this with respect to $\mathbf{s}_A$:

$$\frac{g\mu_B}{N_A s}\frac{\partial E}{\partial\mathbf{s}_A} = \xi B_X\mathbf{s}_B - B_1 s_A^x - B_2 s_A^z - g\mu_{\mathrm{B}}\mathbf{B} + \xi B_D\begin{pmatrix}0\\ s_B^z\\ -s_B^y\end{pmatrix}, \tag{C.10}$$

which can be written as

$$\frac{\partial E}{\partial\mathbf{s}_A} = sN_A\mathbf{B}_{\mathrm{eff}}^A. \tag{C.11}$$

C.3 Probability current

We write the Langevin equation, (C.4) in the form

$$\frac{\partial x_i}{\partial t} = H_i(x) + f_i(x), \tag{C.12}$$

where H_i is a deterministic part, and f_i is a random part.

Let $p(x_t) = p$ be the probability distribution of a physical system having the configuration x at the time t. x and t are considered independent of p. But $p(x_t)$ is linked to $p(y_{t+\Delta t})$, because only a few choices of y have a chance to evolve into x in the time Δt.

Probability current is defined as

$$J_i = p\langle v_i \rangle, \tag{C.13}$$

where $v = \mathrm{d}x/\mathrm{d}t$. Using math, we can find

$$J_i = \frac{\langle \Delta x \rangle}{\Delta t} p(x) - \frac{1}{2} \frac{\langle \Delta x_i \Delta x_j \rangle}{\Delta t} \frac{\partial p}{\partial x_j} \quad \text{for} \quad \Delta t \to 0. \tag{C.14}$$

It can also be shown that

$$\langle \Delta x_i \rangle = H_i \Delta t, \tag{C.15}$$

and

$$\langle \Delta x_i \Delta x_j \rangle = \int_t^{t+\Delta t} dt' \int_t^{t+\Delta t} dt'' \langle f_i(t') f_j(t'') \rangle. \tag{C.16}$$

More calculations can give us

$$\mathbf{J}_A = \left(\gamma \mathbf{s}_A \times \mathbf{B}_{\text{eff}}^A - \lambda\gamma \mathbf{s}_A \times \left(\mathbf{s}_A \times \mathbf{B}_{\text{eff}}^A\right)\right) p + \frac{1}{2}\gamma^2 A \mathbf{s}_A \times \left(\mathbf{s}_A \times \frac{\partial p}{\partial \mathbf{s}_A}\right) \tag{C.17}$$

$$= \gamma \mathbf{s}_A \times \mathbf{B}_{\text{eff}}^A p + \mathbf{s}_A \times \left(\mathbf{s}_A \times \left(-\lambda\gamma \mathbf{B}_{\text{eff}}^A p + \frac{1}{2}\gamma^2 A \frac{\partial p}{\partial \mathbf{s}_A}\right)\right). \tag{C.18}$$

Thermal equilibrium requires the second term to be zero:

$$\lambda\gamma \mathbf{B}_{\text{eff}}^A p = \frac{1}{2}\gamma^2 A \frac{\partial p}{\partial \mathbf{s}_A}. \tag{C.19}$$

From

$$p = \frac{1}{Z} \exp\left(-\beta E\right) \tag{C.20}$$

we find

$$\frac{\partial p}{\partial \mathbf{s}_A} = -\beta \frac{\partial E}{\partial \mathbf{s}_A} p. \tag{C.21}$$

Comparing with above, we finally reach

$$A_A = 2\frac{\lambda}{\gamma g \mu_B s N_A} k_B T. \tag{C.22}$$

Appendix D

Extra simulations

In this chapter, most of the scans described in Section 7.4.1.2 are shown.

D.1 16 nm

Here, the initial scans to determine the influence of the parameters in the simulations on the fitted values are shown. In Fig. D.1 the result of varying N is shown.

The result of changing B_2 is shown in Fig. D.2. Γ decreases with increasing B_2 and $\hbar\omega^+$ increases. A_{SPM} increases with increasing B_2, while A_+ decreases.

The result of scanning B_1 is shown in Fig. D.3. We see that B_1 only influences A_- and $\hbar\omega^-$.

The result of scanning B_X is shown in Fig. D.4. B_X has little influence on the areas. Γ slightly decreases with increasing B_X, whereas $\gamma^{\pm}$ slightly increases increasing B_X. The frequencies of the modes increase as expected.

In the next scan, we adjust B_X and B_2 and B_1, such that $B_X B_2$ and $B_X B_1$ are kept constant. The result of scanning B_X in this way are shown in Fig. D.5.

Finally, we scan ξ, Fig. D.6. Increasing ξ shifts the energies, as expected, and also slightly reduces A^-.

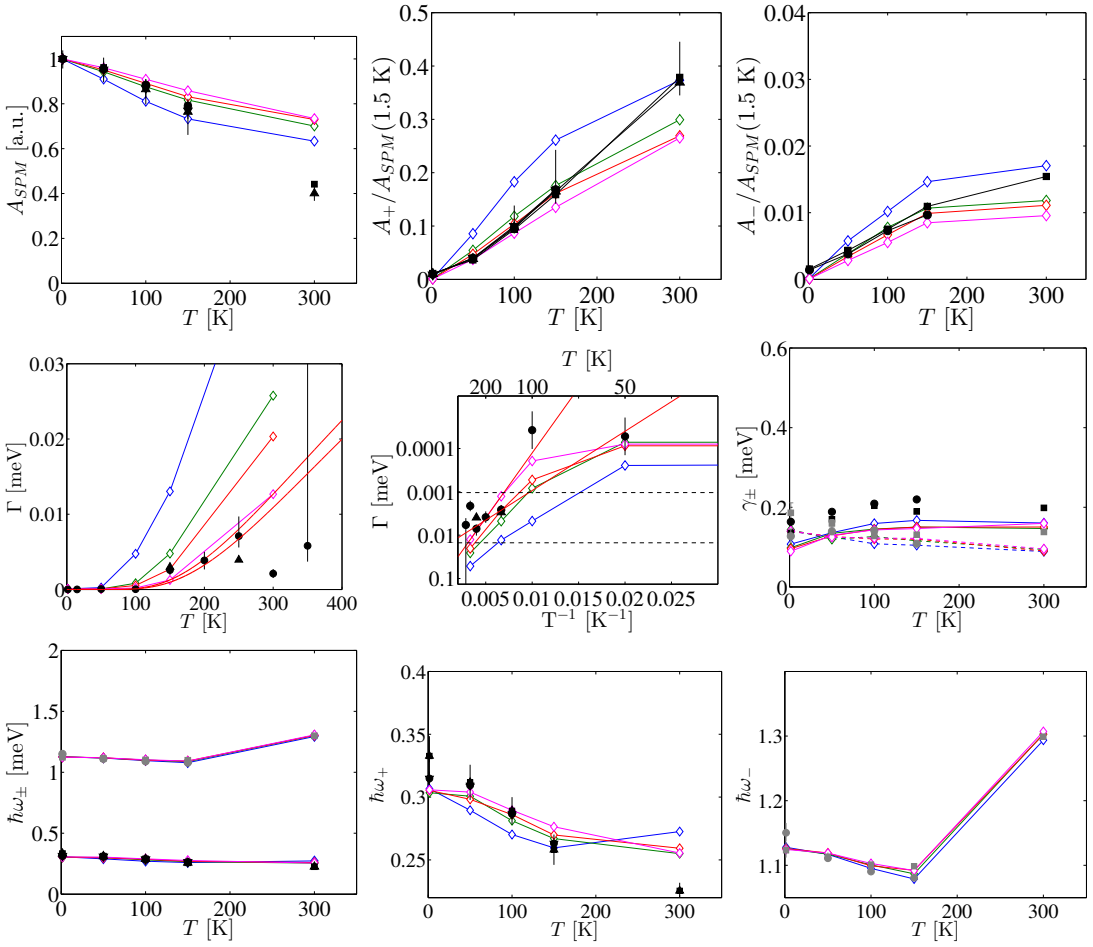

FIGURE D.1: Scan of N. 0.5×10^5 (blue), 0.75×10^5 (green), 8.5×10^5 (red), 1.02×10^5 (magenta). First row shows the areas, from left to right: A_{SPM}, A_+ and A_-. Second row shows the widths, from left to right: Γ, Γ on a scale where the Néel-Brown law is a straight line and $\gamma^\pm$. Third row shows the $q=0$ spin wave frequencies, $\hbar\omega^\pm$. From left to right: Both peaks, $\hbar\omega^+$ and $\hbar\omega^-$.

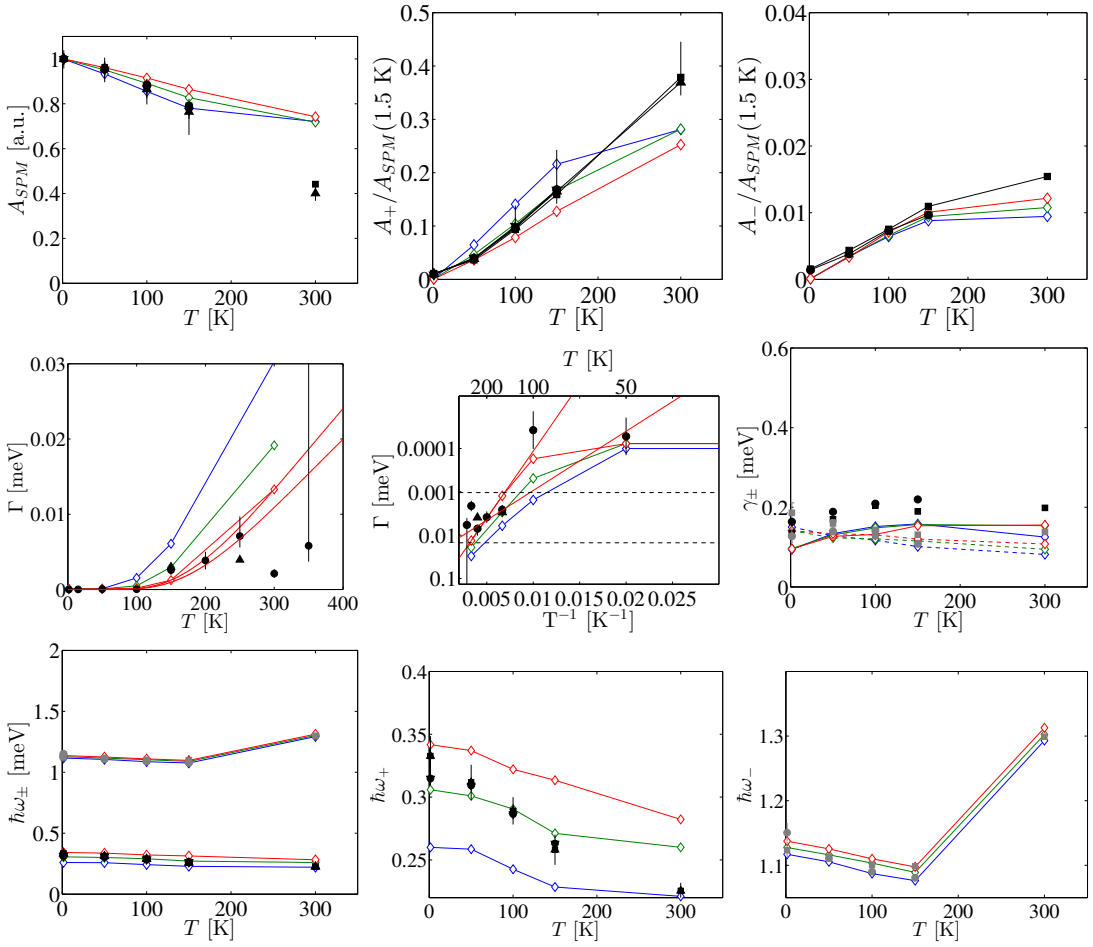

FIGURE D.2: Scan B_2. 3.03 T (purple), 4.04 mT (green), 5.06 mT (red). First row shows the areas, from left to right: A_{SPM}, A_+ and A_-. Second row shows the widths, from left to right: Γ, Γ on a scale where the Néel-Brown law is a straight line and $\gamma^{\pm}$. Third row shows the $q = 0$ spin wave frequencies, $\hbar\omega^{\pm}$. From left to right: Both peaks, $\hbar\omega^+$ and $\hbar\omega^-$.

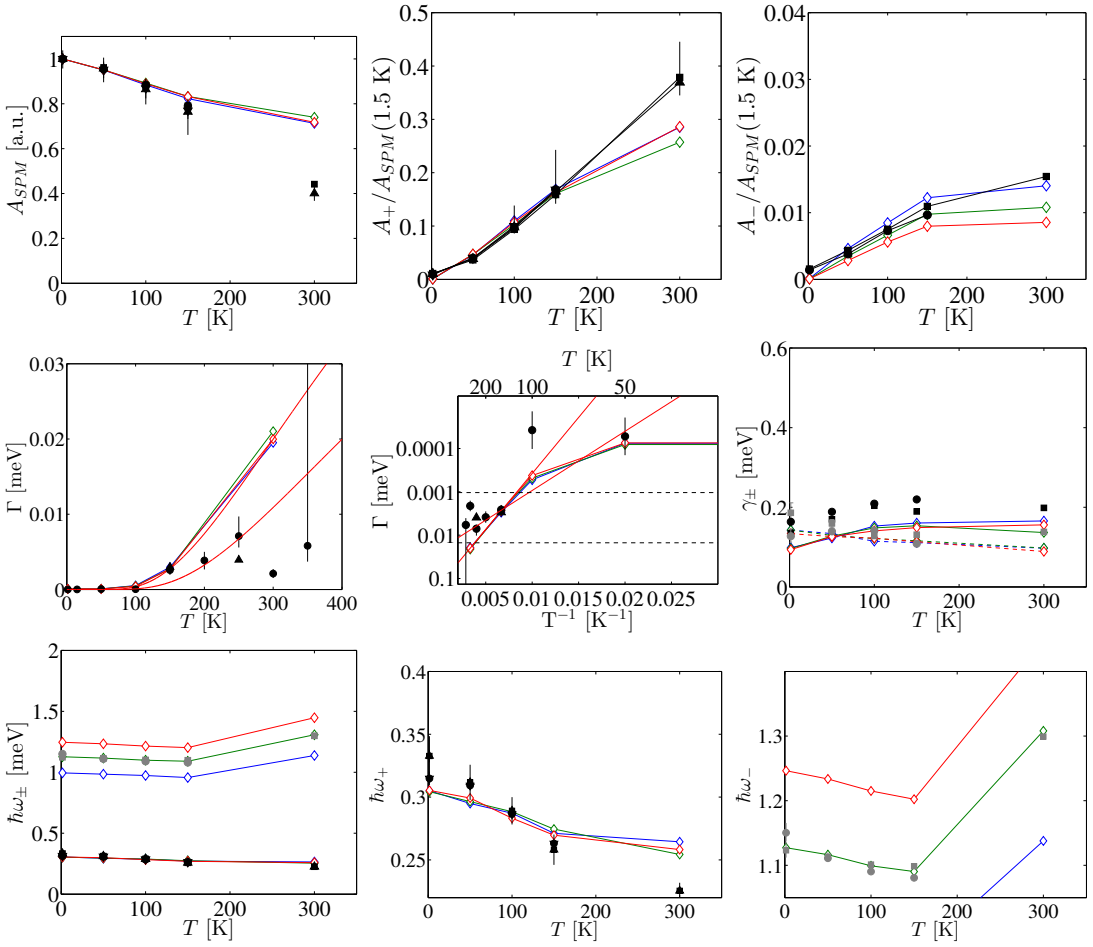

FIGURE D.3: Scan B_1, multiplying the value by 0.75 (blue), 1 (green), 1.25 (red). First row shows the areas, from left to right: A_{SPM}, A_+ and A_-. Second row shows the widths, from left to right: Γ, Γ on a scale where the Néel-Brown law is a straight line and $\gamma^{\pm}$. Third row shows the $q = 0$ spin wave frequencies, $\hbar\omega^{\pm}$. From left to right: Both peaks, $\hbar\omega^{+}$ and $\hbar\omega^{-}$.

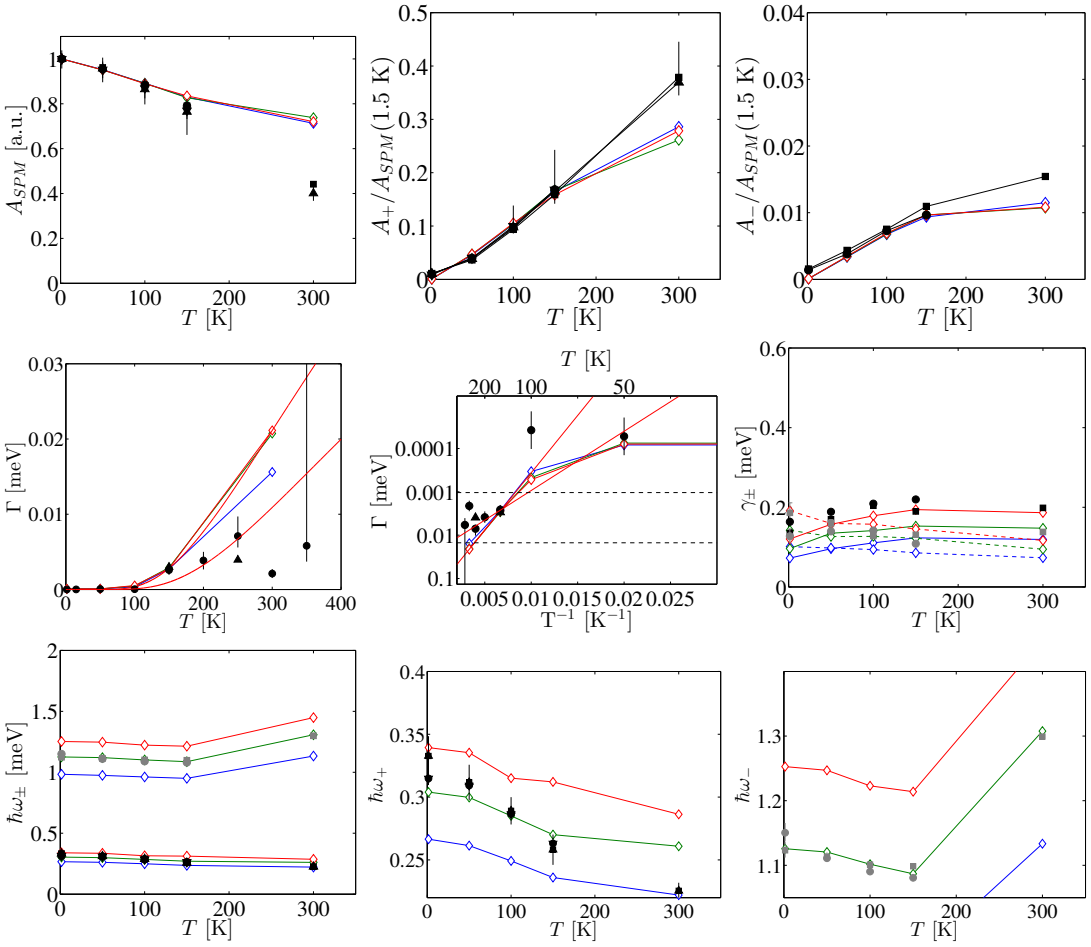

FIGURE D.4: Scan B_X. 675 T (blue), 900 T (green), 1125 T (red). First row shows the areas, from left to right: A_{SPM}, A_+ and A_-. Second row shows the widths, from left to right: Γ, Γ on a scale where the Néel-Brown law is a straight line and $\gamma^{\pm}$. Third row shows the $q = 0$ spin wave frequencies, $\hbar\omega^{\pm}$. From left to right: Both peaks, $\hbar\omega^{+}$ and $\hbar\omega^{-}$.

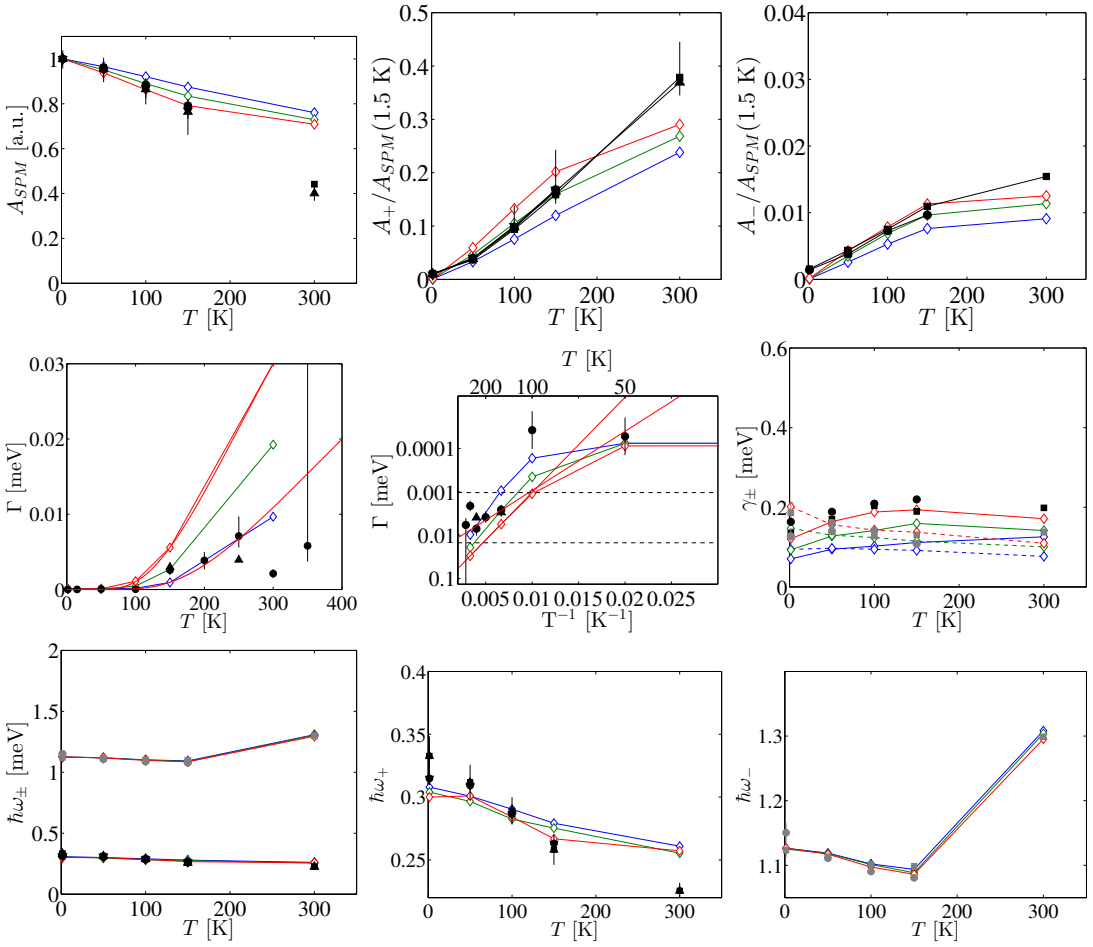

FIGURE D.5: Scan B_X and scale B_1 and B_2 accordingly. Multiply by 0.75 (blue), 1 (green) and 1.25 (red). First row shows the areas, from left to right: A_{SPM}, A_+ and A_-. Second row shows the widths, from left to right: Γ, Γ on a scale where the Néel-Brown law is a straight line and $\gamma^{\pm}$. Third row shows the $q = 0$ spin wave frequencies, $\hbar\omega^{\pm}$. From left to right: Both peaks, $\hbar\omega^+$ and $\hbar\omega^-$.

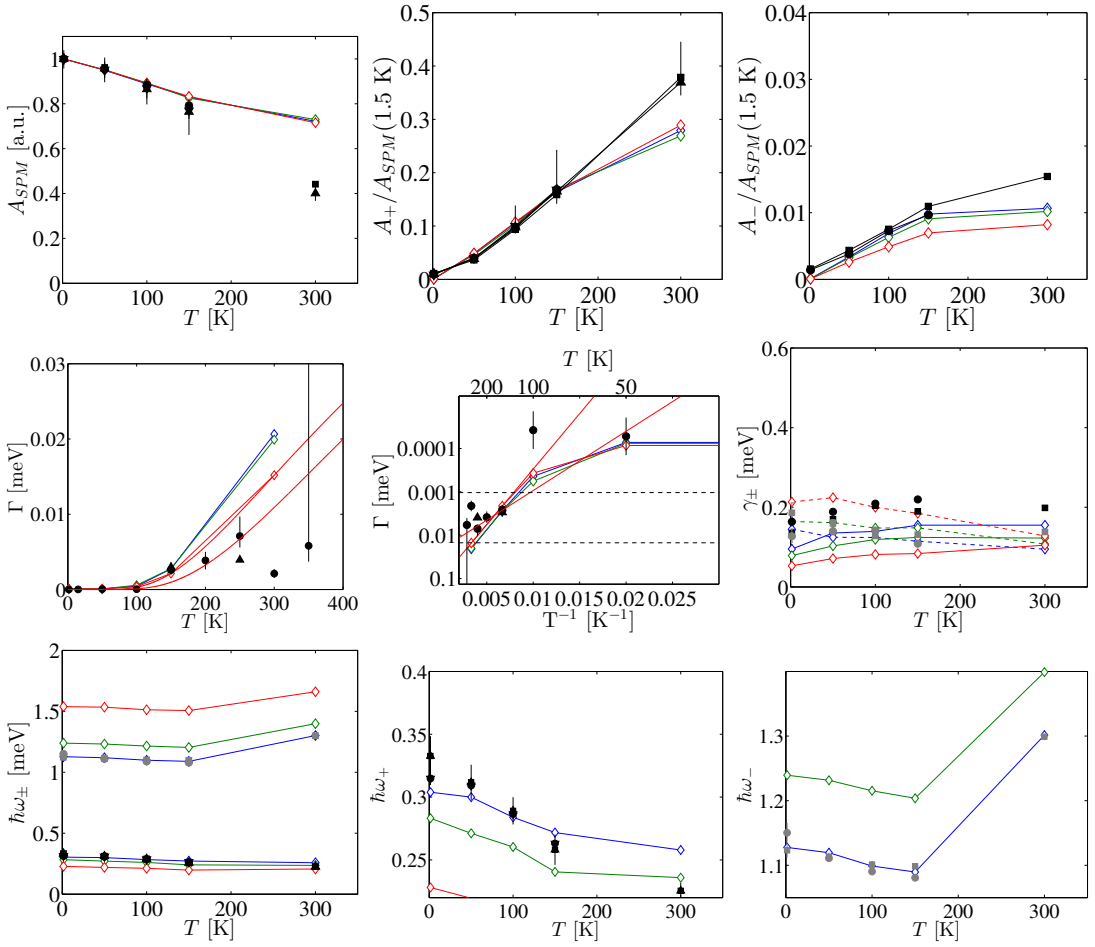

FIGURE D.6: Scan B_X and scale B_1 and B_2 accordingly. Multiply by 0.75 (blue), 1 (green) and 1.25 (red). First row shows the areas, from left to right: A_{SPM}, A_+ and A_-. Second row shows the widths, from left to right: Γ, Γ on a scale where the Néel-Brown law is a straight line and $\gamma^{\pm}$. Third row shows the $q = 0$ spin wave frequencies, $\hbar\omega^{\pm}$. From left to right: Both peaks, $\hbar\omega^+$ and $\hbar\omega^-$.

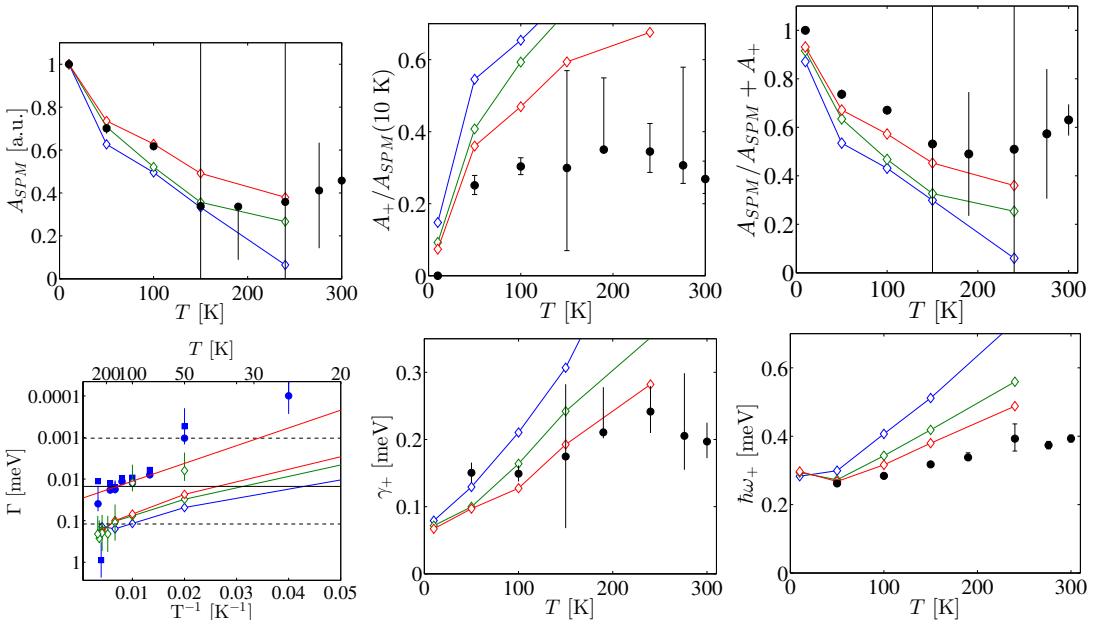

FIGURE D.7: Scan of N for the 8 nm particles, $N = 0.75 \times 10^4$ (blue), $N = 1.27 \times 10^4$ (green), $N = 1.5 \times 10^4$ (red).

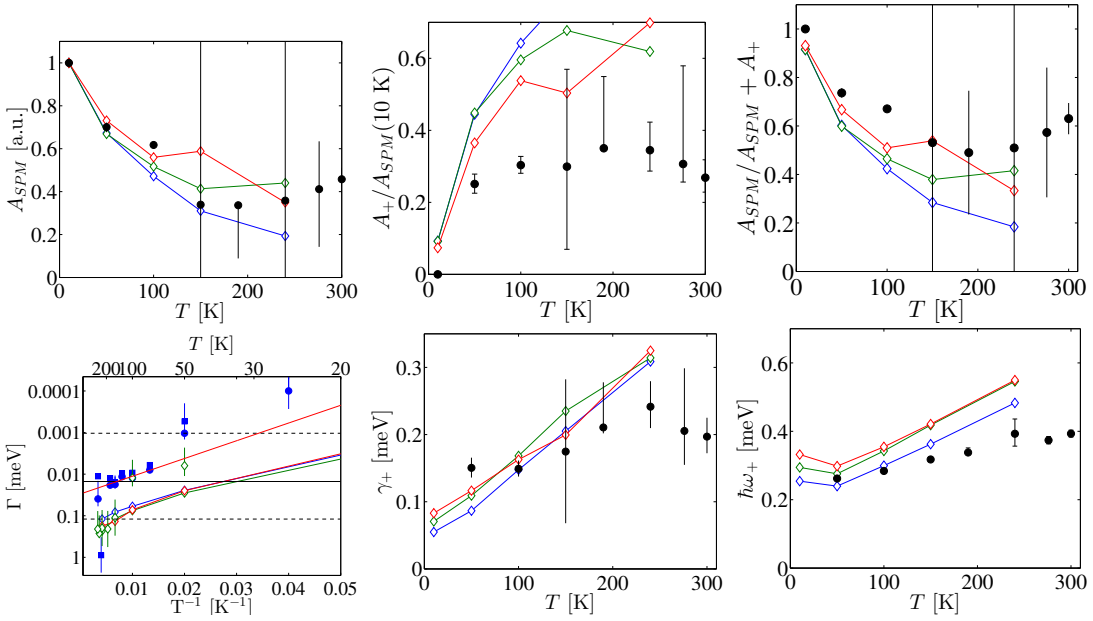

FIGURE D.8: Scan of B_X for the 8 nm particles, $B_X = 675$ T (blue), $B_X = 900$ T (green), $B_X = 1125$ T (red).

D.2 8 nm

Here, the results of varying the parameters for the 8 nm particles are shown. The result of varying N is shown in Fig. D.7. A larger value of N reduces the value of $\hbar\omega_+$ at elevated temperatures.

The result of varying B_X is shown in Fig. D.7. Larger values of B_X increase Γ, γ_+ and $\hbar\omega_+$ at elevated temperatures.

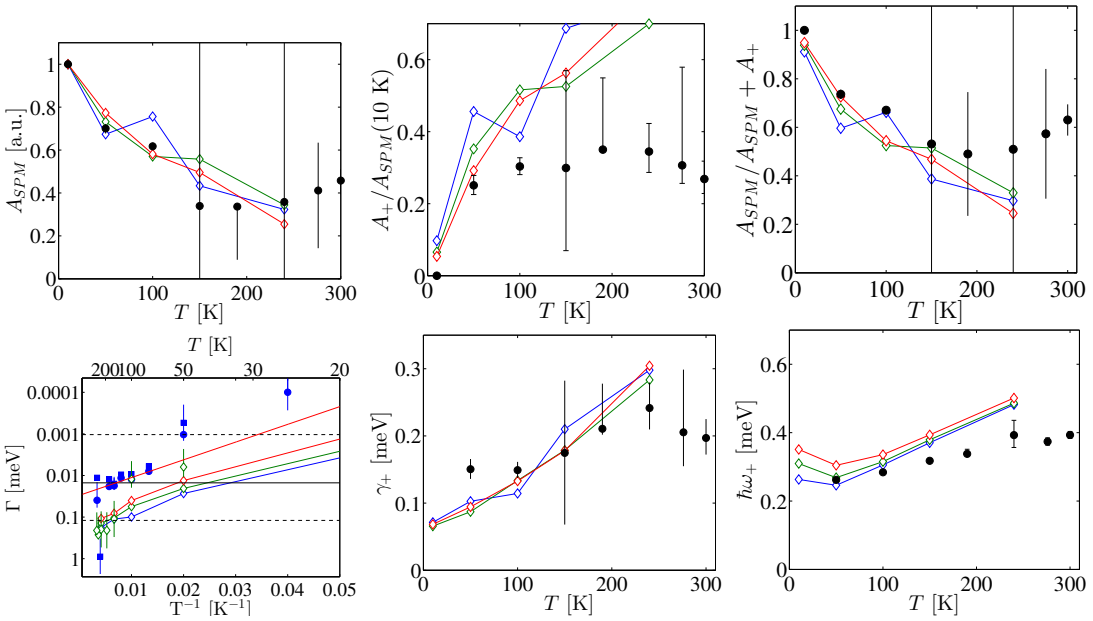

FIGURE D.9: Scan of B_2 for the 8 nm particles, $B_2 = 3.12$ mT (blue), $B_2 = 4.16$ mT (green), $B_2 = 5.20$ mT (red).

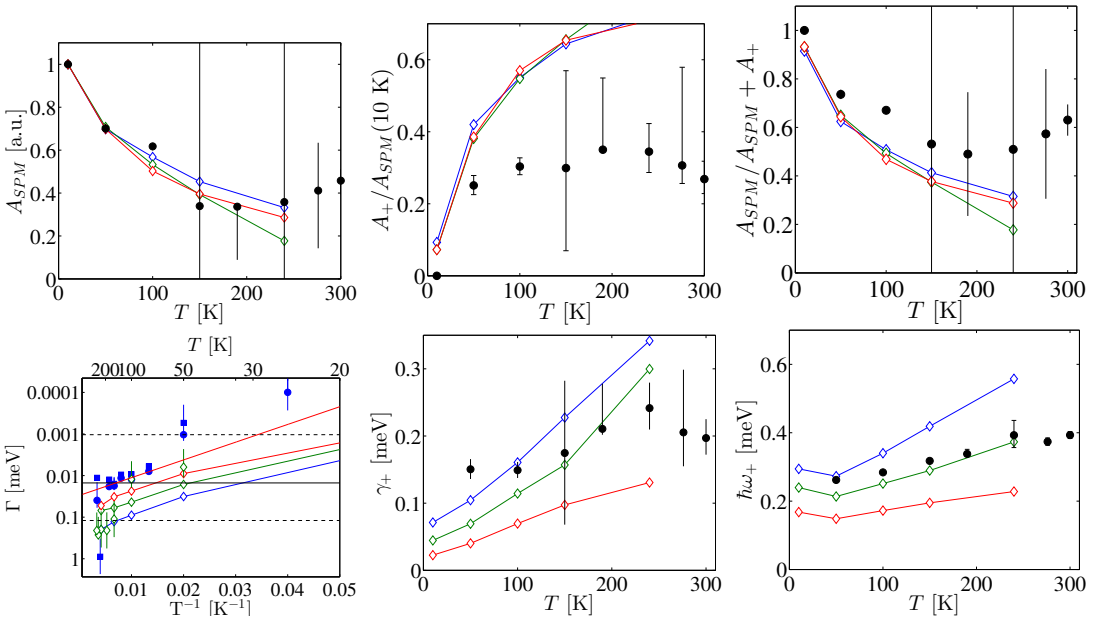

FIGURE D.10: Scan of ξ for the 8 nm particles, $\xi = 1$ (blue), $\xi = 1.0075$ (green), $\xi = 1.015$ (red).

The result of varying B_2 is shown in Fig. D.7. Increasing B_1 primarily changes the value of $\hbar\omega_+$ at low temperatures, not so much at higher temperatures. Also, Γ decreases with B_2

We finally vary ξ as shown in Fig. D.7. A larger value of ξ reduces Γ, γ_+ and $\hbar\omega_+$

The result of varying B_X while varying B_2 accordingly is shown in Fig. D.7. Larger values of B_X increase Γ, γ_+ and $\hbar\omega_+$ at elevated temperatures.

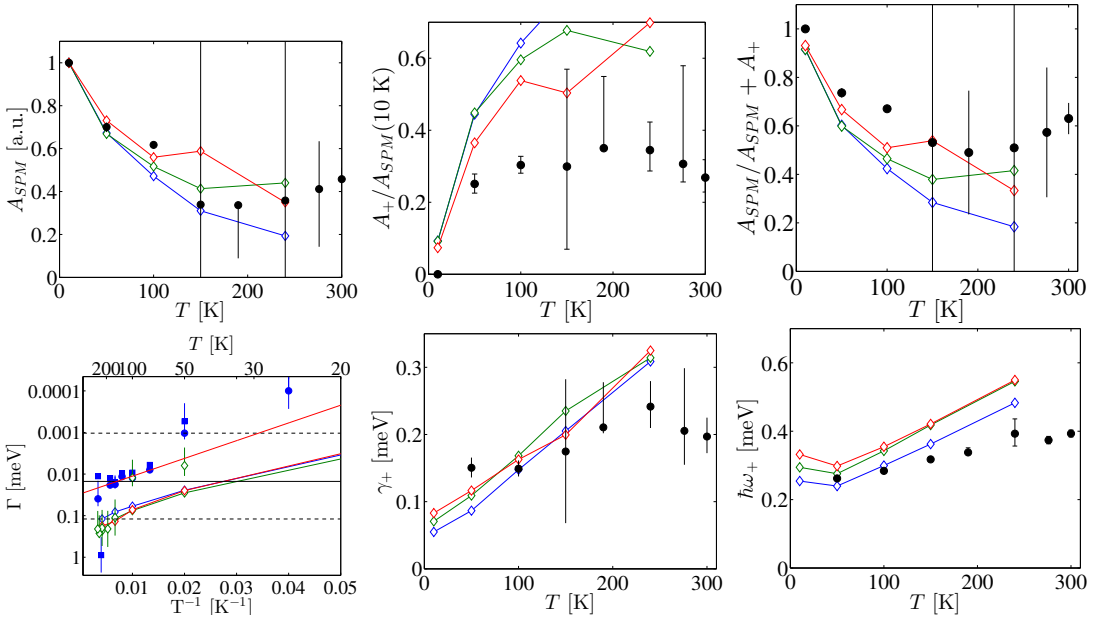

FIGURE D.11: Scan of B_X for the 8 nm particles, while varying B_2 accordingly, B_X = 675 T (blue), B_X = 900 T (green), B_X = 1125 T (red).

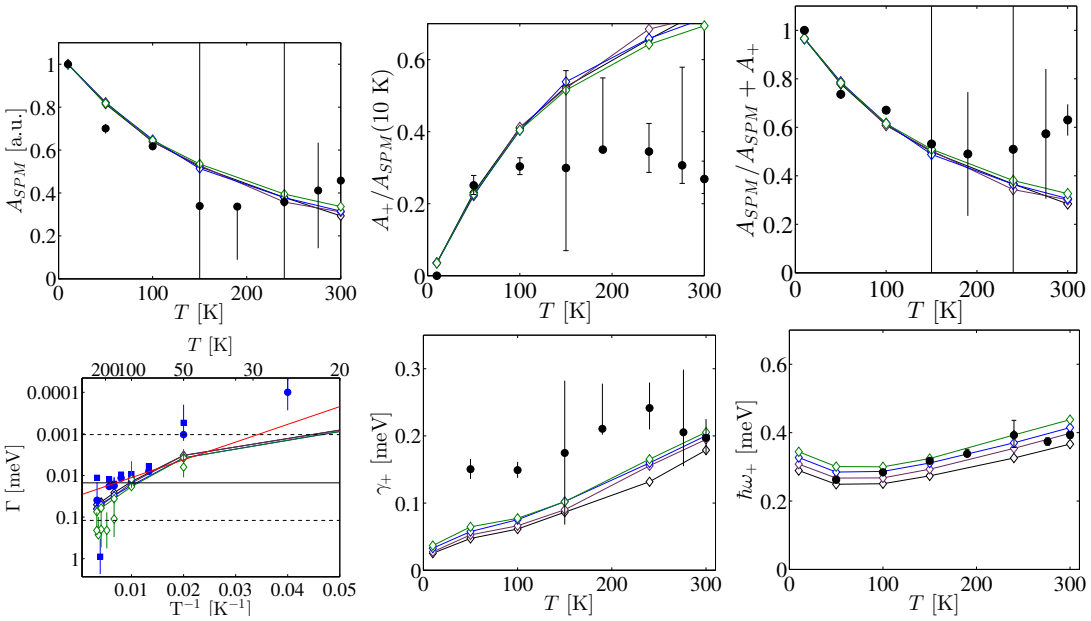

FIGURE D.12: Scan of B_X for the 8 nm particles for $\xi = 1$. $B_X = 350\ T$ (black), $B_X = 400$ T (purple), $B_X = 450$ T (blue) and $B_X = 500$ T (green).

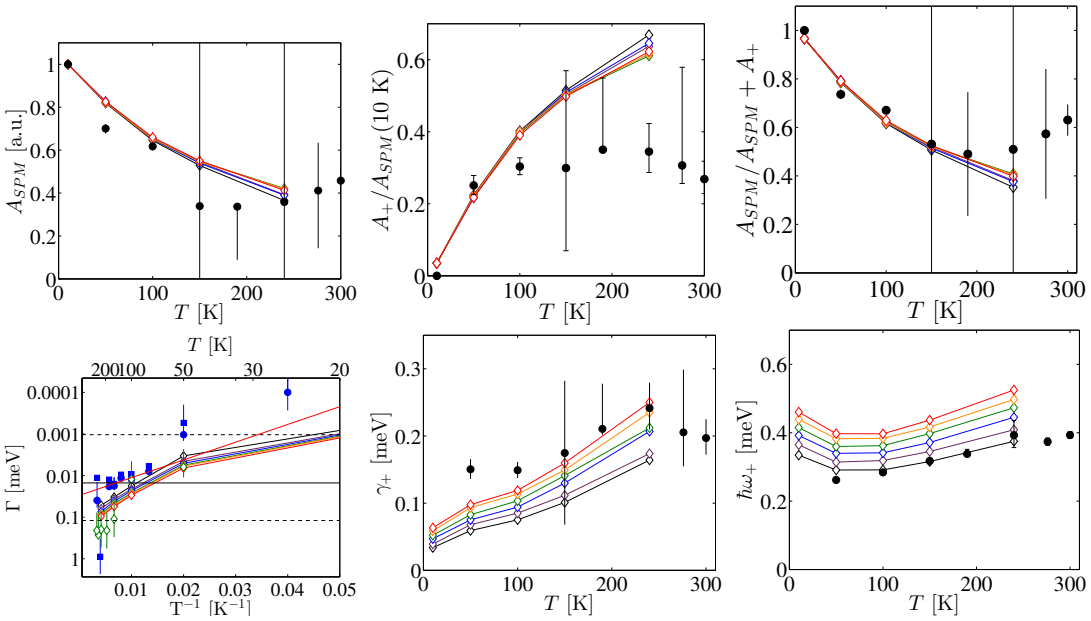

FIGURE D.13: Scan of B_X for the 8 nm particles for $\xi = 1.005$. $B_X = 500\ T$ (black), $B_X = 600$ T (purple), $B_X = 700$ T (blue) $B_X = 800$ T (green), $B_X = 900$ T (orange) , $B_X = 1000$ T (red).

D.2.1 Varying B_X for different values of ξ

Here, the results of varying B_X for different values of ξ are shown, for ξ=1 (Fig. D.12), $\xi = 1.005$ (Fig. D.13), $\xi = 1.010$ (Fig. D.14) and $\xi = 1.015$ (Fig. D.15.

Finally, Fig. D.16 shows the the result of varying ξ for $B_X = 900$ T.

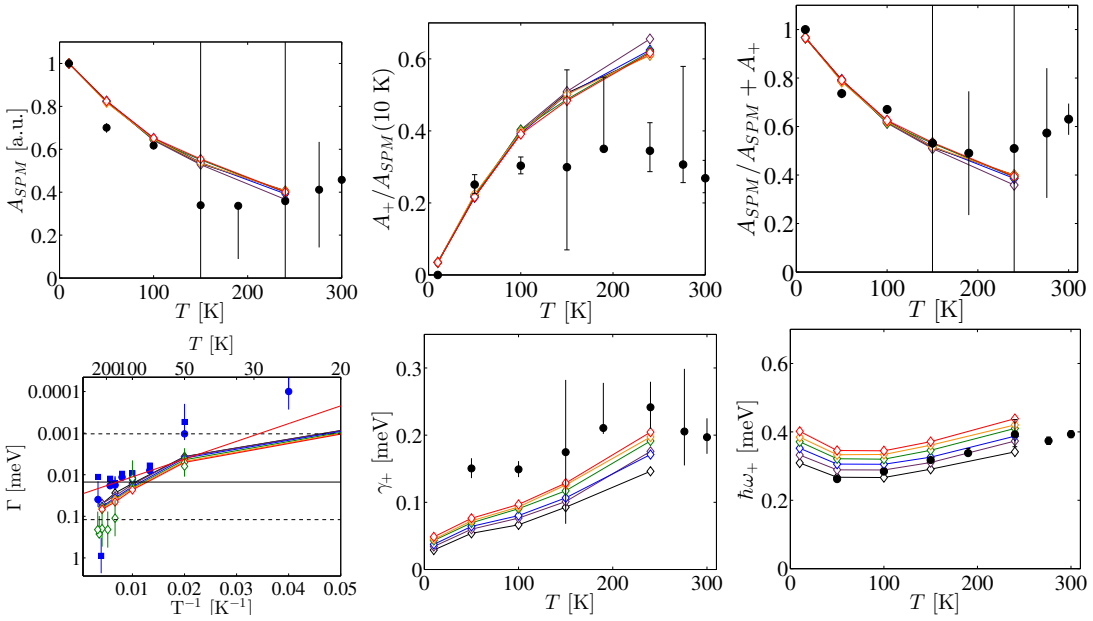

FIGURE D.14: Scan of B_X for the 8 nm particles for $\xi = 1.010$. $B_X = 500\ T$ (black), $B_X = 600$ T (purple), $B_X = 700$ T (blue) $B_X = 800$ T (green), $B_X = 900$ T (orange) , $B_X = 1000$ T (red).

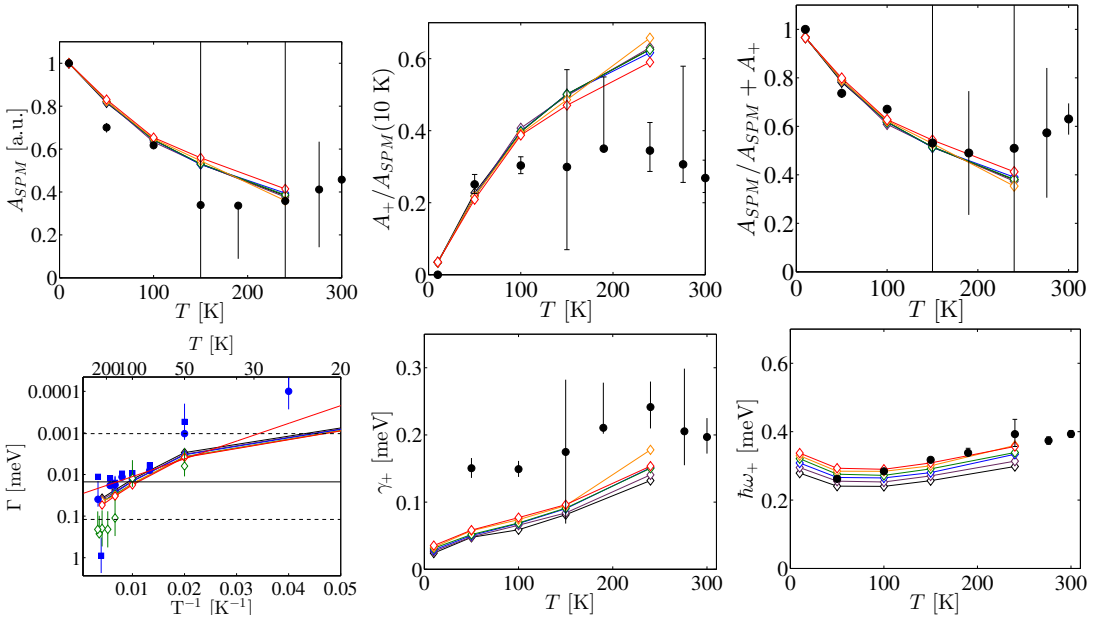

FIGURE D.15: Scan of B_X for the 8 nm particles for $\xi = 1.010$. $B_X = 500\ T$ (black), $B_X = 600$ T (purple), $B_X = 700$ T (blue) $B_X = 800$ T (green), $B_X = 900$ T (orange) , $B_X = 1000$ T (red).

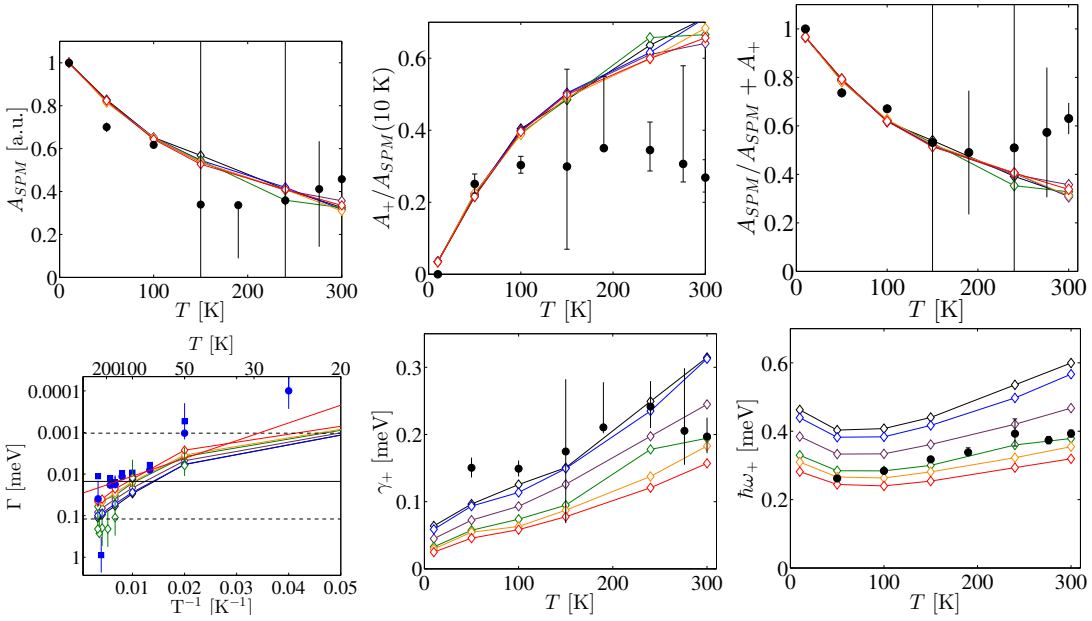

FIGURE D.16: Scan of ξ. 1 (black), 1.005 (purple), 1.010 (blue), 1.015 (green), 1.017 (orange), 1.020 (red).

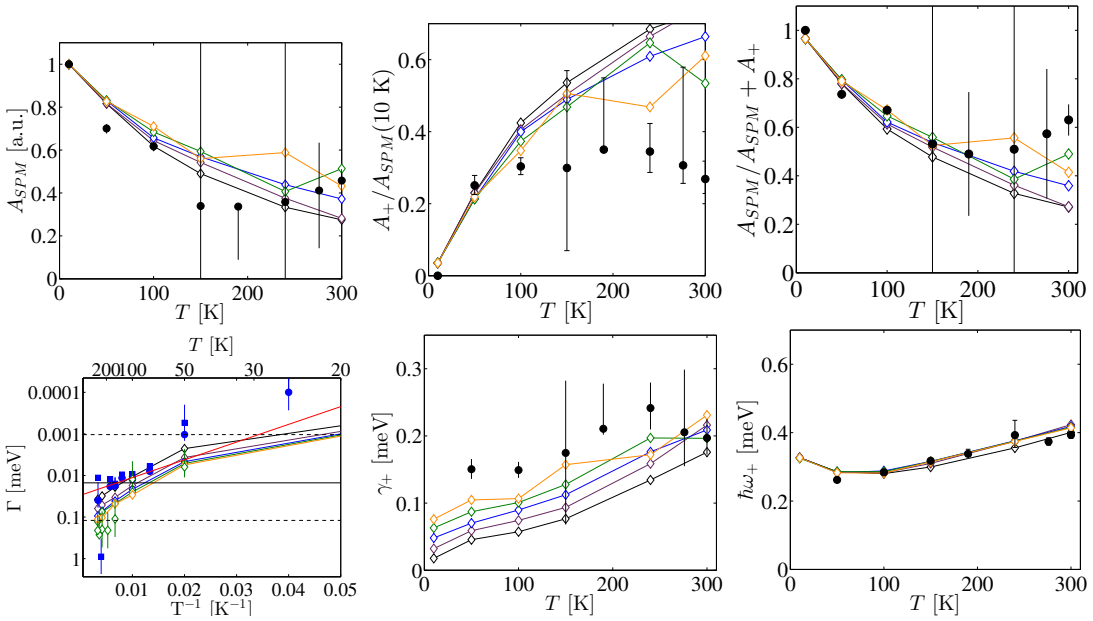

FIGURE D.17: Scan of λ. 3×10^{-4} (black), 6×10^{-4} (purple), 9×10^{-4} (blue), 12×10^{-4} (green), 15×10^{-4} (orange).

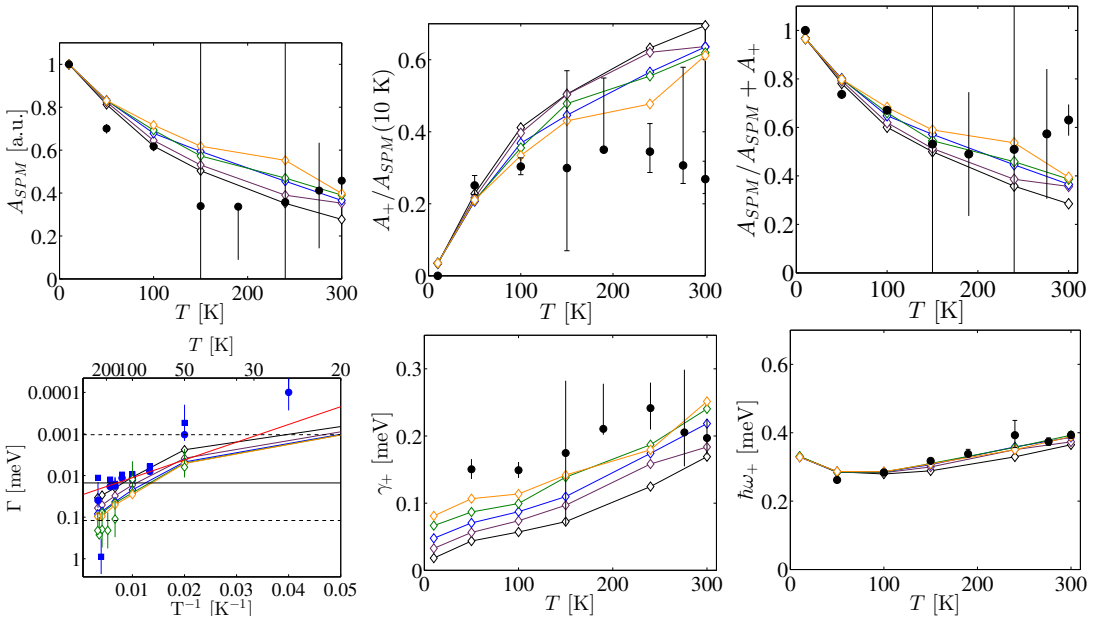

FIGURE D.18: Scan of λ. 3×10^{-4} (black), 6×10^{-4} (purple), 9×10^{-4} (blue), 12×10^{-4} (green), 15×10^{-4} (orange).

D.2.2 Scan of λ

The result of varying λ for the optimal parameters for $\xi = 1$ are shown in Fig. D.17. The same simulation for the optimal parameters for $\xi = 900$ T are shown in Fig. D.18

Appendix E

MATLAB code

Here, some of the most important MATLAB code is presented.

E.1 Initial calculations in simulations

```
% calculate the energy vector
    Nd=double(N);
    NFFT = 2^nextpow2(Nd)*8;
    f = 1/dt;                              % Sampling frequency [Hz]
    freq = f/2*linspace(0,1,NFFT/2+1); %use only half of the power ...
    spectrum
    Energy=freq*2*pi*hbar/meV; %convert to energy
    E_index=Energy<=max_energy;
    Energy=Energy(E_index);
    Energy=[fliplr(-Energy(2:end)) Energy(1) Energy(2:end)];

    % Set numberof spins on each sublattice
    N_A = N_total/(1 + xi);
    N_B = N_total/(1 + 1/xi);

    % Calculate total spin of each sublattice
    S_A = N_A*s;
    S_B = N_B*s;

    % set fluctuating field variance and std. dev. :
    D_A =  2 .* lambda * k_B .* T * hbar * dt /((g*mu_B)^2 * S_A);
    D_B =  2 .* lambda * k_B .* T * hbar * dt / ((g*mu_B)^2 *S_B);
    sigma_A = sqrt(D_A);
    sigma_B = sqrt(D_B);
```

E.2 The code for doing the numerical integration

```
function [m_A, m_B, t] = ...
    integrate_5(angles,B_1,B_2,B_X,B_ext,sigma_A,sigma_B,lambda,...
    T,N,dt,UsePreviousm,u_1,u_2, DM_strength,xi)
% physical constants
k_B = 1.38066e-23;
hbar = 1.05459e-34;
meV = 1.602e-22;
g = 2.002;
mu_B = 9.274e-24;
gamma = - g*mu_B/hbar;
% in terms of  Euler rotations:
% rotate phiS / phiT degrees about the z axis,
% then tetaS / tetaT degrees about the (new) x axis
% S and T refer to the macro-spins of each sublattice.
%%%%%%%%%%%%%%%%%%%%%%%%%%%%%%%%%%%%%%%%%%%%
% m_A and m_B are 3 x N arrays. Each row is a time point
m_A = zeros(3,N+1);
m_B = zeros(3,N+1);
if UsePreviousm ==1 %use the saved values of m_A and m_B to continue ...
    the simulation form there
    m_A(:,1)=u_1;
    m_B(:,1)=u_2;
else %do rotation
    phiA = angles(1,1)*2*pi/360;
    tetaA = angles(1,2)*2*pi/360;
    phiB = angles(2,1)*2*pi/360;
    tetaB = angles(2,2)*2*pi/360;
    DA = [ ...
        cos(phiA) sin(phiA) 0
        -sin(phiA) cos(phiA) 0
        0 0 1];
    DB = [ ...
        cos(phiB) sin(phiB) 0
        -sin(phiB) cos(phiB) 0
        0 0 1];
    CA = [ ...
        1 0 0
        0 cos(tetaA) sin(tetaA)
        0 -sin(tetaA) cos(tetaA)];
    CB = [ ...
        1 0 0
        0 cos(tetaB) sin(tetaB)
        0 -sin(tetaB) cos(tetaB)];
    m_A(:,1) = DA*CA*[0,0,1]';
    m_B(:,1) = DB*CB*[0,0,-1]';
end
t = (1:N)*dt; %create time vector
```

```
46
47  for i=1:N %do integration
48      %     effective fields
49      B_eff_A =( -xi*B_X * m_B(:,i) +  [B_1,0,B_2]'.* m_A(:,i) + ...
        B_ext-xi*DM_strength*[0 m_B(3,i) -m_B(2,i)]');
50      B_eff_B =( -   B_X * m_A(:,i) +  [B_1,0,B_2]'.* m_B(:,i) + B_ext+  ...
         DM_strength*[0 m_A(3,i) -m_A(2,i)]');
51
52      %     Runge-Kutta method of integration
53      k1_m_A = gamma * crossAB(m_A(:,i),B_eff_A)* dt + lambda * gamma * ...
        crossAB(m_A(:,i),crossAB(m_A(:,i),B_eff_A))* dt;
54      k1_m_B = gamma * crossAB(m_B(:,i),B_eff_B)* dt + lambda * gamma * ...
        crossAB(m_B(:,i),crossAB(m_B(:,i),B_eff_B))* dt;
55
56      B_eff_A_2 =( -xi*B_X * (m_B(:,i)+k1_m_B) +  [B_1,0,B_2]'.* ...
        (m_A(:,i)+k1_m_A) + B_ext - xi*DM_strength*[0 (m_B(3,i)+k1_m_B(3)) ...
        (-m_B(2,i)-k1_m_B(2))]');
57      B_eff_B_2 =( -   B_X * (m_A(:,i)+k1_m_A) +  [B_1,0,B_2]'.* ...
        (m_B(:,i)+k1_m_B) + B_ext +    DM_strength*[0 (m_A(3,i)+k1_m_A(3)) ...
        (-m_A(2,i)-k1_m_A(2))]');
58
59      k2_m_A = gamma * crossAB(m_A(:,i) + k1_m_A,B_eff_A_2)* dt + lambda ...
        * gamma * crossAB(m_A(:,i) + k1_m_A,crossAB(m_A(:,i) + ...
        k1_m_A,B_eff_A_2)) * dt;
60      k2_m_B = gamma * crossAB(m_B(:,i) + k1_m_B,B_eff_B_2)* dt + lambda ...
        * gamma * crossAB(m_B(:,i) + k1_m_B,crossAB(m_B(:,i) + ...
        k1_m_A,B_eff_B_2)) * dt;
61
62      if T>0 %include random term
63          b_fl_A = ...
        [normrnd(0,sigma_A),normrnd(0,sigma_A),normrnd(0,sigma_A)]';
64          b_fl_B = ...
        [normrnd(0,sigma_B),normrnd(0,sigma_B),normrnd(0,sigma_B)]';
65
66          m_A(:,i+1) = m_A(:,i) + 1/2*k1_m_A + 1/2*k2_m_A + gamma * ...
        crossAB(m_A(:,i),b_fl_A);
67          m_B(:,i+1) = m_B(:,i) + 1/2*k1_m_B + 1/2*k2_m_B + gamma * ...
        crossAB(m_B(:,i),b_fl_B);
68      else
69          m_A(:,i+1) = m_A(:,i) + 1/2*k1_m_A + 1/2*k2_m_A ;
70          m_B(:,i+1) = m_B(:,i) + 1/2*k1_m_B + 1/2*k2_m_B ;
71
72      end
73      % renormalize m_vectors
74      m_A(:,i+1) = m_A(:,i+1)/sqrt(dot(m_A(:,i+1),m_A(:,i+1)));
75      m_B(:,i+1) = m_B(:,i+1)/sqrt(dot(m_B(:,i+1),m_B(:,i+1)));
76  end;
77  end
```

Bibliography

[1] A. H. Morrish, "Canted Antiferromagnetism: Hematite". World Scientific, Singapore, 1994.

[2] E. Samuelsen and G. Shirane, "Inelastic Neutron Scattering Investigation of Spin Waves and Magnetic Interactions in alpha-Fe_2O_3," *phys. stat. sol.*, vol. 241, no. 42, pp. 241–256, 1970.

[3] G. Shirane, "Inelastic neutron scattering investigation of spin waves and magnetic interactions in Cr2O3," *Physica*, vol. 48, pp. 13–42, 1970.

[4] E. J. Samuelsen, "Spin Waves in Antiferromagnets with Corundum Structure," *Physica*, vol. 43, pp. 353–374, 1969.

[5] L. Néel and C. R. Hebd, "Superparamagnetisme des grains tres fins antiferromagnetiques," *Seances Acad. Sci.*, vol. 252, p. 4075, 1961.

[6] V. Satsangi, S. Kumari, A. Singh, R. Shrivastav, and S. Dass, "Nanostructured hematite for photoelectrochemical generation of hydrogen," *International Journal of Hydrogen Energy*, vol. 33, pp. 312–318, 2008.

[7] D. K. Bora, A. Braun, and E. C. Constable, ""In rust we trust". Hematite – the prospective inorganic backbone for artificial photosynthesis," *Energy & Environmental Science*, vol. 6, no. 2, p. 407, 2013.

[8] D. A. Wheeler, G. Wang, Y. Ling, Y. Li, and J. Z. Zhang, "Nanostructured hematite: synthesis, characterization, charge carrier dynamics, and photoelectrochemical properties," *Energy & Environmental Science*, vol. 5, no. 5, p. 6682, 2012.

[9] M. Hansen, F. Bødker, S. Mørup, K. Lefmann, K. Clausen, and P.-A. Lindgård, "Dynamics of Magnetic Nanoparticles Studied by Neutron Scattering," *Physical Review Letters*, vol. 79, pp. 4910–4913, 1997.

[10] S. Klausen, K. Lefmann, P.-A. Lindgård, K. Clausen, M. Hansen, F. Bødker, S. Mørup, and M. Telling, "An inelastic neutron scattering study of hematite nanoparticles," *Journal of Magnetism and Magnetic Materials*, vol. 266, pp. 68–78, 2003.

[11] S. Klausen, K. Lefmann, P.-A. Lindgård, L. Kuhn, C. Bahl, C. Frandsen, S. Mørup, B. Roessli, N. Cavadini, and C. Niedermayer, "Magnetic anisotropy and quantized spin waves in hematite nanoparticles," *Physical Review B*, vol. 70, pp. 1–6, 2004.

[12] L. Theil Kuhn, K. Lefmann, C. Bahl, S. Ancona, P.-A. Lindgård, C. Frandsen, D. Madsen, and S. Mørup, "Neutron study of magnetic excitations in 8-nm α-Fe_2O_3 nanoparticles," *Physical Review B*, vol. 74, pp. 1–9, 2006.

[13] W. Kündig, H. Bömmel, G. Constabaris, and R. H. Lindquist, "Some Properties of Supported Small alpha-Fe_2O_3 Particles Determined with the Mössbauer Effect," *Physical Review*, vol. 142, p. 137, 1966.

[14] W. B. Yue and W. Z. Zhou, "Crystalline mesoporous metal oxide," *Prog. Nat. Sci.*, vol. 18, pp. 1329–1338, 2008.

[15] Y. Ren, Z. Ma, and P. G. Bruce, "Ordered mesoporous metal oxides: synthesis and applications.," *Chemical Society reviews*, vol. 41, pp. 4909–27, 2012.

[16] C. Perego and R. Millini, "Porous materials in catalysis: challenges for mesoporous materials.," *Chemical Society reviews*, vol. 42, pp. 3956–76, 2013.

[17] A. Katsuhiko, V. Ajayan, Y. Yamauch, W. Ji, and J. P. Hill, "Nanoarchitectonics for Mesoporous Materials," *Bull. Chem. Soc. Jpn.*, vol. 32, pp. 1–32, 2012.

[18] W. Xuan, C. Zhu, Y. Liu, and Y. Cui, "Mesoporous metal-organic framework materials.," *Chemical Society reviews*, vol. 41, pp. 1677–95, 2012.

[19] A. H. Hill, H. Jacobsen, J. R. Stewart, F. Jiao, N. P. Jensen, S. L. Holm, H. Mutka, T. Seydel, A. Harrison, and K. Lefmann, "Magnetic properties of nano-scale hematite , α -Fe 2 O 3 , studied by time-of-flight inelastic neutron spectroscopy," *The Journal of Chemical Physics*, vol. 044709, pp. 1–8, 2014.

[20] K. Lefmann et al., "New dynamic "rotor" mode in antiferromagnetic nanoparticles," *Physical Review B (in preparation).*

[21] H. Jacobsen et al., "Numerical simulations of antiferromagnetic nanoparticles (working title)," *Physical Review B (in preparation).*

[22] S. Blundell, *Magnetism in Condensed Matter*. Oxford University Press, 2001.

[23] H. Bethe, "Zur Theorie der Metalle," *Zeitschrift für Physik*, vol. 71, p. 205, 1931.

[24] P. W. Anderson, "An Approximate Quantum Theory of the Antiferromagnetic Ground State," *Physical Review*, vol. 86, no. 5, p. 694, 1952.

[25] I. Dzyaloshinsky, "A Thermodynamic Theory of "Weak" Ferromagnetism of Antiferromagnetics," *J. Phys. Chem. Solids*, vol. 4, pp. 241–255, 1958.

[26] T. Moriya, "Anisotropic Superexchange Interaction and Weak Ferromagnetism," *Physical Review*, vol. 120, p. 91, 1956.

[27] C. R. Bahl, J. Garde, K. Lefmann, T. B. Jensen, P.-A. Lindgård, D. E. Madsen, and S. Mørup, "Uniform spin wave modes in antiferromagnetic nanoparticles with uncompensated moments," *The European Physical Journal B*, vol. 62, pp. 53–57, 2008.

[28] H. Chow and F. Keffer, "Soft surface magnons and the first-order magnetic phase transitions in antiferromagnetic hematite," *Phys. Rev. B*, vol. 10, no. 1, p. 243, 1974.

[29] F. Bødker and S. Mørup, "Size dependence of the properties of hematite nanoparticles," *Europhysics Letters (EPL)*, vol. 52, no. 2, pp. 217–223, 2000.

[30] C. Frandsen, C. Bahl, B. Lebech, K. Lefmann, L. Kuhn, L. Keller, N. Andersen, M. v. Zimmermann, E. Johnson, S. Klausen, and S. Mørup, "Oriented attachment and exchange coupling of α-Fe_2O_3 nanoparticles," *Physical Review B*, vol. 72, p. 214406, 2005.

[31] F. Jiao, A. Harrison, J.-C. Jumas, A. V. Chadwick, W. Kockelmann, P. G. Bruce, J. B. Building, W. M. Road, E. Eh, L. Agre, M. Cedex, I. Facility, C. Ox, and K. Ct, "Ordered Mesoporous Fe_2O_3 with Crystalline Walls," *J. Am. Chem. Soc.*, no. 128, pp. 5468–5474, 2006.

[32] A. H. Hill, F. Jiao, P. G. Bruce, A. Harrison, W. Kockelmann, and C. Ritter, "Neutron Diffraction Study of Mesoporous and Bulk Hematite ,," *Chem. Mater.*, no. 20, pp. 4891–4899, 2008.

[33] A. H. Hill and M. Allieta, "Pair distribution function (PDF) analysis of mesoporous α-Fe_2O_3 and Cr2O3.," *Physical chemistry chemical physics : PCCP*, vol. 15, pp. 8583–8, 2013.

[34] J. Garde, *Numerical Simulations of Magnetic Dynamics in Nanoparticles*. Master's thesis, University of Copenhagen, 2008.

[35] M. F. Hansen, F. Bødker, S. Mørup, K. Lefmann, K. N. Clausen, and P.-A. Lindgård, "Magnetic dynamics of fine particles studied by inelastic neutron scattering," *Journal of Magnetism and Magnetic Materials*, vol. 221, pp. 10–25, 2000.

[36] F. Bødker, M. F. Hansen, C. B. Koch, and K. Lefmann, "Magnetic properties of hematite nanoparticles," *Phys. Rev. B*, vol. 61, no. 10, pp. 6826–6838, 2000.

[37] C. R. H. Bahl, M. F. Hansen, T. Pedersen, S. Saadi, K. H. Nielsen, B. Lebech, and S. Mørup, "The magnetic moment of NiO nanoparticles determined by Mössbauer spectroscopy.," *Journal of physics. Condensed matter : an Institute of Physics journal*, vol. 18, pp. 4161–75, 2006.

[38] R. J. Elliott, J. A. Krumhansl, and P. L. Leath, "The theory and properties of randomIly disordered crystals and related physical systeIIIs," *Reviews of Modern Physics*, vol. 46, no. 3, p. 465, 1974.

[39] S. Mørup and C. Frandsen, "Thermoinduced Magnetization in Nanoparticles of Antiferromagnetic Materials," *Physical Review Letters*, vol. 92, pp. 1–4, 2004.

[40] L. Néel, "Théorie du traînage magnétique des ferromagnétiques en grains fins avec application aux terres cuites," *Annales de Géophysique*, vol. 5, pp. 99–136, 1949.

[41] W. F. Brown, "Thermal Fluctuations of a Single-Domain Particle," *Phys. Rev.*, vol. 130, pp. 1677–1686, 1963.

[42] J. Lee, "Spin correlation, excitation, and relaxation of antiferromagnetic hematite α-Fe_2O_3 nanoparticles," *Physical Review B*, vol. 70, pp. 3–8, 2004.

[43] P. A. Lindgård, A. Kowalska, and P. Laut, "Investigation of magnon dispersion relations and neutron scattering cross sections with special attention to anisotropy effects," *J. Phys. Chem. Solids*, vol. 28, pp. 1357–1370, 1967.

[44] C. Frandsen, "Mössbauer spectroscopy and its application to studies of magnetic nanoparticles". Lecture notes, Technical University of Denmark, 2014.

[45] K. Lefmann, "Neutron Scattering: Theory, Instrumentation and Simulation". Lecture notes, University of Copenhagen, 2014.

[46] G. L. Squires, "Introduction to the theory of Thermal Neutron Scattering". Cambridge University Press, 1994.

[47] P.-A. Lindgård, "Spin Waves and Magnetic Excitations 1". Elsevier, New York,, 1988.

[48] K. F. Riley, M. P. Hobson, and S. J. Bence, "Mathematical Methods for Physics and Engineering". Cambridge University Press, 2007.

[49] Reslib webpage. http://www.neutron.ethz.ch/research/resources/reslib.

[50] K. Lefmann and K. Nielsen, "McStas, a general software package for neutron ray-tracing simulations," *Neutron News*, vol. 10/3, pp. 20–23, 1999.

[51] K. Lieutenant, G. Zsigmond, S. Manoshin, M. Fromme, H. N. Bordallo, D. Champion, J. Peters, and F. Mezei, "Neutron instrument simulation and optimization using the software package VITESS," pp. 134–145, 2004.

[52] spec1d webpage. http://www.ill.eu/instruments-support/computing-for-science/cs-software/all-software/matlab-ill/spec1d/.

[53] W. H. Press, S. A. Teukolsky, W. T. Vetterling, and B. P. Flannery, "Numerical Recipes in C: The Art of Scientific Computing". Cambridge University Press, 2007.

[54] PSI webpage. http://www.psi.ch/sinq/ritaii/description, Apr. 2014.

[55] H. M. Rietveld, "A Profile Refinement Method for Nuclear and Magnetic Structures," *J. Appl. Cryst.*, vol. 2, p. 65, 1969.

[56] ILL webpage. https://www.ill.eu/instruments-support/instruments-groups/instruments/in5/description/instrument-layout/, Apr. 2014.

[57] W. P. Gates, H. N. Bordallo, L. P. Aldridge, T. Seydel, H. Jacobsen, V. Marry, and G. J. Churchman, "Neutron Time-of-Flight Quantification of Water Desorption Isotherms of Montmorillonite," *The Journal of Physical Chemistry C*, vol. 116, pp. 5558–5570, 2012.

[58] ILL webpage. https://www.ill.eu/instruments-support/instruments-groups/instruments/in16b/description/instrument-layout/, Apr. 2014.

[59] J. Ollivier, H. Mutka, and L. Didier, "The New Cold Neutron Time-of-Flight Spectrometer IN5," *Neutron News*, vol. 21, pp. 22–25, Apr. 2010.

[60] O. G. Randl, H. Franz, T. Gerstendörfer, Q. Petry, G. Vogl, and A. Magerl, "How to rejuvenate an old lady: New crystals for the backscattering spectrometer IN10," *Physica B: Condensed Matter*, vol. 234-236, pp. 1064–1065, 1997.

[61] H. Jacobsen, "Spin dynamics of hematite," Bachelor's thesis, University of Copenhagen, 2011.

[62] B. Frick, H. N. Bordallo, T. Seydel, J.-F. Barthélémy, M. Thomas, D. Bazzoli, and H. Schober, "How IN16 can maintain a world-leading position in neutron backscattering spectrometry," *Physica B: Condensed Matter*, vol. 385-386, pp. 1101–1103, 2006.

[63] E. Farhi, Y. Debab, and P. Willendrup, "iFit : A new data analysis framework . Applications for data reduction and optimization of neutron scattering instrument simulations with McStas," *Journal of Neutron Research*, vol. 17, pp. 5–18, 2014.

[64] D. Richard, M. Ferrand, and G. J. Kearley, "Analysis and visualisation of neutron-scattering data," *J. Neutron Res.*, vol. 4, no. 1–4, pp. 33–39, 1996.

[65] K. S. Singwi and A. Sjölander, "Diffusive Motions in Water and Cold Neutron Scattering," *Physical Review*, vol. 119, no. 3, p. 863, 1960.

[66] O. Petrenko, D. Paul, C. Ritter, T. Zeiske, and M. Yethiraj, "Magnetic frustration and order in gadolinium gallium garnet," *Physica B: Condensed Matter*, vol. 266, pp. 41–48, 1999.

[67] B. Frick, E. Mamontov, L. V. Eijck, and T. Seydel, "Recent Backscattering Instrument Developments at the ILL and SNS," *Zeitschrift für Physikalische Chemie*, vol. 224, pp. 33–60, 2010.

[68] J. L. García-Palacios and F. J. Lázaro, "Langevin-dynamics study of the dynamical properties of small magnetic particles," *Phys. Rev. B*, vol. 58, no. 22, pp. 937–958, 1998.

[69] L. D. Landau and E.M.Lifshitz, "Statistical Physics, vol. 5 of Course of Theoretical Physics". Butterworth-Heinemann, third ed., 1980.

[70] K. Levenberg, "A method for the solution of certain non-linear problems in least squares," *Quarterly Journal of Applied Mathmatics*, vol. II, no. 2, pp. 164–168, 1944.

[71] D. Marquardt, "An algorithm for least-squares estimation of nonlinear parameters," *Journal of the Society for Industrial and Applied Mathematics*, vol. 11, no. 2, pp. 431–441, 1963.

[72] J. Kennedy and R. C. Eberhart, "Particle swarm optimization," *Proc. IEEE Conf. on Neural Networks, Piscataway, NJ*, vol. IV, pp. 1942–1948, 1995.

[73] M. Bertelsen, H. Jacobsen, U. Bengaard Hansen, H. Hoffmann Carlsen, and K. Lefmann, "Exploring performance of neutron guide systems using pinhole beam extraction," *Nuclear Instruments and Methods in Physics Research Section A: Accelerators, Spectrometers, Detectors and Associated Equipment*, vol. 729, pp. 387–398, 2013.